# Transition Metal Fluoride Cathodes in Liquid Lithium Metal Batteries

Lorenz F. Olbrich

The Queen's College
University of Oxford

*A thesis submitted for the degree of Doctor of Philosophy*

Trinity 2024

## Abstract

The aviation industry is responsible for more than 2% of the world's energy-related carbon dioxide emissions. Although it is among the fastest-growing sources of emissions, it is also one of the most challenging sectors to decarbonize. Electrifying aviation to reduce emissions necessitates the development of next-generation batteries that offer higher energy densities and enhanced safety. In addition, rate capabilities that are compatible with the power requirements during take-off and landing are necessary.

Intercalation cathodes are intrinsically limited in energy density and pose an inherent safety risk due to the risk of oxygen release at high temperatures, which can lead to a thermal runaway. In contrast, transition-metal-fluoride (TMF) cathodes offer a three- to five-fold increase in charge capacity due to a multi-electron conversion mechanism and excellent thermal stability due to the ionic nature of the metal-fluoride bond. When paired with a Li-metal anode, stack-level energy densities of over $700\,\mathrm{W\,h\,kg^{-1}}$ can be achieved. Their practical implementation, however, faces challenges due to their low electronic and ionic conductivity and low cycling reversibility. This thesis lays the foundational groundwork for the practical implementation of a TMF-Li-metal battery by comprehensively examining its cathode, electrolyte, and anode.

First, a new $FeF_2$ wet-milling strategy and composite preparation technique are developed, which enable unprecedented cycling reversibility for composites with high active material contents. The cathodes are used to examine the effect of bis(fluorosulfonyl)imide anions and temperature on electrochemical behavior. The results indicate the viability of TMF cathodes to meet technical requirements for electric flight, however, they highlight the importance of electrolyte optimization.

Second, an electrolyte development tool based on operando Raman gradient analysis is presented. Utilizing an external reference enables the visualization of concentration gradients of every Raman active species in the electrolyte. Gradients can be used to extract transport and thermodynamic properties of the electrolyte in a unified setup, which are key parameters to determine a battery's rate capability. The external reference further enables the detection of Li-filament propagation. By incorporating a thermal chamber, the effect of temperature on transport and solvation in electrolytes can be studied.

Third, the electrolyte-Li metal interphase, a crucial determinant for cycling reversibility, is studied using electrochemical impedance spectroscopy. The effect of cell design, Li preparation, temperature, salt concentration, and Li activity on the cell impedance is explored. The results are used to deconvolute interphase impedances from the native passivation layer and solid electrolyte interphase.

# Transition Metal Fluoride Cathodes in Liquid Lithium Metal Batteries


Lorenz F. Olbrich

The Queen's College

University of Oxford

A thesis submitted for the degree of

*Doctor of Philosophy*

Trinity 2024

This thesis is dedicated to
Klaus Wania and Walter Olbrich
Your love, support, and inspiration have shaped who I am today

# List of Publications

This thesis is established based on the following articles:

- Olbrich, L. F., Albert, W. X., Pasta, M. Conversion-type fluoride cathodes: Current state of the art. *Current Opinion in Electrochemistry* **30**, 100779 (2021).

- Olbrich, L. F., Xiao, A. W., Schart, M., Ihli, J., Matthews, G., Sanghadasa, M., Pasta, M. Iron fluoride-lithium metal batteries in bis (fluorosulfonyl) imide-based ionic liquid electrolytes. *Cell Reports Physical Science*, **5**, 2 (2024)

- Olbrich, L. F., Jagger, B., Ihli, J., Pasta, M. Operando Raman Gradient Analysis for Temperature-Dependent Electrolyte Characterization, *ACS Energy Letters*, **9**, 3636-3642 (2024)

- Olbrich, L. F., Jagger, B., Pasta, M. Deconvolution of Li metal interphase formation processes. *Manuscript in preparation*

Other articles contributed to:

- Suttle, M. D., Olbrich, L. F., Bays C. L., Riches, L., Rapid heating rates define the volatile emission and regolith composition of (3200) Phaethon, *Nature Communication*, **15 (1)**, 7178, (2024)

- Dhir, S., Cattermull, J., Jagger, B., Schart, M., Olbrich, L. F., Zhao, J., Sada, K., Goodwin, A., Pasta, M. Characterisation and Modelling of Potassium-ion Batteries. *Nature Communication*, **15(1)**, 7580, (2024)

- Burton, M., Narayanan, S., Jagger, B., Olbrich, L. F., Dhir, S., Shibata, M., Lain M., Astbury, R., Fumany, M., Favillier, H., Butcher, N., Copley, T., Pasta, M. Thin Lithium Metal Anodes for Solid-State Batteries: The Case for Scalable Evaporation. *Nature Energy*, accepted for publication, (2024)

- Zhao, J., Jagger, B.*, Olbrich, L. F.*, Ihli, J., Dhir, S., Zyskin, M., Pasta, M. Transport and Thermodynamic Properties of KFSI in TEP by Operando Raman Microspectroscopy *ACS Energy Letters*, **9**, 1537-1544 (2024)

- Li, J., Shibata, M., Liang, Y., Olbrich, L. F., Safonova, O. V., Ihli, J., Kotaka, T., Aotani, K., Aihara, Y., Pasta, M., Impact of Fabrication Methods on FeF2 Cathode Composites for Li6PS5Cl-Based Solid-State Batteries. *Manuscript in preparation*

- Galatolo, G., Alshangiti, O., Di Mino, C., Matthews, G., Xiao, A.W., Rees, G.J., Schart, M., Chart, Y.A., Olbrich, L. F., Pasta, M., Advancing Fluoride-Ion Batteries with a Pb-PbF2 Counter Electrode and a Diluted Liquid Electrolyte *ACS Energy Letters*, **9.1**, 85-92 (2023)

- Olbrich, L. F., Revolutionising energy storage: Lithium ion batteries and beyond *The Oxford Scientist*, *Opinion* (2023)

- Gelner, A., Eitel, M., Mikhail, M., Olbrich, L. F., Pierri, A., Borgato, A., Landgraf, T., An exploration on the effectiveness of face-to-face and virtual meetings in educational projects dealing with impact innovation. *CERN IdeaSquare Journal of Experimental Innovation*, **7.1**, 12-17 (2023)

- Simons, P., Schenk, S. A., Gysel, M. A., Olbrich, L. F., Rupp, J. L. A Ceramic-Electrolyte Glucose Fuel Cell for Implantable Electronics. *Advanced Materials*, **34.24**, 2109075 (2022)

* B.J. and L.F.O. contributed equally.

# Acknowledgements

First, I would like to express my deepest gratitude to my supervisor and mentor, Professor Mauro Pasta. Thank you for providing me with the opportunity to follow my passion for battery research as a member of your group. The resources you have provided and the lab you have established in recent years are unparalleled. I greatly appreciate the academic freedom I received, your scientific rigor and critical mind, *the getting things done* mindset you teach us, and your unwavering support in my career.

I would also like to extend this gratitude to Dr. Mohan Sanghadasa, our project collaborator and primary point of contact with our funding partners. Our numerous scientific discussions have provided valuable feedback and food for thought on my research directions. Your passion for science is genuinely infectious.

Thank you to the Engineering and Physical Sciences Research Council, the Army Research Office, The Queen's College, the Department of Materials, and the Electrochemical Society for their financial support.

The members of the Pasta Group are the backbone of its success, and it has been a true privilege to work in such an intellectually stimulating environment. In particular, I would like to thank Dr. Albert Xiao for his training and rapid onboarding when I joined the group. The knowledge I gained from you in the first few months has been instrumental in my success in projects years later. I would also like to thank Dr. Johannes Ihli for his guidance and structured project planning. I greatly appreciate that you are always available to listen. Your kindness and foresight have helped me and many others successfully navigate our PhD journeys. Further, I would like to acknowledge Ben Jagger for all our fruitful collaborations. It has been a great pleasure to work with you on challenging problems. Your broad knowledge and sharp insights have fueled my excitement and progress in our research. Next, I want to thank Dr. Shobhan Dhir. You are not only a great science communicator and the social glue who brings people together but have also become a true friend.

I also want to mention the students I had the privilege to supervise and work with. Your work has greatly contributed to the success of our projects. Thank you, Manav Kakkanat, for your dedicated work in assembling impedance cells; Saskia Krefting, for your tireless efforts in working with atomically thin AFM tips; and XinXin Chen, for preparing coin and pouch cells.

Additionally, I would like to thank more collaborators and colleagues, including Dr. Maximilian Schart for always making time to measure last-minute samples and

discuss results, Dr. Giulia Galatolo for being the best office neighbor, the "fluoride-ion queen," and a formidable Blender competitor, and Dr. Guillaume Matthews for his reliability and rapid assistance whenever needed. I also appreciate Dr. Matthew Burton for his project management skills and highly scientific lunchtime discussions. Special thanks to Shibatasan Masafumi and our other Nissan collaborators for our fruitful collaborations, Professor Sudarshan Narayanan for his guidance and advice, and Dr. Krishnakanth Sada and Professor Soochan Kim for our engaging fluoride cathode discussions.

Thank you, Yi Liang and Po-Yuan Huang, for your support, laughs, and companionship, especially during late hours in the office.

A shout-out to Jacob Christianson, Souhard Kotakad, Xinyao Ma, Yvonne Chart, Liwei Dai, Omar Alshangiti, Emily Milan, and the rest of the Pasta group for all the scientific—and not so scientific—discussions in the office and over lunch.

Many thanks also to Neil Cadman, Dr. Esther Townsend, and Dr. Zheng Huang for supporting my travels and lab work, respectively - Rex Richards would not run without you.

In addition to those at Rex Richards, I want to express my gratitude to the staff at the PTCL workshop. I cannot recommend them highly enough. Your work has been consistently flawless, and your experience and willingness to support my design iterations have been tremendously helpful. A workshop staffed with individuals like you elevates a good university to a world-class research hub.

I also want to extend my thanks to Senior Finance Officer Julie Carlin for her continuous support. Your pragmatic and efficient work style has made my life much easier.

I feel incredibly grateful to have met so many remarkable people throughout my stay in Oxford. Starting a PhD during an ongoing pandemic made socializing a bit awkward, but multiple periods of isolation also turned into a unique bonding experience. I am particularly thankful to my Oxley-Wright Crew—especially Nicky, whose banter and chats always crack me up within seconds.

A special group even stayed with me for the remaining years of my stay—thank you to Jeremy, Hans, Havard, Estelle, and Annina. The numerous movie nights, feasts, chess tournaments, and parties we shared were incredible. You guys have truly been my home over the last three years.

Our flat received a valuable addition towards the end. Thank you, Johannes, for being a true friend, a source of inspiration and heated discussions, and a fierce rowing competitor.

The rowing community also brought Saoud into my life, a truly gem of a person with a heart full of kindness and a brain full of knowledge.

Thank you also to KC and Axel (and Paula!). You made rowing so much more enjoyable, even if not faster.

At this point, I would like to extend my gratitude to the Queens College Boat Club, all the people who help run the club, and the partners who fund the sport. Rowing has been an ideal balance to my research, filled with painful erg sessions, crisp sunrises, emotional races, fancy dinners, and even a Hollywood movie, making this an incredibly intense yet rewarding experience.

Besides rowing, I met many wonderful people through my college. Thank you to Kiran for introducing me to the world of politics and for running all the events at the MCR so smoothly.

At a college event, I also met Elle. Thank you for giving me new perspectives, original ideas, and a glimpse into the world of AI. I am excited to see how far you will push the boundaries!

I would also like to mention the staff and students from the Collège des Ingénieurs. The projects I was able to work on provided me with new perspectives, a refreshing change of scenery, and inspiration from business leaders and innovators.

Lastly, I had the privilege of meeting Hannah. You turned my life upside down. I have never met anyone with a moral compass as steadfast as yours, the capability to make the world a better place, and the ambition and tenacity to do so. Thank you for being by my side and giving me strength.

Besides the incredible people I met in Oxford, I have been fortunate to have friends who have supported me throughout my entire life. Moving around can be a scary and lonely experience, yet I never had to face these feelings alone thanks to your continuous presence.

Specifically, I want to mention Lu, who has always been a loyal companion, a great listener, and the best host imaginable whenever I returned home.

Additionally, I want to thank Marco. You have journeyed with me to all my destinations, consistently offering new perspectives and insights, and providing unparalleled hospitality.

Thank you also to Julia, who has kept our group united, providing me with continuous updates, and welcoming me back whenever I'm around.

On that note, I also want to acknowledge Luki, Addi, and Kathrin, who have been constants in my life for over/almost two decades.

Throughout my journey, I also met Gayané, to whom I am deeply grateful for her endless stream of happiness and hospitality. I truly believe you have cracked the code on how to live life, and I am excited to learn it from you one day.

Thank you also to Jorge, my favorite social butterfly and a true fountain of happiness.

Thank you to Anton—you inspired me during critical moments and have always been there for me when needed.

The same goes for Yori—you have shown me the world, provided inspiration and advice, and supported me in all my endeavors. I will never forget that!

Finally, and most importantly, I want to thank my family.

To my grandparents, who inspired me with their lives rich in experiences, stimulated my curiosity during my upbringing, instilled important values, and were nothing but supportive throughout my entire life.

To my sister Margarete and her husband Christopher, thank you for your hospitality, your regular visits, and for always engaging with my provocative discussions.

And lastly, to my parents, Ute and Thomas, I have been incredibly privileged to grow up in such a loving and supportive environment. You taught me to explore the world, instilled in me a gift for curiosity and a critical mindset, and enabled me to follow my passions and dreams. I will be forever thankful for the opportunities you provided me with.

# Abstract

The aviation industry is responsible for more than 2% of the world's energy-related carbon dioxide emissions. Although it is among the fastest-growing sources of emissions, it is also one of the most challenging sectors to decarbonize. Electrifying aviation to reduce emissions necessitates the development of next-generation batteries that offer higher energy densities and enhanced safety. In addition, rate capabilities that are compatible with the power requirements during take-off and landing are necessary.

Intercalation cathodes are intrinsically limited in energy density and pose an inherent safety risk due to the risk of oxygen release at high temperatures, which can lead to a thermal runaway. In contrast, transition-metal-fluoride (TMF) cathodes offer a three- to five-fold increase in charge capacity due to a multi-electron conversion mechanism and excellent thermal stability due to the ionic nature of the metal-fluoride bond. When paired with a Li-metal anode, stack-level energy densities of over $700\,\mathrm{W\,h\,kg^{-1}}$ can be achieved. Their practical implementation, however, faces challenges due to their low electronic and ionic conductivity and low cycling reversibility. This thesis lays the foundational groundwork for the practical implementation of a TMF-Li-metal battery by comprehensively examining its cathode, electrolyte, and anode.

First, a new $FeF_2$ wet-milling strategy and composite preparation technique are developed, which enable unprecedented cycling reversibility for composites with high active material contents. The cathodes are used to examine the effect of bis(fluorosulfonyl)imide anions and temperature on electrochemical behavior. The results indicate the viability of TMF cathodes to meet technical requirements for electric flight, however, they highlight the importance of electrolyte optimization.

Second, an electrolyte development tool based on operando Raman gradient analysis is presented. Utilizing an external reference enables the visualization of concentration gradients of every Raman active species in the electrolyte. Gradients can be used to extract transport and thermodynamic properties of the electrolyte in a unified setup, which are key parameters to determine a battery's rate capability. The external reference further enables the detection of Li-filament propagation. By incorporating a thermal chamber, the effect of temperature on transport and solvation in electrolytes can be studied.

Third, the electrolyte-Li metal interphase, a crucial determinant for cycling reversibility, is studied using electrochemical impedance spectroscopy. The effect of cell design, Li preparation, temperature, salt concentration, and Li activity on the cell impedance is explored. The results are used to deconvolute interphase impedances from the native passivation layer and solid electrolyte interphase.

# Contents

# List of Figures

# List of Abbreviations

**AFM** atomic force microscopy

**AGGs** aggregates

**ARC** accelerating rate calorimeter

**BSE** backscattered electrons

**CAD** computer-aided design

**CD** co-dispersion

**CE** coulombic efficiency

**CEI** cathode electrolyte interphase

**CIPs** contact-ion-pairs

**CNF** carbon nano fiber

**CNT** carbon nano tubes

**CP** chronopottentiometry

**CPE** constant-phase-element

**CST** concentrated solution theory

**DFN** Doyle-Fuller-Newman

**DRT** distribution of relaxation time

**DSC** differential scanning calorimetry

**ECM** equivalent circuit model

**EDX** energy dispersive x-ray spectroscopy

**EIS** electrochemical impedance spectroscopy

**EV** electric vehicle

**EVs** electric vehicles

**G4** tetraethylene glycol dimethyl ether

**GCPL** galvanostatic cycling with potential limitation

**GEIS** galvanostatic electrochemical impedance spectroscopy

**GF** glass fiber

**GITT** galvanostatic intermittent titration technique

**IL** ionic liquid

**LCO** lithium cobalt oxide

**LiBs** lithium-ion batteries

**LiFSI** lithium bis(fluorosulfonyl)imide

**LiTFSI** lithium bis(trifluoromethanesulfonyl)imide

**MDI** mean decrease in impurity

**MP** mortar and pestle

**MRI** magnetic resonance imaging

**NMR** nuclear magnetic resonance

**NPL** native passivation layer

**OCV** open circuit voltage

**ORGA** operando raman gradient analysis

**OSM** Onsager-Stefan-Maxwell

**PDE** partial differential equation

**PECS** precision etching coating system

**PFA** perfluoroalkoxy alkanes

**pfg-NMR** pulsed-field gradient nuclear magnetic resonance spectroscopy

**PI** polyimide

**PID** proportional–integral–derivative

**PITT** potentiostatic intermittent titration technique

**PP** polypropylene

**RE** reference electrode

**rmse** root square mean error

**SEI** solid electrolyte interphase

**SEM** scanning electron microscopy

**STA** simultaneous thermal analyzer

**STA-cell** tailor-made battery casing for STA measurements

**STEM** scanning transmission electron microscopy

**SVF** solvent velocity factor

**TEM** transmission electron microscopy

**TLM** transmission line model

**TMF** transition metal fluoride

**UHV** ultrahigh vacuum

**US** ultra-stirring

**WE** working electrode

**XANES** x-ray absorption near edge structure

**XAS** x-ray absorption spectroscopy

**XPS** x-ray photoelectron spectroscopy

**XRD** x-ray diffraction

# 1 Introduction

## Contents



## 1.1 Contextualization

Climate change represents the most significant challenge of modern times and necessitates urgent action. Representatives from 195 countries have signed the Paris Agreement, committing to the objective of limiting the increase in global average temperature to well below 2 °C above pre-industrial levels. [1] Achieving this goal requires a dramatic reduction in emissions.

Key strategies include the transition to renewable energy sources and the electrification of transportation, both of which heavily rely on advancements in electrochemical energy storage. While the first batteries were developed in the 18$^{\text{th}}$

century, a significant revolution in energy storage was triggered by the development and commercialization of lithium-ion batteries (LiBs) in the 1990s.

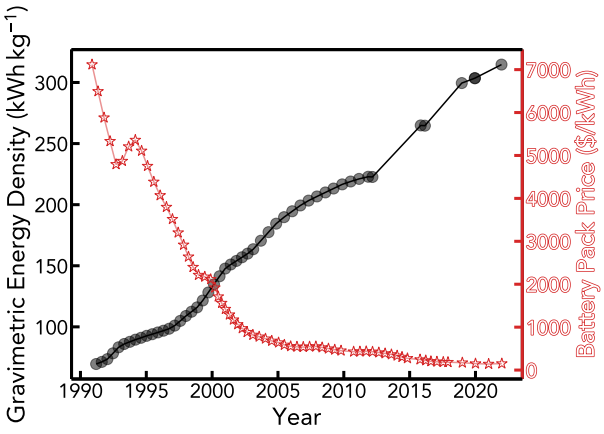


**Figure 1.1: Development of gravimetric energy density and battery pack price over the last 30 years: a,** Cell level energy density over the last 30 years and **b,** corresponding battery pack price. Data collected from [2] and [3].

LiBs allow the storage of more energy in smaller and lighter batteries at an increasingly low cost. Over the last 30 years, the gravimetric cell level energy density has been rapidly increasing from below 50 kW h kg$^{-1}$ to over 300 kW h kg$^{-1}$ while the corresponding pack price was at a record low of \$139 kW$^{-1}$ h in 2023 as depicted in Figure 1.1. [2, 3] The price competitiveness, improvements in cell safety, and fast charging capabilities have enabled the advent of portable technologies and, in recent years, electric vehicle (EV). The industry now faces major challenges in large-scale battery manufacturing and supply chain management to meet the rapidly increasing demand for LiBs. [4] Simultaneously, it is crucial to explore new chemistries for electrochemical energy storage to maintain continuous improvements in energy densities. LiBs are intrinsically limited in energy density, and we are rapidly approaching their theoretical limit. [2] Specifically, to electrify the aviation industry, a sector which contributed to 2% of global $CO_2$ emission, a step increase in energy density is necessary, requiring cell level energy densities above 500 kW h kg$^{-1}$, which is physico-chemically impossible with conventional LiBs. [2, 5, 6] Moreover, cell safety, rate capability, and cycle life cannot be compromised for practical implementation. In particular, during take-off and landing, electric flight applications require high

power loads. [6] These can range from 1C up to 5C depending on the aircraft design. [6–8] While a battery's energy density is fundamentally determined by its electrode materials, cell safety, rate capability, and cycle life are strongly dependent on the electrolyte. Therefore, a holistic approach that covers the cathode, electrolyte, and anode in material development for next-generation batteries is required.

## 1.2 Fundamentals of Batteries

A battery comprises two electrodes, made of a species $i$, separated by an ion-conducting electrolyte and connected via an external circuit. The change of energy for the reaction occurring at the electrode is given by the change in Gibbs free energy for each half-cell reaction. Consider an arbitrary reduction reaction at the left electrode and an arbitrary oxidation reaction at the right electrode.

$$\Delta G = \left(\sum_i s_i \mu_i\right)_{\text{right}} - \left(\sum_i s_i \mu_i\right)_{\text{left}} \tag{1.1}$$

where $G$ is the Gibbs free energy, $\mu_i$ is the electrochemical potential of species $i$, and $s$ is the stoichiometric coefficient of species $i$. The sign of $s$ is positive if the species is a reactant, and negative if it is a product. If $\Delta G$ is negative electrons will flow spontaneously from the left electrode to the right electrode. [9] If the external circuit is controlled by a potentiostat, and the potential is set so that no electrons flow, the equilibrium or open circuit voltage (OCV) potential, $E_{OCV}$ is measured. The equilibrium potential is related to the Gibbs free energy by:

$$\Delta G = -zFE_{OCV} \tag{1.2}$$

$z$ is the number of electrons involved in the electrode reaction, and $F$ is Faraday constant. The electrochemical potential of a species can be related to its activity $a_i$.

$$\mu_i = \mu_i^\circ + RT \ln a_i \tag{1.3}$$

where $\mu_i^\circ$ represents the standard electrochemical potential of a species, independent of its concentration, $R$ is the universal gas constant, and $T$ the temperature. Combining equations 1.1, 1.2, and 1.3 , yields:

$$E_{OCV} = -\frac{(\sum_i s_i\mu_i^\circ)_{\text{right}} - (\sum_i s_i\mu_i^\circ)_{\text{left}}}{zF} - \frac{RT}{zF}\ln\left(\prod_i a_i^{s_i}\right)_{\text{right}} + \frac{RT}{zF}\ln\left(\prod_i a_i^{s_i}\right)_{\text{left}} \tag{1.4}$$

with

$$E^0 = -\frac{(\sum_i s_i\mu_i^\circ)_{\text{right}} - (\sum_i s_i\mu_i^\circ)_{\text{left}}}{zF} \tag{1.5}$$

$$E_{OCV} = E^0 - \frac{RT}{zF}\ln\left(\frac{(\prod_i a_i^{s_i})_{right}}{(\prod_i a_i^{s_i})_{left}}\right) \tag{1.6}$$

1.4 is the Nernst equation and relates the equilibrium potential to the activity of reactants and products. Often, equation 1.4 is written without the components from the "left" term which implies that the potential of the right electrode is measured with respect to some unspecified left electrode. [9] When the electrode is connected to an external power supply the electrochemical potential of electrons in the electrode can be controlled, perturbating the equilibrium and driving a reaction. Noteworthy, the potential of an electrode cannot be controlled by itself. Instead, it must always be controlled relative to another electrode. In the same way, potentials can only be measured relative to some reference state. [9]

$$E_{OCV} = E_{left} - E_{right} \tag{1.7}$$

In a battery, two half-cell reactions occur simultaneously and are spatially separated. If $E_{OCV}$ is positive, *i.e.* $\Delta G$ is negative, both half-cell reactions will occur spontaneously when electrons are allowed to flow between the electrode through the external circuit. Thus, $E_{OCV}$ is a descriptor for the driving force of the half-cell reactions to proceed. In the battery community, the positive electrode is conventionally referred to as the cathode, and the negative electrode is the anode. Once a current is drawn $E_{OCV}$ is reduced by overpotentials, $\eta_{total}$, to a cell potential $E_{cell}$:

$$E_{cell} = E_{OCV} - \eta_{total} \tag{1.8}$$

$\eta_{total}$ is the sum of all overpotentials, further elaborated on in section 2.1.2. During the discharge of a cell, a reduction reaction occurs at the cathode, while simultaneously, an oxidation reaction occurs at the anode. Specifically, in LiBs, oxidation at the anode involves the release of positively charged lithium ions ($Li^+$) into the electrolyte and negatively charged electrons ($e^-$) into the external circuit. Concurrently, at the cathode, a $Li^+$ is intercalated, and the metal center of the cathode accepts an electron, undergoing reduction. A schematic of a conventional LiB is shown in Figure 1.2a. The electrolyte, spatially separating the two half-cell reactions and thus preventing a short-circuit of the cell, serves as an ion-conducting medium. Since $Li^+$ release and uptake at the electrodes is only possible if $Li^+$ is locally available at the interface, the electrolyte must exhibit a high ionic conductivity. In fact, transport through the electrolyte can often be the charge or discharge limiting process in a battery. Chapter 4 of this thesis addresses lithium transport in liquid electrolytes.

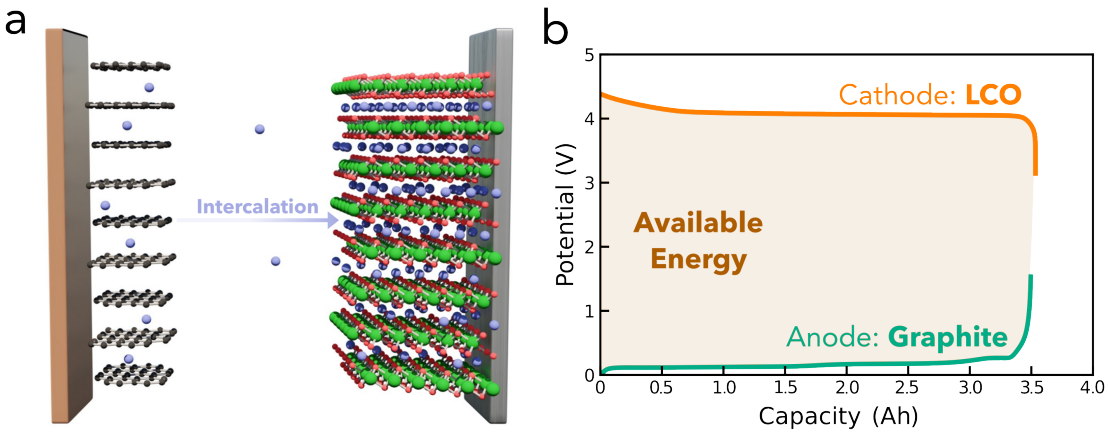


**Figure 1.2: Conventional LiB: a,** Schematic of a conventional LiB where lithium is released from a graphite anode, shuttled through the electrolyte and intercalated into the cathode. The graphic was adapted from Isaac Capone. **b,** Galvano static plot with potential limitation for a LiB. Cathode (LCO) and anode (Graphite) potentials are plotted separately. The available energy of the battery is highlighted. Both electrodes are adjusted in weight so that the capacities are balanced. The total capacity of the battery is inspired by a commercial 18650 cell.

Besides the cell potential $E_{cell}$, the gravimetric capacity $q_{gravimetric}$ $(mAhg^{-1})$ of electrodes is of fundamental importance when determining the theoretical energy

density of a battery. $q_{gravimetric}$ can be calculated from the number of electrons ($z$), and therefore $Li^+$ that is stored, and its molar mass ($M$).

$$q_{gravimetric} = \frac{zF}{M} \tag{1.9}$$

Figure 1.2b shows the electrode potentials as a function of capacity for a commercial 18650 LiB, comprising a lithium cobalt oxide (LCO) cathode and a graphite anode. LCO has a theoretical capacity of $274\,\mathrm{mA\,h\,g^{-1}}$, of which around $140\,\mathrm{mA\,h\,g^{-1}}$ can be reversibly used. Graphite, on the other hand, has a theoretical capacity $372\,\mathrm{mA\,h\,g^{-1}}$, of which around $360\,\mathrm{mA\,h\,g^{-1}}$ can be used. Consequently, the masses of active material are balanced so that the capacities of both electrodes match.

In a standard two-electrode cell, only the potential difference of cathode and anode $E_{cell}$ would be measurable, however, a reference electrode was employed to illustrate both cathode and anode potential in Figure 1.2b respectively. The integral of the potential difference $E_{cell}$ over the capacity corresponds to the available energy ($Energy_{cell}$) that can be stored in a battery.

$$Energy_{\mathrm{cell}} = \int_0^Q E_{\mathrm{cell}}\, dq \tag{1.10}$$

where $Q$ indicates the maximum capacity of the cell, $E_{\mathrm{cell}}$ the measured cell potential, and $q$ the cell capacity. It becomes evident that in order to maximize the energy density of a cell, the potential difference and capacity of the cell should be maximized.

## 1.3 Cathode

Commercial LiBs comprise intercalation-type cathode materials. These are layered structures such as LCO, $LiNi_xMn_yCo_zO_2$ (NMC), and $LiNi_{0.8}Mn_{0.15}Al_{0.05}O_2$ (NCA), olivine structures such as $LiFePO_4$ (LFP), and spinel structures such as in $LiMn_2O_4$. [10, 11] Charge is stored via intercalation of $Li^+$ into a limited number of interstitial sites within the stable host lattice. However, this storage mechanism imposes an upper physicochemical limit in energy density because capacities

approach their theoretical values and a further increase in potential imposes safety concerns and electrochemical stability complications with electrolytes. [12]

Consequently, new chemistries are explored with higher capacities. Conversion cathodes can store multiple lithium equivalents per metal center and, therefore, increase the theoretical capacity three- to sixfold compared to intercalation materials. Promising conversion cathodes are based on sulfur [10] or transition metal fluoride (TMF) chemistries. An extensive literature review on TMF cathodes is presented in chapter 3.1.1. A schematic of a $FeF_2$-Li-metal battery is shown in Figure 1.3a.

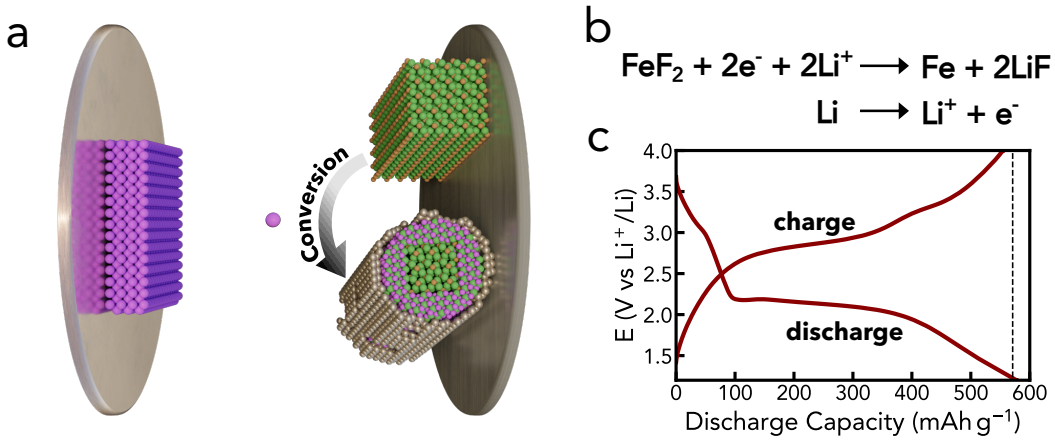


**Figure 1.3: TMF-Li-metal Battery: a,** Schematic of a $FeF_2$-Li-metal battery. **b,** Oxidation and reduction reaction during discharge occur at the anode and cathode, respectively. **c,** GCPL of a TMF-Li-metal battery at the second cycle.

TMF cathodes are unique in that, unlike other conversion compounds, they exhibit electrode potentials high enough to be practically viable cathodes. For example, $Fe_3O_4$ is reduced at a potential around 1 V lower than $FeF_2$ due to the ionic character of the metal-fluoride bond. The electronegative fluoride draws valence electrons from the metal center and thus reduces the shielding of the d-electrons, increasing its electrochemical potential. [13] In the case of a $FeF_2$-Li-metal battery, two Li-equivalents can be stored, and metallic iron and LiF are formed upon discharge as shown in Figure 1.3b. This results in a theoretical capacity of 571 mA h $g^{-1}$, which, as shown in Figure 1.3c, can be fully utilized. The practical capacity is almost four times larger than the one of LCO. Chapter 3.1 of this thesis is dedicated to the development and characterization of energy-dense $FeF_2$ cathodes.

## 1.4 Electrolyte

Electrolytes are crucial components in batteries because they determine their performance. Critical metrics for electrolytes are lithium transport to enable rapid mass transfer in the bulk electrolyte, fast charge transfer at the electrode, electrochemical stability, decomposition products suitable to form a stable solid electrolyte interphase (SEI), thermal stability and toxicity, and costs. [14]

### 1.4.1 State-of-the-art Electrolytes

Classically, electrolytes comprise a lithium salt dissolved in a solvent. Over time, various combinations of salt additives and co-solvents have been added to improve cell performance. Initially, lithium-metal anode electrolytes were based on carbonates, which were then substituted by more stable ethers. In the 2010s, fluorinated salts and solvents gained popularity due to their beneficial SEI-forming properties. [15] Promising salts include lithium bis(fluorosulfonyl)imide (LiFSI) and lithium bis(trifluoromethanesulfonyl)imide (LiTFSI). They have shown particularly good performance when used in high concentrations. As such, fluorinated ionic liquid (IL) electrolytes have demonstrated promising cycling performance as well. [16] Recently, Localized-High-Concentration-Electrolytes (LHCE) were developed, which enable the beneficial properties of highly concentrated electrolytes at low salinity concentrations. [17]

### 1.4.2 Electrolyte Properties

To understand and model electrolytes, concentrated solution theory (CST) has been developed, which describes lithium transport in liquid electrolytes. Parts of its derivation are described in more detail in 4.1.2. CST describes how four fundamental transport and thermodynamic properties determine lithium transport, that is, the salt diffusivity $D_{\mathrm{app}}$, the transference number $t_+^0$, the thermodynamic factor $\chi_{\mathrm{M}}$, and the ionic conductivity $\kappa$. The accurate measurement of these properties is experimentally challenging, time- and resource intensive, and consequently, reports are scarce. Their dependence on temperature is explored even less and is commonly

limited to a few temperature points. Chapter 4 addresses this limitation by introducing a holistic experimental approach that combines the measurement of temperature-dependent thermodynamic and transport properties with macroscopic cycling phenomena in a unified setup.

**Salt Diffusivity**

$D_{\text{app}}$ quantifies the rate at which ions move through the electrolyte under a concentration gradient. It can be measured via the restricted-diffusion method. [14, 18–20] Therein, a two-electrode cell of known interelectrode distance ($L$) is polarized. Following the OCV ($\phi_{OCV}$) during subsequent relaxation allows calculation of $D_{\text{app}}$.

$$\lim_{t\to\infty} \frac{d\ln(\phi_{OCV})}{dt} = -\frac{\pi^2 D_{\text{app}}}{L^2} \tag{1.11}$$

To study self-diffusivities ($D_i$), pulsed-field gradient nuclear magnetic resonance spectroscopy (pfg-NMR) can be used. In contrast to $D_{\text{app}}$, $D_i$ describes the ionic movement of individual ions. By calculating the harmonic mean, $D_{\text{app}}$ can be estimated from $D_i$.

In binary electrolytes, $D_{\text{app}}$ decreases with concentration due to the increased viscosity of the solution. High $D_{\text{app}}$ are beneficial for fast lithium transport and mitigate concentration gradient formation.

**Transference Number**

$t_+^0$ describes the fraction of the total ionic current carried by a specific ion ($i$) in the electrolyte. It is defined as:

$$t_{\text{i}} = \frac{I_i}{I_{total}} \tag{1.12}$$

Further, $t_+^0$ can be related to ion mobilities $\mu$ via:

$$t_+ = \frac{z_+\mu_+}{z_+\mu_+ + z_-\mu_-} \tag{1.13}$$

The most common practice to measure the transport number $t_+$ is the Hittorf method. [18, 20, 21] The technique involves polarizing a cell and measuring the

change in concentrations in separate cell compartments. The concentration change in each compartment is then proportional to $t_+$.

$$t_+ = 1 - \frac{\Delta n_{\text{cell}}}{n_{\text{charge}}} = \frac{F(\Delta c_s)A}{Q} \tag{1.14}$$

$$\Delta c_s = c_s^i - c_s^f \tag{1.15}$$

here $n_{\text{charge}}$ is the number of moles of $e^-$ passed through the cell during polarization, $n_{\text{cell}}$ is the molar difference of the compartment close to both electrodes before and after polarization, $t$ is polarization time, $Q$ is the amount of charge passed over time, $A$ is the area of the electrodes, and $c_s^i$ and $c_s^f$ are the initial and final concentration of each compartment respectively. It is important to highlight that the Hittorf method determines $t_+$ and not $t_+^0$. The key difference is that $t_+$ assumes the electrolyte is infinitely dilute, or thermodynamically ideal implying that ions are perfectly dissociated in solution and there is no interaction with the solvent. In contrast $t_+^0$ describes the relative lithium movement referenced to solvent movement, *i.e.* accounting for solvent velocity. [18]

In order to use the Hittorf method to calculate $t_+^0$, Monroe *et al.* derived an equation to include the solvent reference velocity. [18]

$$t_+^0 = \frac{F(\Delta c_s)A}{Q(1 - c_s^i)V_s} \tag{1.16}$$

where $V_s$ is the partial molar volume of the salt, which is accessible through the concentration dependency of the electrolyte density $\rho$.

High $t_+^0$ are desirable for electrolytes; however, they are difficult to achieve due to the high charge density and strong solvation of $Li^+$ in most electrolytes, slowing down its relative movement compared to anions. In some IL electrolytes, negative $t_+^0$ have been observed as a result of nano-aggregate formation. [22]

### Thermodynamic Factor

$\chi_M$ provides a link between observed concentration and thermodynamic activity. According to the extended Debye-Hueckel theory, quantifying the electrostatics of ions in solution, $\chi_M$ and its variation with concentration and temperature are reflective of the non-ideality behavior of electrolytes. [14, 18, 23] The Debye-Hueckel-Guggenheim equations contain competing contributions from ion-ion and ion-solvent interactions. By definition, $\chi_M$ is 1 at infinite dilution. With increasing salt concentration, $\chi_M$ decreases due to electrostatic interactions between ions in solution. [14] At higher salt concentrations, $\chi_M$ deviates from classical electrostatic theory, and several models have been developed to describe ionic species in solution. [14, 20, 24, 25] Generally $\chi_M$ increases with solute concentrations since the solvent becomes increasingly bound, which decreases its vapor pressure, leading to an increase in salt activity. [20] The concentration where $\chi_M$ is one indicates where ion-solvent interaction out-compete ion-ion interaction.

$\chi_M$ is conventionally determined in concentration cells by measuring the liquid junction potential. [18, 20] Concentration cells comprise two electrodes and two chambers, filled with different electrolyte concentrations and separated by a porous frit to enable electrochemical contact while reducing interdiffusion. The measured OCV can be used to, in combination with $t_+^0$, to calculate $\chi_M$

$$\chi_M = \frac{nF}{2RT(1-t_+^0)} \frac{\nabla \phi_{OCV}}{\nabla \ln \frac{c_2}{c_1}} \tag{1.17}$$

$c_1$ and $c_2$ are the electrolyte concentrations in both chambers, respectively.

### Ionic Conductivity

$\kappa$ is a descriptor for the mobility of ions in the presence of an electric field and the absence of concentration gradients, and thus, it determines the electric current. At high dilution, $\kappa$ increases with salt concentration since more charge carriers are available to conduct current. However, it reaches a maximum when the increase in ion-ion interactions and electrolyte viscosity outweighs the benefits of having more available charge carriers. Since $\kappa$ is the reciprocal of the ohmic drop, it

is, in contrast to the other three properties, straightforward to measure using high-frequency electrochemical impedance spectroscopy (EIS). [19, 26, 27]

$$\kappa = \frac{L}{R_0 A} \tag{1.18}$$

where $L$ is the interelectrode distance and $A$ the electrode surface area. Ideally, measurements are conducted in a conductivity cell with blocking electrodes and a known cell constant $\tau = \frac{L}{A}$ to maximize the accuracy of the impedance measurement.

High ionic conductivities are crucial for rapid lithium transport, keeping ohmic drop overpotentials as low as possible, particularly during fast cycling rates.

## 1.5 Anode

Ideal anode materials operate at low reduction potentials and exhibit large capacities to maximize the energy density of the full cell. Most LiBs available to date use graphite anodes. In recent years the development of silicon anodes has made substantial progress with announcements of its commercial use in premium EVs in the near future. [28] However, the holy grail of anodes is metallic lithium, as it exhibits the lowest reduction potential ($-3.04\,\mathrm{V}$ vs SHE) and the highest possible capacity due to the absence of a host structure ($3860\,\mathrm{mA\,h\,kg^{-1}}$). [29, 30] Unfortunately, commercial use of lithium metal anodes is impeded by insufficient cycling reversibility. [15, 30]

As illustrated in Figure 1.4, most anodes lie outside the electrochemical stability window of electrolytes. Consequently, the electrolyte decomposes, and a solid electrolyte interphase (SEI) forms. An ideal SEI passivates the anode and thus prevents continuous reaction with the electrolyte. Unlike graphite anodes, existing electrolytes cannot form fully passivating SEI on lithium metal anodes. [15, 30]

A good measure for cycling reversibility is coulombic efficiency (CE), which is the ratio of the amount of lithium that can be stripped from the negative electrode to that plated in the subsequent cycle. The formation of a SEI inevitably consumes lithium, thereby reducing the CE during the first charge. However,

lithium plating/stripping through the SEI can be inhomogeneous, exposing fresh lithium to the electrolyte and resulting in active lithium loss due to additional electrolyte decomposition or isolation of electronically insulated "dead" lithium, and consequently reducing the CE to below 100% after the first cycle. [15, 29, 30]

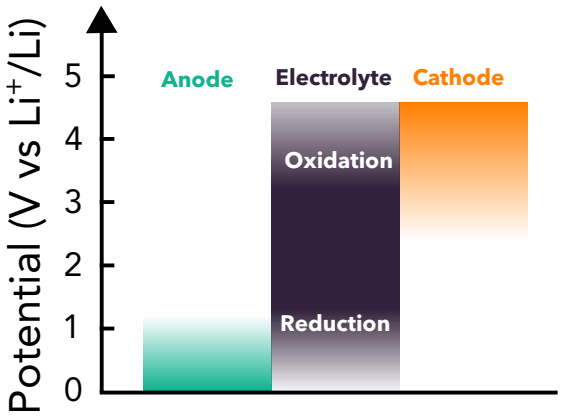


**Figure 1.4: Electrolyte Stability Window Schematic:** Operating potential of anodes and cathodes compared to the electrochemical stability window of the electrolyte.

Therefore, the SEI on lithium anodes is studied extensively to understand its microstructure and physico-chemical properties better using a wide range of characterization techniques including (cryo) transmission electron microscopy (TEM) [31–37], x-ray photoelectron spectroscopy (XPS) [38, 39], atomic force microscopy (AFM) [40], and EIS. [41–43] Chapter 5 is an in-depth investigation of the lithium metal - electrolyte interphase using EIS. A historical overview of EIS studies on the lithium SEI is provided separately in section 5.1.2.

## 1.6 Thesis Objective

This thesis aims to provide a holistic investigation of TMF-Li-metal batteries in liquid electrolytes. Therefore, the three main active components — cathode, electrolyte, and anode — are investigated in dedicated chapters. The focus is on the development and characterization of $FeF_2$ cathodes, lithium transport in liquid electrolytes, and the lithium metal-electrolyte interphase, respectively. More precise objectives for each sub-project are provided in their respective chapters.

# 2
# Methods

## Contents



## 2.1 Electrochemical Characterization

### 2.1.1 Electrochemical Impedance Spectroscopy (EIS)

EIS is an experimental technique to characterize electrical, electrochemical, and physical processes over a wide range of timescales. The electrochemical system is perturbated from its equilibrium state by a sinusoidal signal (AC current or AC voltage) $x(t)$ over a wide range of frequencies. The system's sinusoidal signal response (AC voltage or AC current) $y(t)$ is monitored as illustrated in Figure 2.1

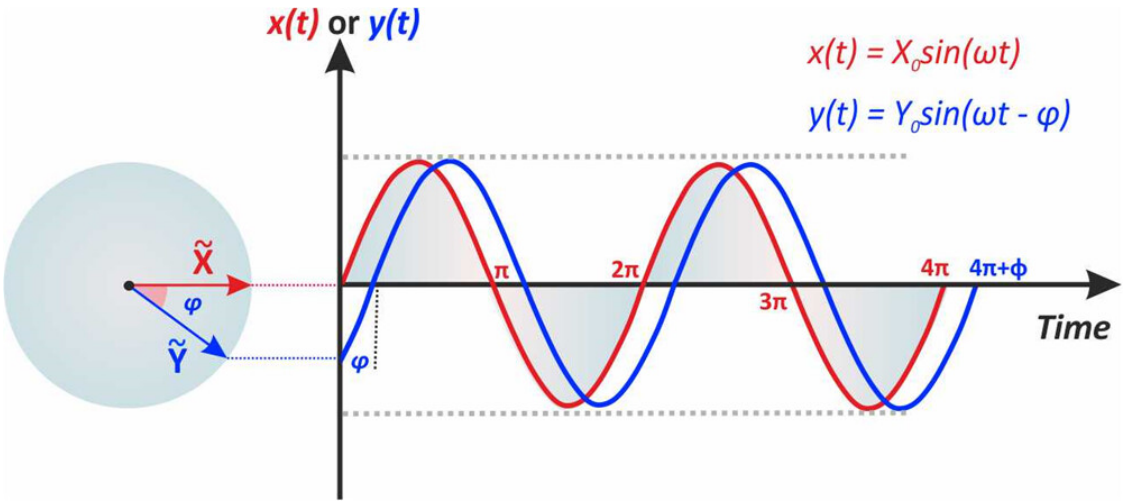


**Figure 2.1: System Pertubation in EIS**. Input signal $x(t)$ and output signal $y(t)$ over time. Reprinted from Lazanas et al. [44]

If the system under investigation is linear and time-invariant, a transfer function relates the input and output signal. This is generally the case if three requirements are satisfied.

a) Linearity: The input and output signals must have the same frequency. Electrochemical systems are generally nonlinear, but linearity can be reasonably assumed when using small-amplitude perturbation signals. To verify this, the system can be perturbed at various amplitudes. If the assumption of linearity holds, the system should produce the same impedance regardless of the perturbation amplitude. This concept can be demonstrated with Lissajous plots. The symmetry and behavior of the Lissajous plot over time help determine whether a system adheres to the constraints of linearity.

b) Causality: The output signal is exclusively determined by the input signal.

c) Stability: The system remains stable until it is disturbed by a perturbation and should return to its original state once the perturbation is over. Measurement repeats can indicate if this is the case. Since many electrochemical systems are not stable, great care should be taken when choosing the lower frequency limit, where the effect of system instabilities becomes more visible. Modern potentiostats and control software allow a drift correction, where the perturbation signal is evaluated in consideration of adjacent frequencies.

The validity of impedimetric data can be evaluated using the Kramers-Kronig relations. In the Kramers-Kronig relation test, the real part of the impedance is calculated from the imaginary part and vice versa, which allows the detection of errors in the impedance measurement. [44]

Assuming the input signal is a voltage perturbation $V(t)$ and the output signal a current response $I(t)$ with

$$V(t) = V_0 \sin(\omega t) \tag{2.1}$$

$$I(t) = I_0 \sin(\omega t + \varphi) \tag{2.2}$$

where $\varphi$ is the angular phase shift and $\omega$ is the angular frequency which relates to the the frequency $f$ by

$$\omega = 2\pi f \tag{2.3}$$

The impedance can then be calculated from the Fourier transforms of $V(t)$ and $I(t)$ and the resulting phaser $\tilde{V}(\omega)$ and $\tilde{I}(\omega)$. A phasor is a complex number that represents the amplitude and phase of a sinusoidal signal.

$$Z(\omega) = \frac{\tilde{V}(\omega)}{\tilde{I}(\omega)} = |Z|e^{j\varphi} = |Z|(\cos\varphi + j\sin\varphi) = Z' + jZ'' \tag{2.4}$$

where $Z'$ and $Z''$ are the real and imaginary parts of the impedance, respectively. It is noteworthy that when the input signal is voltage, and the output signal is a current, measurements correspond to admittance, the inverse of impedance.

Impedance data can be analyzed by simulating it to an equivalent circuit model (ECM). The most common circuit components for electrochemical systems are resistors $R$, capacitors $C$, and inductances $L$.

$$Z_R = R \tag{2.5}$$

$$Z_C = \frac{1}{i\omega C} \tag{2.6}$$

$$Z_L = i\omega L \tag{2.7}$$

Circuit components can be combined in series

$$Z_{tot} = \sum Z_i \tag{2.8}$$

and in parallel.

$$\frac{1}{Z_{tot}} = \sum \frac{1}{Z_i} \tag{2.9}$$

For a meaningful analysis, the ECM must be an accurate representation of components in the system under investigation. ECMs are not unique to impedance data, nor are all ECMs mathematically different. Orazem showed the ambiguous nature of EIS analysis, where experimental data can be fitted with excellent agreement to multiple, different ECMs, which implied different surface chemistries and, thus, physical interpretations. [45] It is, therefore, necessary to develop the model based on solid physical evidence. However, designing such a physical model becomes challenging as soon as one deviates from a simple (ideal) experimental setup. Take, for example, the Randles circuit, one of the most common and simplest equivalent circuits to fit an electrochemical system. [46] Its physical interpretation is the immersion of a perfectly flat, metal electrode into a redox-active liquid electrolyte. It describes the ionic resistance of the electrolyte, $R_0$, in series with a capacitor, $C_{dl}$, which represents the charging of an electric double layer in parallel to a resistor, originating from the charge transfer resistance, $R_{CT}$ associated with the Faradaic reaction. Finally, there is a Warburg element to describe the semi-infinite linear diffusion of particles to the metal electrode. However, most electrochemical systems of interest, and in particular Li-metal electrodes, are far more complicated. For example, the metal surface is not atomically flat and covered by passivation layers. As a result, experimental data rarely shows good fits with a Randles circuit, and a common practice is to substitute the capacitor with a constant-phase-element (CPE). [44, 47–52] CPEs do not have physical meanings, and their application is commonly rationalized with a distribution of time constant caused by surface inhomogeneities and roughness [53] Yet its application entails complications that

many researchers are negligent about. For example, calculating the true capacitance of a CPE is far from trivial and only valid under certain assumptions. [54]

Ultimately, the choice of ECM depends on the objective of the EIS fit. If one aims to quantify a total interphase resistance on an electrode surface, a CPE fit can yield a straightforward and fast analysis. However, if one seeks to gain more in-depth insights into the origin and deconvolution of interphase impedances, a more advanced fitting approach is required. [53]

Once a suitable ECM is found, the impedance data is fit, in this thesis using a non-linear least squares regression, to the ECM, and physical properties from the circuit components are obtained. [55]

EIS measurements are prone to measurement artifacts. A flawed experiment design due to unshielded wiring or instrument limitations can falsify the data or give rise to features that are not related to the investigated system. As elaborated on in section 5.3.1, custom-made cell designs and shielded measurement cables were used to avoid measurement artifacts in this study. [44, 45, 56, 57]

### 2.1.2 Galvanostatic Cycling

Cell cycling is conducted using a galvanostatic cycling with potential limitation (GCPL) protocol. Therefore, a constant current is drawn or supplied to discharge and charge a cell, respectively, as illustrated in Figure 2.2.

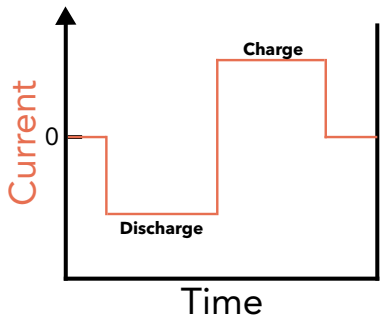


**Figure 2.2: GCPL Schematic:** Current as a function of time for GCPL.

The potential is monitored over time. The half cycle is stopped once the potential reaches an upper and lower potential threshold. Commonly, a resting period before,

between charge and discharge, and after cell cycling is incorporated into the protocol. A capacity can be calculated from the current and the measurement time. GCPL is often plotted for cell potentials over gravimetric capacities.

The measured potential is the sum of an equilibrium potential and overpotentials which can be grouped into three categories.

- **Ohmic Drop:** An instantaneous overpotential that is present as soon as a current is drawn. It originates from the ionic conductivity of the electrolyte and the contact resistances of the wires. The ohmic drop scales linearly with the current.

- **Surface Overpotential:** The surface overpotential, or activation overpotential, is the potential difference above the equilibrium required to initiate the redox event. The rate of a redox reaction can be related to the surface overpotential by the Butler-Volmer equation.

- **Concentration Overpotential:** The concentration or mass transfer overpotential is a result of charge carrier depletion at the reaction site. A concentration gradient can form inside an electrode composite or within the electrolyte. It is commonly more dominant at larger currents and requires some time to form. Fick's law of diffusion can be used to relate a concentration difference with an areal current.

Quantification of overpotentials can be a powerful way to gain insights into the fundamentals and limitations of a redox reaction. Electrochemical techniques such as galvanostatic intermittent titration technique (GITT) are used to deconvolute the ohmic drop, surface activation overpotential, from the concentration overpotential, which can serve as an estimate for the diffusion coefficients inside electrode composites.

Processing the GCPL data enables a differential capacity analysis. $\frac{dQ}{dV}$ describes the capacity change to potential change ratio and can be used to study redox reactions, e.g., with the onset of a potential plateau or growing overpotentials.

### 2.1.3 Three-Electrode Cells

In three electrode cells a reference electrode (RE) is added to the working and counter electrode. A three-electrode cell configuration enables the deconvolution of working electrode (WE) and counter electrode (CE) contributions. This can be used to plot the WE and CE as a function of cycling time, which allows the identification of capacity limitation, electrode degradation, etc. Further, an RE allows the deconvolution of impedances from both electrodes, respectively. As discussed in section 5.3.1, there are challenges associated with measuring EIS in three-electrode configurations. In this study, all reported three-electrode data was collected in commercial EL-cells. Prior experiments involved custom-made Swagelok cells. However, due to a lack of pressure control in the cell design, they were replaced. A schematic of the EL cell is shown in Figure 2.3a and b.

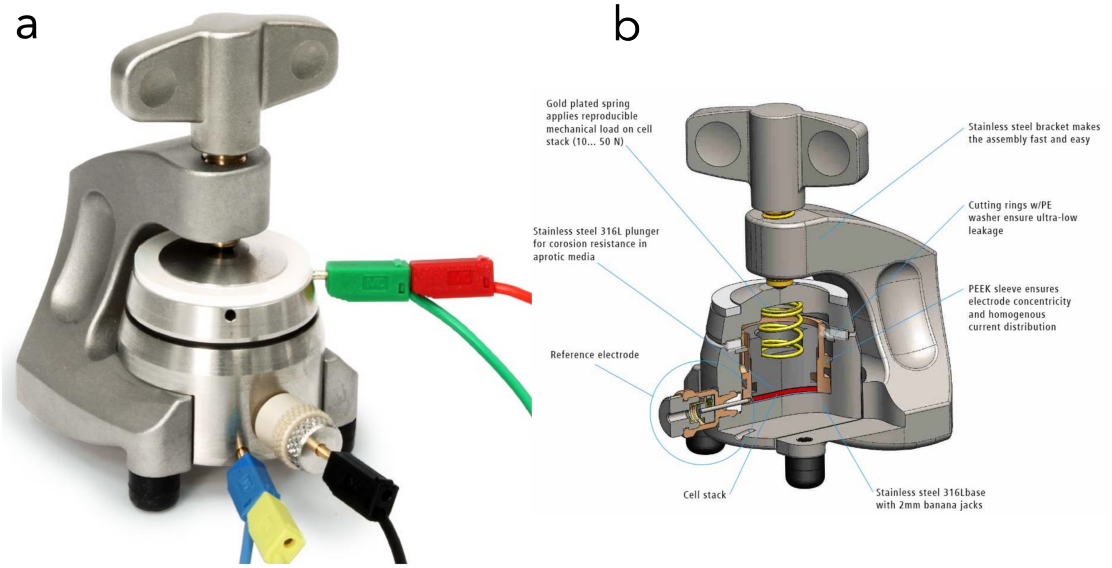


**Figure 2.3: EL Cell: a,** Photo of an EL-cell **b,** Schematic of an EL-cell. Reprinted from the supplier. [58]

## 2.2 Materials Characterization

### 2.2.1 Scanning Electron Microscopy (SEM)

scanning electron microscopy (SEM) is an essential tool for examining the morphology of materials at sub-micron scales. The limitations of optical microscopes,

confined by the wavelength of visible light, are surpassed by SEM which employs a high-energy electron beam. This beam has a wavelength much shorter than visible light, enabling finer resolution. As the electron beam scans the sample, it generates secondary electrons, backscattered electrons, and characteristic x-rays through various scattering and adsorption interactions, as illustrated in Figure 2.4. The tear-shape interaction volume can range from 100 nm to approximately 5 µm depending on the electron energy, atomic number of the specimen, and the specimen's density. [59] Within the top layer of the interaction volume, low energy secondary electrons (<50 eV) are ejected from the conduction or valence band of the specimen. Secondary electrodes provide the highest resolution for morphological mapping. The contrast in the images comes from the angle of the surface from which the electrons are emitted, offering detailed morphological and topological insights into the material's surface. [59]

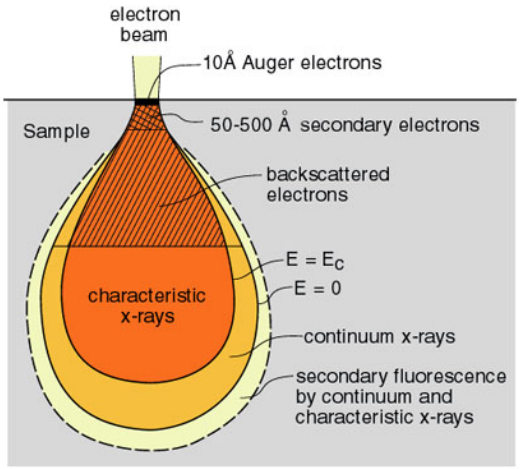


**Figure 2.4: SEM Interaction Volume:** Schematic of the interaction volume of SEM. Reprinted from the web. [60]

Deeper into the sample below the secondary electrons is the area where backscattered electrons (BSE) (keV) originate from. The primary beam is backscattered by atoms and the intensity of BSEs can be correlated with the atomic number of the specimen since heavy atoms scatter stronger and thus appear brighter and vice versa. Hence BSEs are used to detect a contrast of areas with different chemical compositions. Even deeper into the substrate, an electron beam can lead to the

ejection of an electron from the inner shell of an atom, creating an electron hole. This hole can be filled with an electron from an outer, higher energy shell, releasing the energy difference of the shells in the form of an x-ray. Since the emitted x-rays are characteristics of each atom in the observed sample, elemental analysis is possible. This technique is called energy dispersive x-ray spectroscopy (EDX). Besides, there are further interactions that can be detected, such as photons within the visible light spectrum, Auger electrons, and secondary fluorescence. SEM can achieve image resolutions as fine as around 1 nm. [59]

### 2.2.2 Powder X-ray Diffraction (XRD)

x-ray diffraction (XRD) is a characterization technique based on the diffraction of an incident x-ray at the atoms of the specimen. A constructive or destructive interference can occur depending on the phase relationship of the wave. Constructive interference is defined by Bragg's law: [61]

$$n\lambda = 2d\sin(\theta) \tag{2.10}$$

where $\lambda$ is the radiation wavelength, $d$ the interplanar spacing, $\theta$ the angle of incident x-rays, and $n$ an integer.

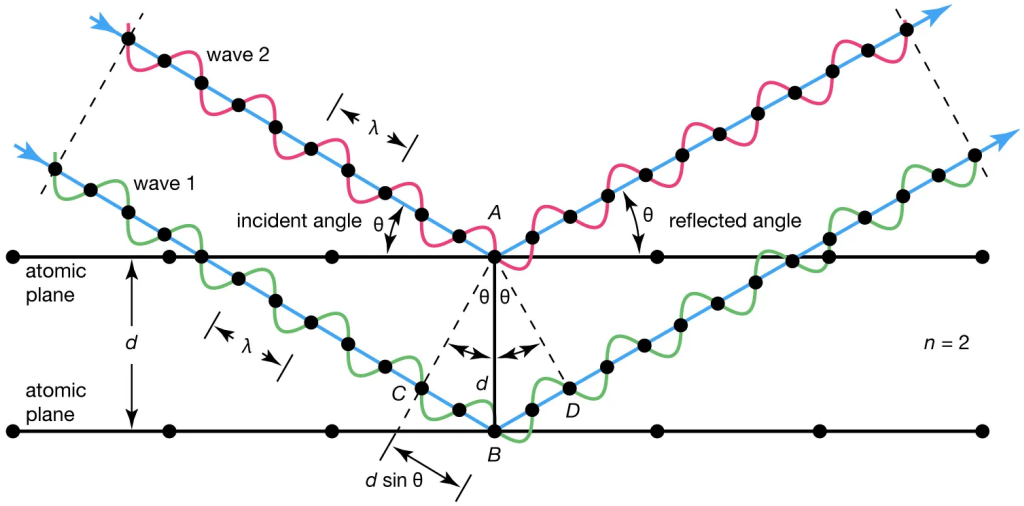


**Figure 2.5: XRD Operation Principle:** x-ray diffracted on atomic planes. Reprinted from the web. [**x-rayXRD**]

A specimen is measured from different $\theta$ angles, and whenever Bragg's law is met, *i.e.* interference occurs, peaks are measured. Thus the number, position, and intensity of diffraction peaks can help to quantitatively describe the crystal structure of a specimen. [61]

### 2.2.3 Atomic Force Microscopy (AFM)

AFM is a high-resolution imaging technique that allows for the examination of surfaces at the atomic level. It operates primarily through a cantilever with a sharp tip that gently contacts or hovers near the surface of a sample. This tip, only a few nanometers in diameter, scans across the sample in a controlled manner. [62]

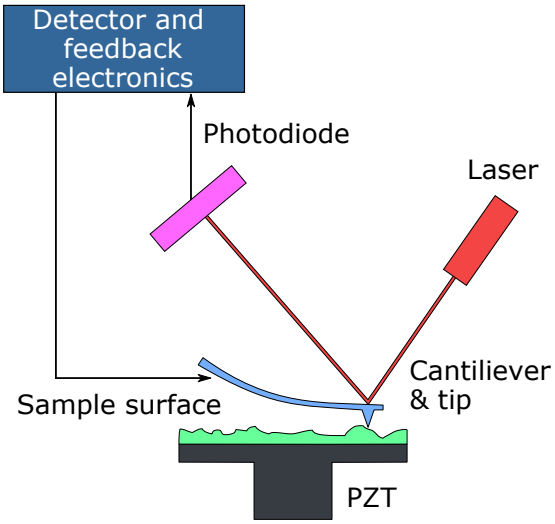


**Figure 2.6: AFM Operation Principle:** Schematic of the operation principle of an AFM. Reprinted from the web. [63]

As the tip moves over the sample surface, it experiences forces such as van der Waals forces or electrostatic forces, depending on the distance to the surface molecules. These interactions cause the cantilever to deflect. A laser beam, typically aimed at the back of the cantilever, reflects onto a position-sensitive photodetector. The cantilever deflections alter the direction of the reflected laser beam, which is recorded by the photodetector. [62]

The data from the photodetector is then converted into a topographic map of the surface. This map reflects the sample's surface features at very high resolution,

often down to the atomic level. AFM can operate in various modes, including contact, non-contact, and tapping modes, each suitable for different types of samples and analysis purposes. [62]

All AFM measurements in this study were conducted by Ben Jagger and Saskia Krefting. [64]

### 2.2.4 X-ray Photoelectron Spectroscopy (XPS)

XPS is a surface-sensitive spectroscopy technique used to investigate the chemical composition and electronic state of materials at the atomic level. It involves exposing a specimen with x-rays to eject electrons from its surface layers, a process fundamentally based on the photoelectric effect discovered by Albert Einstein. [61]

When a material is exposed to x-rays, electrons are emitted from the surface. The energy of these photoelectrons is highly specific to the elements from which they originate and their chemical environment. By measuring the kinetic energy ($E_{kinetic}$) of the photoelectron, one can calculate the binding energy ($E_{binding}$) via [61]

$$E_{binding} = E_{photon} - (E_{kinetic} + \phi) \tag{2.11}$$

where $\phi$ is a work function-like term for the specific surface. From there, it is possible to determine the elemental composition, chemical states, and electronic states of the atoms present in the top few nanometers of the material's surface. XPS can be coupled with an ion beam to etch away surface layers of the specimen and thus yield a depth profile. [61]

All XPS measurements in this study were conducted by Ben Jagger.

### 2.2.5 Raman Spectroscopy

Raman spectroscopy is a characterization technique used to determine vibrational modes of molecules. This non-destructive spectroscopic method relies on the inelastic scattering of monochromatic light, usually from a monochromatic laser in the visible to near-infrared range. The incident electromagnetic wave excites the molecule into a virtual energy state for a short time before a photon is emitted.

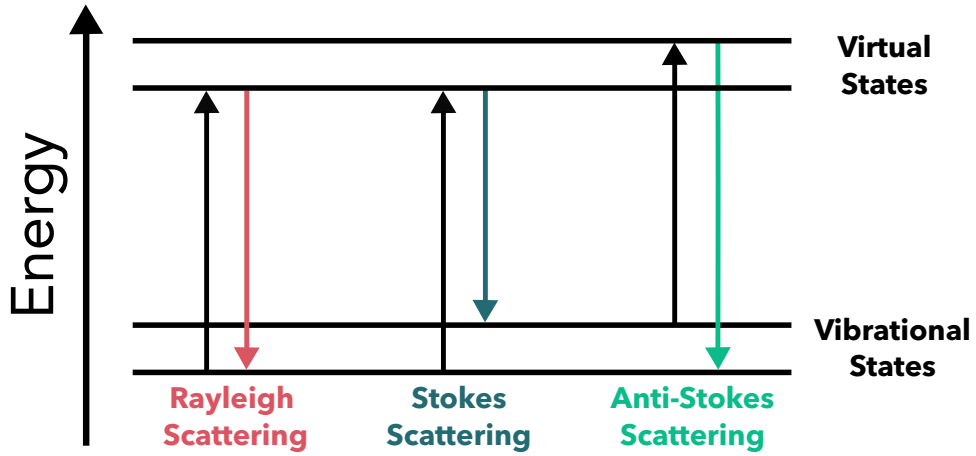


**Figure 2.7: Energy Levels in Raman Spectroscopy:** Illustration of elastic (Rayleigh) and inelastic (Raman) scattering.

Three types of scattering are distinguished as illustrated in Figure 2.7: elastic scattering (Rayleigh scattering) and inelastic scattering (Raman scattering). When energy gains are observed in Raman scattering, it is further specified as Stokes scattering, while energy losses describe anti-Stokes scattering. Since Rayleigh scattering is significantly more intense than Raman scattering and a notch filter is required to filter out the laser line, *i.e.* the elastic scattering. For Raman scattering to occur, molecules must experience a change in polarizability upon virtual energy level excitation, a key distinction from infrared (IR) spectroscopy, which requires a change in dipole moment. This principle renders Raman spectroscopy complementary to IR spectroscopy. [65] Raman spectra are typically reported in counts per second over wavenumber, that is, the energy shift from the incident laser wavelength. Consequently, positive wavenumbers correspond to Stokes, and negative wavenumbers correspond to anti-Stokes measurements.

# 3

# Transition Metal Fluoride Cathodes

## Contents

# 3.1 Introduction

## 3.1.1 Conversion-type fluoride cathodes: Current state of the art

A significant portion of this chapter was published in *Current Opinions in Electrochemistry*. [12] Additional figures and explanations have been included where appropriate to enhance clarity and depth.

### The Potential of Conversion Cathodes

State-of-the-art LiBs utilize open-framework transition metal cathodes, which intercalate $Li^+$ into a limited number of interstitial sites within the stable host lattice. This storage mechanism imposes an upper physico-chemical limit for $Li^+$ storage (or charge storage), rendering such technologies unsuitable for applications that require even higher gravimetric energy densities, such as electric passenger aircraft. [2, 66]. TMF cathodes, on the other hand, can store multiple $Li^+$ per metal center due to a multi-electron conversion reaction and hence offer a 200% to 300% increase in theoretical energy density if high redox potential metals are employed (Fe, Co, Ni, Cu). [67] In addition, the low cost per kilowatt-hour and environmentally benign properties of Cu and Fe make TMFs a promising class of next-generation cathode materials for high-energy density applications. [10, 68]

Unfortunately, TMF cathodes suffer from poor ionic and electronic conductivity due to a large bandgap induced by the ionic character of the TM-fluoride bond. [69] The initial cycling performance of TMF cathodes reported from 2003 onward by Badway and Li *et al.* exhibited short cycle lives, sluggish kinetics, and a significant hysteresis, which was ascribed to the insulating nature of TMFs and structural rearrangement required for the conversion reaction. [69–71] Despite these inherent obstacles, a considerable improvement in performance was achieved in the following 15 years through a variety of cathode engineering techniques, including utilization of various carbon composites, cation and anion substitution and nanostructuring. [72–77]

On the other hand, the mechanistic understanding of the conversion reaction evolved concurrently in a rather disconnected fashion. The most widely studied compound is $FeF_x$ (x = 2, 3), often used as a prototypical model for other TMFs. A discussion on the symmetry of phase evolution, the presence of intermediate phases, and the nature of morphological transformations upon lithiation and delithiation ignited the scientific literature. The most widely accepted theory described a three-phase direct conversion of $FeF_2$ to Fe and LiF. In the case of $FeF_3$, an initial reduction via the insertion of $Li^+$ forms $Li_xFe_yF_z$ intermediate phases and $FeF_2$, followed by direct conversion to LiF and metallic iron. [69, 70, 78–86] However, in the last three years alone, the understanding of the conversion mechanism has changed drastically. In 2018, Karki *et al.* first suggested that $FeF_2$ conversion is topotactic in nature. [87] Subsequently, Xiao *et al.* demonstrated that the fluoride anion sublattice acts as a stable host enabling the topotactic transformation between LiF, $FeF_2$ and intermediate fluoride phases. [88] Very recently Hua *et al.* provided additional evidence corroborating the role of the fluoride sublattice and elucidating the crystallographic characteristics of occurring intermediate phases in $FeF_3$ reduction. [89]

In light of this new mechanistic understanding, the most recent developments on the electrochemical performance of transition metal fluorides is reviewed, and a framework for further improvement of these battery chemistries is provided. The impact of the electrolyte on cycle life, realistic prospects for rate capability, and utility of the lesser-studied transition metal fluoride compositions and their realistic energy densities will be discussed herein.

### Improving Cycle Life Through Electrolyte Design

In general, TMF cathodes suffer from three major failure mechanisms, as illustrated in Figure 3.1. Active materials dissolution is reported for all transition metals of interest and is exacerbated by metallic phase segregation to the particle surface. [10, 68, 88] In addition, continuous electrolyte decomposition enabled by a low cut-off potential (commonly set at around 1.2 V vs $Li^+/Li$) which is required for a complete

transition metal reduction, can lead to the formation of a steadily growing cathode electrolyte interphase (CEI) and an accompanying rise in electrode and ohmic impedance. [88, 90] More importantly, CEI formation is further facilitated by the catalytic activity of the metal phase formed during discharge. [68] Lastly, ionic and electronic conductivity can diminish due to structural disintegration (loss of contact to the current collector) or particle fusing. Fusing can substantially increase particle sizes beyond the diffusion lengths of conversion reactants, leading to the formation of isolated and unconverted material. [10, 88, 91] Rational electrolyte design can provide a pathway to tackle all of these, as research from the last few years has shown.

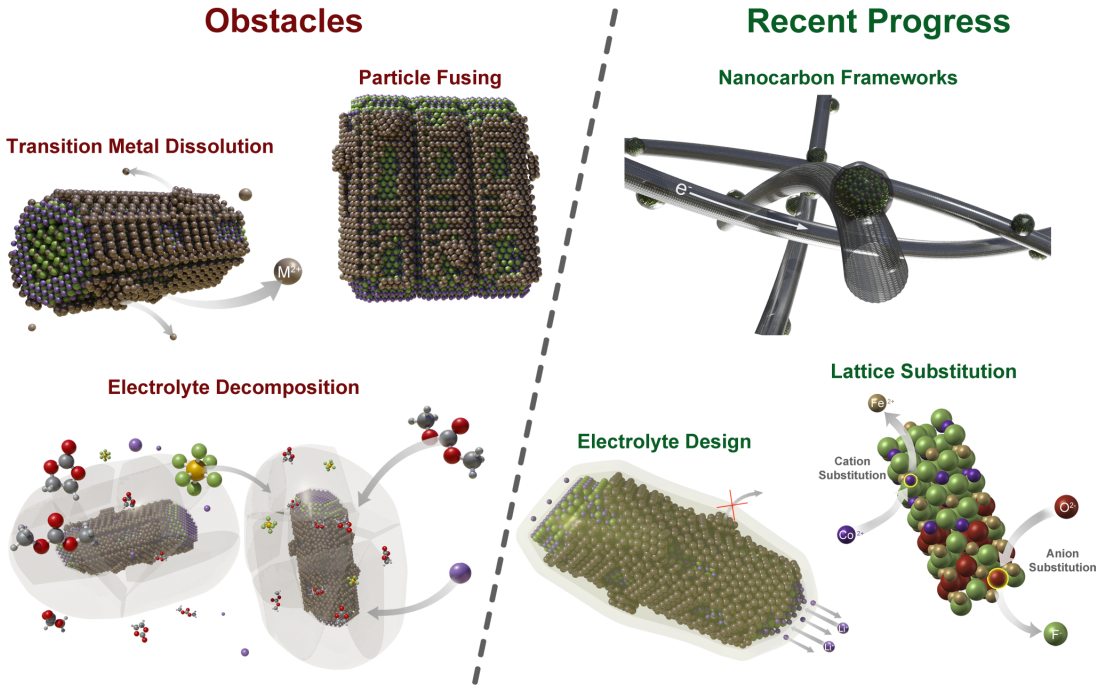


**Figure 3.1: Bottlenecks and recent developments in the field of TMF cathodes:** Capacity fade and high overpotentials in transition metal fluoride cathodes can be caused by active material dissolution, particle fusing, and continuous electrolyte consumption. Recent developments demonstrated successful mitigation thereof by rational electrolyte design, carbon supports, and metal-anion concerted doping. Reprinted from Olbrich et al. [12]

Gu *et al.* described the benefits of using a 4.6 M lithium bis(fluorosulfonyl)imide (LiFSI) in dimethoxyethane (DME) electrolyte combined with a $FeF_2$ carbon nanocomposite. Cyclic voltammetry, postmortem XPS and EDX indicated the formation of a stable passivation layer which prevented iron dissolution. At the

same time, the expected capacity fade within the first 20 cycles was drastically reduced. The best-performing cell retained 80% discharge capacity after 1000 cycles. [92] In a subsequent publication, the same group showed nearly complete capacity retention of more than $500\,\mathrm{mA\,h\,g^{-1}}$ for 400 cycles using $FeF_3$ particles embedded on a carbon nano fiber (CNF) network in the same electrolyte. [93] Zhao *et al.* described a synergistic double protection layer effect by adding lithium bis(oxalato)borate (LiBOB) salt to different organic electrolytes in conjunction with $Al_2O_3$ coated $FeF_3$ cathode particles. The CEI contained lithium oxalate and B-F bonds which successfully prevented iron dissolution and increased the capacity retention after 300 cycles from around 60% to 90%. [94]

Huang *et al.* studied the impact of organic electrolyte compositions on $FeF_2$ cycling in more detail. [90] They found that LiFSI fails to prevent cathode dissolution when dissolved in a fluoroethylene carbonate/ethyl-methyl carbonate (FEC/EMC) mixture contrary to a LiFSI DME solution. The authors rationalized this by the electrochemical instability of FEC which, when combined with LiFSI, can form an excessive CEI leading to cathode polarization. In contrast, the more electrochemically stable lithium bis(trifluoromethanesulfonyl)imide (LiTFSI) salt, showed superior performance when dissolved in FEC-EMC. In general, a thin uniform CEI was determined to be most beneficial for capacity retention. A new approach was reported by Huang *et al.* in 2019. $FeF_2$ was deposited on a carbon nano tubes (CNT) network and infiltrated by a polymeric electrolyte. [90] The cathode exhibited a dense uniform distribution of $FeF_2$ which enabled acceptable ionic and electronic conductivity and an increased ductility. The all-solid-state cell operated at 50 °C and showed a discharge capacity of $450\,\mathrm{mA\,h\,g^{-1}}$ for over 100 cycles and almost complete capacity retention over 300 cycles, albeit at more limited cycling rates. Postmortem analysis revealed the formation of a 6 nm thin, stable CEI, which most likely originates from the decomposition of the polymer and prevents cathode dissolution.

Xiao *et al.* reported multiple benefits of using LiFSI dissolved in an IL with monodisperse $FeF_2$ nanorods. [88] In contrast to an organic electrolyte (LP30),

which leads to cell degradation within the first 20 cycles, the IL electrolyte (1 M LiFSI in $Pyr_{1,3}FSI$) enabled unprecedented near-theoretical capacity retention ($571\,mA\,h\,g^{-1}$) throughout the first 50 cycles and stable operation for over 200 cycles at 50 °C. EIS revealed a constant interphase resistance during the initial five cycles and a minor increase thereafter, which was in stark contrast to a rapid impedance rise observed in the organic electrolyte (Figure 3.2a). Furthermore, XPS and TEM analysis indicated a high inorganic content in the 10 nm thick $[FSI]^-$-derived CEI. Since no iron was detected on the counter electrode in postmortem XPS, it was concluded that iron dissolution was successfully hindered.

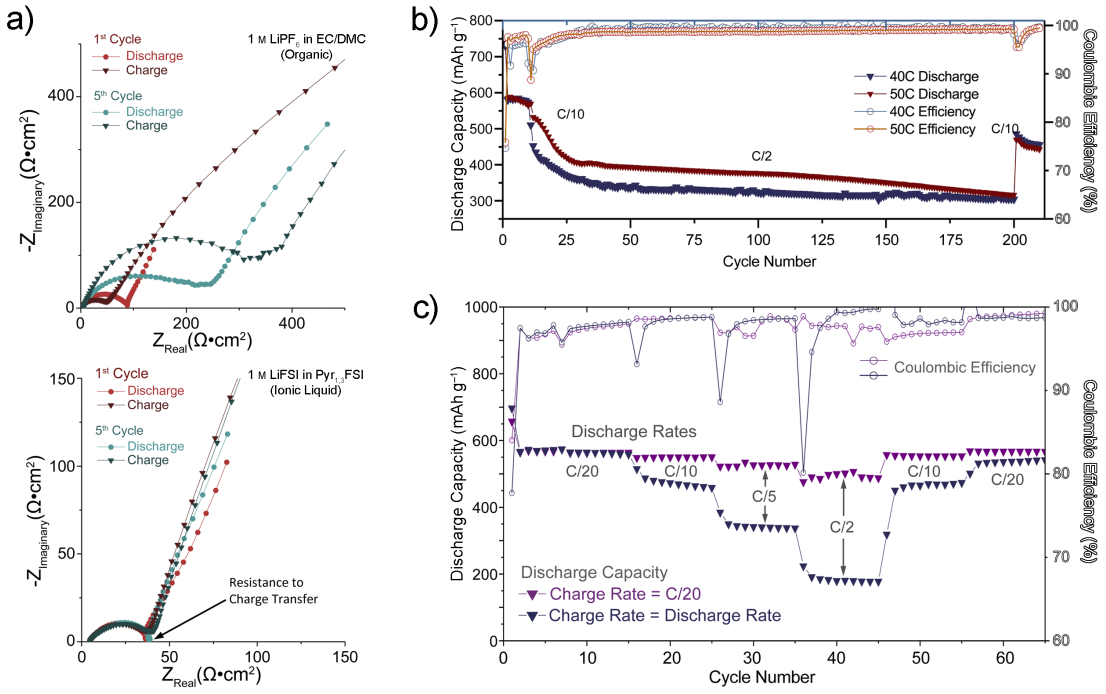


**Figure 3.2: Electrochemical characteristics of $FeF_2$.** **a**, Nyquist electrochemical impedance plots showing the difference in the magnitude and evolution of charge transfer resistance between an unstable electrolyte (1 M $LiPF_6$ in EC/DMC) and a stable electrolyte (1 M LiFSI in $Pyr_{1,3}FSI$). **b**, Plot of discharge capacity and CE vs. cycle number for $FeF_2$ electrodes at 40 °C and 50 °C showing stable cycling at elevated temperatures in an ionic liquid electrolyte. **c**, Plot of discharge capacity and CE vs. cycle number for $FeF_2$ electrodes cycled at various current densities. The dark purple plot shows cycling at equal charge and discharge rates. The light purple plot demonstrates the inherent discharge rate capability of the material when a slow charging rate (C/20) is applied to recover the full capacity. Reprinted from Xiao *et al.* [88]

Interestingly, the nanorods did not fuse and remained monodisperse during

operation, which might be explained by the electrostatic interaction between the IL and $FeF_2$, and thus facilitated a high capacity retention (Figure 3.2b).

$[FSI]^-$ anions are often implicated in the formation of a robust SEI on Li-metal anodes, which improves their cycling stability. [16] As recent publications indicate, $[FSI]^-$ anions also support the formation of a stable CEI on TMFs in either highly concentrated solutions (*e.g.* 4.6 M LiFSI in DME) or specific solvents (*e.g.* in DME or $Pyr_{1,3}FSI$). [88, 90, 92, 93] Since the CEI is formed during discharge (*i.e.* lithiation), the species solvating $Li^+$ have a significant impact on its structure and physical properties. [95, 96] In carbonate electrolytes, $[FSI]^-$ is generally reported to enter the solvation sheath of $Li^+$ only at very high LiFSI concentrations. [97, 98] In contrast, when employing weakly solvating electrolytes such as DME, $[FSI]^-$ readily contributes to $Li^+$ solvation at more moderate concentrations. [99]. Hence, electrolyte design aiming for a $[FSI]^-$ derived CEI should consider its solvating power and salt concentrations carefully.

**A Realistic Look at Rate Capability**

As discussed in section 3.1.1, TMFs are conversion-type cathodes with intrinsically low electrical conductivity. As a consequence, higher charging/discharging rates are particularly plagued by high overpotentials or even complete cell failure. The most common techniques to overcome this hurdle use excessive amounts of conductive additives, often in the form of nanostructured carbon composites. For example, using the $FeF_3$ CNF composite mentioned in section 3.1.1, Fu *et al.* demonstrated the highest rate capability for $FeF_3$ systems, with a stable discharge capacity retention of $285\,mA\,h\,g^{-1}$ at $1000\,mA\,g^{-1}$. [93] The free-standing CNFs prevent the coarsening of the $FeF_3$ nanoparticles and the consequent formation of "dead material" and further enhance electronic conductivity, enabling fast discharge rates. The best-performing composite contains 56wt% active material (no additional binder and carbon required), which is still higher compared to other publications with similar carbon architectures. [90, 100–104]

Another approach was published by Li *et al.* based on a hetero-nanostructure of lithiated $TiO_2$ and FeOF combined with a CNT network. [105] $TiO_2$ becomes electronically conductive upon lithiation, which when combined with the CNT reduces the charge transfer impedance in the compound as evident from their EIS data. $TiO_2$ also provides reversible $Li^+$ storage capacity and can act as mechanical confinement. Although discharge capacities of around $165\,mA\,h\,g^{-1}$ at $500\,mA\,g^{-1}$ are lower than in other reports, the group does achieve a stable areal capacity of $1.74\,mA\,h\,cm^{-2}$ for 300 cycles (at $100\,mA\,g^{-1}$). Thermogravimetric analysis indicates an active material (FeOF and $TiO_2$) weight content of around 50 wt%.

In general, carbon architectures do not only enable higher cycling rates but also represent a successful strategy to mitigate particle fusing and can potentially be used to stabilize nanoparticles with an artificial CEI layer. [75] Unfortunately, carbon additives in excess of 40 wt% would reduce the specific energy of an $FeF_2$-Li cell below that of commercial intercalation-based cells, and indeed an active material mass fraction of less that 70% would render most TMF chemistries noncompetitive with next-generation, intercalation-based Li-metal cells as discussed in more detail in section 3.1.1. The high rate performance comparison shown in Figure 3.3 illustrates the trade-off between areal capacity and discharge currents and their corresponding discharge capacities as a function of active material loading.

However, with the novel description of the topotactic reaction mechanism within a stable fluoride sublattice in $FeF_x$, the discharge rate appears to be not as intrinsically slow as initially assumed. Xiao *et al.* showed that the charging process is limited by the diffusion rate of iron across a high energy Fe-LiF interface whereas discharging is limited by $Li^+$ diffusion along open channels in the $\langle 1\,0\,0\rangle_{FeF_2}$ direction, which is inherently faster. Hence, by maintaining a slow charging rate to reach the full capacity ($28.6\,mA\,g^{-1}$), unprecedented high discharge capacities of $500\,mA\,h\,g^{-1}$ at $285.5\,mA\,g^{-1}$ could be demonstrated while maintaining an active material loading of 70wt% and an areal capacity of around $600\,\mu A\,h\,cm^{-2}$ (Figure 3.2c).

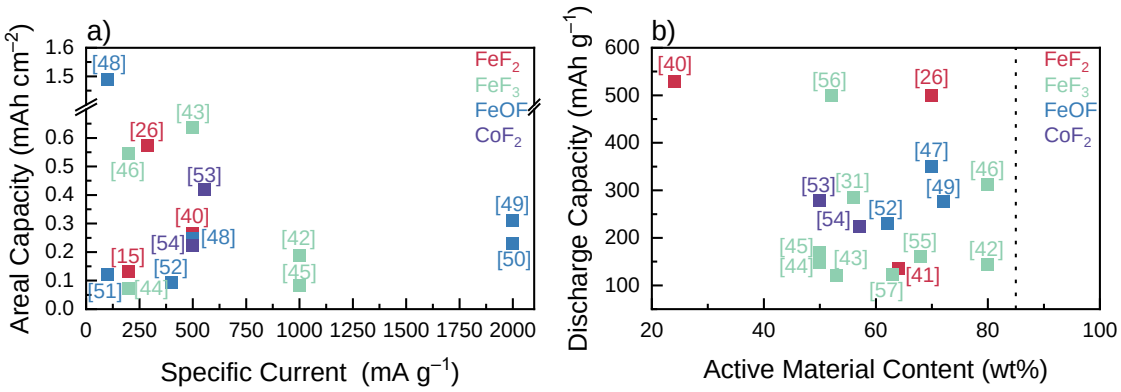


**Figure 3.3: High rate performance comparison of various TMF cathodes.**[77, 88, 90, 93, 95, 100–116] **a** shows the areal capacity obtained at a given current density and **b** the corresponding discharge capacities as a function of active material content in the cathode. The dotted line indicates the threshold of 85 wt% used for the techno-economic calculation. It is noteworthy that not every publication reports enough information to calculate both the areal capacity and active material content. The colors indicate elements used in the cathode. The numbers attached to the data points correspond to the citations in the original publication and not this thesis. Reprinted from Olbrich *et al.*[12]

### The Origin of Voltage Hysteresis

Another setback of TMF cathodes is a peculiar large voltage hysteresis resulting in energy efficiency below 80%. Despite numerous studies on the reaction mechanism, its origin remains disputed. [86]

Li *et al.* conducted an extensive GITT study on $FeF_3$ cathodes and proposed that the observed hysteresis is kinetic in nature and originates from three components. [85] First, there is an ohmic voltage drop which was determined in the GITT study as a sudden voltage jump ($< 100\,\text{mV}$) when the current was set off. The second contribution is a reaction overpotential corresponding to phase nucleation, mass transport inside the particle, and interfacial penalties of nanophases. A quantification thereof using GITT in conversion cathodes is, however, difficult due to composition inhomogeneities in the particle *i.e.* the coexistence of converted and unconverted phases. Instead, reverse-step potentiostatic intermittent titration technique (PITT) is suggested as a more suitable technique since it allows to eliminate the polarization effect seen in galvanostatic mode. Referring to an earlier PITT study by Ko *et al.*, the authors conclude a reaction overpotential of 300 mV for the conversion reaction ($FeF_2$ reduction) and 70 mV for the reconversion reaction

(both measured at $x_{Li} = 1.2$ per $FeF_3$). [91] The third contribution determined by Li *et al.*, is induced by differences in the spatial distribution of electrochemically active phases when comparing the discharge and charge mechanism as indicated in Figure 3.4. For example, the outer phase, which is in contact with the electrolyte and current collector and thus is responsible for $Li^+$ and electron supply, changes from a Li-rich ($Fe^0$ + LiF) phase during discharge to a Li-poor ($FeF_2$ + LiF) phase during charge despite being at the same lithiation state of $x_{Li} = 1.8$ per $FeF_3$. This alters the respective potential versus the $Li^+/Li$ and thus introduces a voltage difference during cycling similar to a concentration overpotential. The authors quantified this contribution by the voltage gap at a given lithiation state after four hours of potential relaxation (around 400 mV at $x_{Li} = 1.8$ per $FeF_3$). In accordance with this explanation, the observed voltage gap increases with a higher $Fe^{3+}$ content (small $x_{Li}$ in $FeF_3$ in Figure 3.4) since the level of inhomogeneity further increases.

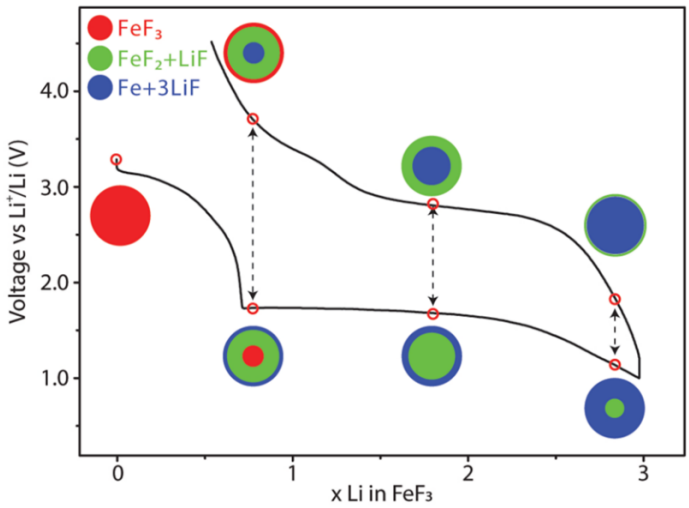


**Figure 3.4: Differences in the spatial distribution of active species during discharge and charge.** A a schematic composition illustration is of a $FeF_3$ particle is and the corresponding hysteresis during the galvanostatic cycling is shown. Reprinted from Li *et al.* [85]

It should be emphasized that the graphical representation of the conversion mechanism in Figure 3.4 is significantly simplified and should only serve as an illustration for voltage hysteresis induced by composition inhomogeneities. A state-of-the-art mechanistic description of $FeF_3$ cycling was recently published by Hua *et*

*al.* [89] In there, the authors provide a thorough characterization of intermediate $Li_xFe_yF_3$ phases, and highlight that lithiation and delithitation of $FeF_3$ and $MF_2$ (M = Cu, Fe) cathodes preliminarily occur *via* a diffusion controlled displacement mechanism. [89] An important characteristic of a displacement reaction is a so-called path hysteresis which was described by Yu *et al.* in an earlier publication. [117] Therein, the authors apply first principle computational methods in a $CuTi_2S_4$ model system and determine the origin of the large hysteresis by analyzing intrinsic thermodynamic and kinetic properties of high capacity electrodes that exhibit a displacement mechanism (such as $FeF_3$). They identify that the large voltage hysteresis commonly observed in those systems arises from different reaction paths in the composition space during dis- and recharge. Unlike dissipative hysteresis, which originates solely from slow Li diffusion and sluggish interface mobilities, and thus can be mitigated by slowing down charge and discharge rates, path hysteresis is a result of a substantially higher Li mobility relative to the displaced metal cation. [117] Transferring this description to the $FeF_3$ system, the discharge rate is limited by Fe diffusion rather than concurrent Li insertion, which consequently results in an almost invariant overpotential and thus a constant operation voltage. In contrast, a more rapid Li removal than Fe insertion during charge leads to a more sloppy voltage profile. Consequently, the authors suggest the exploitation of materials with higher metal (ion) mobilities for effective mitigation of intrinsic path hysteresis. A similar explanation for the observed voltage hysteresis in a $FeF_2$ compound has been given earlier by Xiao *et al.* [88]

In a publication by Seo *et al.* the effect of metal (Fe, Cu, Ni) nanoparticle sizes on the reaction potential is studied with first principle calculations and electrochemical experiments. [118] The authors propose an increasing energy penalty to the free energy of reaction, causing voltage hysteresis with a decreasing size of the formed metal particles. While $CuF_2$ was observed to form larger metal particles than $NiF_2$ due to a higher metal diffusivity, some large copper agglomerates were found isolated from LiF in the carbon matrix. This illustrates the dilemma of employing

material systems with improved metal (ion) mobilities as it can come at the prize of sacrificing accessible capacity due to the formation of isolated metal particles.

## Beyond Iron Fluorides

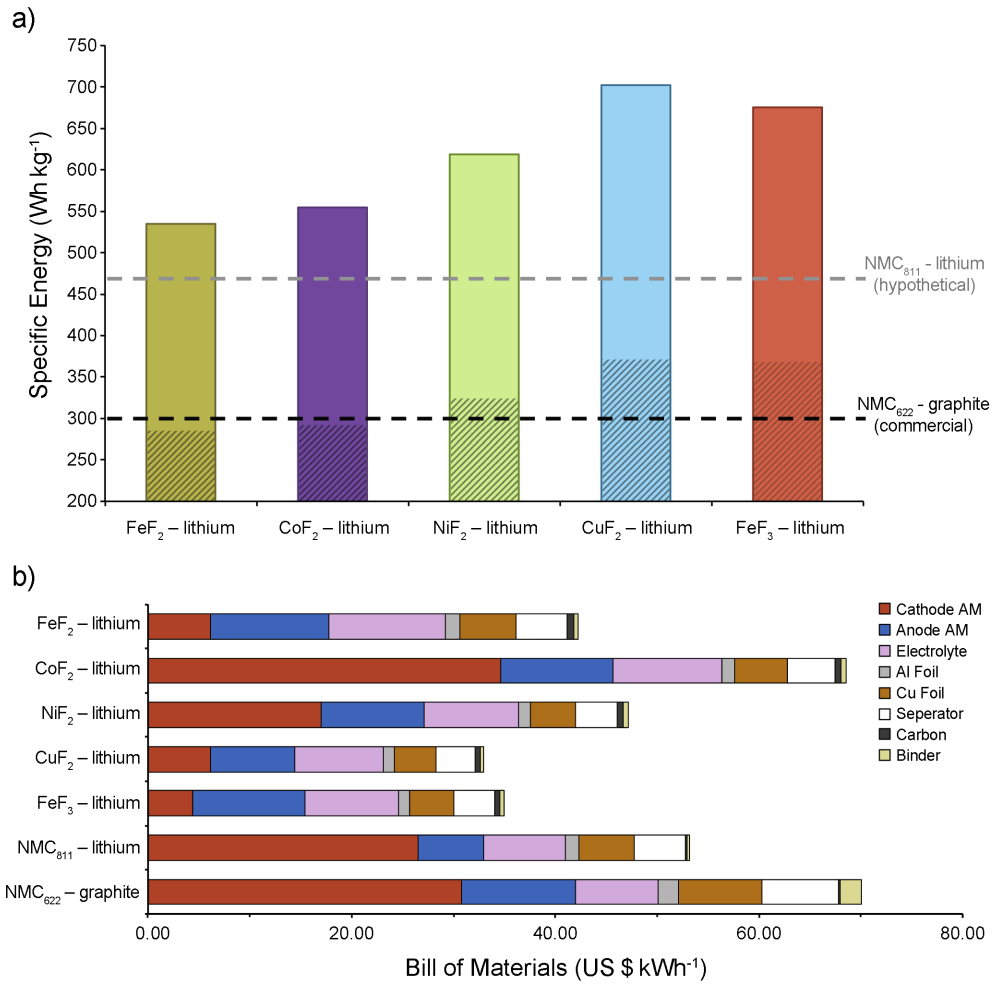


**Figure 3.5: Techno-econmic analysis of TMF chemistries. a**, Chart showing the projected specific energy at the stack level for TMF-Li metal batteries. Calculation were made assuming 90 µm thick cathodes 30% porosity, 85% active material mass fraction, a usable capacity of 90%, an average cathode overpotential of 300 mV, 30% excess Li capacity, and 150% excess electrolyte mass as realistically achievable parameters. The textured regions of the chart represent a drop in active material mass fraction from 85% to 50%. The grey and black dashed lines represent the stack-level specific energy of a commercial scale $NMC_{622}$ graphite cell and a hypothetical $NMC_{811}$ Li cell, respectively. **b**, corresponding costs per kW h. Costs were estimated from the most recent bulk prices. Details on the calculations can be found in the appendix (see section 7.1). Reprinted from Olbrich *et al.*[12]

In Figure 3.5 a simplified techno-economic model for the later 3d TMF-Li chemistries is presented to establish a reasonable perspective on achievable energy densities and associated costs. The model extends to the stack level, with realistic

penalties placed on usable capacity, overpotential, excess Li/electrolyte, and, most importantly, active material mass fraction. A full description of the assumptions and calculations made herein can be found in the appendix (see section 7.1).

It is more pertinent to compare TMF chemistries with a hypothetical $LiNi_{0.8}Co_{0.1}Mn_{0.1}O_2$ ($NMC_{811}$) Li system, as both cases depend on a Li-metal anode. While all the TMF systems considered here exhibit higher energy densities, it is questionable whether the modest advantage ($50\,W\,h\,kg^{-1}$ to $70\,W\,h\,kg^{-1}$ increase compared to $NMC_{811}$-Li) of the lower potential cathodes ($FeF_2$, $CoF_2$) could justify the use of a chemistry with inferior cycle life and rate capability (Figure 3.5a). The increase in cathode potential from $FeF_2$ to $CuF_2$ yields a drastic increase in energy density, highlighting the importance of incorporating more electronegative transition metals and decreasing discharge overpotentials (<300 mV). $NiF_2$, $CuF_2$, $FeF_3$ systems could exceed $600\,W\,h\,kg^{-1}$ at the stack level, with potential for use in high specific energy applications. Additionally $CuF_2$ and $FeF_3$ are highly competitive in terms of cost of energy stored (US $ per kWh), with the main cost drivers being the Li-anode and electrolyte as illustrated in Figure 3.5b.

Despite the obvious theoretical advantages of $FeF_3$ over the divalent compound (higher redox potential and larger specific capacity), intrinsic kinetic limitations undermine its practical implementation. As a result of the higher LiF concentration in a converted $FeF_3$ compound (3 LiF per $Fe^0$), reaction kinetics are intrinsically more sluggish compared to $FeF_2$ (2 LiF per $Fe^0$) thus negatively affecting rate capability. [91] To the best of my knowledge, reversible capacity retention corresponding to all three Li equivalents ($712\,mA\,h\,g^{-1}$) has not been demonstrated for more than ten cycles yet. [115] While capacity loss induced by isolation of iron particles in a $FeF_2$ compound can be compensated by oxidation of other metal centers beyond $Fe^{2+}$, this is not possible in $FeF_3$. [88]

Albeit $CuF_2$ holds the greatest potential value, it is the only 3d TMF cathode that shows little to no intrinsic reversibility. Despite its structural similarities ($CuF_2$ exhibits a monoclinic structure, which is Jahn-Teller distorted from the typical tetragonal rutile of other transition metal difluorides), $CuF_2$ cycling exhibits poor

reversibility, which restricted its application to primary batteries so far. [72, 119, 120] Studies have suggested that metallic copper does not nucleate inside the fluoride sublattice on discharge but instead forms large aggregates on the particle surface due to the high diffusivity of copper cations. [79, 120] During charge, substantial copper dissolution by the formation of fluoride rich complex ions, such as $[Cu^{I}F_4]^{3-}$ and $[Cu^{II}F_6]^{4-}$, associated with the consumption of LiF is observed. [121]

Promising results were published by Wang *et al.*, who reported reversible Cu redox reaction over a two-step reduction in a $Cu_yFe_{1-y}F_2$ solid-solution compound. [113] An unprecedentedly low voltage hysteresis (<150 mV in GITT) was observed, which suggested ternary compounds as an avenue for overcoming low energy efficiencies characteristic of TMF cathodes. [85] However, more recent publications have tempered this enthusiasm.

Gordon *et al.* investigated a number of solid-solution ternary difluoride (Fe-Co, Fe-Mn, Fe-Ni) nanoparticles decorating multi-wall carbon nanotubes (MWCNT). [122] In contrast to Wang *et al.* the authors did not observe any mitigation of the voltage hysteresis compared to plain $FeF_2$. Additionally, mixed metal reduction appeared to occur in a single step reaction and the average discharge potentials lied in between the ones corresponding to the binary fluorides. Although this does suggest a certain degree of tunability, it should be noted that all of the ternary fluorides exhibited lower average discharge potentials compared to $FeF_2$. On the contrary, substituting copper into a nickel fluoride compound is reported to increase the discharge potential by a few hundred millivolts. [123] Interestingly, further oxidation of some metal centers to a +3 state of charge in Mn and Fe containing compounds was indicated in their voltage profiles. [122]

A similar observation was made by Omenya *et al.* The group showed fairly reversible cycling in a $Cu_{0.5}Fe_{0.5}F_2$ compound. However, x-ray absorption near edge structure (XANES) measurements suggested that only a small amount of copper is re-oxidized during charge. Instead, reversible oxidation beyond $Fe^{2+}$ compensates for capacity loss due to copper isolation and dissolution into the electrolyte. [120] In addition, a significantly higher hysteresis was monitored by PITT measurements

compared to the GITT data from Wang *et al.* It should be noted that GITT measurements are more sensitive to concentration polarization within the electrode than PITT measurements since the constant potential step minimizes the build-up of concentration gradients. Ko *et al.* discussed this in detail in a comparative electrochemical study of $FeF_2$ and FeOF. [91]

To address the problem of copper dissolution, Seo *et al.* prepared a NiO protection layer on a $CuF_2$/C electrode. In contrast to a bare $CuF_2$/C composite the cathode could be recharged and five subsequent cycles are demonstrated. Inductively coupled plasma optical emission spectroscopy (ICP-OES) of the electrolyte indicated a substantial alleviation of copper dissolution by the NiO coating. [118] Nevertheless, significant capacity fading is observed, indicating the existence of vast overpotentials for the reconversion of $CuF_2$. A further investigation of the interfaces formed between metallic Cu and $CuF_2$/LiF may help to explain the origin of this anomalous behavior.

An alternative approach to tackle the problem of copper dissolution was introduced by Xia *et al.* The authors prepared $CuF_2$ sodium alginate composites through an aqueous wet casting technique. The alginate forms a complex with $Cu^{2+}$ and thus helps to prevent copper dissolution into the electrolyte. While this technique allowed the authors to demonstrate reversible capacity retention for over 50 cycles (at around $420\,\mathrm{mA\,h\,kg^{-1}}$) over 60% of the capacity is retained at around below 2.5 V vs $Li^+$/Li. [124] The low reduction potential is explained by the formation of a Cu(OH)F phase during the aqueous composite preparation. Their approach thus significantly reduces the energy density gains hoped to be achieved by using a copper metal center.

Very recently, Jiang *et al.* submitted a manuscript for peer review and published a pre-print on reversible $CuF_2$ cathodes. [125] The authors stabilize the intermediate $Cu^+$ phase by adding an electron-accepting polymer interphase layer to the composite. Allegedly, the polymer adsorbs preferentially to CuF and accepts some charge from metallic copper, further promoting $Cu^+$ formation. The authors employ a range of characterization techniques, including XRD, NMR, HRTEM, XPS, and XAS, to prove the presence and stabilization of the intermediate CuF phase (not

further specified). By stabilizing this phase, the authors claimed to unlock a new conversion reaction pathway, reducing the voltage hysteresis to unprecedented 50 mV. By combining the copper composite with a solid electrolyte, which prevents copper dissolution, the authors demonstrate reversible cycling for 30 cycles at around 3.2 V vs $Li^+/Li$. [125] If this study should prove to be authentic and reproducible, this could mark a leap in the development of $CuF_2$ cathodes.

In addition to mixed cation TMFs, mixed anion oxyfluoride compounds (formed by substituting $O^{2-}$ at the $F^-$ lattice site) have also demonstrated improved performance in the past. [91, 126, 127] A recent publication by Fan *et al.* reported co-substituted $Fe_{0.9}Co_{0.1}OF$ nanorods. In contrast to the pristine phases (FeOF, $FeF_3$), the compound showed remarkable cycling stability, retaining 350 mA h $g^{-1}$ for over 1000 cycles which corresponds to a capacity fade of 0.005% per cycle. As evident from GITT, the potential hysteresis could be significantly reduced down to 0.27 V at 50% SOC compared to FeOF (0.57 V) and $FeF_3$ (1.1 V). Supported by first principle calculations, the authors rationalize the outstanding electrochemical performance by suppressing the conversion reaction due to concerted Co/O doping. An intercalation-extrusion mechanism is enabled by stabilizing a defected-rocksalt parent phase ($Li_{1-0.5z}Fe(Co)O_{2-z}$), where only small amounts of metallic Fe(Co) is formed (extruded) and a high lattice coherence with LiF is maintained. [110] The study is a pioneering example of how co-substitution can be used to modify the reaction mechanism and thus tune the electrochemical performance of TMF cathodes.

**High Temperature Operation**

As discussed in section 3.1.1 TMF cathodes suffer from poor ionic and electronic conductivity and sluggish reaction kinetics which imposes a large voltage hysteresis and restricted rate capability. A potential strategy to mitigate both is cell operation at elevated temperatures. A higher thermal energy can *e.g.* enable more transition metal atoms to jump high energy interfaces, increase atom and ion mobility and their diffusion length inside the particle, reduce composition inhomogenities, and

incentivise the formation of larger metal agglomerates associated with reduced energy penalties. All of which is expected to improve the electrochemical performance of TMF cathodes according to the latest literature discussed above. [85, 88, 89, 117, 118]

A successful reduction of the voltage hysteresis in a $FeF_3$ cathode was demonstrated in a study by Tawa *et al.* [128] By increasing the operation temperature from 25 °C to 90 °C the potential plateau corresponding to the conversion reaction was increased from around 1.5 V to 2.2 V. The authors rationalized this by a suppression of the diffusion overpotential. Unfortunately, cathode dissolution, electrolyte decomposition, and parasitic reactions are also accelerated at elevated temperatures. In the study by Tawa *et al.* a rapid capacity fade within the first ten cycles was observed. Particle aggregation was given as a possible explanation. However, the authors did not consider the limited electrochemical stability of their LiFSI in EMIFSI electrolyte, particularly for a voltage window of 2.5 V to 4.5 V at 90 °C. Another recent mechanistic study on the $Fe^{3+}/Fe^{2+}$ redox reaction in a lithiated $FeF_3$ compound reports continuous oxidative decomposition in the exact same electrolyte (1 M LiFSI in EMIFSI) at 90 °C (around 4 V vs $Li^+/Li$) resulting in low CEs around 90%. [129]

In an earlier study by Badway *et al.* the complete three electron transfer in a $FeF_3$ compound (1.5 V to 4.5 V) is studied at 70 °C. [69] Therein, only $FeF_2$ could be detected upon complete recharge, despite exhibiting a subsequent $Fe^{3+}$ to $Fe^{2+}$ reduction feature in the galvanostatic profile. The authors explained this anomalous behavior by a pseudocapacitive surface reaction of the electrolyte ($PF_6^-$ adsorption and $Fe^{III}F_2(PF_6^-)$ formation) enabled by the high surface area of the electrode composite. To the best of my knowledge, reversible cycling has only been demonstrated up to 50 °C so far. [88, 90]

### 3.1.2 Project Goals

In this first part of the thesis, $FeF_2$ cathodes are used as a model system to address the intrinsically low electronic and ionic conductivity of TMF cathodes. The goal is to establish a scalable synthesis route that allows to access the full

capacity of $FeF_2$ during cycling. Ball milling is a desirable processing technique that allows for high throughput, minimal waste production, and the use of commercially available materials. However, reports on ball-milled TMF cathodes in the literature typically don't show full capacity retention and rapid fading even at extremely slow cycling rates. [69, 114]

Further, different composite preparation techniques are compared and optimized in order to increase the active material content of composites and thus increase their energy density to a competitive level. A target value of 85wt% active material is aimed for, in accordance with the techno-economic analysis conducted earlier (see Figure 3.5)

All cycling will be conducted in a LiFSI N-propyl-N-methylpyrrolidinium bis(fluorosulfonyl)imide ($Pyr_{1,3}FSI$) IL electrolyte due to the beneficial SEI and CEI forming properties described above, and the excellent thermal stability. The long-term cycling behavior of $FeF_2$ in this IL will be elucidated with the goal of grasping a better understanding of the role of the $[FSI]^-$ anion.

Further, a better understanding of the effect of temperature on the cell chemistry during OCV and cycling is necessary to assess cell safety and rate capabilities, both highly relevant for electric flight applications.

Lastly, testing in larger cell formats is necessary to assess the viability of upscaling and practically achievable energy densities.

A significant portion of this chapter was published in *Cell Reports Physical Science*. [130] Additional figures and explanations have been included where appropriate to enhance clarity and depth.

## 3.2 Experimental

### 3.2.1 Synthesis

#### High Energy Milling

Ball milling was conducted using 7 g of $FeF_2$ (99.8%, Sigma-Aldrich), 7 mL of dry octadecene (Sigma-Aldrich), and 3 mL of dry oleic acid (Sigma-Aldrich) and 166 5 mm zirconia balls in a 45 mL jar (Fritsch) at different milling speeds. Each

milling cycle lasted 5 min with a 7 min rest. Samples were collected from the mill at various milling times and then washed three times using 2 mL of anhydrous ethanol and 10 mL of anhydrous hexane. All cathodes tested from the following section were prepared from one milling batch, which had a particle size range of D10-D90 140 nm to 330 nm and a particle median of 226 nm. They were prepared by high-energy milling at 700 rpm for 24 h.

### 3.2.2 Material Characterisation

#### XPS and XAS

XPS was performed with an ULVAC PHI Versaprobe III XPS system generating monochromatic AlK X-rays (1486.6 eV, 15 kV anode voltage, 25 W beam power) under ultrahigh vacuum (UHV) conditions ($1 \times 10^{-6}$ Pa to $1 \times 10^{-7}$ Pa). Samples were prepared in an argon-filled glovebox and were immediately transferred into the XPS chamber using a vacuum transfer vessel (ULVAC PHI GmbH) to avoid contamination and ambient exposure. A 500 µm times 500 µm area from each sample was analyzed. Survey scans were acquired at pass energies of 224 eV, and a lower pass energy of 55 eV was used for core-level spectra. In-built electron and low-energy $Ar^+$ sources were utilized for charge neutralization. Depth profiling was achieved with consecutive XPS analysis and$Ar^+$ sputtering (4 keV, 3 mm times 3 mm) for a total of 60 min. Acquired spectra were fitted with Voigt lineshapes, after the application of a Shirley background, using CasaXPS software. Data processing was conducted using CasaXPS software. Fe-K-edge XANES measurements were performed using a lab-source x-ray absorption spectroscopy (XAS) from easyXAFS in transmission mode. Powdered samples, extracted from the respective cathode layers and synthesis batch, were diluted with cellulose and pressed into pellets. For the calibration of the incident beam energy, a pristine, standard $FeF_2$ cathode was measured before the measurement. Reference spectra of $FeF_2$, $FeF_3$, $Fe_3O_4$, $Fe_2O_3$, FeO, and Fe were acquired. Spectra preprocessing, i.e., energy calibration, background subtraction, edge-step normalization, and XANES data analysis, *i.e.* edge energy determination and compositional linear combination fitting, were performed in Athena.

**SEM, TEM, STEM**

For TEM measurements, the cathodes were loaded into a glass vial with anhydrous NMP and stirred for 24 h under argon to disperse the active material and dissolve the binder. The dispersion was centrifuged and the supernatant was discarded. The resulting pellet was redispersed in fresh NMP, and dropcast on holey-carbon TEM grids (Agar) in a glovebox. All TEM samples were placed in a Schlenk tube under argon, dried under vacuum at 80 °C overnight, and transported to the TEM in airtight vials under argon. Air exposure was limited to 30 s during transfer to the TEM column. Bright-field TEM/HRTEM imaging was performed on a JEOL 3000F field emission gun transmission electron microscope operated at 300 kV and equipped with a Gatan Ultrascan charge-coupled device camera. SEM samples were prepared similar to TEM samples. Instead of drop casting onto a TEM grid, the dispersion was drop cast onto an aluminum stub. The cross-sections were realized by mounting electrodes on a Ti blade with Electrodag which were subsequently milled with an 8 kV Ar beam for 5 h using a Gatan PECS instrument.

### 3.2.3 Cell Fabrication

All electrodes were fabricated using a conventional tape-casting method. The as-synthesized active material was dispersed in anhydrous hexane and mixed with Super-P carbon (TIMCAL) in different ways as described in the following section. The composite was dried under vacuum and hand-ground with additional Super-P before mixing with PVDF and NMP. The resulting slurry (70:20:10, $FeF_2$: carbon black, 99+% Alfa Aesar:poly(vinylidene fluoride) Sigma Aldrich) was cast via doctor blade on aluminum foil dried in a fume hood for 24 h and under vacuum for another 24 h. Circular electrodes were punched with a diameter of 10 mm. All electrodes tested contained between 1 mg cm$^{-2}$ and 2 mg cm$^{-2}$ active material. Ionic liquids were purchased from Solvionic ($Pyr_{1,3}$FSI 99.5%) and dried under vacuum at 70 °C. Electrolytes were prepared by solving 1 mmol of the respective salt (LiFSI from TCI >98%) per gram of IL. All cells were assembled in an argon-filled glovebox using glass fiber separators (Whatman, GF/D), metallic Li foil (Sigma, 99.9%) as

the counter/reference electrodes, and 150 µL of electrolyte. For batteries operating at 30 °C, regular 2032 coin cell components with a polypropylene gasket were used (MTI Corporation). For higher temperatures, 2032 coin cell components with a temperature-resistant perfluoroalkoxy alkane gasket were used to prevent cell leakage (Hohsen Corporation). Cell cases in contact with the WE are aluminum coated (CVD) from both suppliers to prevent corrosion at high potentials. Cells were cycled between 4 V and 1.2 V in an oven using either a Biologic BCS-805 battery cycler or a Biologic VMP3 potentiostat. Three-electrode cells were prepared using commercial ECC-Ref cells from EL-CELL and Li reference electrodes.

## 3.3 Results & Discussions

### 3.3.1 Wet Milling Strategies for Improved Performance

Nanosizing of the active material is required to access the full capacity of TMF cathodes despite the short ionic and electronic diffusion lengths in metal fluorides. Ball milling is arguably the most scalable processing technique to decrease and control particle size. Inspired by standard milling conditions reported in the literature, initial experiments involved "dry" ball milling of commercial $FeF_2$ powder. [69]

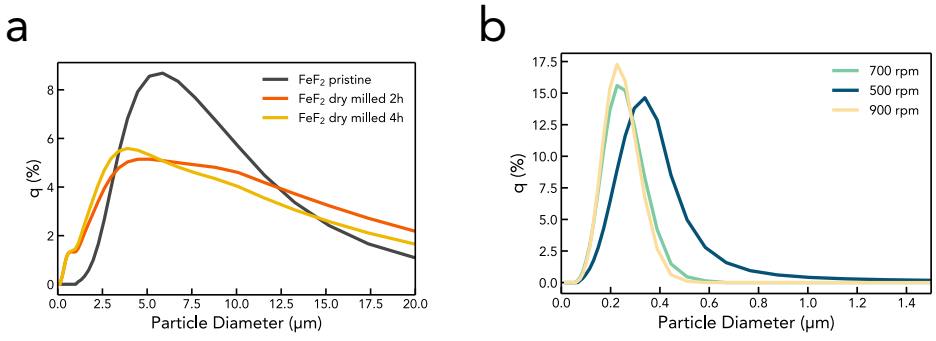


**Figure 3.6: Milling Strategies:** **a,** Particle size distribution determined by DLS (volume fraction) for $FeF_2$ particles during dry milling at 500 rpm. **b,** Particle size distribution determined by DLS (volume fraction) for $FeF_2$ particles ball milled at different rotation speeds.

Dynamic light scattering (DLS) was used to track the particle size distribution. Figure 3.6a shows the obtained particle size distribution by the dry milling approach. Unfortunately, this resulted in a wide particle size distribution and insufficient

particle size reduction due to coarsening caused by the local heating generated in the process. [131, 132] To overcome this limitation, octadecene, a high-boiling solvent, was added to the mixture. This "wet" milling technique prevented the adhesion of $FeF_2$ to the milling surfaces, lowered the impact, and increased the sheer forces generated by the milling process. [131, 132] In addition, small amounts of oleic acid was added as a surfactant to the mixture to maintain a colloidal dispersion of separate particles throughout the milling. [88] The wet milling approach yielded a narrow, mono-modal particle size distribution as shown in Figure 3.6b.

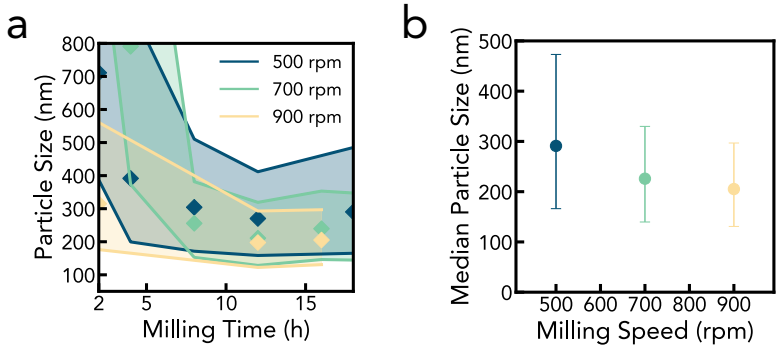


**Figure 3.7: Particle Size in Wet Milling: a,** D10 to D90 of $FeF_2$ particles determined by DLS as a function of milling time at different rotation speeds. The diamond-shaped dots inside the plot indicate respective particle median. **b,** Median (final) $FeF_2$ particle size as a function of rpm. The error bar corresponds to the respective D10 to D90 values.

Figure 3.7a compares the median particle sizes and the width of distribution as a function of milling time for three different ball milling speeds (500, 700, 900 rpm). The D90 and D10 values indicate the average diameter for the $90^{\text{th}}$ and $10^{\text{th}}$ percentile, respectively; that is, 80% of particles in the sample are sized between the D90 and D10 values. In all cases, particle sizes decreased steadily with milling time up to 8 h. After 12 hours of milling, a slight increase in the D90 values can be observed, which might be due to particle coarsening facilitated by the generated heat. A similar trend was observed in an earlier study on $FeF_3$-carbon composites. [69] To prevent a further particle size increase in the 900 rpm run, the synthesis was stopped after 16 hours. The final particle size as a function of milling speed is plotted in Figure 3.7b. The maximum size reduction and narrowest particle size distribution are achieved with increased rotation speeds.

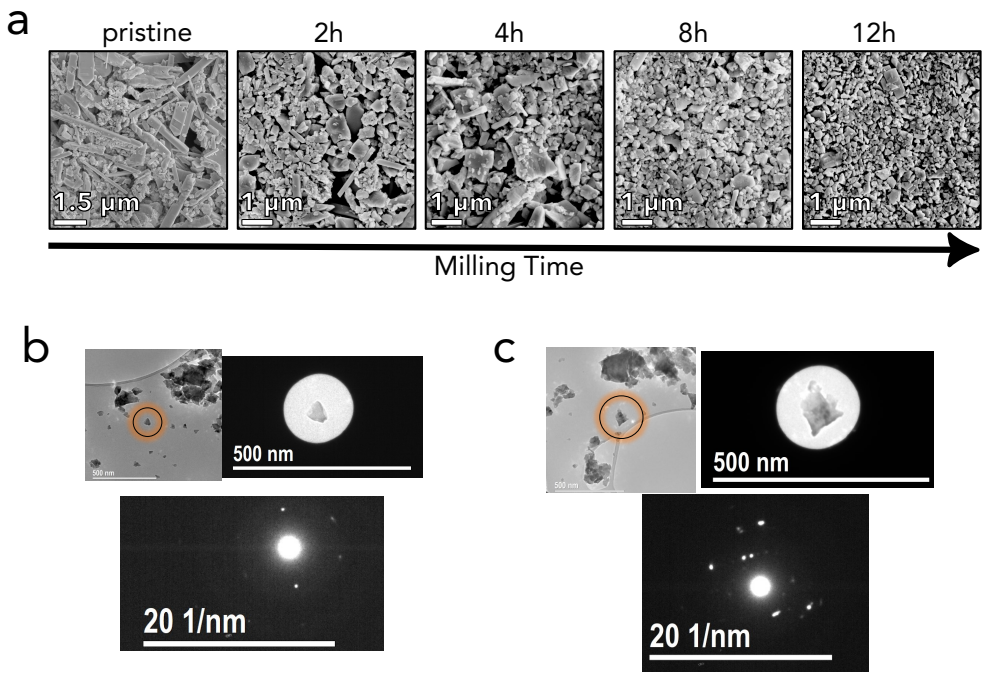


**Figure 3.8: Electron Microscopy of Ball Milled Particles: a,** SEM images of $FeF_2$ particle aliquots extracted from a wet milling process (700 rpm) at increasing milling times. **b,** and **c,** show post-milling electron diffraction of ball milled $FeF_2$. Both particles exhibit single crystallinity.

Particle size quantification using SEM images in Figure 3.8a corroborates the determined size profile by DLS.

Post-milling electron diffraction micrographs are shown in Figure 3.8b and c. Electron diffraction of selected particles (particles that did not overlap) proves that the milling process produces single crystals.

This is critical since a stable fluoride-anion host structure has been identified as a key enabler for the high cycling reversibility of $FeF_2$ cathodes. [87–89] The novel solvent-surfactant-based wet milling recipe demonstrated here enables improved control of the particle size range and benign processing conditions, resulting in single-crystalline active material.

The recipe can be transferred to other transition metal fluoride cathodes. In Figure 3.9, the particle size distribution of wet-milled $CoF_2$ and $CuF_2$ is plotted and compared to $FeF_2$. All particles were ball-milled for 12 h at 700 rpm. It is clearly evident that equally small average particle sizes and narrow size distribution can be produced using the wet-milling recipe.

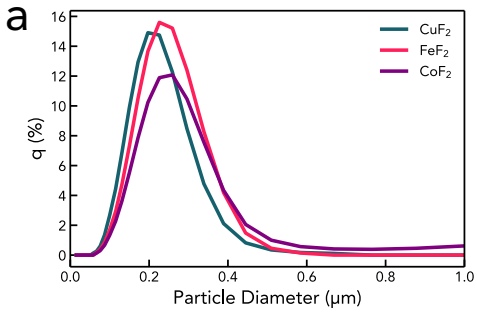


**Figure 3.9: Particle Size of other Transition Metal Fluorides:** Fluoride particle size distribution determined by DLS (volume fraction) for different transition metal fluoride cathodes. The commercial powder was milled for 5 min on, 7 min off for in total 12 h at 700rpm.

To test the effect of particle size on the electrochemical properties of milled $FeF_2$, electrodes from different milling batches were prepared using the co-dispersion method described in section 3.3.2. The cathodes were tested in a coin cell configuration with a Li-metal counter electrode and filled with a 1 M LiFSI $Pyr_{1,3}FSI$ IL electrolyte. The IL electrolyte has demonstrated beneficial electrochemical properties for reversible $FeF_2$ cycling in earlier studies due to the formation of a stable CEI and compatibility with Li-metal anodes. [16, 88, 133, 134]

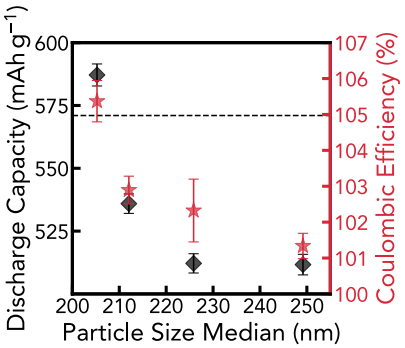


**Figure 3.10: Particle Size vs Capacity:** Average discharge capacity (black) and CE (red) of $FeF_2$ prepared under different ball milling conditions and evaluated in a coin cell using a 1 M LiFSI $Pyr_{1,3}FSI$ electrolyte and a Li-metal anode. Cells were cycled at C/20 at 30 °C. The dotted line corresponds to the theoretical capacity of $FeF_2$

The average discharge capacity and CE at the third cycle at C/20 are compared and depicted as a function of particle diameter median in Figure 3.10. The data suggests that a smaller particle diameter leads to an increase in accessible discharge

capacity and CE. The poor ionic and electronic conductivity of $FeF_2$ can explain the lower accessible capacity in larger particles, as the inner particle core becomes isolated if the particles exceed the diffusion length of $Li^+$ and electrons. [69, 91, 101, 135] Ko *et al.* determined a $Li^+$ diffusion coefficient of around $1 \times 10^{-18}\,cm^2\,s^{-1}$ in $FeF_2$ and suggested that particle sizes below 20 nm are required to achieve a complete conversion reaction. Nanoparticles of that size commonly demand laborious and unscaleable synthesis techniques (*e.g.* solution and colloidal synthesis or direct fluorination [88, 91, 104, 136, 137]) and catalyze parasitic electrolyte reactions. [12] Other studies demonstrated capacities above $500\,mA\,h^{-1}$ in single crystals (around 200 nm long) and measured significantly larger diffusion coefficients. [87, 88, 138, 139] Here, we report that a particle median of around 200 nm is sufficiently small to access the theoretical capacity ($571\,mA\,h\,g^{-1}$) of ball milled, single crystalline $FeF_2$ particles at slow cycling rates (C/20) and 30 °C.

### 3.3.2 Comparative Analysis of Carbon Mixing Techniques

For practical applications, cathodes need to operate at higher current densities while keeping overpotentials and dilution by conductive additives low to enable high energy densities. This can be achieved by ensuring that the active material is well dispersed and in good contact with the conductive additive. In the following section, conventional and novel $FeF_2$-carbon black mixing techniques are characterized and compared, to optimize practical power and energy densities.

- mortar and pestle (MP): A conventional lab scale mixing technique where the active material and the carbon black were thoroughly ground with a mortar and pestle.
- co-dispersion (CD): A meta-stable dispersion of both the active material and the carbon black was prepared in separate solvents, mixed, and centrifuged to remove the liquid phase.
- ultra-stirring (US): A novel technique combining CD with additional ultrasonication (20% amplitude sonication and continuous stirring for 1h in

1,2-dichloroethane) to further improve the mixing by breaking up clusters or aggregates of material.

An illustration of the three different composite preparation techniques is given in Figure 3.11.

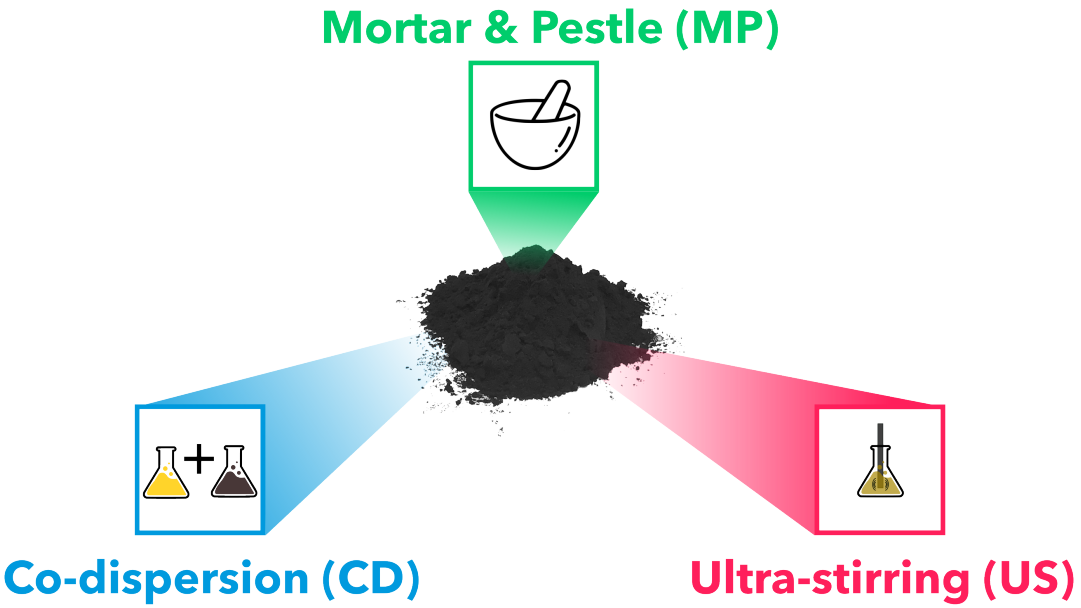


**Figure 3.11: Composite Preparation Technique Overview:** Illustration of the different carbon composite preparation techniques compared in this study.

Electrodes were fabricated from the different composites with an active material content of 70 wt%. The cathodes were wet cast and calendered to a thickness of 15 µm using identical amounts of composite and solvent, resulting in reproducible areal capacities of around 1.5 mg cm$^{-2}$. Figure 3.12 shows the powder XRD patterns of cathodes from all three composites. All of them show clear diffraction peaks, indicating that the process of creating the composite did not affect the crystallinity of the active material.

The particle morphology in each electrode was carefully examined. In Figure 3.13a, d, and g, top-view SEM images are shown. Besides, cross sections were prepared using a precision etching coating system (PECS) as described in section 3.2.2 The cross sections were then imaged using SEM and are shown in Figure 3.13b, e, and h. The SEM images show that the active material morphology remains

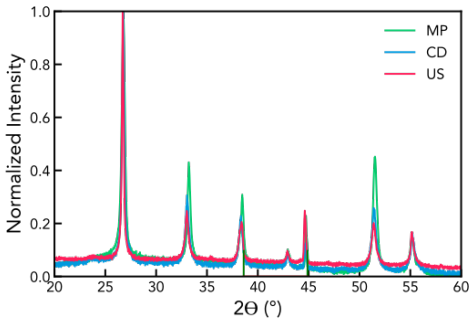


**Figure 3.12: XRD of Cathode Composites:** Powder XRD of cathodes from three different composites. Patterns were collected using a monochromated Cu K$\alpha$ X-ray source from 20° to 60° $2\theta$, at a scan rate of $1\,^{\circ}\,\mathrm{min}^{-1}$. The green lines indicate the diffraction peaks of the underlying aluminium current collector.

unchanged during the composite preparation corroborating the benign conditions during the composite preparation. Occasional larger particles are found in all three composites. These larger particles originated from incomplete size reduction during milling, as depicted in Figure 3.8a.

Elemental mapping using EDX of MP and CD indicates carbon agglomeration between the $FeF_2$ particles, while the US composite exhibits a more homogeneous carbon distribution. The elemental maps are shown in Figure 3.13c, f, and i.

GCPL was conducted at a low rate of C/20 (approximately $35\,\mu\mathrm{A\,cm}^{-2}$) to test the cycling performance of the electrodes prepared with the three different techniques. The normalized potential profiles of the third cycles are plotted in Figure 3.14a.

The profiles are very similar, with slightly higher potential observed in the US cathodes. The voltage hysteresis, defined here as the differences of the re- and discharge potential at 50% state-of-charge (SOC), is reduced from 1.01 V to 0.89 V and down to 0.84 V for the MP, CD, and US cathode respectively, suggesting an improved electronic conductivity in the US composite. Similarly, at the $100^{\mathrm{th}}$ cycle at a C/5 rate, the hysteresis follows the same trend (MP: 1.39 V CD: 1.19 V US: 1.03 V) (see Figure 3.14b)

To further quantify the effectiveness of the carbon mixing techniques, the composites were wet cast onto an insulating glass substrate, and their electronic conductivity was measured using a Van der Pauw four-probe setup. Figure

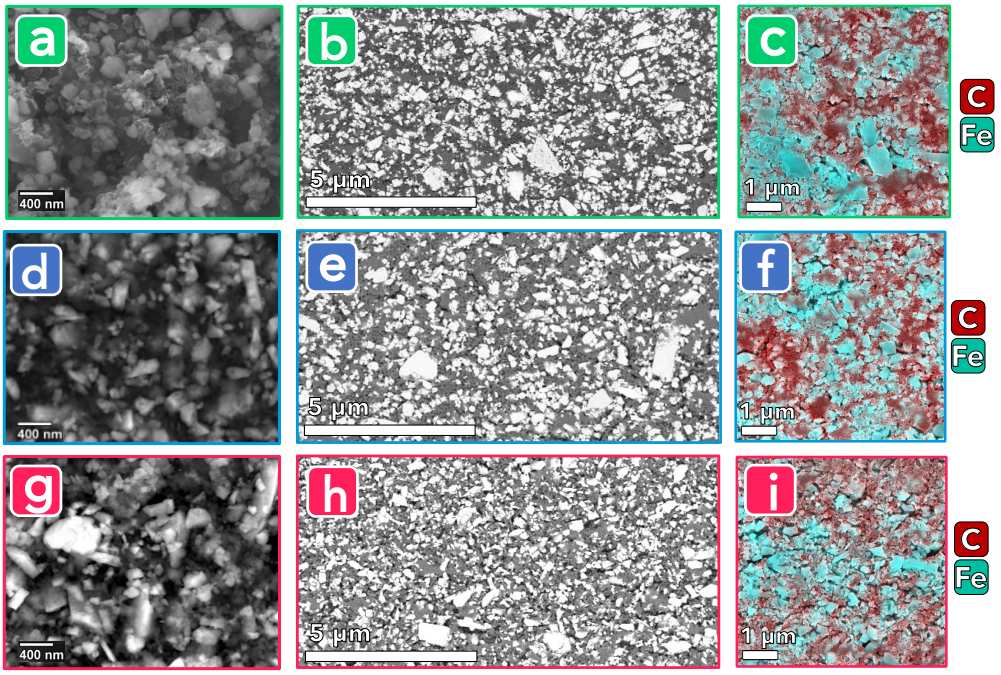


**Figure 3.13: Particle Morphology: a,d,g** Top-view SEM images of the three different $FeF_2$ composites. **a,** Mortar & Pestle, **d,** Co-dispersion, and **g,** ultra-stirred. **b,e,h** SEM Cross-section SEM images prepared with broad beam argon milling tool (Gatan Precision Etching Coating System or PECS using a Ti-blade with electrodag of the three different FeF2 composites, **b,** Mortar & Pestle, **e,** Co-dispersion, and **g,** ultra-stirred. **c,f,i** EDX of the cross sections.

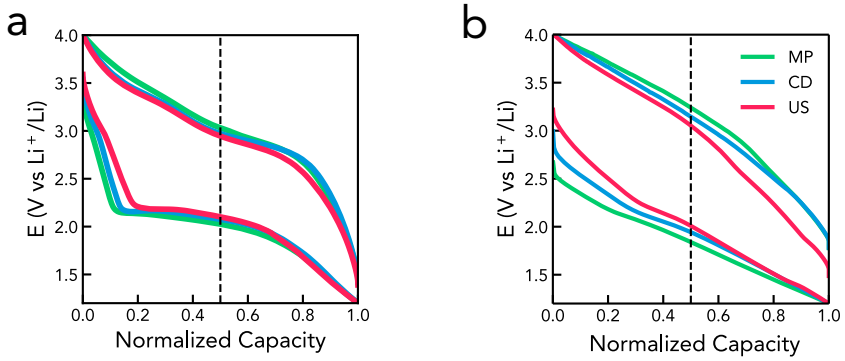


**Figure 3.14: Voltage Hysteresis of Composites: a,** GCPL of three different composites, mortar and pestle (MP), co-dispersion (CD), and ultra-stirring (US), at the third cycle in a 1 M LiFSI $Pyr_{1,3}FSI$ electrolyte at 30 °C. **b,** at the $100^{th}$ cycle.

3.15a shows the conductivity of the composites and their corresponding discharge capacities at a cycling rate of C/5 at cycle number 50. A higher discharge capacity can be obtained with cathodes that exhibit a high conductivity. While the EDX cross-sections of the MP and CD castings showed a very similar carbon distribution,

the conductivity of the latter is almost an order of magnitude larger. This suggests that CD improves carbon distribution compared to mechanical grinding (MP). When mixing the two dispersions during CD, the carbon particles aggregate onto the $FeF_2$ surface to minimize the interfacial energy, resulting in a more homogeneous carbon distribution. Correspondingly, the discharge capacity of CD cathodes is almost $100\,\mathrm{mA\,h\,g^{-1}}$ higher than in MP.

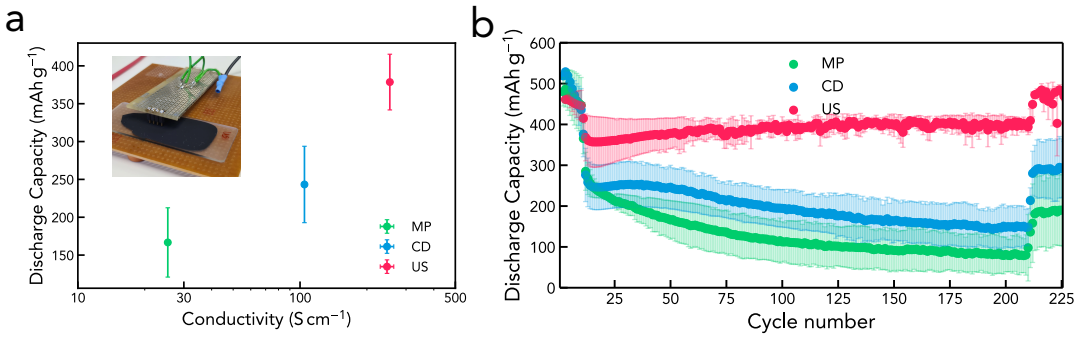


**Figure 3.15: Electronic Conductivity of Composites and Cycling: a,** Average cathode discharge capacity at cycle number 50 (C/5) as a function of conductivity measured by a four-probe setup. The setup is shown in the inset picture. **b,** Average discharge capacity as a function of cycle number for different $FeF_2$ composites. The rate was changed after 10 cycles from C/20 to C/5 and then back to C/20 at cycle number 210. Three different composites are compared, mortar and pestle (MP), co-dispersion (CD), and ultra-sonication (US).

The highest conductivity was found for the US casting, which aligns well with the most homogeneous carbon distribution observed in the cross-section. While the CD relies on a single aggregation event of active material and carbon, the US allows continuous aggregation and re-dispersion throughout the mixing, which further improves the carbon distribution and, consequently, the electronic conductivity.

Considering that the active material particles are of identical size in different composites, *i.e.* the Li diffusion lengths are identical, and the accessible capacity increases with electronic conductivity, we conclude that electronic transport in the composite is the limiting factor over ionic conductivity in the investigated system. Furthermore, the capacity retention in Figure 3.15b suggests that the distribution of super p on the active material affects the cycling reversibility. Electrolyte decomposition is expected to occur along electronic pathways in the composite and thus affects the homogeneity of the CEI.

The US cathode showed excellent capacity retention for over 500 cycles as shown in Figure 3.16.

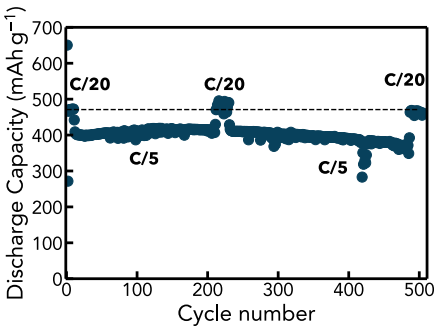


**Figure 3.16: Long-term Cycling of US Cathodes:** Discharge capacity as a function of cycle number for US cathodes with an active material content of 70 wt%. The cell was cycled at a C/20 rate for the first ten cycles, then switched to a C/5 rate for 190 cycles, followed by twenty cycles at C/20, back to C/5 for another 280 cycles, and finally ten more cycles at C/20.

As described in our previous techno-economic analysis [12], a high discharge capacity with an active material mass fraction closer to 85% is required to produce a cell with a competitive energy density. This has not been achieved to date due to the low electronic conductivity of TMF cathodes. Using the US composite preparation technique, $FeF_2$ electrodes with active material mass fractions between 70 and 85% were prepared, as shown in Figure 3.16 and Figure 3.17a. The 70% cell was able to deliver the full discharge capacity over more than 500 cycles (see Figure 3.16).

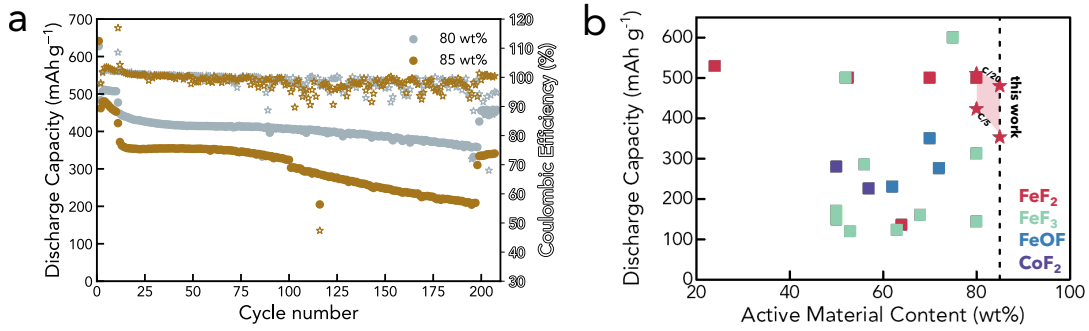


**Figure 3.17: High Active Material Cycling and Literature Comparison: a,** Discharge capacity (dots) and CE (stars) as a function of cycle number of US $FeF_2$ cathodes with 80 and 85 wt% active material content in a 1 M LiFSI $Pyr_{1,3}FSI$ electrolyte at 30 °C. **b,** Literature comparison of TMF cathodes. The plot shows the retained discharge capacity as a function of its active material content. The data was collected from the literature. [77, 88, 90, 93, 95, 100–116]

The 80% and 85% wt cells exhibit near theoretical capacities with no discernible difference in capacity retention at slow cycling rates (C/20) and maintained 90% and 72% capacity over 220 cycles. The high capacity retention in US $FeF_2$ cathodes at such a high active material content marks the best cycling performance reported for TMF cathodes to date. A comparison with the literature is shown in Figure3.17b. The CE of the cells stabilizes at around 100.6% until roughly the $100^{th}$ cycle when CEs below 100% are measured. Further characterization of the cycled electrodes was conducted to investigate the origin of parasitic reactions causing the decay in CE.

### 3.3.3 Aging Mechanisms and Morphological Evolution during Cycling

A CE of 101.77% and 99.26% were measured on the second and the $505^{th}$ cycle of a US cathode, respectively. $FeF_2$ commonly exhibits excess discharge capacity during the first cycle resulting in CE above 100% due to the formation of a CEI. The CEI formation is further facilitated by the catalytic activity of the metal phase formed during discharge, and as a result, a CE above 100% is characteristic for TMF cathodes. [12, 88, 134] However, a drop below 100% is indicative of parasitic reactions occurring with progressing cycling.

In order to better understand the electrochemical cycling behavior, the GCPL of the second and the $505^{th}$ cycle and the evolution of differential capacity (dQ/dV) are plotted in Figure 3.18a and Figure 3.18b, respectively. A discharge capacity of $461\,\mathrm{mA\,h\,g^{-1}}$ is maintained over more than 500 cycles (1% capacity fading) which corresponds to 81.5% of the theoretical capacity of $FeF_2$. However, the voltage profiles exhibit different features, which indicate a change in redox reactions. The main voltage plateau located at 2.25 V vs $Li^+$/Li and 2.8 V vs $Li^+$/Li in the second dis- and recharge cycle gradually shifts to lower potentials (marked green in the dQ/dV plot). A the same time, the plateau-specific voltage hysteresis, defined as the voltage distance of the respective dQ/dV peaks, shrinks from 731 mV to 552 mV over 500 cycles. Consequently, the plateau shift to a lower potential is not a result of a growing overpotential.

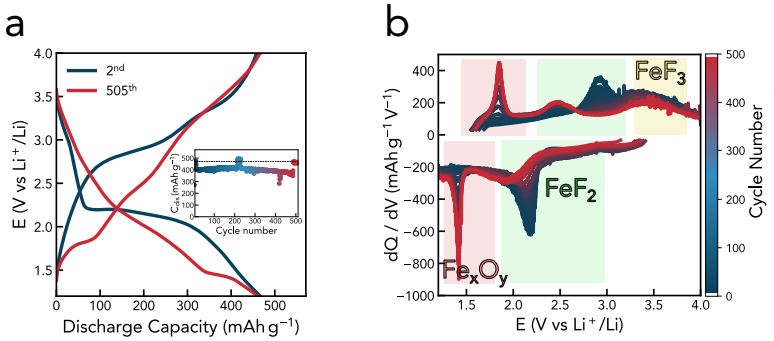


**Figure 3.18: $FeF_2$ Cathode Composite Aging Electrochemistry: a,** GCPL of an ultra-stirred FeF-IL Li-metal cell after 2 and 505 cycles at 30 °C. **b,** Corresponding differential capacity plot highlighting different redox processes occurring at different potentials (yellow for $FeF_3$; green for $FeF_2$; red for $Fe_xO_y$).

Additionally, the GCPL at cycle 505 shows a capacity of around 100 mA h g$^{-1}$ over 2.5 V vs Li$^+$/Li during dis- and recharge. The increased potential can be ascribed to the occurrence of $Fe^{3+}$-$Fe^{2+}$ redox reactions and has previously been reported. [88] Moreover, an additional reduction and oxidation plateau emerges at 350 mA h g$^{-1}$ to 450 mA h g$^{-1}$ and 0 mA h g$^{-1}$ to 100 mA h g$^{-1}$ during cell dis- and recharge at 1.45 V and 1.85 V vs Li$^+$/Li, respectively. The dQ/dV plot clearly shows its gradual occurrence after about 250 cycles (red box). The evolution of this additional redox feature at low potentials suggests the gradual formation of a new redox-active species during cycling. It is noteworthy that the redox plateau was also observed in cells cycled inside an argon-filled glovebox. A plausible reversible redox couple that could be formed at this potential is $Fe_2O_3$ or $Fe_3O_4$. Indeed, both iron-oxides exhibit an initial lithiation potential of around 1.4 V, which aligns well with the observed reduction potential in the GCPL. [69, 140–142] The formation of a $Fe_3O_4$ surface layer on $FeF_2$ has been previously reported. [143]

To further elucidate the aging mechanism of $FeF_2$ cathodes, the cycled cell was disassembled at 100% SOC, analyzed, and compared to an identical cathode that was only cycled twice. XPS was used to characterize the chemical composition and binding environment of the active material in the cathodes. The complete XPS spectra in the iron energy range are shown in Figure 3.19a and b, and in the carbon energy range in Figure 3.19c, d for a cathode cycled twice and 505 times respectively.

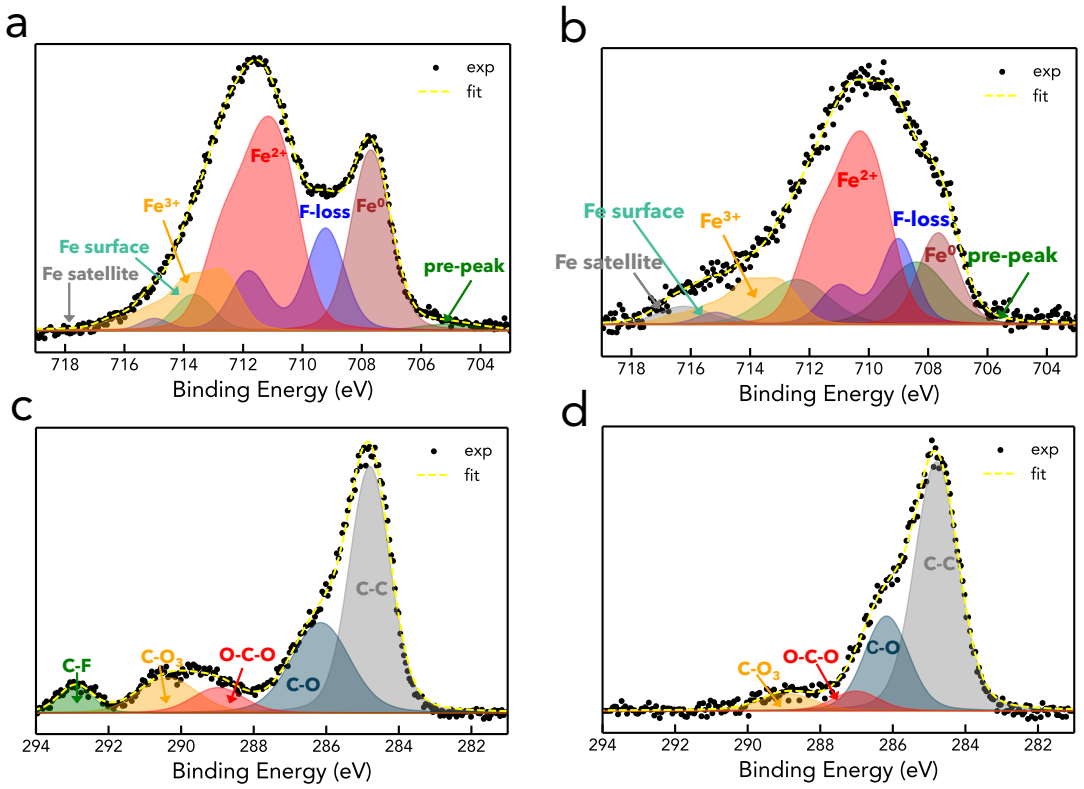


**Figure 3.19: XPS of cycled cathodes:** Cathodes XPS fit in the iron energy range for two different US cathodes. **a,** corresponds to a cathode after the second cycle and **b,** was fitted to the cathode cycled 505 times. The measurements were collected after 3600s of argon sputtering. All fits were set up using constraints for peak splitting and FWHM extracted from [144] Below are the cathodes XPS fit in the carbon energy range for two different US cathodes. **c,** corresponds to a cathode after the second cycle and **d,** was fitted to the cathode cycled 505 times. The measurements were conducted without any argon sputtering to preserve the cathode's CEI.

Analyzing XPS spectra in the iron energy range is complicated due to the multitude of peaks ($Fe^0$, $Fe^{2+}$, $Fe^{3+}$, satellite, pre-peak, fluorine loss). Grovenor *et al.* published a comprehensive overview of how to process and fit various iron compounds. [144] Their work is taken as a guideline when analyzing the obtained XPS data of the cycled cathodes. Spectra were calibrated using the carbon peak located at 284.8 eV and sputtered for one hour with argon ions to remove the CEI and thus increase the iron signal. For the analysis of the carbon XPS energy range, unsputtered spectra were used.

Around 20% of metallic iron can be detected in both cathodes, the one cycled twice, and the one cycled 505 times. Isolation of metallic iron, which is trapped in

a disordered surface layer of the active material, irreversible capacity loss, and the formation of $Fe^{3+}$ has been previously observed by Xiao *et al.* in the first cycle of $FeF_2$ cathodes. [88] Both, capacity above 2.5 V vs $Li^+/Li$, which is indicative of $Fe^{3+}$ redox and a capacity below the theoretical value of $FeF_2$, are observed in Figure 3.18a, in agreement with the detection of metallic iron in the presented XPS results.

To facilitate visual comparison, the Fe $p_{3/2}$ energy range is isolated and shown for the cathode after 505 cycles and an identical cell after two cycles in Figure 3.20. Interestingly, a shift of the $Fe^{2+}$ $p_{3/2}$ peak from 710.7 to 709.6 eV can be observed. Both peaks align with reported values for $FeF_2$ and $Fe_2O_3$ or $Fe_3O_4$, respectively. [144] This further corroborates the formation of an $Fe^{3+}$-oxide species during cycling.

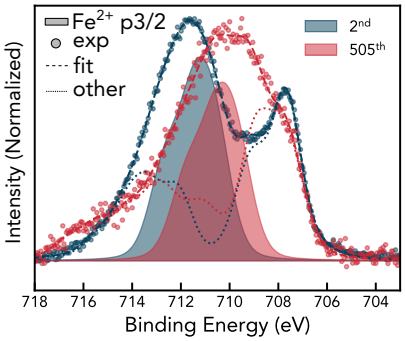


**Figure 3.20: Isolated XPS of Cycled Cathodes:** XPS of iron highlighting the $Fe^{2+}$ $p_{3/2}$ peak position after 2 and 505 cycles respectively.

To collect further information on the morphology and elemental composition of the active material, the cathode was washed and re-dispersed in N-methyl-2-pyrrolidone to remove the binder and electrolyte decomposition products. scanning transmission electron microscopy (STEM) and TEM micrographs (Figure 3.21a) after cycling display primary active material particle size in the 250 nm to 400 nm range, which is comparable to the size of the pristine material. Particle agglomeration is one of the main origins of capacity loss in TMF cathodes [12]. We attribute this behavior to the robust CEI derived from the IL electrolyte. [88] Figure 3.21b shows the cell impedance before and after cycling. Indeed, a negligible interphase impedance increase can be observed, which supports this observation of a robust

CEI. The surface of the cycled particle is partially covered in a grainy texture which might originate from surface trapped metallic iron. At larger magnifications, two types of morphology can be observed. In Figure 3.21a, the STEM image of an active material particle and its corresponding Fourier transform, shown as inset, display short-range ordering with an amorphous halo, respectively. In an additional particle shown in Figure 3.21c, the absence of lattice fringes is observed. This morphology is fundamentally different from the single crystalline pristine particles described above and indicates the active material undergoes structural changes throughout extensive cycling. This is corroborated by ex-situ XRD shown in Figure 3.21d, where the cathode cycled 505 times did not display any diffraction peaks. EDX analysis of another cycled $FeF_2$ particle shows a uniform distribution of iron, oxygen, and fluorine atoms in the particle.

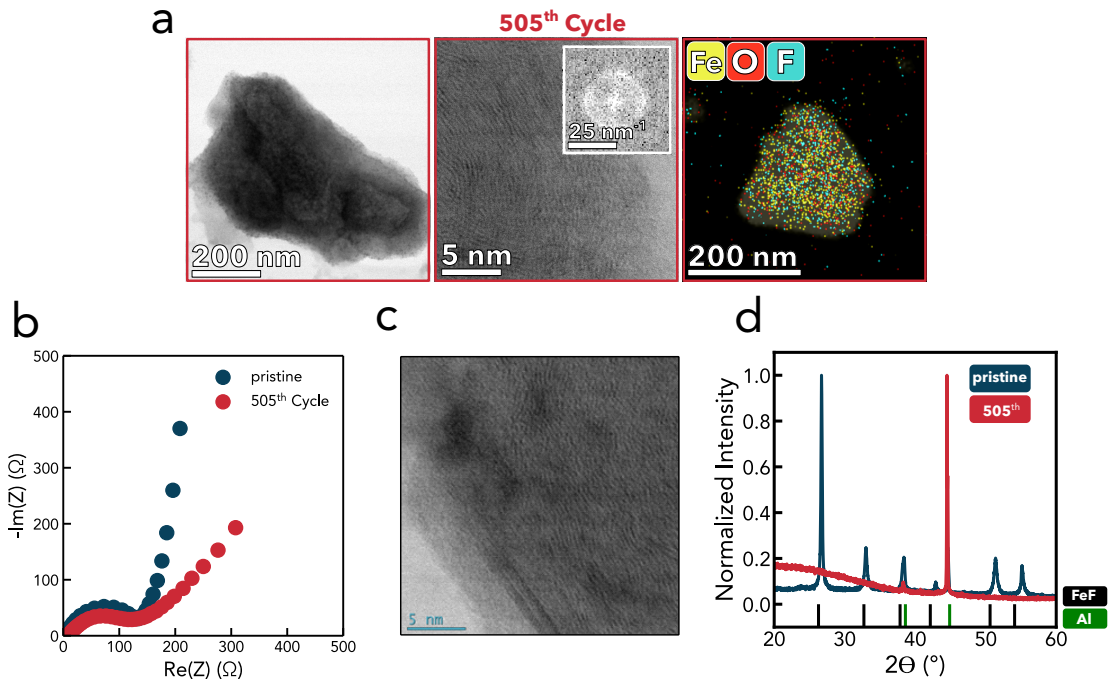


**Figure 3.21: Characterization of Cycled $FeF_2$ cathodes: a,** Post mortem STEM of US cathodes after 500 cycles. **b,** Impedance of the US cathode before and after cycling. **c,** Zoom-in on post mortem STEM images of US cathodes after 500 cycles. **d,** XRD pattern of a disassembled US cathode cycled twice and 505 times at 30 °C. The reference spectrum of $FeF_2$ and aluminum are inserted.

To further investigate the bulk active material composition, XANES spectroscopy was used to characterize a pristine cathode and the cycled cathodes (cycle 2 and 505)

shown in Figure 3.22. A comparison of Fe K-edge spectra reveals that the white line intensity is significantly reduced in the cycled cathode, a change indicative of either a lower overall iron oxidation state in the cathode material or a less defined electronic structure. Since all three cathodes exhibit similar edge energies (7126.2, 7125.8, and 7125.1 eV), a drastic change in oxidation state (*e.g.* continued formation of metallic iron) is unlikely. In view of the increasing disorder, reduced crystallinity detected by XRD, and the loss of defined $FeF_2$ particle morphology, we suggest the decreased white line intensity to be rooted in a continuing amorphization of the active material. In addition, the cycled cathodes exhibit a pre-edge feature which is characteristic for $Fe^{3+}$-oxygen species such as $Fe_2O_3$ or $Fe_3O_4$ but is not expected in $FeF_x$ compound. [145, 146] This further validates the presence of an iron-oxide phase in the bulk of the cycled active material.

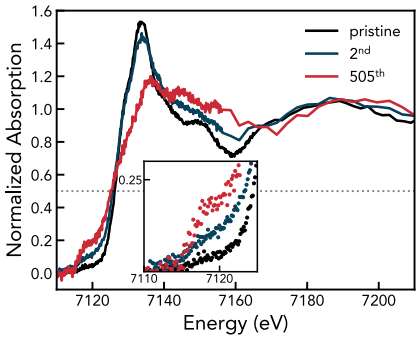


**Figure 3.22: XANES of Cycled Cathodes:** Fe K-edge XANES measurement of the cycled cathodes in comparison to a pristine $FeF_2$ cathode.

Considering all of the above, we suggest the following aging mechanism of $FeF_2$ cathodes in the LiFSI $Pyr_{1,3}FSI$ electrolyte. From the first cycle on, $FeF_2$ exhibits an incomplete re-conversion reaction with trapped metallic iron on the surface of the active material. Some of the metallic iron on the surface reacts over the course of several hundred cycles with oxygen-containing electrolyte decomposition products in the CEI, gradually forming $Fe_xO_y$ during recharge. Lithium oxide, sulfonyl-, and organic oxygen compounds were detected in the CEI (see Figure 3.19) and were previously reported by our group. [88] As a result, excess charge capacity can be observed, which results in CE fluctuating between 95% and 99%

(see Figure 3.17a). Simultaneously, an additional redox plateau appears at low potentials. We estimate that after 500 cycles, around 20% of the total capacity originates from lithiation of the iron-oxide species at low potentials, indicating that the oxide layer extends into the bulk of the active material.

Further, TEM, XRD, and XAS analysis indicate a gradual amorphization of the active material. The evolving iron-oxide phase does not share semi-coherent lattice interphases with the existing fluoride anion-host structure and thus results in a loss of long-range ordering and, ultimately, amorphization. The results suggest that the cycled cathode exhibits faster reaction kinetics as a reduced voltage and improved energy efficiencies are observed (70.6% to 72.8% from the $2^{nd}$ to $505^{th}$ cycle). An earlier study comparing crystalline and amorphous $FeF_2$ using GITT determined faster reaction kinetics in the amorphous material. [139]

$[FSI]^-$ is the only oxygen-containing active component in the cell. Since the iron-oxide phase gradually forms throughout cycling, $[FSI]^-$ anions are expected to be consumed beyond the initial CEI and SEI formation. Due to the presence of excess electrolyte, cell performance in this work has not been significantly affected.

In order to quantify the amount of $[FSI]^-$ consumption, the LiFSI concentration in the electrolyte was measured. Calculation of LiFSI concentration in a $Pyr_{1,3}FSI$ ionic liquid electrolyte was inspired by research using operando raman gradient analysis (ORGA), which was originally developed by Fawdon *et al.* and will be at the core of the second project in this thesis. [22, 147, 148] In ORGA, the local LiFSI concentration is visualized by measuring the peak of the S-N-S bending mode in $[FSI]^-$. The peak of the bending mode shifts to higher wavenumbers monotonically with increasing $Li^+$ concentration because of the continuing formation of high-energy bonding $Li(FSI)_2$ structures. Therefore, the peak maximum can be used to calculate the LiFSI concentration in the electrolyte. A calibration line was established by measuring varying amounts of LiFSI in $Pyr_{1,3}FSI$. The bending mode was fit with a Gaussian and the maximum of the fit was determined. The peak maximum is plotted as a function of LiFSI concentration in Figure 3.23a. Subsequently, the electrolyte was extracted from the cell that was cycled 505 times. Figure 3.23b shows

the bending mode and the corresponding peak maximum, compared to pristine electrolyte. The peak maximum of the cell cycled 505 times shifts to lower wave numbers, indicating a reduction in LiFSI concentration.

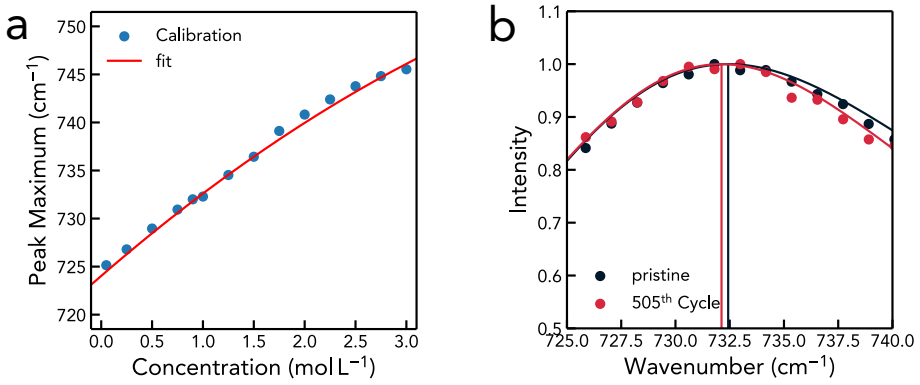


**Figure 3.23:** c onsumption]**Quantification of [FSI]$^-$ consumption: a,** Calibration line to relate LiFSI concentration in LiFSI $Pyr_{1,3}FSI$ with the S-N-S bending mode peak **b,** S-N-S bending mode peak for a cycled electrolyte (505 cycles) and a pristine one.

During the course of 500 cycles the LiFSI concentration decreases from an initial value of 0.98 mol L$^{-1}$ to 0.94 mol L$^{-1}$. This decrease corresponds to an [FSI]$^-$ consumption rate of 11 µmol g$^{-1}$ per cycle. It's important to acknowledge that the Li-metal anode is also anticipated to play a role in the depletion of [FSI]$^-$, and there is also the likelihood of $[Pyr_{1,3}]^+$ being consumed, which adds complexity to the calculation of the LiFSI concentration decline. As a result, a more comprehensive analysis of electrolyte consumption is essential for accurately determining the rate of [FSI]$^-$ consumption.

### 3.3.4 Investigating the Electrochemical Behavior at Elevated Temperatures

Electric flight applications require high power loads during take-off and landing. [6–8] At larger discharge currents, a large overpotential limits the accessible capacity of $FeF_2$ cathodes, particularly at a high active material content. The high thermal stability of TMF cathodes and ionic liquid electrolytes enables cell operation at elevated temperatures. Higher thermal energy increases ion transport and reaction kinetics, improving rate capability. [85, 88, 89, 117, 118] Battery packs in electric

aircrafts contain active cooling to control the operating temperature. By carefully managing the active cooling system, a controlled battery heat-up during flight sections that require critical power loads could enhance the power output capabilities of $FeF_2$ cathodes. Therefore we investigated the electrochemical performance of $FeF_2$-IL cells at elevated temperatures.

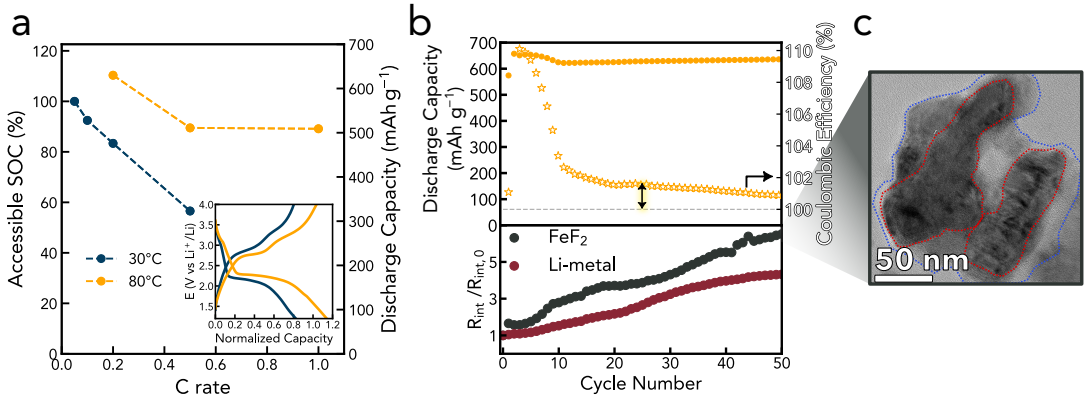


**Figure 3.24: High-temperature Cycling of $FeF_2$-Cathodes: a,** Accessible state-of-charge as a function of cycling rate at different temperatures. The inset shows the corresponding, normalized GCPL at 30 °C, 80 °C, and 120 °C. **b,** Discharge capacity of three-electrode cells cycling $FeF_2$-IL at 30 °C and 80 °C at a C/20 and C/5 rate respectively. Below are the corresponding cathode interphase impedances as a function of cycle number determined by EIS. **c,** TEM image of the particles found in the cathode cycled 50 times at 80 °C.

The normalized GCPLs of $FeF_2$ cells (third cycle) at 30 °C and 80 °C, are plotted in Figure 3.24a (inset). With increasing temperature, the overpotential decreases, and thus the corresponding energy efficiencies increase from 71.3% to 77.0%. Figure 3.24a shows the accessible SOC and discharge capacity for different cycling rates. Around 90% of SOC can be accessed at 1C at 80 °C. 1C discharging speed of $FeF_2$ cathodes corresponds to around 1.3 kW $kg^{-1}$, which satisfies power requirements during take-off and landing in some electric aircraft designs. [8]

In order to test if the same cycling stability can be maintained at elevated temperatures, three-electrode cells were prepared. Using a Li-metal reference electrode enables the deconvolution of interphase impedances from the CEI and SEI, respectively, and thus can provide insights into the electrode interphase stability

under galvanostatic conditions. Figure 3.24b shows the discharge capacity, CE, and both cathode and anode interphase impedances as a function of cycle number 80 °C.

The cell cycled at 80 °C shows an increase of discharge capacity in the first ten cycles beyond the theoretical capacity of $FeF_2$ (571 mA h $g^{-1}$) before it stabilizes at about 630 mA h $g^{-1}$ for over 50 cycles. Concurrently, the CE increases to around 110% before stabilizing at around 100.8%. A comparison with cells cycled at 30 °C shows that both discharge capacity and CE are increased at elevated temperatures (compare to Figure 3.17a). The CE of more than 100% indicates that continuous electrolyte consumption contributes to the Faradaic current. Accordingly, the normalized cathode and anode interphase impedances steadily increase at 80 °C in contrast to the cell cycled at 30 °C, which displays a constant interphase impedance (Figure 3.24b). An increase in temperatures accelerates and exacerbates parastic reaction, thus resulting in a higher CE, SEI, and CEI growth.

TEM imaging of cycled particles showed the presence of a 10 nm thick amorphous layer covering the cycled $FeF_2$ particles as shown in Figure 3.24c. Even at elevated temperatures, the particles did not fuse, maintaining a primary particle size within the diffusion length of $Li^+$ and consequently enabling full capacity retention.

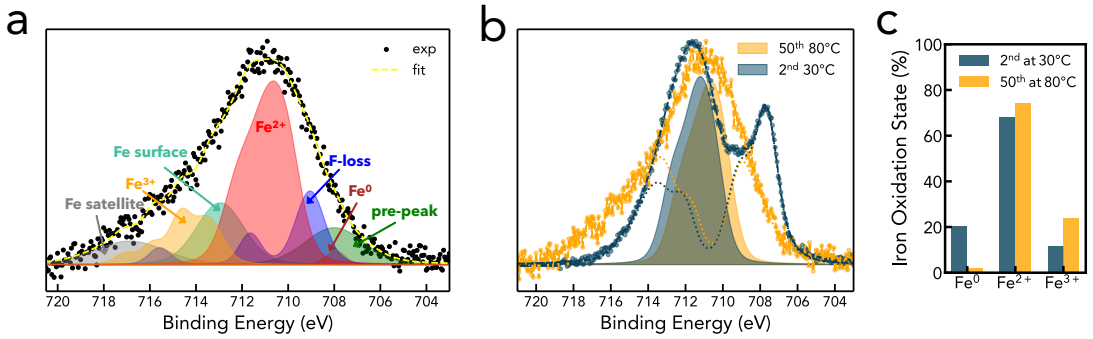


**Figure 3.25: XPS of High Temperature Cycled Cathodes: a,** XPS fit in the iron energy range for a cathode cycled 50 times at 80 °C after 3600 s of argon sputter. The metallic iron peak was set at the same energy and full width at half maximum values where it has been detected before to enable comparability (707.7±2 eV; 1.5 ±0.2) **b,** Comparison of the iron energy range highlighting the $Fe^{2+}$ $p_{3/2}$ peak position after 2 cycles at 30 °C vs 505 cycles at 505 °C respectively. **c,** Iron oxidation state determined by XPS of the cathode cycled 50 times at 80 °C and twice at 30 °C.

When comparing the iron oxidation state composition determined by XPS (Figure 3.25), of charged particles at 30 °C and 80 °C it becomes evident that no

metallic iron is present in the cell operated at 80 °C. This observation aligns well with the increased accessible capacity compared to operation cycling at 30 °C. As thermal energy increases, the diffusion length of $Li^+$ cations in $FeF_2$ increases, allowing the conversion of the previously inaccessible inner particle core.

Moreover, the inset in Figure 3.24a highlights an increased capacity contribution from the potential plateau at 3.1 V vs $Li^+$/Li at 80 °C, attributed to a $FeF_3 + e^- \rightarrow FeF_2$ redox process (theoretical specific capacity of 237 mA h $g^{-1}$). [88, 89, 93] Post-mortem XPS analysis (Figure 3.25c) also confirms a higher $Fe^{3+}$ content in the charged cathode compared to a cell cycled at 30 °C. This additional capacity accounts for the specific capacity exceeding the theoretical value for $FeF_2$. The additional fluoride necessary for the formation of $FeF_3$ might stem from the decomposition products in the CEI. Further experiments are needed to verify this hypothesis.

To explore cell operation at even higher temperatures, the testing apparatus was modified. Therefore, coin cell gaskets made of thermally-resistant perfluoroalkoxy alkanes (PFA) were purchased and used to substitute conventional polypropylene (PP) gaskets due to their improved thermal stability. Since conventional coin cell holders are only designed for temperatures up to 80 °C, we manufactured a custom-made rack made of polyimide (PI) and high-temperature wiring as shown in Figure 3.26b.

Optimized $FeF_2$ with an active material content of 80 wt% were used for all subsequent testing. All cells were precycled at 30 °C to enable the controlled formation of a CEI and SEI. Once heated up to 120 °C, all cells were cycled at a 1C cycling rate.

Figure 3.27b shows the discharge capacity of two coin cells cycled at 120 °C as a function of cycle number. The best-performing cell comprises a 1 M LiFSI $Pyr_{1,3}FSI$ electrolyte and shows a theoretical capacity retention for up to 40 cycles. It should be noted that this particular cell had to be stopped and restarted multiple times due to unrelated maintenance issues which caused the irregular discharge capacity variations (visible at cycle 28 and 40).

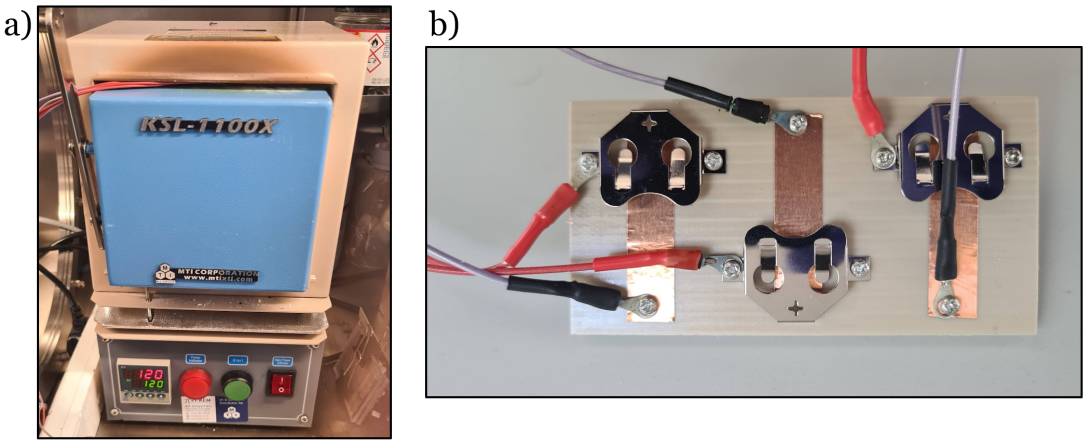


**Figure 3.26: High temperature cycling setup: a,** Furnace inside argon-filled glovebox for high temperature testing and **b,** custom-made coin cell holder for high temperature measurements.

When operating at 30 °C and cycling at high potentials (∼4 V) we normally use cell casings with an aluminium coating at the positive electrode. Similar to $LiPF_6$, $[FSI]^-$ anions are reported to form a passivating layer with aluminium which prevents corrosion of the current collector and the steel casing. [149] Depending on the quality of the steel, this might or might not be detrimental to the cycling performance of the cell. However, the formation mechanism and stability of this $[FSI]^-$ -derived layer is expected to change at temperatures as high as 120 °C. However, more experiments are required to test this hypothesis.

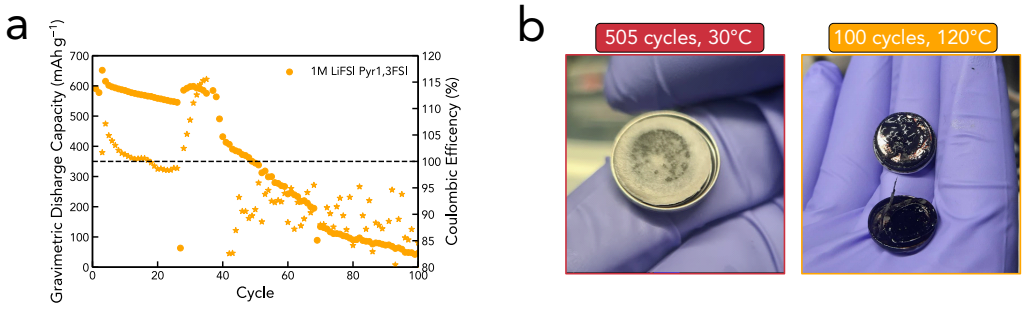


**Figure 3.27: Cycling at** 120 °C **a,** Discharge capacity as a function of cycle number in a coin cell cycling at 120 °C **b,** shows the decrimped cells cycled at 30 °C and 120 °C respectively. The cell cycled at 120 °C shows disintegration of the composite, indicating the PVDF binder is not stable enough for continuous operation at such a high temperature.

Our results demonstrate that the $FeF_2$-IL cells can be cycled reversibly at

up to 120 °C. With increasing temperature, more $Fe^{3+}$ is accessed, the voltage hysteresis is reduced, and rate capability is improved, overall increasing the energy and power density of the cells.

### 3.3.5 Cell Safety

Electric flight applications require batteries with improved cell safety features due to the critical nature of operation failures. [6] Consequently, we investigated the thermal stability of the proposed cell chemistry individually and in a full-cell configuration. The full configuration allows monitoring of the heat flow of any reaction within the battery, including the ones originating from the liquid-solid interphases. Therefore, we designed a that was suitable to be mounted into an simultaneous thermal analyzer (STA) setup. A computer-aided design (CAD) drawing of the tailor-made battery casing for STA measurements (STA-cell) is shown in Figure 3.28

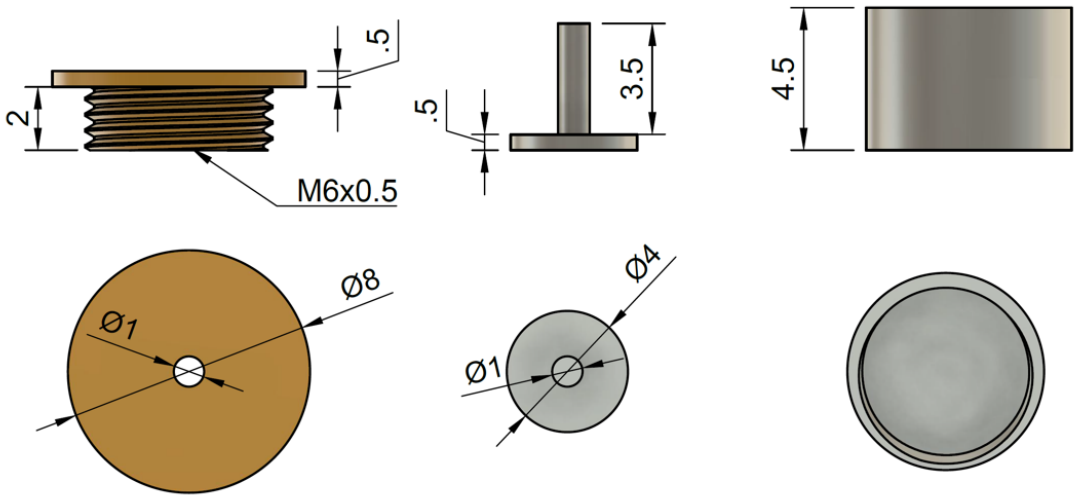


**Figure 3.28: CAD Drawing of STA-Cell:** In-house developed CAD drawing of a cell that could be mounted onto a STA sample carrier.

To account for the formation of a CEI and SEI, the STA-cell was dis- and recharged before its investigation on the STA. The observed heat flow was calibrated by the endothermic Li melting peak and plotted over the individual cell components. Before testing the STA-cell, all active cell components were characterized in a conventional alumina crucible. For comparison, an identical thermal analysis

of a conventional layered-oxide in organic electrolyte (lithium-nickel-manganese-oxide, LNMO in LP30, 1 M $LiPF_6$ in ethylene carbonate : dimethyl carbonate 1:1) cell was conducted.

Figure 3.29a shows the heat flow and mass loss (dotted line) as a function of temperature. The LP30 electrolyte shows a significant mass loss and an endothermic heat flow peak at around 150 °C, most likely due to the evaporation of DMC (Figure 3.29a) In contrast, the LMNO cathode and Li-metal anode are stable up to the melting point of Li (Figure 3.29a). However, the STA-cell, containing all active components and both electrode-electrolyte interphases, shows additional heat flow peaks and a significant exothermic drift from 140 °C up to the melting point of Li. This indicates thermally induced electrode interphase reactions and serves as a proof-of-concept to monitor heat flow in the STA-cell.

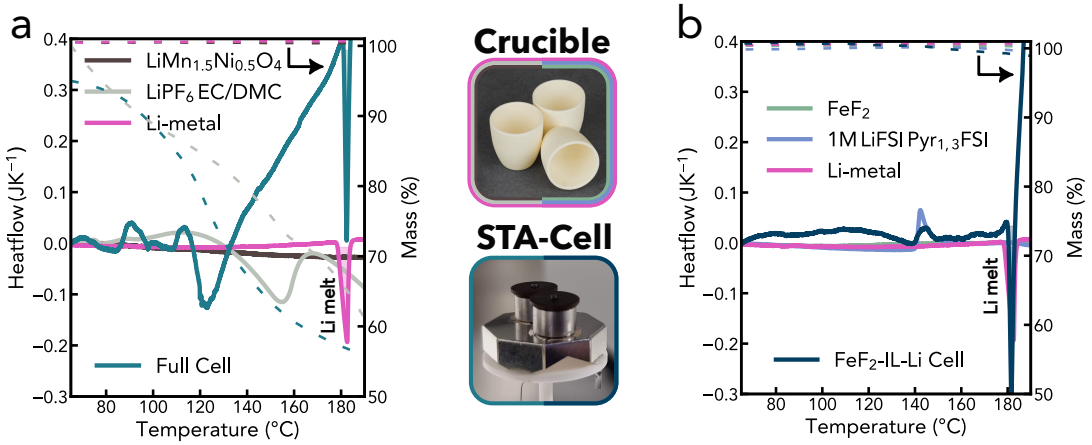


**Figure 3.29: Cell Safety Testing:** **a,** STA profile of LMNO, 1 M $LiPF_6$ EC/DMC=50/50, Li-metal measured in crucibles, and a full cell configuration measured in an in-house developed STA-cell. The heat flow (solid line, left axis) and mass loss (dashed line, right axis) are shown. **b,** STA profile of $FeF_2$, 1 M LiFSI $Pyr_{1,3}FSI$ (IL), Li-metal in crucibles, and a full cell configuration measured in the STA-cell.

Next, the $FeF_2$-IL-Li-metal chemistry was investigated. Similar to before, all components were individually measured in a crucible, as shown in Figure 3.29b. Neither of the three components displays any mass loss within the investigated temperature range. Differential differential scanning calorimetry (DSC) of the IL shows one exothermic peak at around 140 °C. LiFSI melts at a similar temperature range as indicated by the endothermic melting peak of the pure salt.

Consequently, the exothermic peak observed in the IL might originate from a structural reorganization of the $Li^+$-$FSI^-$ ions. Besides, only a Li melting peak is visible amongst the active cell components.

The STA-cell exhibited the same exothermic peak that was visible when measuring the pure electrolyte. The small exothermic drift observed between 80 °C to 140 °C is attributed to minor differences in the sample and reference STA-cell. No additional peaks were detected, which indicates the full cell, including its interphases, is stable to at least 140 °C. The results indicate that no thermal runaway occurs up to the melting point of Li-metal. However, additional accelerating rate calorimeter (ARC) measurements in larger cell formats are required for verification.

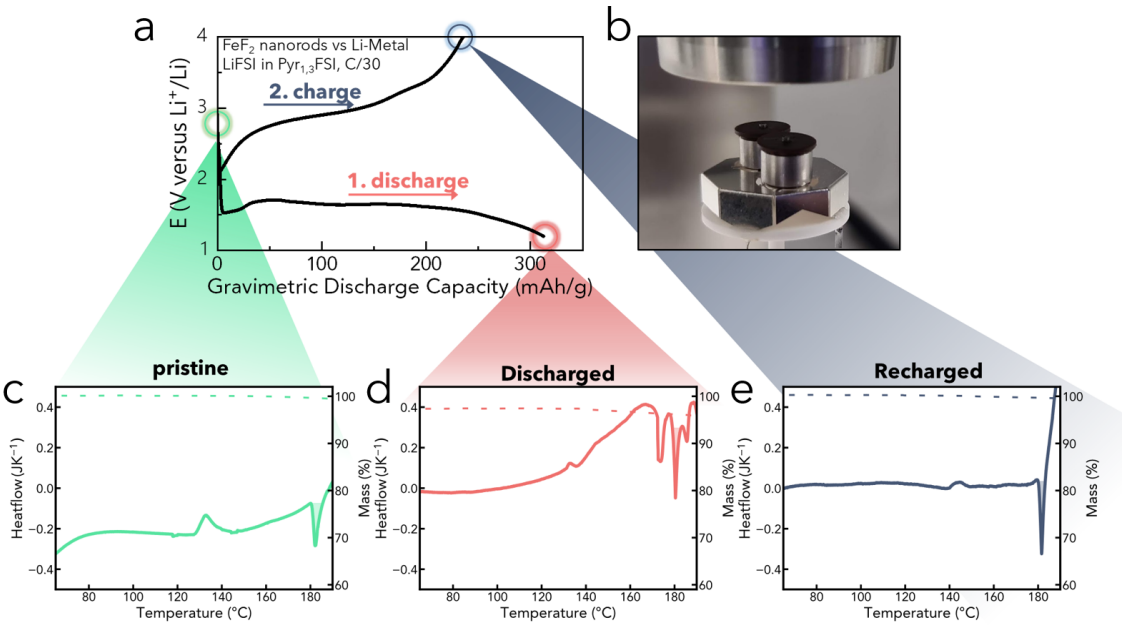


**Figure 3.30: State-of-charge Dependent STA-Cell Experiments: a,** GCPL of a STA-cell that uses $FeF_2$-Li-metal 1 M LiFSI $Pyr_{1,3}FSI$. The cell was can be successfully dis- and recharge which enables a SOC dependent stability study. **b,**

The stability experiment was repeated at different states-of-charge (SOC) for the $FeF_2$-Li-metal 1 M LiFSI $Pyr_{1,3}FSI$ chemistry. As shown in Figure 3.30a the STA-cell can be successfully dis- and recharged. No heat flow could be detected below the exothermic peak at 140 °C. However, an exothermic drift was observed in the discharged cell, which could be attributed to electrolyte decomposition catalyzed by iron metal covering the surface of the discharge cathode. [12] This is an interesting

finding as it suggests the thermal stability of the cells decreases with SOC, which is contrary to most cell chemistries. Overall the STA-cell characterisation showcases improved cell safety features in $FeF_2$-IL cells over conventional chemistries. Our results further indicate the full-cell configuration is stable up to the melting point of Li of 181 °C, providing further versatility for high-temperature applications.

### 3.3.6 Pouch Cell Performance and Energy Density Calculations

To test if the cycling performance could be reproduced in larger electrodes, pouch cells were prepared. For that, US cathode composites of different sizes were prepared and combined with a 30 µm thin Li-metal anode and 1 M LiFSI $Pyr_{1,3}FSI$ electrolyte (around 150 mL $g^{-1}$). Figure 3.31a shows the discharge capacity as a function of cycle number in a 42 mA h (32.64 $cm^2$) pouch cell compared to a control coin cell. The pouch cell performs similarly to the coin cell and can reversibly access over 480 mA h $g^{-1}$ at slow cycling rates while showing small capacity fading at a higher rate. Figure 3.31b shows how the prepared pouch cells can power a oxford LED logo.

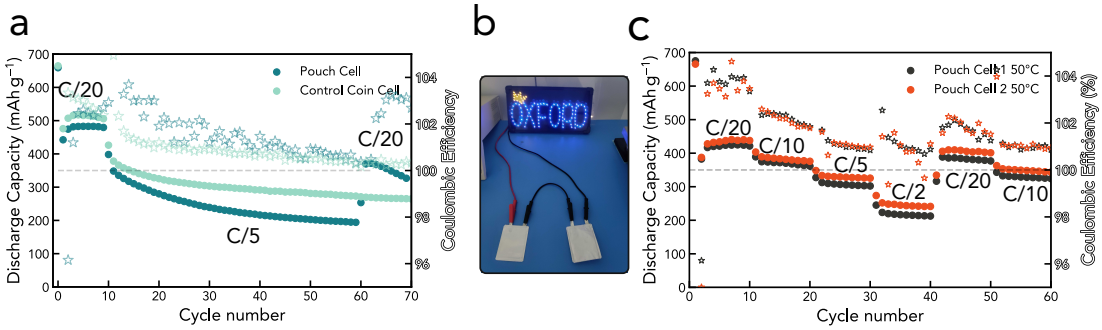


**Figure 3.31: Pouch Cell Experiments: a,** Discharge capacity and CE of a 42 mA h $FeF_2$-Li-metal pouch cell with a cathode surface area of 32.64 $cm^2$ in a 1 M LiFSI $Pyr_{1,3}FSI$ electrolyte **b,** Picture of two $FeF_2$ pouch cells powering an Oxford LED **c,** Average cathode discharge capacity as a function of cycle number at different rates of 10 mA h, 6.25 $cm^2$ pouch cells. The pouch cells were assembled in collaboration with the Oxford Suzhou Centre for Advanced Research

Slightly smaller pouches cells with a capacity of 10 mA h (6.25 $cm^2$ area of $FeF_2$ composite) were prepared and cycled at different rates at 50 °C. As shown in

Figure 3.31c, the pouch cells demonstrate a good rate capability and high cycling reversibility in the first 60 cycles.

The cycling data shown in Figure 3.31 is a promising first step towards prototyping in a more realistic cell format. However, excess amounts of electrolyte are still required to operate the cells to amend the following shortcomings of our current cell configuration. All cells prepared in this study comprise a glass fiber (GF) separator due to the poor wetting properties of the IL electrolyte. In addition, the cathodes exhibit a porosity of around 66%. Considering the high viscosity of the IL electrolyte (ca. 40 cP), a reduction of porosity could lead to insufficient wetting of the active material, thus affecting the accessible capacity. As a result of the highly porous separator and cathode, excess electrolyte per cathode material (around $150\,\mathrm{mL\,g^{-1}}$) were used in the coin and pouch cell format, which significantly reduces their practical energy density. In order to increase the practical energy density optimization of the composite and electrolyte are required as discussed in more detail in section 3.5.2.

Despite the excess amounts of electrolyte used in this study, it is of general interest what energy densities are achievable with the demonstrated $FeF_2$ performance. As discussed in section 3.1.1, a high active material content is necessary to be competitive with next-generation nickel-rich Li-metal chemistries. Therefore, full cell energy densities based on the electrochemical data collected in this study and the following assumptions were calculated.

It is assumed that the same capacity retention can be maintained at higher cathode loadings ($39\,\mathrm{g\,cm^{-2}}$) and under lean electrolyte conditions ($0.03\,\mathrm{mL\,g^{-1}}$). A detailed energy calculation sheet can be found in the appendix (see section 7.2). [130] A cell level energy density of $400\,\mathrm{W\,h\,kg^{-1}}$ is extrapolated after 500 cycles, $479\,\mathrm{W\,h\,kg^{-1}}$ after 200 cycles and $531\,\mathrm{W\,h\,kg^{-1}}$ after 3 cycles for the 70, 80 wt%, and 85 wt% cells shown in section 3.3.2, respectively. For the cells cycled at 80 °C (see section 3.1.1), a cell level energy density of $540\,\mathrm{W\,h\,kg^{-1}}$ and $597\,\mathrm{W\,h\,kg^{-1}}$ for 70 wt% and 80 wt% is calculated, respectively .

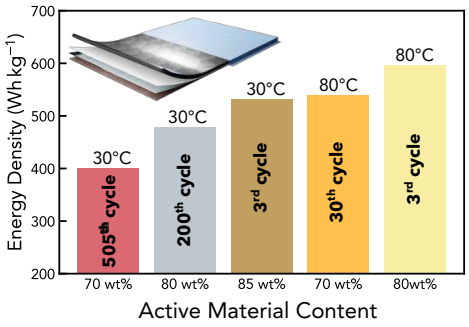


**Figure 3.32: Energy Density Calculation:** The cell level energy densities were calculated using the cycling data showcased in this project. In addition, some parameters were approximated based on industry standards further elaborated on in the appendix (see section 7.2). [130] The most important assumptions made are that the capacity retention, described in the manuscript from coin cell cycling data, can be maintained under higher cathode loadings of $39\,\mathrm{g\,cm^{-2}}$ and under lean electrolyte conditions ($0.03\,\mathrm{mL\,g^{-1}}$).

Under those assumptions, our proposed cell chemistry is competitive with next-generation intercalation cathode - Li-metal systems. [150, 151] In particular at elevated temperatures, a highly competitive energy density, and power density (see Figure 3.24b) can be achieved. In light of the high energy density, improved thermal stability and cell safety of $FeF_2$-IL-Li-metal cells (see section 3.29), the conversion cathode could provide a unique edge as a future high-energy-density electrode material.

## 3.4 Summary

In this study, a systematic investigation of $FeF_2$ cathodes in a 1 M LiFSI $Pyr_{1,3}FSI$ electrolyte is described.

A wet-milling strategy is developed that enables the production of a homogeneous particle size distribution. The particle median can be tuned by adjusting the milling speed. It shows that the particle median correlates with the accessible discharge capacity at a slow cycling speed. Using the ball-milled particles, different carbon mixing strategies are compared, and a novel co-dispersion mixing technique is presented. The optimized composites show excellent capacity retention for over 500 cycles and a high cycling reversibility for active material contents up to 85%. An in-depth characterization of the cycled cathode reveals the aging mechanism

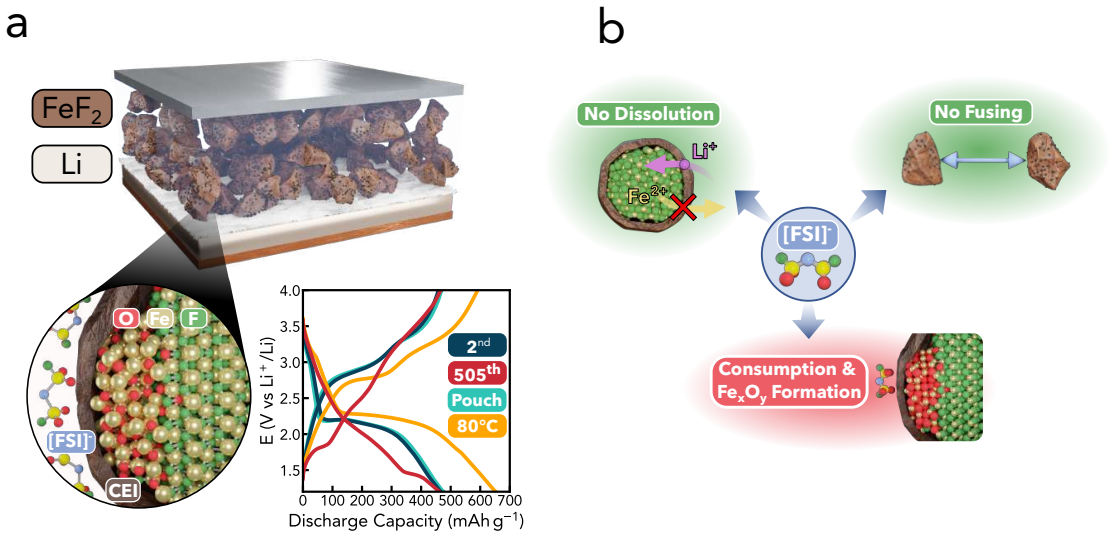


**Figure 3.33: Project Summary: a,** Illustration of a $FeF_2$-Li-metal cell in a liquid electrolyte. Magnification of the interphase illustrates the proposed ageing mechnaism in a $[FSI]^-$ electrolyte. Comparison of different GCPLs at different temperatures. **b,** Schematic overview of the role of $[FSI]^-$ on the cycling performance of $FeF_2$ cathodes. $[FSI]^-$ enables the formation of a CEI which prevents active material dissolution and particle fusing. However, over extensive cycling $[FSI]^-$ decomposition products are consumed, and a redox-active $Fe_xO_y$ phase is formed. Reprinted from Olbrich et al. [130]

of $FeF_2$ in the bis(fluorosulfonyl)imide electrolyte. $[FSI]^-$ is an integral component to form a passivating CEI which prevents particle fusing and active material dissolution and thus enables a high cycling reversibility. However, the gradual formation of a redox-active oxide phase is correlated with $[FSI]^-$ consumption. Figure 3.33a and b illustrate the aging mechanism and the role of $[FSI]^-$ during cycling. Subsequently, the high-temperature cycling performance was investigated. While higher capacities can be accessed and better rate capability can be demonstrated at elevated temperatures, the ageing mechanism is accelerated as parasitic reactions exacerbate. Cycling up to 120 °C is demonstrated. The cell safety of the $FeF_2$-Li-metal- IL chemistry is studied and compared to an oxide analog in a STA-setup. The results indicate that the fluoride chemistry is stable up to the melting point of Li. Lastly, pouch cells were prepared to demonstrate the cycling reversibility in a larger cell format. Energy density calculation using cycling data from this study and assumptions that the performance can be reproduced at a high active

| TMF | Capacity ($mAhg^{-1}$) | $E^0$ vs $Li^+/Li$ (V) |
|---|---|---|
| $FeF_2$ | 571 | 2.66 |
| $FeF_3$ | 712 | 2.74 |
| $CoF_2$ | 553 | 2.8 |
| $CoF_3$ | 694 | 3.617 |
| $NiF_2$ | 554 | 2.96 |
| $CuF_2$ | 528 | 3.55 |

**Table 3.1:** Overview of theoretical reduction potential and capacity of different TMF cathodes.

material loading and under lean electrolyte conditions indicate the competitiveness of the demonstrated cell chemistry.

## 3.5 Outlook

### 3.5.1 Other Transition Metal Fluorides

In order to further increase the energy density of TMF cathodes, metal centers with a higher reduction potential can be employed. TMFs with a higher theoretical reduction potential than $FeF_2$ are for example $CoF_2$, $NiF_2$, and $CuF_2$. The respective reduction potentials and theoretical capacities are listed in Table 3.1. [68]

In section 3.3.1 a new wet-milling strategy was introduced. As discussed in that section, the recipe can be used to prepare other TMF cathodes with a homogeneous particle size distribution. Since a small particle size is important for all TMF cathodes, the wet milling recipe is a good starting point to explore the potential of other TMF cathodes. Therefore, wet-milling batches at 700 rpm were prepared for $NiF_2$, $CoF_2$, and $CuF_2$. The particle size of all fluorides is very similar as shown in Figure 3.9. Coin cell were prepared using a 1 M LiFSI $Pyr_{1,3}FSI$ electrolyte. The first dis- and recharge of the TMF cathodes are shown in Figure 3.34a. The reduction plateau is dependent on the transition metal. However, although $NiF_2$ and $CoF_2$ have a higher theoretical reduction potential than $FeF_2$, the plateau is at a lower potential, indicating a larger overpotential. This is an interesting observation and can be the starting point for an in-depth mechanistic study on other TMF cathodes.

In contrast, the $CuF_2$ plateau is at around 2.9 V vs. $Li^+/Li$, which presents a substantial increase in energy density over the $FeF_2$. All four TMF cathodes achieve a discharge capacity equally or larger than the theoretical threshold indicated by the vertical dotted line. This indicates that the wet milling recipe indeed enables access to the full capacity of all the TMF cathodes showcased here, regardless of the metal center. It further illustrates how CEI formation contributes to excess discharge capacity in the first cycles, as discussed in the introduction (3.1) During recharge, $CoF_2$ and $FeF_2$ are able to access the full charge capacity, while $NiF_2$ displays some losses. Only 200 mA h $g^{-1}$ were reconverted in the $CuF_2$ cathode, which is higher than in many reports on this compound (see section 3.1).

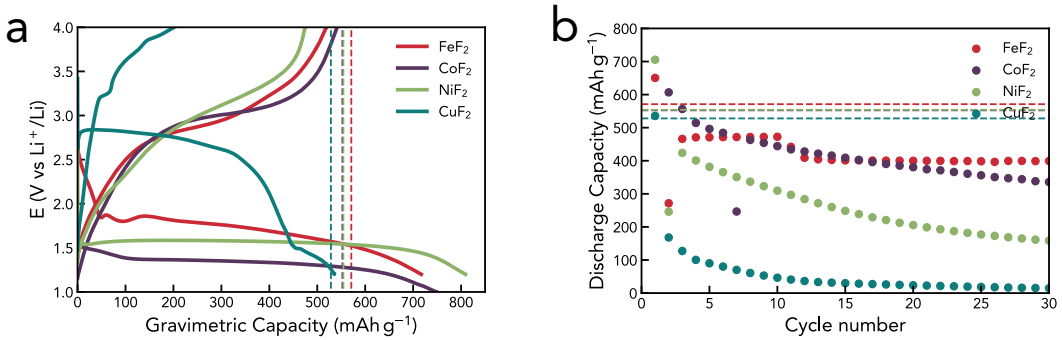


**Figure 3.34: Other Transition Metal Fluoride Cathodes: a,** First cycle of ball milled TMF cathodes. The dotted vertical lines indicate the theoretical capacity of the respective fluoride cathode. All cells were cycled in a 1 M LiFSI $Pyr_{1,3}FSI$ electrolyte. **b,** Capacity retention as a function of cycle number for different ball-milled TMF cathodes.

The discharge capacities as a function of cycle number of the TMF cathode are shown in Figure 3.34b. While the $FeF_2$, $NiF_2$, and $CoF_2$ show a decent cycling reversibility, the $CuF_2$ displays rapid capacity fading.

Future experiments could combine multiple transition metals to produce ternary compounds using the wet milling recipe showcased here. The goal is to balance energy density with cycling stability. Furthermore, the $3^+$-$2^+$ redox chemistry of $FeF_3$ and $CoF_3$ could be investigated to further increase the capacity and potential of the cathodes.

### 3.5.2 Electrolyte Optimization

As discussed in detail in section 3.3.3 the [FSI]$^-$ has a unique role in the cycling reversibility of $FeF_2$ cathodes. While it enables high capacity retention over several hundreds of cycles, its gradual consumption is suspected. With a rough depletion rate estimate of 11 µmol g$^{-1}$ per cycle, unpractical amounts of [FSI]$^-$ are required to keep the LiFSI concentration close to 1 at higher active material loadings. Consequently, to enable cell upscaling with competitive energy densities, electrolyte optimization is required to stabilize the CEI and keep [FSI]$^-$ consumption limited to the initial formation cycle.

A strategy to limit the consumption is simply reducing the amount of [FSI]$^-$ in the electrolyte. Bis-(trifluoromethanesulfonyl)imide ([TFSI]$^-$) anions are structurally very similar to [FSI]$^-$ with the addition of a trifluoromethane group as shown in Figure 3.35a. As a result, [TFSI]$^-$ exhibits a larger thermal stability and increased electrochemical stability. [152, 153] Combining both anions in an electrolyte formulation could combine the beneficial CEI formation properties of [FSI]$^-$ with the increased electrochemical stability of [TFSI]$^-$.

Motivated by this idea, mixed anion electrolytes with [FSI]$^-$ weight ratios of 0%, 25%, 50%, 75%, and 100% were prepared and tested in coin cells at 30 °C. The 0% and 100% electrolyte mixture corresponds to 1 M LiTFSI in $Pyr_{1,3}$TFSI and 1 M LiFSI in $Pyr_{1,3}$FSI, respectively. Figure 3.35b shows the excess discharge capacity and CE measured in during the first discharge cycle as a function of the [FSI]$^-$ to [TFSI]$^-$ ratio.

The initial discharge capacity increases significantly with increasing [FSI]$^-$ content beyond the theoretical capacity of $FeF_2$ and therefore resulting in CE over 100%. This can be ascribed to the decomposition of the [FSI]$^-$ anion, resulting in the formation of a CEI. It further indicates that the [TFSI]$^-$ anion is indeed more stable and thus contributes less to the CEI formation. The discharge capacities as a function of cycle number are shown in Figure 3.35c with their corresponding CEs in Figure 3.35b). The data indicates that cells can reversibly cycle as long as some [FSI]$^-$ is present in the solution since the 0% [FSI]$^-$ fades rapidly. Particularly,

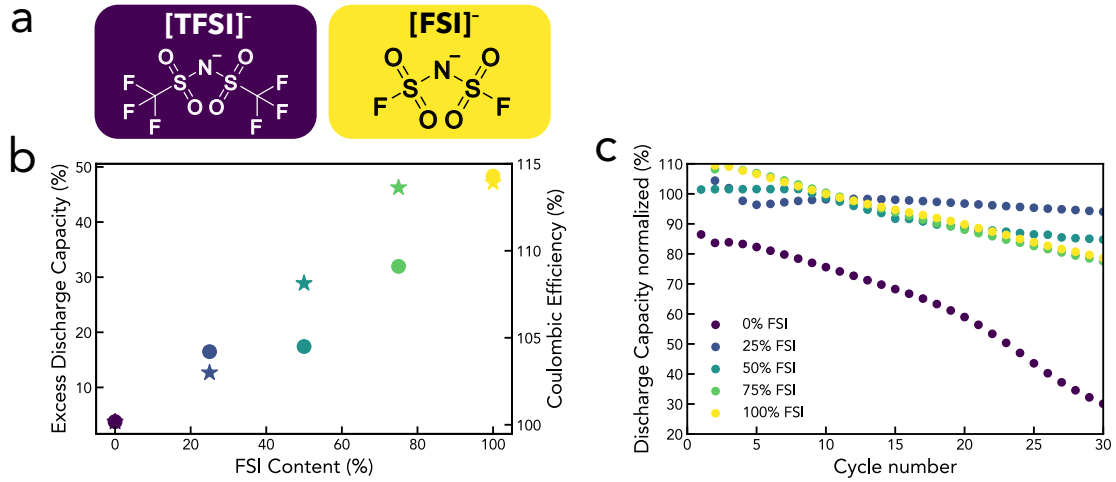


**Figure 3.35: Mixed Anion Electrolytes: a,** Chemical structure of $[TFSI]^-$ and $[FSI]^-$ anions. **b,** Excess discharge capacity (beyond the theoretical 571 mA h $g^{-1}$ of $FeF_2$, dots) and CE (stars) as a function of $[FSI]^-$ content in mixed anion electrolytes **c,** Discharge capacity as a function of cycle number for mixed anion electrolytes.

the 25% shows a promising capacity retention. This can be the starting point for a systematic electrolyte optimization study, reducing the amount of $[FSI]^-$ while maintaining a high cycling reversibility.

Other types of solvents should also be explored. As mentioned in section 3.3.6, a less viscous electrolyte is required to produce cells with higher practical energy density. When exploring different solvent options for electrolyte formulations, it is important to study their compatibility with Li-metal anode. While LiFSI in $Pyr_{1,3}FSI$ is reported to inhibit dendrite formation on Li-metal due the the formation of a stable SEI [16], other solvents might be less compatible. A comprehensive review of different electrolyte formulations and their compatibility with Li-metal and graphite is discussed by Hobold *et al.* [15] tetraethylene glycol dimethyl ether (G4) has a high cathodic stability, low viscosity, low flammability, and low volatility which make glymes a promising solvent to be used in TMF-Li-metal batteries. [147, 154] Its chemical structure is shown in Figure 3.36a. [155] Preliminary cycling data of $FeF_2$ cathodes in a 1 M LiFSI G4 electrolyte are shown in Figure 3.36b.

The cell shows good cycling reversibility with some capacity fading after 20 cycles. One interesting observation is the improved rate capability - where the same discharge capacity can be maintained when increasing the rate from C/20 to C/5 as

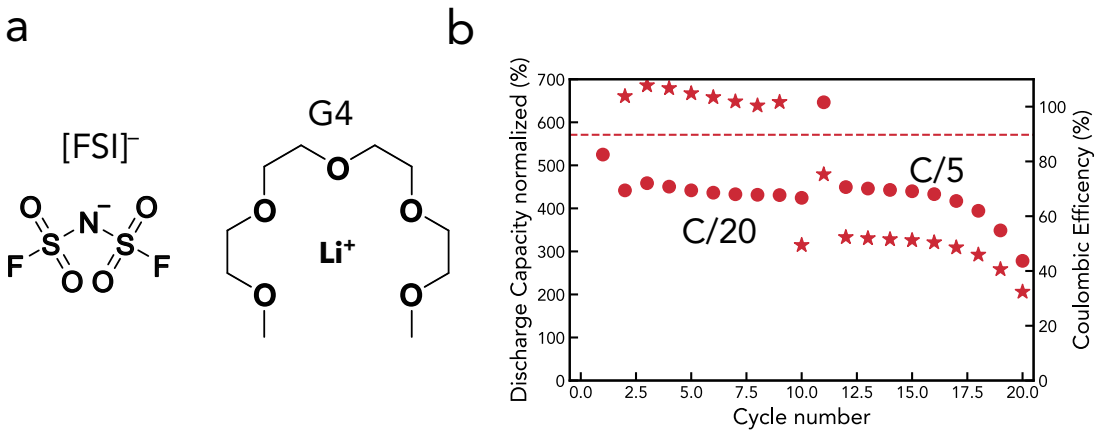


**Figure 3.36: LiFSI in G4: a,** Chemical structure of LiFSI and G4 **b,** Discharge capacity (dots) and CE (stars) as a function of cycle number of $FeF_2$ cathodes in a 1 M LiFSI G4 electrolyte.

shown in Figure 3.36b. At 30 °C, the IL already displayed a lower capacity retention at a cycling rate of C/5 (see Figure 3.24b). This indicates that $FeF_2$-Li-metal cells in the current configuration are limited by transport through the electrolyte and not the kinetics of the $FeF_2$ conversion reaction. The rate capability of a liquid electrolyte is determined by its transport and thermodynamic properties. In the next chapter of this thesis, a technique capable of measuring bespoke properties in a unified setup is introduced, and Li transport in liquid electrolytes is discussed.

# 4

# Operando Raman Gradient Analysis for Electrolyte Characterization

## Contents



## 4.1 Introduction

A significant portion of this chapter was published in *ACS Energy Letters*. [156] Additional figures and explanations have been included where appropriate to

enhance clarity and depth.

### 4.1.1 Motivation

Transport and thermodynamic properties of an electrolyte are crucial determinants of a battery's rate capability. Properties, such as the Fickian (or "apparent") diffusion coefficient ($D_{\text{app}}$), the ionic conductivity ($\kappa$), the lithium transference number ($t_+^0$), and the molar thermodynamic factor ($\chi_{\text{M}}$), influence the uniformity of lithium plating, filament nucleation, and the overall cycle life. [157, 158]

The development and temperature-resolved characterization of electrolytes is, as such, paramount to the optimization of state-of-the-art batteries and the advancement of next-generation electrode materials, [159, 160] required to accommodate the variable operational temperatures of electric vehicles (EVs). This is particularly pertinent during fast charging and discharging phases, where temperatures can reach up to 80 °C. [161, 162]

$D_{\text{app}}$ quantifies the rate at which ions move through the electrolyte under a concentration gradient, $\kappa$ measures the electrolyte's ability to conduct electric current via the movement of ions, $t_+^0$ describes the fraction of the total ionic current carried by lithium ions in the electrolyte (referenced to the solvent velocity), and $\chi_{\text{M}}$ relates to the non-ideality of the electrolyte solution. [14] A more elaborate description of the transport and thermodynamic properties can be found in the introduction of this thesis (see section 1.4.2).

Conventional methods for measuring these properties encompass restricted diffusion measurements [14, 18], high-frequency Electrochemical Impedance Spectroscopy (EIS) [19, 26, 27], the Hittorf method [18, 20, 21], and the assessment of liquid junction potentials in concentration cells [18, 20], among others. However, these conventional methods are resource-intensive and beset with various drawbacks. [147]

An alternative approach involves calculating $D_{\text{app}}$ and $t_+^0$ by measuring salt concentration as a function of position and time during polarization and fitting time-resolved concentration gradients to equations from CST. [14, 147] In recent years, a number of operando characterization techniques have been developed

to visualize these concentration gradients, including magnetic resonance imaging (MRI) [163, 164], nuclear magnetic resonance (NMR) imaging [165, 166], and Laser interferometry. [167]

We recently extended and refined this approach by combining electrochemical measurements with operando confocal Raman microscopy in a technique we called Operando Raman Gradient Analysis (ORGA). [22, 147, 148] In addition to gradient extracted $D_{\text{app}}$ and $t_+^0$, chronopottentiometry (CP) and EIS, allow for the calculation of $\kappa$ from the resistance observed in high-frequency EIS and $\chi_{\text{M}}$ from the surface overpotential $\eta_s$ and the interfacial gradient $\left.\frac{dc_s}{dz}\right|_{z=0,L}$, enabling the determination of all four electrolyte properties in a unified setup and in a single measurement. [147]

The underlying theory to determine bespoke transport and thermodynamic properties is introduced in the following.

### 4.1.2 Properties to Describe Lithium Transport

In the 1960s, Newman developed CST to describe electrolyte transport which at its core is still the basis for most electrolyte modeling to date. Combining CST with porous electrode theory yields the so-called Doyle-Fuller-Newman (DFN) model. DFN is used in state-of-the-art LiBs modeling software such as COMSOL Multiphysics and PyBamm. [168] Its derivation is described in detail in Newman's works. A summary of the most important aspects of CST is provided below. [9]

For simplicity electrolyte transport in infinitely dilute solutions is considered to begin with. Consider an electrolyte comprising a neutral solvent and a dissolved, binary salt at infinitely low concentrations. In the following, the solvent is abbreviated with the subscript 0, the solute or salt with $s$, and the cation and anion with $+$ and $-$ respectively. Equations for the movement of ions, current flow, material balances, and electroneutrality are required to fully describe mass transfer in solution. The flux density of each species (cation $N_+$, anion $N_-$, solvent $N_0$) is given by:

$$N_i = -z_i u_i F c_i \nabla\phi - D_i \nabla c_i + c_i \mathbf{v} \tag{4.1}$$

where $z_i$ is the number of charges carried by an ion, $u_i$ is the mobility of the species, $F$ is the Faraday constant, $c_i$ is the molar concentration of the species, $\nabla\phi$ represents the gradient of the electric potential, $D_i$ is the diffusion coefficient, $\nabla c_i$ represents the gradient of the concentration, and $\mathbf{v}$ is the bulk velocity vector (convective flow). The first part of equation 4.1 describes migration, the movement of a species induced by an electric field, and the gradient of an electrostatic potential $\phi$. The second one describes diffusion, a system's response to concentration differences, and the last part of equation 4.1 is convection, species movement due to bulk motion of the medium.

Flux density can easily be converted into a current by summing up the transport of all charged species via

$$i = F \sum_i z_i N_i \tag{4.2}$$

where $i$ is the current density in $\mathrm{A\,cm^{-2}}$.

The material balances are defined by:

$$\frac{\partial c_i}{\partial t} = -\nabla \cdot N_i + R_i \tag{4.3}$$

where $R_i$ is the rate of production of a species due to a chemical reaction. Lastly, electroneutrality is defined as

$$\sum_i z_i c_i = 0 \tag{4.4}$$

This assumption is valid since the Debye screening length of electrolytes (nanometer scale) is around three orders of magnitudes smaller than the probing volume of the confocal laser (micrometer scale). Newman dedicated a section in his book to calculate the magnitude of the electric field required to break electroneutrality concluding the validity of this assumption. [9] These four equations enable a consistent description of transport processes and lay the foundation for all subsequent, refined calculations.

To accurately model transport in more concentrated solutions, the flux density equation (4.1) necessitates modifications. This is because species cannot be considered in isolation, in contrast to the assumptions made for infinitely dilute solutions. Instead, it is essential to account for the interactions between them. The Onsager-Stefan-Maxwell (OSM) formalism can be used to describe this phenomenon. OSM theory is based on principles of both classical thermodynamics and irreversible linear thermodynamics and takes electrochemical-potential gradients ($\nabla\mu_i$) as the fundamental driving forces for mass transport. The complete derivation is beyond the scope of this thesis, however it can be found in the original works of Newman and Curtis [9, 169], and in a recent conference paper which re-derived the principle. [170] In the OSM formalism, $\nabla\mu_i$ is balanced by species friction. The friction is proportional to the difference in species velocity ($\vec{\mathrm{v}}_i - \vec{\mathrm{v}}_j$) and the concentration of species $c_i$ and $c_j$, normalized by the total concentration $c_T = \sum_i c_i$. Lastly, a friction coefficient $\mathcal{D}_{ij}$ characteristic for species $i$ and $j$ is introduced, which yields:

$$-c_i\nabla\mu_i = \sum_{j\neq i} K_{ij}(\vec{\mathrm{v}}_i - \vec{\mathrm{v}}_j) = \sum_{j\neq i} \frac{RTc_ic_j}{c_T\mathcal{D}_{ij}}(\vec{\mathrm{v}}_i - \vec{\mathrm{v}}_j) \tag{4.5}$$

A general description that connects the flux density $\vec{N}_i$ and species velocity $\vec{\mathrm{v}}_i$ is given by:

$$\vec{N}_i = c_i\vec{\mathrm{v}}_i \tag{4.6}$$

Since both fluxes and rates have directions, they are sometimes represented in literature as $\vec{\mathrm{v}}_i$ and $\vec{N}_i$. For simplicity, the arrows are omitted in the following.

Combining the OSM formalism 4.5 with the flux density definition 4.6 yields a set of three equations, for the cation +, anion -, and the solvent 0:

$$-c_+\nabla\mu_+ = \frac{RT}{c_T}\left(\frac{c_0N_+ - c_+N_0}{\mathcal{D}_{0+}} + \frac{c_-N_+ - c_+N_-}{\mathcal{D}_{+-}}\right) \tag{4.7}$$

$$-c_-\nabla\mu_- = \frac{RT}{c_T}\left(\frac{c_0N_- - c_-N_0}{\mathcal{D}_{0-}} + \frac{c_+N_- - c_-N_+}{\mathcal{D}_{+-}}\right) \tag{4.8}$$

$$-c_0 \nabla \mu_0 = \frac{RT}{c_T} \left( \frac{c_+ N_0 - c_0 N_+}{\mathcal{D}_{0+}} + \frac{c_- N_0 - c_0 N_-}{\mathcal{D}_{0-}} \right) \tag{4.9}$$

Using equation 4.2 provides an expression for the anion flux density.

$$N_- = \frac{i}{z_- F} - \frac{z_+ N_+}{z_-} \tag{4.10}$$

The Guggenheim condition states that for a set of components in a mixture or reaction, the sum of the products of their stoichiometric coefficients ($v_i$) and their charges ($z_i$) must be zero:

$$\sum_i z_i v_i = 0 \tag{4.11}$$

Using the Guggenheim condition converts the anion flux 4.10 into:

$$N_- = \frac{i}{z_- F} - \frac{v_- N_+}{v_+} \tag{4.12}$$

The molar flux for the solvent is defined according to equation 4.6 as:

$$N_0 = c_0 \mathrm{v}_0 \tag{4.13}$$

Inserting 4.13 and 4.12 into the solvent electrochemical gradient equation 4.9, applying the Guggenheim condition (4.11 ), excluding and rearranging yields:

$$N_+ = \frac{v_+ c_T}{RT} \left( \frac{\mathcal{D}_{0+} \mathcal{D}_{0-}}{v_- \mathcal{D}_{0+} + v_+ \mathcal{D}_{0-}} \right) \nabla \mu_0 + \left( \frac{v_- \mathcal{D}_{0+}}{v_- \mathcal{D}_{0+} + v_+ \mathcal{D}_{0-}} \right) \frac{i}{z_+ F} + c_+ \mathrm{v}_0 \tag{4.14}$$

Newmann describes in his book a definition of the electrochemical potential that takes the non-ideality into account with: [9]

$$\mu_s = \mu_s^\theta + vRT \ln f_\pm c_s + RT \ln(v_+^{v_+} v_-^{v_-}) \tag{4.15}$$

where $\mu_s^\theta$ is the standard electrochemical potential, $v = v_- + v_+$ the stoichiometric coefficient, representing the number of ions produced when the salt dissociates, $f_\pm$ the mean activity coefficient of the ions, accounting for non-ideal behavior in the

solution, and $v_+^{v_+} v_-^{v_-}$ the product of the stoichiometric coefficients of the cation and the anion, raised to the power of their respective stoichiometric coefficients. The gradient can then be calculated and simplified by identifying the constant terms and applying the chain and product rule:

$$\nabla \mu_s = \nabla(\mu_s^\theta + vRT \ln f_\pm c_s + RT \ln(v_+^{v_+} v_-^{v_-})) \tag{4.16}$$

$$\nabla \mu_s = vRT \left( \frac{d \ln f_\pm}{d \ln c_s} + 1 \right)_{T,p} \frac{1}{c_s} \nabla c_s \tag{4.17}$$

which contains the thermodynamic factor.

$$\chi_M = \left( \frac{d \ln f_\pm}{d \ln c_s} + 1 \right)_{T,p} \tag{4.18}$$

Taking the Gibbs-Duhem equation [9]

$$\sum_{i=1} n_i d\mu_i = -SdT + VdP \tag{4.19}$$

where $n_i$ is the number of moles of compound $i$, $S$ is entropy, and $V$ the volume, and $p$ the pressure. Formulating the Gibbs-Duhem equation for salt and solvent concentrations, under isothermal and isobaric conditions yields:

$$(c_0 \nabla \mu_0)_{T,p} + (c_s \nabla \mu_s)_{T,p} = 0 \tag{4.20}$$

Using this expression and equation 4.17 the electrochemical potential of the solvent can be expressed as:

$$\nabla \mu_0 = -\frac{vRT\chi_M}{c_0} \nabla c_s \tag{4.21}$$

Using the definition of the transference number: [9]

$$t_+^0 = 1 - t_-^0 = \frac{v_- \mathcal{D}_{0+}}{v_- \mathcal{D}_{0+} + v_+ \mathcal{D}_{0-}} \tag{4.22}$$

and the definition of the thermodynamic diffusion coefficient: [9]

$$\mathcal{D} = \frac{v_- \mathcal{D}_{0+} \mathcal{D}_{0-}}{v_- \mathcal{D}_{0+} + v_+ \mathcal{D}_{0-}} \tag{4.23}$$

and inserting both, with the gradient of the electrochemical potential of the solvent into the cation flux expression 4.14, results in:

$$N_+ = -v_+ \mathcal{D} \chi_M \frac{c_T}{c_0} \nabla c_s + t_+^0 \frac{i}{z_+ F} + c_+ \mathrm{v}_0 \tag{4.24}$$

The Fickian diffusion coefficient is related to the thermodynamic diffusion coefficient via [9]

$$D_{\mathrm{app}} = \mathcal{D} \frac{c_T}{c_0} \left(1 + \frac{d \ln f_{+-}}{d \ln c_s}\right)_{T,p} \tag{4.25}$$

Inserting this expression and the thermodynamic factor 4.18 leads to:

$$N_+ = -v_+ D_{\mathrm{app}} \left(1 - \frac{d \ln c_0}{d \ln c_s}\right)_{T,p} \nabla c_s + t_+^0 \frac{i}{z_+ F} + c_+ \mathrm{v}_0 \tag{4.26}$$

Inserting the flux equations into the overall material balance equation 4.3 while neglecting the convection term ($c_+ \mathrm{v}_0$) yields the following partial differential equation (PDE) for the salt concentration.

$$\frac{\partial c_s(t,x)}{\partial t} = \nabla \cdot \left( D_{\mathrm{app}} \left(1 - \frac{d(\ln c_0)}{d(\ln c_s)}\right)_{T,p} \nabla c_s \right) - \frac{i \cdot \nabla t_+^0}{z_+ \cdot v_+ \cdot F} \tag{4.27}$$

where $\left(1 - \frac{d(\ln c_0)}{d(\ln c_s)}\right)_{T,p}$ is the solvent velocity factor (SVF) or excluded-volume factor, a descriptor for how solvent concentration changes with respect to salt concentration. SVF can be calculated from the partial molar volume of the solvent $V_0$, which is accessible through the concentration dependency of the electrolyte density $\rho$ by [9, 171]:

$$SVF = \frac{1}{c_0 V_0} \tag{4.28}$$

$$V_0 = \frac{M_0}{\rho - c_s \frac{d\rho}{dc_s}} \tag{4.29}$$

$M_0$ is the molar mass of the solvent. Since all electrolytes in this study are prepared in molality, due to increased reliability and accuracy of electrolyte preparation, they need to be converted into molarity via:

$$c_i = \frac{\rho c_{i,molal}}{1 + c_{i,molal} M_i} \tag{4.30}$$

For completeness, the partial molar volume of the salt is defined as: [9, 171]

$$V_s = \frac{M_s - \frac{d\rho}{dc_s}}{\rho - c_s \frac{d\rho}{dc_s}} \tag{4.31}$$

Ultimately, to describe the spatial and time-resolved salt concentration in an electrolytic solution, it is necessary to solve the PDE 4.27 with boundary conditions as discussed in section 4.1.3. To connect species concentration with battery performance, the electrochemical potential of the cell needs to be considered. A general equation for a reference electrode is defined as [168]

$$\nabla\phi = -\frac{i}{\kappa} - \frac{RT}{nF}\sum_i s_i \nabla \ln c_i f_{i,n} - \frac{RT}{F}\sum_j \frac{t_j^0}{z_j}\nabla \ln c_j f_{j,n} \tag{4.32}$$

where $\kappa$ is the ionic conductivity, a measure of the electrolyte's ability to conduct electric current via the movement of ions and the reciprocal of the electrolyte's ohmic resistance, and $s_i$ is the stoichiometric coefficient of the electrode reaction. For the binary electrolyte system under investigation, we consider the single electron reference redox reaction:

$$\mathrm{Li(s)} \rightleftharpoons \mathrm{Li^+} + e^- \tag{4.33}$$

Inserting this into equation 4.32 yields

$$\nabla\phi = -\frac{i}{\kappa} - \frac{2RT}{nF}\chi_{\mathrm{M}}(1 - t_+^0)\nabla \ln c_s \tag{4.34}$$

where $-\frac{i}{\kappa}$ describes potential drop due to current flow, and the second part of equation 4.34 describes a potential difference as a result of a concentration gradient. [18, 171]

We have now introduced the four transport and thermodynamic properties, $\kappa$, $D_{\text{app}}$, $t_+^0$, $\chi_{\text{M}}$, which by solving equation 4.27 and 4.34 are able to describe the time and spatially resolved salt concentration in a system and its effect on the electrochemical potential of the cell.

### 4.1.3 Extracting Transport Properties from Concentration Gradients

ORGA uses Raman spectroscopy to visualize the local lithium concentration as a function of cell height ($z$) and plating time ($t$). When combined with electrochemical measurements, all four electrolyte transport and thermodynamic properties can be determined in a unified setup and in a single measurement. [22, 147, 171] Jack Fawdon initially introduced ORGA, and a detailed description of his works has been published. [22, 147, 171] Chapter 4 of this thesis is dedicated to describing how ORGA is transformed from a technique that allows measurement of transport properties in binary electrolytes into an electrolyte development tool for multi-component formulations. Some of the data processing was adapted from Fawdons original work and will be briefly described herein. A more detailed description can be found in his thesis [171] and follow-up publications. [22, 147, 148] All data analysis was automatized using a Python package, developed as part of this thesis and is publicly available on Github. [172]

Multiple concentration gradients at different timestamps are collected in ORGA. Each gradient is determined via a series of confocal Raman line scans collected at different cell heights. In order to extract the transport properties, $D_{\text{app}}$, $t_+^0$, and $\chi_{\text{M}}$, described in 4.1.2, each lithium concentration gradient is fit to a solution of the diffusion equation 4.27. The solution of the PDE 4.27 can be derived using three boundary conditions. The first describes that the cell exhibits a uniform initial concentration $c_s^*$ at the beginning of the experiment ($t = 0$).

$$c_s(z, 0) = c_s^* \tag{4.35}$$

The second describes that the salt concentration at an infinite distance from the electrodes approaches $c_s^*$.

$$\lim_{z \to +\infty} c_s(z,t) = c_s^* \tag{4.36}$$

The third is a description of the local salt concentration at the electrodes ($z = 0$) derived from the cation flux laws.

$$-D_{\text{app}} \left(1 - \frac{d(\ln c_0)}{d(\ln c_s)}\right) \left.\frac{\partial c_s(t,z)}{\partial z}\right|_{x=0} = \frac{i \cdot (1 - t_+^0)}{z_+ \cdot v_+ \cdot F} \tag{4.37}$$

The PDE 4.27 can be analytically solved through a Laplace transform and inverse transform under the following assumptions.

- $(1 - \frac{d(\ln c_0)}{d(\ln c_s)})$ is constant with respect to $x$
- $D_{\text{app}}$ and $t_+^0$ are constant with respect to $x$

The solution is a description for the space- and time-dependent salt concentration of the ORGA half-cell. When adding the solution for the other half of the cell, an expression for the final concentration function is derived.

$$\begin{aligned} c_s(t,z) = c_s^* + \frac{i\left[c_0 V_0\left(1 - t_+^0\right)\right]}{\nu_+ z_+ F D_{app}} \Bigg[ & 2\sqrt{\frac{D_{app}t}{\pi}} e^{-\left(\frac{z}{2\sqrt{D_{app}t}}\right)^2} - z\,\text{erfc}\left(\frac{z}{2\sqrt{D_{app}t}}\right) - \\ & 2\sqrt{\frac{D_{app}t}{\pi}} e^{-\left(\frac{L-z}{2\sqrt{D_{app}t}}\right)^2} + (L-z)\,\text{erfc}\left(\frac{L-z}{2\sqrt{D_{app}t}}\right) \Bigg] \end{aligned} \tag{4.38}$$

The concentration function can be simplified by introducing the parameters $a$ and $b$.

$$c_s(t,z) = c_s^* + a\left[\frac{b}{\sqrt{\pi}} e^{-\left(\frac{z}{b}\right)^2} - z\text{erfc}\left(\frac{z}{b}\right) - \frac{b}{\sqrt{\pi}} e^{-\left(\frac{(L-z)}{b}\right)^2} (L-z)\text{erfc}\left(\frac{L-z}{b}\right)\right] \tag{4.39}$$

with

$$a = \frac{i\left[c_0 V_0\left(1 - t_+^0\right)\right]}{\nu_+ z_+ F D_{app}} \tag{4.40}$$

and

$$b = 2\sqrt{D_{app}t} \tag{4.41}$$

Consequently, when the concentration gradients collected in the ORGA setup are fit to equation 4.39, arrays of $a$ and $b$ values are obtained where each entry corresponds to a timestamp $t$. $D_{\mathrm{app}}$ can then be calculated by fitting $b$ as a function of the square root of polarization time. $t_+^0$ can be calculated from the partial molar volumes (see equation 4.29) obtained through density measurements and $a$. To calculate $\chi_{\mathrm{M}}$ and $\kappa$ electrochemical data was required. Upon completion of a line scan series (which yields one concentration gradient), an EIS measurement was conducted during ORGA. When fitting the EIS data to a simple $R_0 - p\,(R_{interphase} - CPE)$ the ohmic drop ($R_0$) and interphase impedance $R_{interphase}$ can be determined. Fits were conducted as part of the automated script. [55, 172] The concentration overpotential can then be calculated:

$$\eta_{conc} = \eta_{total} - I\,(R_0 + R_{interphase}) \tag{4.42}$$

Using $\eta_{conc}$, $\chi_{\mathrm{M}}$ can the be calculated via

$$\chi_M = \frac{F}{2RT(1-t_+^0)} \frac{\partial \eta_{conc}}{\partial \ln\left(\frac{c_{s,z=L}}{c_{s,z=0}}\right)} \tag{4.43}$$

Lastly, $\kappa$ can be obtained by

$$\kappa = \frac{L}{R_0 A} \tag{4.44}$$

where $L$ is the inter-electrode distance (determined on a cell-to-cell basis but roughly around 15 mm) and $A$ is the geometrical surface area of the electrode ($A = \pi \times (0.4\,\mathrm{cm})^2 = 0.503\,\mathrm{cm}^2$).

Figure 4.8 shows exemplarily how $D_{\mathrm{app}}$, $t_+^0$, and $\chi_{\mathrm{M}}$ are calculated for a 1 M LiFSI G4 ORGA cell at 20 °C.

### 4.1.4 Project Goals

One fundamental limitation of ORGA, and by extension of any quantitative spectroscopy technique, is the requirement for a suitable spectrum normalization standard. So far, a vibrational mode of the solvent has been used to normalize all spectra which limits the visualization of gradients to the solute. [22, 147, 148]

The goal of this project is to introduce an external reference to the ORGA setup. An external reference has huge potential to increase the functionality and accuracy of the setup. For example, an external reference enables the visualization of the local concentration of any Raman-active species in the electrolyte. It could further be used to detect lithium filament nucleation and propagation.

A second objective of this project is to incorporate temperature control into ORGA. This would enable measurements of activation energies, open up discussions on the temperature dependence of transport and thermodynamic properties, and provide modelers with important parameters to calculate temperature-dependent fast charging capabilities.

All experiments are conducted in a 1 M LiFSI G4 electrolyte to verify the validity of the technique since a wealth of information is available on this electrolyte.[147] It is noteworthy that transport in the IL used in section 3 of this thesis is significantly more complicated and discussed in the outlook.

## 4.2 Experimental

### 4.2.1 Materials

LiFSI (Battery Grade-99%) was purchased from Fluorochem Ltd. G4 (anhydrous, 99%+) was purchased from Sigma Aldrich. Handling of LiFSI and G4 was always performed in an argon-filled glovebox (MBraun) with low $H_2O$ content (<1 ppm) and low $O_2$ content (<1 ppm). LiFSI was dried further under a high vacuum at 70 °C for 48 h. G4 has dried over 3 Å molecular sieves, which were washed and then dried for one week. All glassware was dried at 80 °C under vacuum before being used and brought into the glovebox. The $H_2O$ content of the electrolyte solutions

was determined by Karl Fischer titration, also performed in an argon-filled glovebox, and recorded to be below 15 ppm of $H_2O$. Experimental information describing density measurements and partial molar volume calculations are described below.

### 4.2.2 ORGA Cell Assembly

Two stainless steel pistons were designed to fit inside a single-crystalline tube with 20 mm in length, with an inner diameter (ID) of 8 mm and an outer diameter (OD) of 10 mm. The sapphire tubes were custom-made by Rayotek Scientific, Inc. (CA, US). An interelectrode distance of 15 mm was chosen because it was sufficiently large to detect a concentration gradient with good spectral resolution and the diffusion layer not to progress too quickly into the center of the cell, which would make the fitting equation invalid. If it were longer, the diffusion layer would not progress quickly enough, and the measurement would take substantially longer. Each piston was further equipped with an O-ring made of FFKM for increased chemical resistance against ethers. The lithium metal foil (99.9%, 750 µm thickness, Alfa-Aesar) acting as lithium reservoir and electrodes for the symmetric cell, was prepared by scraping off the native oxide layer of the foils and calendaring to a thickness of 300 µm. The ORGA cell was assembled in an Ar-filled glovebox. Circular lithium discs were prepared with a diameter of 8 mm and placed onto each of the stainless steel pistons. One piston was then placed inside the quartz tube, 1 mL of electrolyte was added, and then the second piston was introduced on the opposite side cell, sealing the cell. As an extra layer of protection from atmospheric contamination, the cell was sealed using a UV Curing Optical Adhesive NOA61 from THORLABS Ltd (UK). Care was taken not to introduce any gas bubbles into the system. Before any tests were run, the cell was set up inside the A Renishaw inVia Reflex laser confocal Raman microscope equipped with a near-IR 785 nm laser and connected to a Biologic SP150 potentiostat. Important to note, the cell was vertically placed on the sample stage to avoid natural convection.

### 4.2.3 ORGA Operation

The cell was rested for four hours prior to drawing a current to enable lithium passivation. 1D line scans in the $z$-direction (along the cell height) were continuously measured throughout the experiment. A 1200 lines mm grating, a 5 × magnification objective (Leica, 0.12 NA, 14 mm WD) providing a 7.89 µm spot size, and a 90° mirror was used to collect Raman spectra. Measurements were performed with 10% laser power (30 mW), with 1 s exposure time and 20 accumulations. As previously demonstrated, the conditions are benign enough to prevent any laser-induced electrolyte decomposition and heating. [147] As described in Figure 4.3 an optimum focal spot location was chosen to measure both the sapphire reference peak and the electrolyte. One line scan took around 20 minutes, and prior to every new line scan, a PEIS scan with a voltage amplitude of 100 mV and frequencies from 100 kHz to 1 Hz, was performed. The large voltage amplitude was chosen for a reasonable signal-to-noise ratio. Linearity was still maintained. After the four hours, the interphase impedance stabilized, and a constant areal current of 300 µA $cm^{-2}$ was drawn for ten hours for the concentration gradient to form. During polarization, 1D line scans and EIS were continuously collected. A laser power of 10% was deemed optimal as it provided good spectral resolution whilst showing no evidence of thermal heating or oxidation of the solvent. This has been documented elsewhere where no change in the solvent peaks nor emergence of additional peaks was detected; thus, there was no evidence of decomposition products. [147] Also, there was no decrease in the overpotential with time, indicating no thermal heating.

In section 4.3.2 it is described how transport properties at different temperatures are obtained. Therefore, density measurements at different temperatures were required to convert molality into molarity and calculate the partial molar volume of the solvent, which is necessary to calculate the solvent velocity factor and, ultimately, the transference number at different temperatures. Figure 4.1a shows the density values obtained as a function of temperature for LiFSI G4 at a 0.75 M, 1 M, and 1.25 M concentration. Using a linear fit allows calculation of the partial molar volume of the solvent (Figure 4.1b) and salt (Figure 4.1c) as a function of temperature. In Figure

4.1d and e, the corresponding molar concentrations for a 1 M LiFSI G4 electrolyte are plotted. Lastly, Figure 4.1f shows the SVF as a function of temperature.

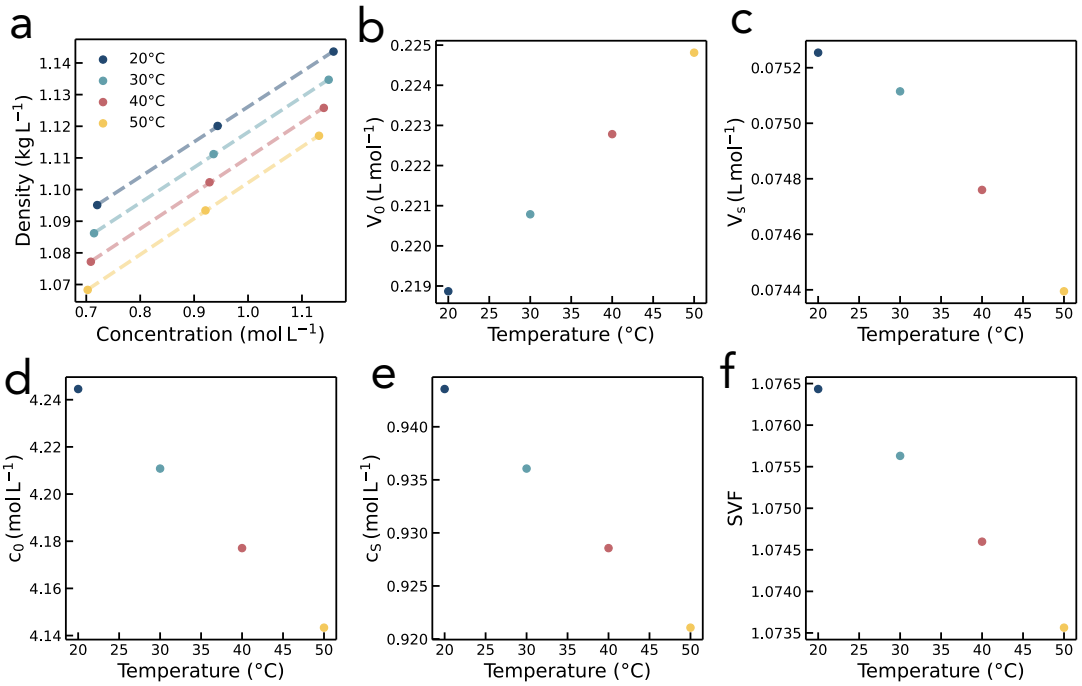


**Figure 4.1: Temperature dependent density, partial molar volume, and SVF a,** Density measurements of LiFSI G4 at a 0.75 M, 1 M, and 1.25 M concentration between 20 °C to 50 °C. **b,** G4 partial molar volume **c,** LiFSI partial molar volume **d,** molar concentration of G4 in 11 M LiFSI G4 **e,** molar concentration of LiFSI in 11 M LiFSI G4 **f,** SVF

## 4.3 Results & Discussions

### 4.3.1 Introduction of External Reference Validation

Time-resolved lithium concentration gradient visualization enables the calculation of transport properties as discussed in an earlier publication and section 4.1.3. [147, 148] This is achieved by quantifying concentration-sensitive vibrational modes of the salt as a function of polarization time along the $z$-axis of a vertically oriented optical cell using Raman microspectroscopy as schematically illustrated in Figure 4.2a. [147] To account for laser energy fluctuations and enable comparability across multiple measurements, all spectra need to be normalized by a reference. In previous

publications, a vibrational mode of the solvent was used to normalize all spectra (the -$CH_2$ bending/scissoring mode of the solvent (G4) for LiFSI in G4). [147]

However, this intrinsically limits the setup in that it requires the presence of an inert Raman-active species in the electrolyte, which is not the case, for example, in ionic liquid electrolytes and is problematic in multi-component electrolyte systems. Furthermore, Raman intensity normalization by the solvent assumes that interfacial solvent reactions and solvent migration, *i.e.* the motion of a dielectric species towards an electric field, and Faradaic convection, are negligible. [173] Put differently, normalization by a solvent mode assumes that the solvent concentration across the ORGA is solely determined by the salt concentration *i.e.* the SVF or excluded-volume factor. [173, 174] The SVF is a descriptor for how solvent concentration, $c_0$, changes with respect to salt concentration, $c_s$.

A potential strategy to overcome this limitation is to introduce an internal standard, *i.e.* dissolve an additional species in the electrolyte. However, an internal standard would affect the local solvation structure of lithium and thus alter the transport properties. Besides, the electrolyte standard would have to satisfy several requirements such as solubility in the electrolyte, chemical inertness to the electrolyte and lithium metal electrodes, active Raman modes, and the absence of an electric dipole moment (homonuclear or symmetry induced), all of which are unlikely to be met by one standard simultaneously.

The most rigorous approach is to introduce a field-of-view external reference standard. We achieved this by incorporating single-crystal sapphire into the cell tube design. Sapphire has exceptional chemical resistance, good durability, and compressive strength. Moreover, it exhibits high optical transmittance and distinct, sharp vibrational Raman peaks, as depicted in Figure 4.2.

These properties qualify it as a material for constructing the cell body and for serving as an external reference. When measuring Raman spectra in the sapphire-incorporated ORGA setup, both the electrolyte and sapphire peaks can be detected simultaneously. As shown in Figure 4.3, the relative intensity of sapphire and electrolyte peak can be tuned by adjusting the laser focal point. The closer the focal

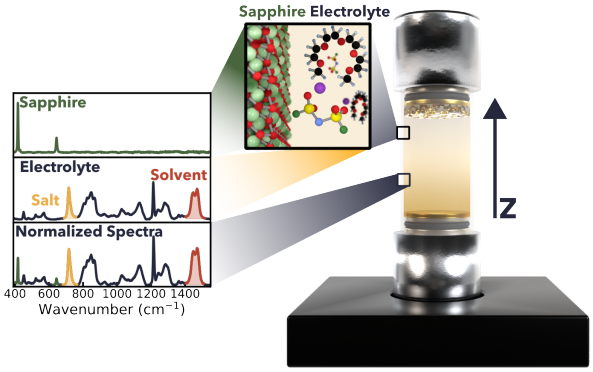


**Figure 4.2: Operando Raman Gradient Analysis using an External Reference:** **a,** Schematic of an ORGA cell setup with a field-of-view external reference incorporated into the cell body. The Raman spectra of the isolated cell body (single-crystal sapphire), the isolated electrolyte (1 M LiFSI G4), and the normalized spectra measured in the ORGA setup where reference and electrolyte overlap are shown.

point is to the center of the Raman cell, the smaller the sapphire peaks becomes (see peak intensity decline at 418 $cm^{-1}$ in Figure 4.3b).

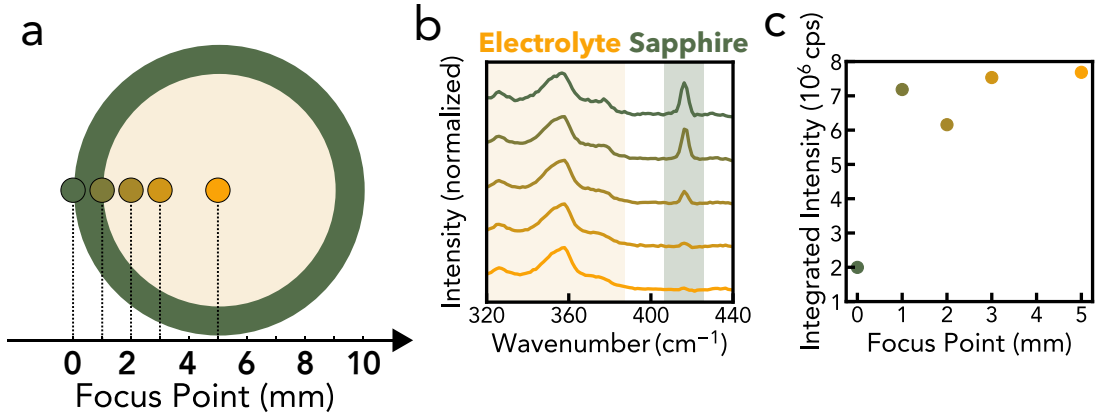


**Figure 4.3: Focal Point Adjustment:** Note: This experiment was done in a 1 M LiFSI $Pyr_{1,3}FSI$ electroylte. (**a**) Schematic of the laser focal point in the ORGA setup. Green indicates sapphire glass and yellow the electrolyte. **b,** Relative peak intensity of sapphire and electrolyte when adjust the focal point. The color code corresponds to the same color code in a, and b, **c,** Integrated intensity of raman spectra when focusing on different focal points.

While the sapphire peak is at its maximum intensity when the focal point is at 0 mm, *i.e.* on the outside of the sapphire glass, the overall signal intensity is reduced. This can be seen in Figure 4.3c, where the integrated Raman spectrum intensity (after baseline correction) is plotted as a function of focus point. Thus the

ideal focus point is set to a distance where both signal intensities are maximized to reduce noise-induced measurement uncertainty. Since the overall integrated intensity does not increase significantly beyond the 1 mm (see Figure 4.3c) focus point, it was chosen as the standard focus point for all subsequent measurements.

Subsequently, all spectra can be normalized using the $A_{1g}$ vibrational mode ($418\,cm^{-1}$) of sapphire and thereby correct for laser-induced intensity fluctuations. [175] This new spectrum normalization method improves measurement accuracy by overcoming the assumptions described earlier and allows monitoring of concentration profiles of any Raman-active species in the electrolyte.

The normalized spectra can now be used to quantify the local lithium concentration. Since lithium does not exhibit any Raman scattering itself, its concentration can be determined by quantifying the anion concentration and assuming charge neutrality, *i.e.* equating the local $[Li]^+$ and $[FSI]^-$ concentration. This assumption is valid since the Debye screening length of electrolytes (nanometer scale) is around three orders of magnitudes smaller than the probing volume of the confocal laser (micrometer scale). [14] The $[FSI]^-$ S–N–S bending peak (from $680\,cm^{-1}$ to $760\,cm^{-1}$), for example, can be used to quantify $[FSI]^-$ concentrations. In consideration of the increasing fraction of contact-ion-pairs (CIPs) and aggregates (AGGs) with $[FSI]^-$ concentration, resulting in peak broadening and formation of secondary "shoulder peaks", peak area integration rather than peak intensity evaluation yields more accurate $Li^+$ concentration gradients, as discussed in earlier publications. [147]

To convert the Raman peak area to a concentration, a calibration line is necessary. Previously, calibration lines were established by measuring various salt concentrations ex-situ, *i.e.* before characterization in ORGA. [22, 147, 148] This is time- and resource-intensive since a new calibration is needed for every electrolyte formulation and measurement condition. We alleviate this limitation by introducing a two-point operando calibration procedure where a new calibration line is created in every measurement during the cell passivation period.

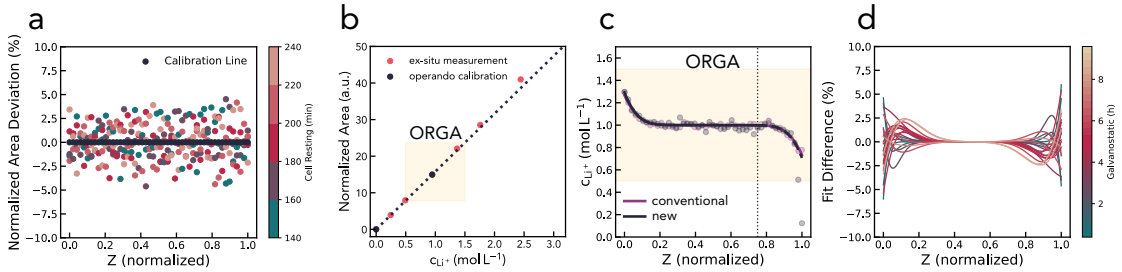


**Figure 4.4: External Reference for normalization and operando calibration:** **a,** shows the mean normalized [FSI]$^-$ bend mode area at each z-value and the respective scattering around it of individual measurements. All areas were collected during OCV conditions. **b,** Normalized areas as a function of lithium concentration obtained from a conventional calibration line measurement ('ex-situ measurement') is shown in red. The dotted line is a linear fit through the 1M area and the origin ('operando-calibration'). The yellow box indicates the concentration range where ORGA is operated. **c,** Shows the concentration profiles and their respective fits obtained through the conventional method (solvent normalization and ex-situ calibration) and new method (external reference normalization and operando calibration). The new fitting method neglects all concentration points above Z (normalized) = 0.75 to account for artefacts induced by lithium filaments. **d,** shows the fit differences residual of the conventional and new processing method.

Before polarization, the ORGA cell is resting under OCV conditions for four hours to enable passivation of the lithium metal electrodes via the formation of a SEI. [30] During this resting phase, line scans along the $z$-axis of the cell are performed every 20 minutes, yielding a total of 12 complete line scans during the cell's resting period. The mean normalized [FSI]$^-$ bending mode area at each $z$-value (after reaching thermal equilibrium) was calculated. The deviation of individual measurements from their respective mean values is depicted in Figure 4.4a. An uncertainty of at maximum ±5% around the mean can be observed. Since no systematic offset or drift of the normalized area is detected, it can be concluded that a homogeneous lithium concentration equal to the initial electrolyte concentration ($= c_s^* = 1\,\text{M}$ LiFSI) is measured along the $z$-axis.

As shown in Figure 4.5a, the absolute area of the normalized and integrated [FSI]$^-$ peak is dependent on the $z$-value (cell height). A similar cell-height dependency trend can be observed for the normalized and integrated G4 peak (in Figure 4.5b), which indicates the noise originates from the surface roughness of the sapphire tube.

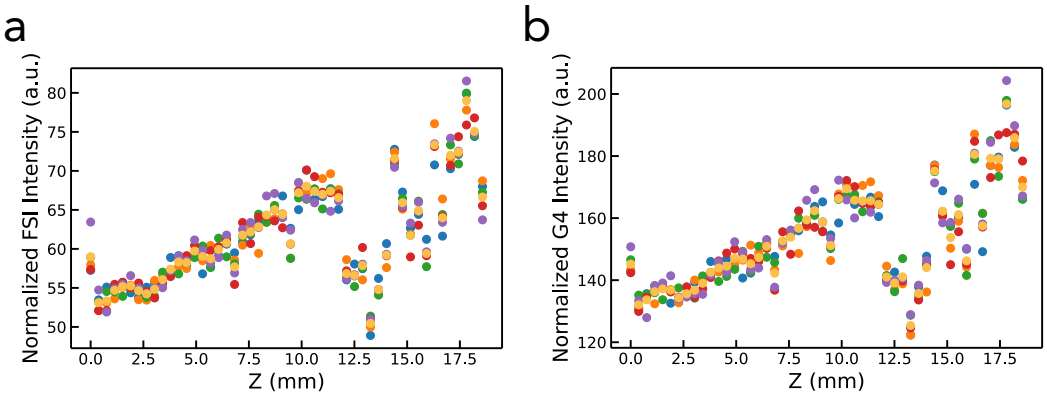


**Figure 4.5: Absolute Peak Area:** Absolute peak areas as a function of cell height of **a,** the FSI 680 $cm^{-2}$ to 750 $cm^{-2}$ and b) G4 at 1380 $cm^{-2}$ to 1500 $cm^{-2}$. Different colours illustrate different times for each of each linescan.

Consequently, the measurement noise is attributed µm position fluctuations of the here utilized Raman stage. The mean normalized area is the best estimate of $c_s^*$ and thus can serve as a data point for an operando calibration. The origin serves as a second data point enabling the construction of a two-point linear calibration line.

Such a calibration line, however, is valid only within the linear regime of the area-to-concentration ratio. A deviation of the linear behavior is expected close to the saturation point of the electrolyte. Figure 4.4b shows normalized areas as a function of lithium concentration obtained from a conventional calibration line measurement. In addition, a two-point operando calibration line is plotted (linear fit of $c_s^*$ through the origin). The operando calibration line shows an excellent agreement of $R^2$ 0.9992 and 0.9988 up to 2 M LiFSI and 2.5 M LiFSI, respectively. Since ORGA measurements are conducted in a concentration range of around $c_s^*$ ± 0.5 M (here 0.5 M to 1.5 M LiFSI in G4) we conclude that the linear operando calibration line can be used to convert normalized areas into concentrations. In fact, commercially relevant electrolytes are almost exclusively in a moderate salt concentration range and thus expected to exhibit a linear area-to-concentration relationship since electrolytes close to their saturation point exhibit high viscosities which impede $\kappa$ and the cell throughput during electrolyte injection on an industrial scale. [176, 177]

A comparison of the differences in the conventional workflow developed by Fawdon et al. [147] (solvent normalization and ex-situ calibration) and the new workflow (external reference normalization and operando calibration) is shown in Figure 4.6.

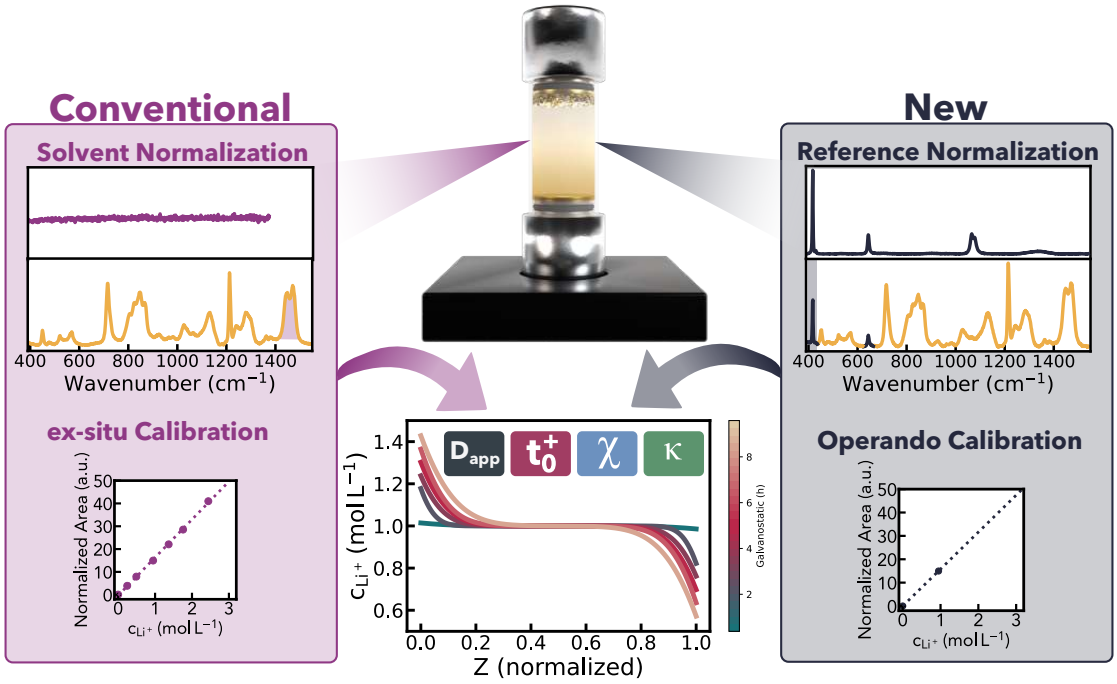


**Figure 4.6: Workflow Comparison:** Conventional covers the workflow developed by Fawdon et al. where the Raman data is normalized by the solvent peak, and an ex-situ calibration line is used to convert the spectra into a concentration. The new workflow uses the external reference to normalize the spectra and a two-point calibration line.

To verify the validity of the new normalization and calibration method, the concentration gradients of a 1 M LiFSI in G4 at 20 °C cell were processed using the conventional (solvent-normalization and ex-situ calibration curve) and new (sapphire reference and operando calibration) method. Two concentration gradients are exemplarily shown for a line-scan after 2 h of polarization in Figure 4.4c. While most calculated concentrations align with both processing methods, one key difference can be observed close to the plating side ($Z_{normalized}$ approaching 1). The lithium concentrations seem to drop rapidly when determined by the external reference processing method. A comparison with the G4 concentration gradient (shown in Figure 4.7) reveals that a steep drop close to the plating side is observed as well.

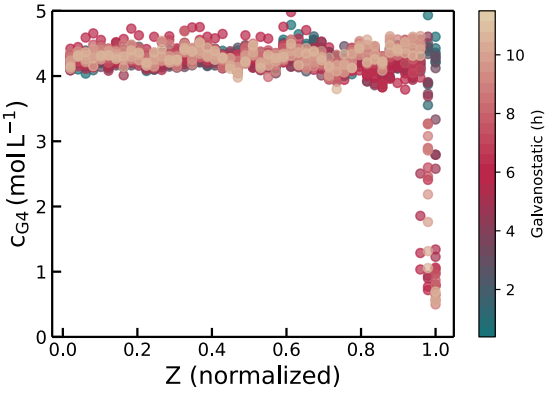


**Figure 4.7: Concentration drop close to plating side:** Calculated G4 concentration as a function of polarization time shows a drop at the plating side.

Upon inspection of the ORGA cell after polarization, a significant amount of lithium dendrites can be observed. When the dendrites grow from the plating electrode into the cell, the amount of electrolyte in the probing volume is reduced, and thus both $c_s$ and $c_0$ decline. In conventional normalization (normalizing the gradients by the solvent peak), the effect of lithium dendrites is obscured since both Raman bands decline simultaneously. According to CST, and under the assumption that transport properties are constant within the ORGA concentration range, the concentration profiles exhibit rotational symmetry, and thus the data points close to the plating side (the dotted line in Figure 4.4 shows the cut-off at $Z_{normalized}$ = 0.75) can be neglected in the new fitting method. [14] The resulting fit shows an excellent agreement with the original solvent-normalization fitting. Figure 4.4d shows the time-resolved residual of the solvent and external reference fitting. Both fits align well and the fit differences lie within the measurement scatter determined earlier. The fit difference approaching zero in the middle of the cell is a result of the boundary conditions to solve the CST equations used in both methods ($c_{s,L/2} = c_s^*$).

The transport properties were calculated from the concentration gradients as described in more detail in section 4.1.3. Figure 4.8a and b shows how $D_{app}$ was calculated by linear fitting the diffusion length $L_d$ or the fitting parameter $b$. Figure 4.8c and d display $t_+^0$ as a function of polarization time, was calculated from the interfacial gradient or the fitting parameter $a$. Lastly, Figure 4.8e and f

show $\chi_M$, which was calculated using electrochemical data and linear fitting the concentration overpotential. $\kappa$ was excluded from this comparison since it is only dependent on the electrochemical data.

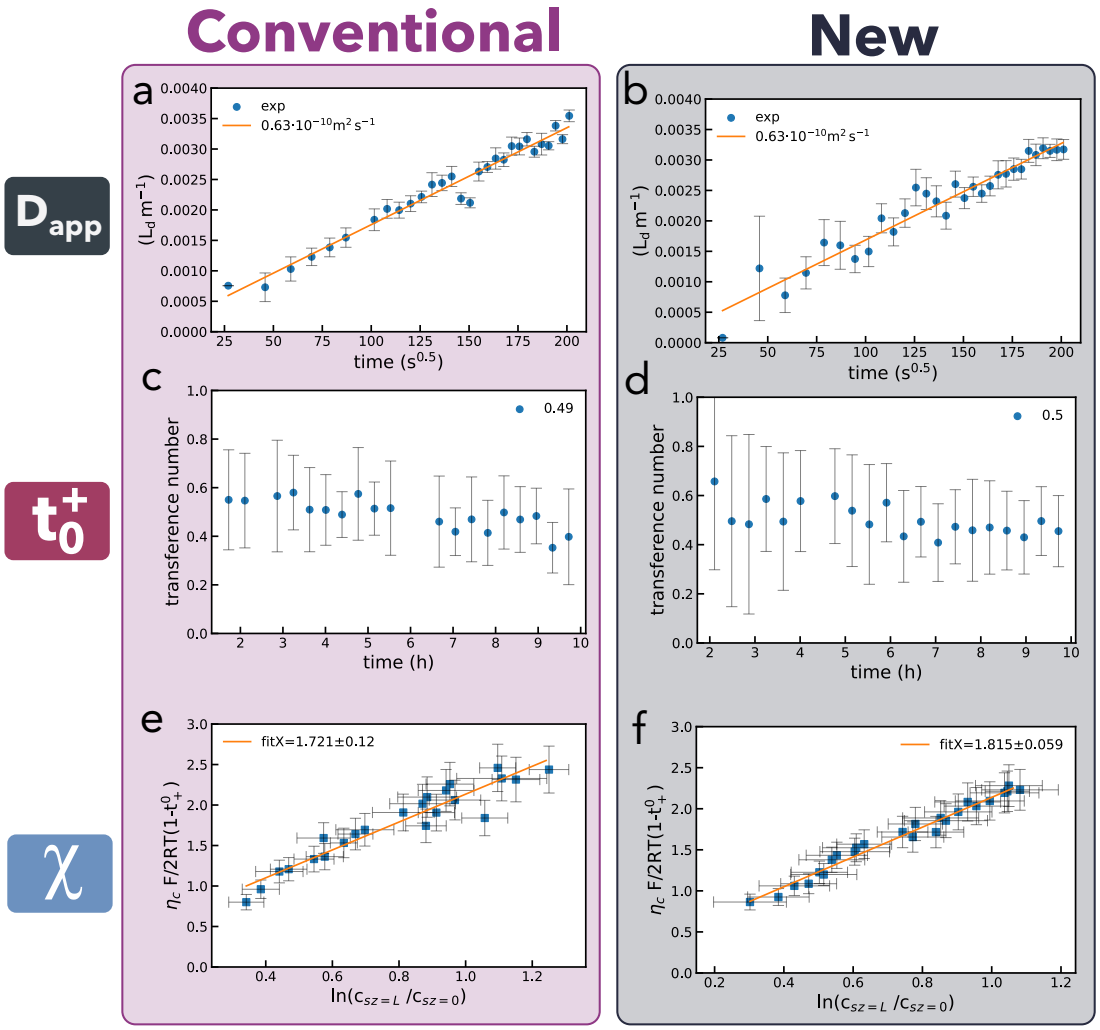


**Figure 4.8: Calculation of Transport Properties:** Comparison of electrolyte transport properties ($D_{app}$, $t_+^0$, $\chi_M$) **a,c,e** calculated using the conventional ORGA method, *i.e.* using solvent normalization and an ex-situ calibration data set compared to the new method using the internal reference for spectrum normalization and operando calibration in **b,d,f**.

The resulting transport properties are listed in Table 4.1 and show satisfactory agreement.

Figure 4.10 shows the measured concentration gradients of LiFSI and G4, the fitted LiFSI gradient, the fitted G4 gradient, and the predicted G4 gradient,

**Table 4.1:** Comparison of transport properties calculated from conventional (solvent normalization and ex-situ calibration) and a new (external reference normalization and operando calibration) Raman processing method.

| **Method** | $D_{\text{app}}$ ($\text{m}^2\,\text{s}^{-1}$) | $t_+^0$ | $\chi_{\text{M}}$ |
|---|---|---|---|
| **Conventional** | $6.3 \pm 0.5 \times 10^{-11}$ | $0.49 \pm 0.06$ | $1.72 \pm 0.12$ |
| **External Reference** | $6.3 \pm 0.6 \times 10^{-11}$ | $0.50 \pm 0.06$ | $1.82 \pm 0.06$ |

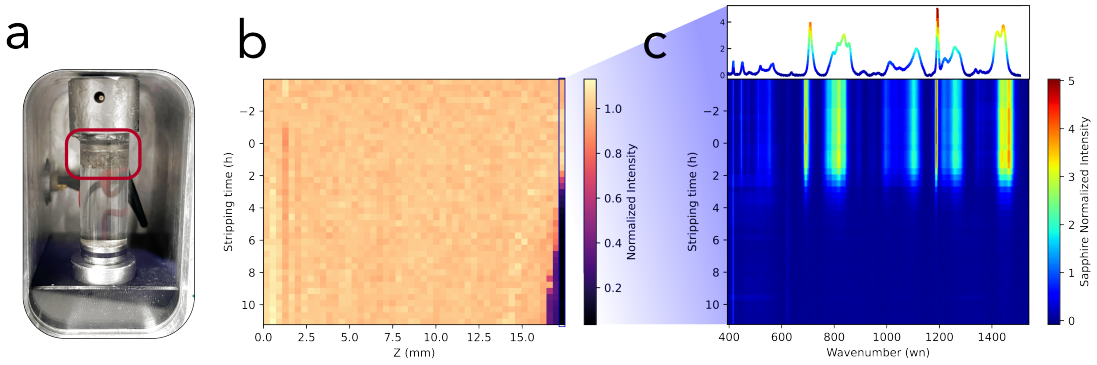


**Figure 4.9: Filament Nucleation Monitoring:** (**a**) Photograph of a post-mortem ORGA cell which shows how lithium filaments have formed on the lithium plating side. (**b**) Heatmap showing the integrated intensity of each (external reference normalized) Raman spectrum as a function of stripping time (y-axis) and cell height (x-axis). (**c**) Shows the acquired normalized Raman spectra as a function of stripping time at the highest z-value, *i.e.* closest to the plating side.

calculated from the local LiFSI concentration and the corresponding partial molar volumes. The measured G4 gradient follows the predicted trend of depletion and accumulation at the stripping and plating sides, respectively. The G4 fit and the predicted G4 values align closely. However, the measured G4 concentrations show a larger measurement noise, which, as described above (see Figure 4.5, originates from small fluctuations of the stage position. Since the G4 concentration ($c_0^*$) is about four times larger than the LiFSI concentration, the measurement uncertainty is amplified, resulting in an apparent larger measurement noise. Further elaboration on how to reduce the measurement noise can be found in the outlook 4.5.

As validated in table 4.1, the sapphire normalization and two-point calibration showcased here can be used to convert raw Raman spectra into accurate concentration profiles. To the best of our knowledge, this is the first time both the solute and solvent of an electrolyte are visualized. This is crucial as, from now on, ORGA allows gradient visualization of any Raman active species in the

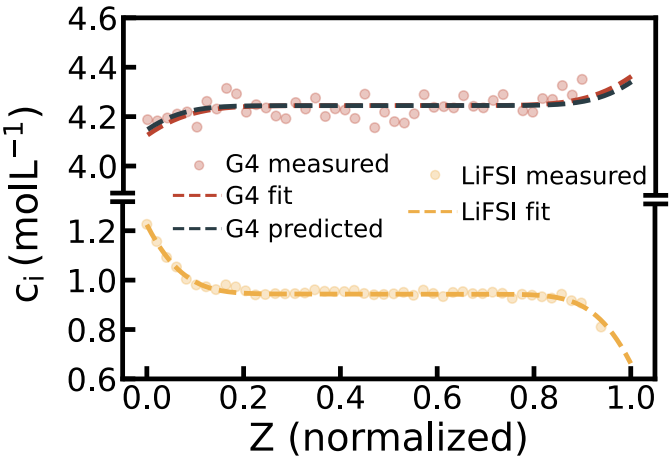


**Figure 4.10: Concentration Gradient Visualization:** Using the external reference to normalize the spectra enables visualization of all Raman active species in the electrolyte, including solute and solvent. The experimentally measured LiFSI and G4 concentrations are plotted as a function of normalized cell height. The LiFSI and G4 concentrations are both fit according to CST. The G4 fit is compared to the predicted G4 concentration calculated from the local LiFSI concentration and the corresponding partial molar volumes.

electrolyte. This paves the way to guide and verify theorists in their ongoing ambitions to advance the theoretical understanding of transport in commercially relevant multi-component electrolytes. [178]

Besides gradient visualization, the external reference can be used to track the time when lithium dendrites are formed and thus provide additional functionality to the ORGA setup. Figure 4.9a displays a photograph of the dendrites formed on the plating side. Figure 4.9b shows a heatmap of all the Raman spectra collected in one ORGA run. The external-reference-normalized spectra are integrated and plotted as a function of lithium stripping time and cell height $z$. At the $z$-value closest to the plating side, a gradual intensity loss after around 3 h of lithium stripping can be observed. After around 7 h and 9 h the intensity loss extends further into the ORGA cell. Figure 4.9c shows the corresponding, normalized Raman spectra as a function of stripping time verifying the electrolyte (all salt and solvent peaks) intensity loss with respect to the external reference peaks (see 410 $\mathrm{cm}^{-1}$ and 610 $\mathrm{cm}^{-1}$). This can be used to track and compare lithium filament nucleation in different electrolyte systems and under different measurement conditions, as demonstrated later.

### 4.3.2 Solvation Structure and Temperature Dependence of Electrolyte Transport Properties

To extend the parameter space of measurement conditions, a Raman microscopy-compatible environmental chamber, able to regulate the ORGA cell temperature, was developed and utilized. When designing the chamber, the spatial restriction imposed by the Renishaw Raman chamber and the movable stage to execute the line scans needed to be considered. Furthermore, it was important to maintain uniform heating inside ORGA to prevent any thermal diffusion processes. A CAD drawing of the temperature chamber is shown in Figure 4.11a and a photograph of the manufactured chamber with an ORGA cell is shown in Figure 4.11b.

An overview of the entire setup to operate the temperature chamber is shown in Figure 4.11c. To power the temperature chamber, a feedback loop between a thermocouple inserted into the back of the chamber (illustrated in Figure 4.11a and c) and two resistive 110 V heating elements, controlled by a proportional–integral–derivative (PID) controller was incorporated. The chamber was sealed with an amorphous quartz window, custom-made for this design by *UQG Optics Ltd*, to mitigate heat loss from the chamber window. An electronic connection through the wall of the chamber was incorporated to connect the ORGA cell to a potentiostat.

To determine the electrolyte's temperature during an ORGA experiment, *i.e.* determine and correct for possible temperature differences between electrolyte temperature and the set temperature of the chamber, we utilize sapphire's bond-distance temperature dependency. A material's Raman-active bond distance and temperature are positively and linearly correlated, with peaks shifting to a lower wave number as the material's temperature increases. [179]

Figure 4.12 shows the relative peak shift of the $A_{1g}$ vibrational mode of sapphire as a function of temperature. The relative peak shift is determined as the peak position difference between the very first measurement (no heating applied yet) and the one after two hours when thermal equilibrium has been reached. A linear relationship between temperature increase and peak shift can be observed (linear fit, $R^2 = 0.997$), validating that the temperature set point and

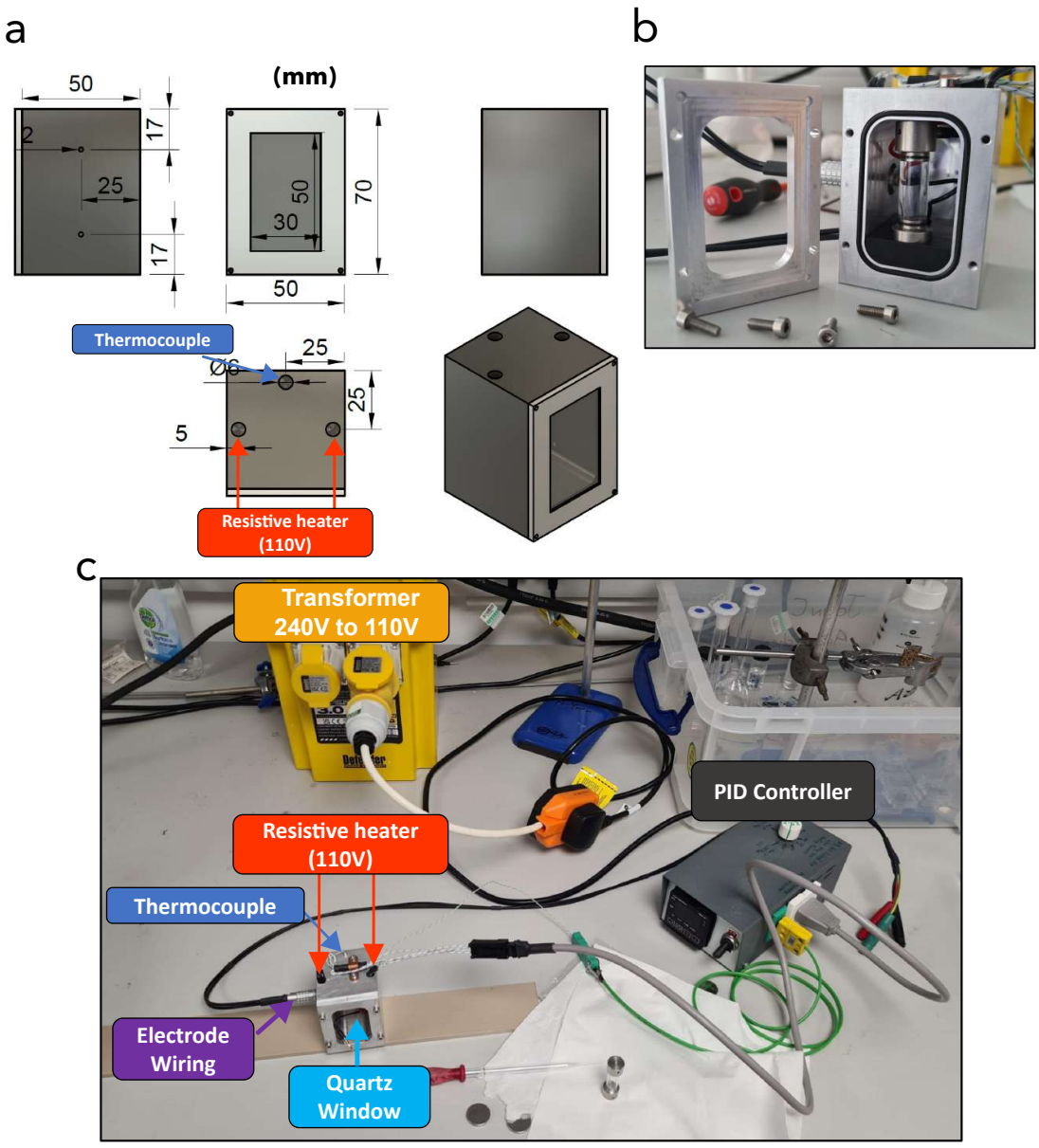


**Figure 4.11: Temperature Chamber for ORGA: a,** CAD drawing of the temperature chamber. Numbers are in milli meter b, Photograph of the temperature chamber with an ORGA cell mounted. **c,** Overview of the setup used for the temperature chamber.

ORGA temperature increase accordingly. The temperature calibration line and its corresponding slope of $-0.013\,\mathrm{cm^{-1}\,K^{-1}}$ can be used to determine temperature set points across future experiments.

To cross-validate the peak shift method, the $\kappa$ determined in ORGA is compared to measurements in a blocking-electrode conductivity cell. $\kappa$ determined from both techniques are plotted in Figure 4.13a, aligning closely and thus verifying

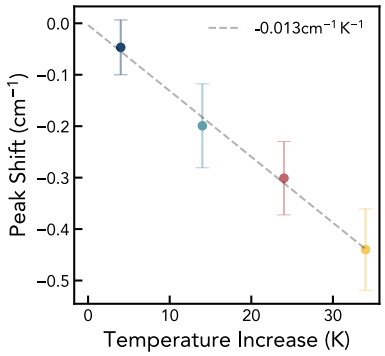


**Figure 4.12: Sapphire Peak Shift:** Shows the relative peak shift of the $A_{1g}$ vibrational mode of sapphire as a function of temperature averaged over five points across the cell length over three cells for each temperature respectively.

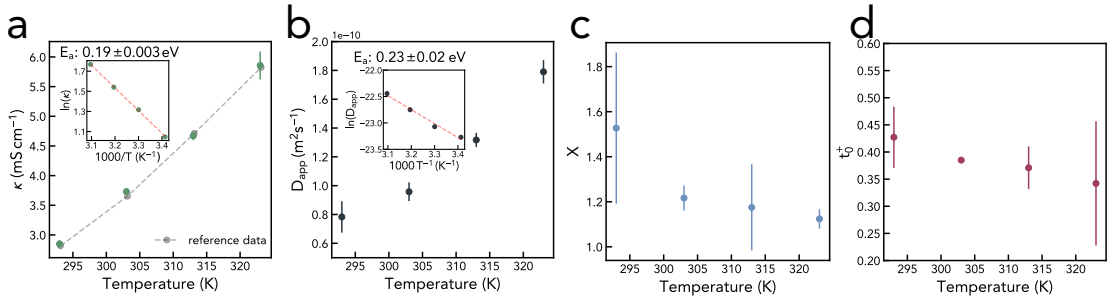


**Figure 4.13: Temperature Dependence of Electrolyte Transport Properties:** (**a**) shows $\kappa$ as a function of temperature obtained through EIS measurements in ORGA and reference data determined via EIS in a conductivity cell. The inset shows an Arrhenius fit. (**b**) shows $D_{\text{app}}$ as a function of temperature. The inset shows Arrhenius fit. (**c**) $\chi_{\text{M}}$ as a function of temperature (**d**) $t_+^0$ as a function of temperature.

the accuracy of the temperature reading. An increase in $\kappa$ from 2.8 mS cm$^{-1}$ to 5.9 mS cm$^{-1}$ is observed between 20 °C to 50 °C, reflecting the increased charge carrier mobility due to the reduced electrolyte viscosity at elevated temperatures. [176] Arrhenius fitting showed excellent agreement ($R^2 = 0.9997$, see Figure 4.13a inset) and returned an activation energy of 0.19 eV. The activation energy is more than twice as high as for a 1 M LiFSI in 1,2-dimethoxyethane electrolyte (DME) electrolyte reported elsewhere (0.08 eV). [180] Considering that 1 M LiFSI DME exhibits a significantly lower viscosity (1.137 mPa s at 20 °C) compared to its G4 electrolyte analog (12.30 mPa s at 20 °C), this can at least partially account for the increased temperature sensitivity and, consequently, the higher activation energy observed in $\kappa$ in LiFSI G4.

Figure 4.13b shows $D_{\mathrm{app}}$ as a function of temperature. Just like $\kappa$, $D_{\mathrm{app}}$ depends on the ionic mobility, and thus a positive correlation of $D_{\mathrm{app}}$ and temperature can be observed with an increase from $0.78 \times 10^{-10}\,\mathrm{m^2\,s^{-1}}$ to $1.79 \times 10^{-10}\,\mathrm{m^2\,s^{-1}}$ from 20 °C to 50 °C. However, the increase is more rapid, which is reflected in a larger activation energy of 0.23 eV determined by Arrhenius fitting (see Figure 4.13c inset, $R^2 = 0.9926$) While both $\kappa$ and $D_{\mathrm{app}}$ strongly depend on the ionic mobility, $\kappa$ is even more sensitive to the number of free charge carriers than $D_{\mathrm{app}}$. [176, 181] This could be an indication that the solvation environment of lithium is changing as a function of temperature.

For a better understanding of the solvation environment, $\chi_{\mathrm{M}}$ is plotted as a function of temperature in Figure 4.13c. According to the extended Debye-Hueckel theory, quantifying the electrostatics of ions in solution, $\chi_{\mathrm{M}}$ and its variation with concentration and temperature are reflective of the non-ideality behavior of electrolytes. [18, 23] Despite the larger error bar, a general decrease of $\chi_{\mathrm{M}}$ from 1.53 to 1.12 can be observed between 20 °C and 50 °C in Figure 4.13c. As shown before [147], the transition point for LiFSI G4 lies at around 0.72 M, and thus a $\chi_{\mathrm{M}}$ larger than one for the 1 m (around 0.95 M) LiFSI G4 electrolyte aligns with previous studies and indicates that classical electrostatic theory is not able to explain the temperature dependency of $\chi_{\mathrm{M}}$. While there is no universal understanding of how temperature affects $\chi_{\mathrm{M}}$ at moderate concentrations, short-range species interactions such as ion association and pairing are expected to play a crucial role. [14, 20, 24, 25] Reports on temperature dependencies of $\chi_{\mathrm{M}}$ are scarce due to the laborious nature of conventional measurement techniques, with the existing few reports reporting varying temperature dependencies, even within the same electrolyte chemistries. [19, 181, 182]

Figure 4.13d shows the $t_+^0$ number as a function of temperature. Visible is a slight decrease from 0.42 to 0.34, indicating less current is transported by lithium cations compared to $[\mathrm{FSI}]^-$ at elevated temperatures. Similar to $\chi_{\mathrm{M}}$, the temperature dependency of $t_+^0$ is scarcely reported. The few reports vary in their conclusions, some describing $t_+^0$ as independent of temperature [19, 183] whereas others observe

a temperature dependency in either direction. [181, 184] Regardless, $t_+^0$ and its temperature dependence are expected to depend strongly on the chemical composition of the electrolyte formulation.

To complement the discussion on the temperature dependency of $\chi_M$ and $t_+^0$, the coordination structure of $[FSI]^-$ was scrutinized, focusing on the S–N–S bending peak in the Raman spectra. As shown in Figure 4.14 and Figure 4.15a, the peak shows the growth of a shoulder with temperature, indicative of the formation of more CIPs. The peaks can be deconvoluted using Pseudo-Voigt fitting (Figure 4.14). [185] The analysis indicates an increase of bound $[FSI]^-_{bound}/([FSI]^-_{bound}+[FSI]^-_{free})$ from around 50% to around 59% between 20 °C and 50 °C.

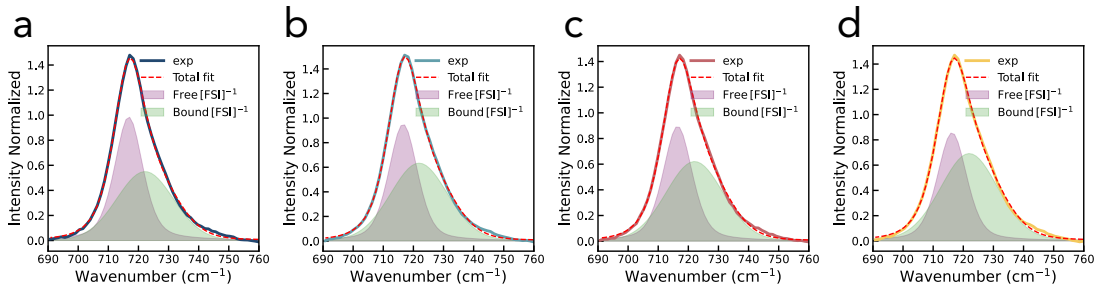


**Figure 4.14: Pseudo Double Voigt Fitting:** Double pseudo Voigt fit of the S-N-S bending mode of $[FSI]^-$ as a function of temperature. **a,** measured at 20 °C and corresponding peak areas of $[FSI]^-_{free}$ = 13.3 and $[FSI]^-_{bound}$=13.1 **b,** at 30 °C and corresponding peak areas of $[FSI]^-_{free}$ = 12.7 and $[FSI]^-_{bound}$ = 15.3 **c,** at 40 °C and corresponding peak areas of $[FSI]^-_{free}$ = 12.3 and $[FSI]^-_{bound}$ =15.0 and **d,** at 50 °C and corresponding peak areas of $[FSI]^-_{free}$ = 11.7 and $[FSI]^-_{bound}$ = 17.0

This is an interesting finding since the effect of temperature on ion association is far from trivial and strongly dependent on the investigated electrolyte formulations. Since lithium salt dissociation in organic solvents is generally exothermic, a shift towards more associated ions could be rationalized at higher temperatures. [186] Besides, the extent to which association dominates is primarily influenced by the relative dielectric constant ($\epsilon_r$) of the solvent. Smaller $\epsilon_r$ result in weaker ion solvation and thus increased association and vice versa. Wang et al. recently demonstrated this in a comparative study of $LiPF_6$ in propylene carbonate (PC) and ethyl methyl carbonate (EMC). [20]. $\epsilon_r$ are generally declining with increasing

**Table 4.2:** Transport and thermodynamic properties as a function of temperature.

| T (°C) | $D_{\text{app}}$ ($\text{m}^2\,\text{s}^{-1}$) | $t_+^0$ | $\chi_{\text{M}}$ | $\kappa$ ($\text{mS}\,\text{cm}^{-1}$) |
|---|---|---|---|---|
| **20** | $0.78 \pm 0.11 \times 10^{-10}$ | $0.43 \pm 0.06$ | $1.53 \pm 0.33$ | $2.85 \pm 0.07$ |
| **30** | $0.96 \pm 0.07 \times 10^{-10}$ | $0.39 \pm 0.01$ | $1.22 \pm 0.06$ | $3.73 \pm 0.03$ |
| **40** | $1.32 \pm 0.05 \times 10^{-10}$ | $0.37 \pm 0.04$ | $1.17 \pm 0.19$ | $4.67 \pm 0.07$ |
| **50** | $1.79 \pm 0.08 \times 10^{-10}$ | $0.34 \pm 0.11$ | $1.12 \pm 0.04$ | $5.86 \pm 0.24$ |
| $E_a$ (eV) | $0.23 \pm 0.03$ | — | — | $0.19 \pm 0.003 \times 10^{-2}$ |

temperature, thus favoring ion association. [187] However, entropical gains through dissociation become energetically more relevant with increasing temperature. [188] The multitude of competing contributions towards solvation and thus $\chi_{\text{M}}$ and $t_+^0$ at different temperatures highlight the complexity of the concepts, and a definite conclusion is beyond the scope of this project. Yet it underlines the importance of being able to experimentally access transport properties at different conditions within a unified setup. All thermodynamic and transport properties and the corresponding activation energies determined in this study are listed in table 4.2.

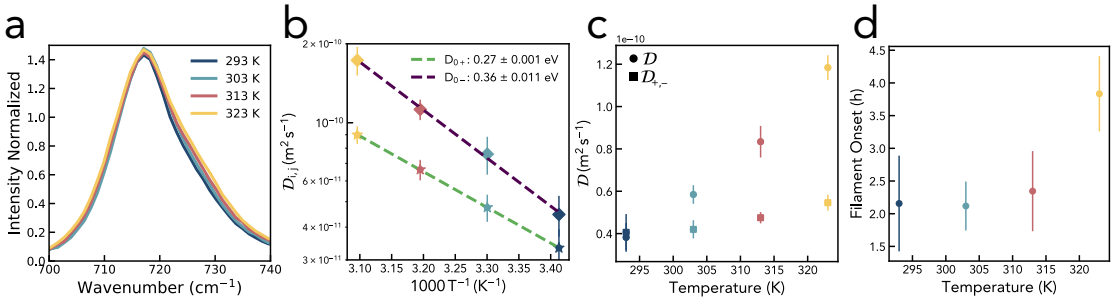


**Figure 4.15: Temperature Dependence of Electrolyte Transport Properties:** (**a**) S–N–S bend peak of $[\text{FSI}]^-$ for different temperatures (**b**) OSM Diffusion coefficient for different temperatures with Arrhenius fit. (**c**) thermodynamic diffusion coefficient and the $\mathfrak{D}_{+,-}$ OSM Diffusion coefficient. (**d**) Average filament onset time as a function of temperature.

The increasing amount of CIPs with temperature aligns with the earlier observation that the activation energy of $\kappa$ is smaller than that of $D_{\text{app}}$. This is because ionic conduction is strongly affected by the amount of free charge carriers, which is reduced by the formation of CIPs.

Having measured $\kappa$, $D_{\text{app}}$, $t_+^0$, $\chi_{\text{M}}$, and partial molar volumes allows further calculation of the thermodynamic ($\mathfrak{D}$) and OSM diffusion coefficients at each

temperature point (see section 4.1.2 for calculation). In contrast to $D_{\text{app}}$, the OSM diffusion coefficients provide a more detailed description of frictional interactions between each species ($\mathfrak{D}_{0,+}$ lithium$^+$-solvent, $\mathfrak{D}_{0,-}$ [FSI]$^-$-solvent, $\mathfrak{D}_{+,-}$ lithium$^+$-[FSI]$^-$) The thermodynamic diffusion coefficient ($\mathfrak{D}$) is affected by salt chemical potential gradients rather than concentration gradients and thus considers gradients created by temperature, pressure, or composition differences. It is used for a more comprehensive and fundamental understanding of diffusion processes and is especially relevant in theoretical models and simulations. Figure 4.15b and c show the temperature dependency of Stefan-Maxwell Diffusion coefficients and $\mathfrak{D}$. Both $\mathfrak{D}_{0,+}$ and $\mathfrak{D}_{0,-}$ increase with temperature from $3.3 \times 10^{-11}\,\mathrm{m^2\,s^{-1}}$ to $9.0 \times 10^{-11}\,\mathrm{m^2\,s^{-1}}$ and $4.5 \times 10^{-11}\,\mathrm{m^2\,s^{-1}}$ to $1.7 \times 10^{-10}\,\mathrm{m^2\,s^{-1}}$ respectively. Besides, both show excellent agreement with Arrhenius fitting ($R^2 > 0.999$) $\mathfrak{D}_{0,-}$ is larger than $\mathfrak{D}_{0,+}$ at all temperatures since [FSI]$^-$ has a lower charge density than Li$^+$ and thus is less solvated by G4, reducing its drag. This is also reflected in the $t_+^0 < 0.5$. As seen in Figure 4.15b, $\mathfrak{D}_{0,-}$ has a larger activation energy than $\mathfrak{D}_{0,+}$ thus their differences in diffusion become more pronounced with increasing temperature. This supports the observation that $t_+^0$ is reducing with temperature as relatively more charge is carried by the anion. Figure 4.13c demonstrates that $\mathfrak{D}$, along with $\mathfrak{D}_{+,-}$, generally increases with temperature. However, unlike the more pronounced increases observed for $\mathfrak{D}_{0,+}$, $\mathfrak{D}_{0,-}$, and $\mathfrak{D}$, the rise in $\mathfrak{D}_{+,-}$ with temperature is marginal. As demonstrated before, more CIPs are formed at elevated temperatures. Consequently, Li$^+$ and [FSI]$^-$ have stronger correlated motion, which negatively contributes to $\mathfrak{D}_{+,-}$, counteracting the increased ion mobility induced by the increased thermal energy.

Lastly, the filament onset time was calculated based on the intensity loss of normalized Raman spectra as described in Figure 4.9. Figure 4.15d shows the average time stamp where the integrated Raman intensity dropped below 75% of its initial value as a function of temperature. The data indicates that with increasing temperature, the onset of filament nucleation can be delayed. A similar trend has been observed elsewhere. [189] As shown in table 4.2, lithium transport is

accelerated at elevated temperatures, and thus lithium depletion near the plating site is slowed down, which, analogously to Sand's time, [190] should delay inhomogeneous plating. However, within the time scale of the ORGA measurements (10 h), the lithium concentration gradient does not deplete at the plating side, emphasizing the multifaceted origins of filament nucleation on lithium metal electrodes.

## 4.4 Summary

In conclusion, this part of the thesis introduces a single-crystal sapphire cell body as an external reference in the ORGA setup. We validate the reliability of this novel approach by comparing the measured transport and thermodynamic properties of the model electrolyte system LiFSI in G4 to those measured using the traditional approach, which employs the solvent as an internal standard. Furthermore, we extend the investigation to explore the temperature dependence of these properties. As expected, we observe an increase in ionic conductivity and diffusion coefficient, and we report the respective activation energies. In contrast, $t_+^0$ and $\chi_{\mathrm{M}}$ decrease with increasing temperature. We attribute this behavior to the formation of more CIPs as the temperature increases. The temperature-dependence of the OSM diffusion coefficients is in agreement with this hypothesis. We also visualize, for the first time, the concentration gradients of both salt and solvent, paving the way for the investigations of the most relevant electrolyte systems comprising multiple components (salt additives and co-solvents). Finally, we demonstrate the capability to detect lithium filament growth. [147, 191]

The addition of an external reference makes ORGA a holistic experimental approach that combines the measurement of temperature-dependent thermodynamic and transport properties with macroscopic cycling phenomena to ultimately help elucidate the origin of dendrite formation and support the down-selection of the most promising Li-metal anode electrolyte formulations.

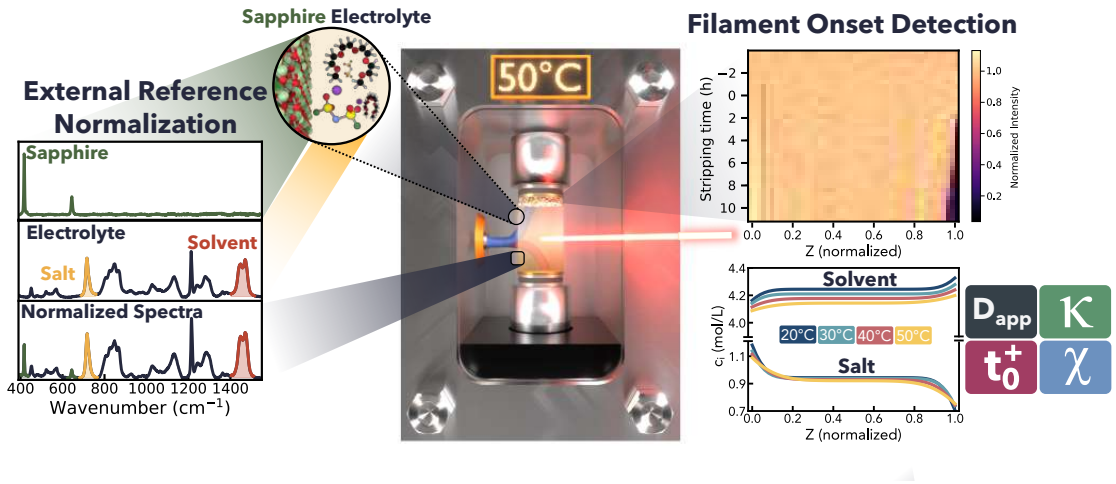


**Figure 4.16: Summary of ORGA for Advanced Electrolyte Characterization**

## 4.5 Outlook

With the improved functionality, the next experiments should focus on visualizing and analyzing multi-component electrolyte formulation. The proof-of-concept for visualizing a solvent next to the salt was demonstrated in Figure 4.10. The G4 gradient shown in Figure 4.10 was also fit to the concentration function (see 4.39). However, as discussed in section 4.3.1, a large measurement error was detected due to stage fluctuation, the surface roughness of the sapphire tube, and general signal-to-noise. (see Figure 4.5). One way to ameliorate this problem is to increase the laser power, which would increase the counts per second in the sapphire and electrolyte spectrum. Figure 4.17 show three ORGA cells where data was collected at 30 mW, 150 mW, and 300 mW respectively. Just like in Figure 4.4, the Raman spectra collected during cell resting were integrated, and the scattering of individual measurements around the mean value is plotted as a function of cell height. The scattering directly translates to measurement noise. It is noteworthy that it will be multiplied by the initial concentration $c_i^*$ and thus amplified at higher concentrations. With increasing laser power, a reduced scattering can be detected (see Figure 4.17a to c).

The standard deviation of the scattering is calculated for each $z$-value and plotted as a function of cell height in Figure 4.17d to f showing the same trend of reduced

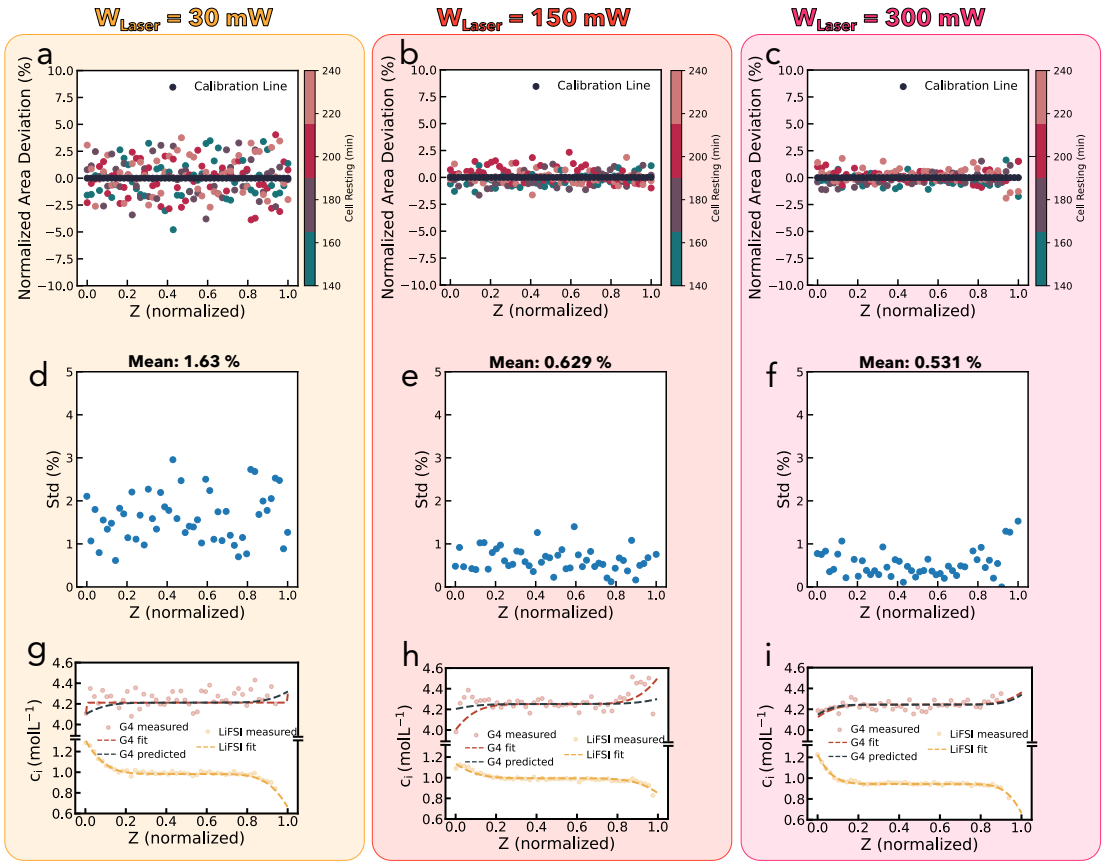


**Figure 4.17: Laser Power Variation:** Scattering of integrated Raman spectrum around the mean determined during OCV and used for the baseline creation at **a,** 30 mW **b,** 150 mW, and **c,** 300 mW. The standard deviation of the scattering is plotted in **d,** for 30 mW **e,** 150 mW, and **f,** 300 mW. The resulting concentration gradients are shown in **g,** 30 mW **h,** 150 mW, and **i,** 300 mW.

scattering with increasing laser power. The mean standard deviation reduces from 1.63% over 0.629% to 0.531%. The resulting concentration gradients are plotted in Figure 4.17g to i. It can be observed that with increasing laser power, the features of the G4 gradient, depletion on the stripping side, and accumulation on the plating side are easier to identify, and consequently, the fit improves. Consequently, for an in-depth analysis of a high-concentration compound, a high laser energy is required.

For every new electrolyte formulation investigated in ORGA, the stability of the electrolyte with the laser power must be verified to ensure there is no electrolyte decomposition or local heating happening as a result of laser exposure. Furthermore, the experimental settings can be further optimized by investigating the effect of exposure time and the number accumulation per measurement. Fine-tuning the

settings will enable a resolution that is high enough to fit and investigate the gradients of all Raman active species while ensuring the stability of the electrolyte formulation throughout the experiment's duration.

When selecting a multi-component electrolyte formulation for ORGA analysis, the following aspects should be considered.

- At least one peak of each salt or solvent must be quantifiable, *i.e.*, it must be possible to deconvolute peaks by fitting them, for example, using a Pseudo-Voigt function. Furthermore, it is still necessary to clearly identify the Raman $A_{1g}$ peak to normalize the spectra.

- Dual solvents, often comprising a high and low dielectric constant compound, are highly relevant as they are commonly used in commercial electrolyte formulations. Recent studies have provided preliminary evidence that in an $LiPF_6$ in EC/EMC electrolyte, EC and EMC migrate at different rates, thus violating the single-solvent approximation. [178] The new ORGA setup is ideally suited to verify these observations and expand on other multi-solvent systems.

- Essentially, all commercial electrolytes comprise multiple salts to optimize the SEI. ORGA can be used to not only track and compare the local salt concentration of each compound but also relate it to the onset and propagation of filaments and thus provide a quantitative measure to judge the quality of the SEI.

- Transport in IL is different from diluted solutions due to the formation of mesoscopic aggregates, which can result in negative $t_+^0$. Both the theoretical understanding and experimental design to probe theory are still evolving and ORGA can be used to investigate a wide range of IL formulations and their respective transport properties. [22, 155, 192–195]

A lot of electrochemical data is collected in ORGA and, up to this point, the EIS data is only used to calculate the concentration overpotential of the system. However,

if more advanced fitting were used to analyze the data, a lot more information could be extracted from EIS. The next chapter of this thesis is dedicated to deconvoluting interphase impedances using EIS on lithium anodes.

# 5

# Deconvolution of Li-Metal Interphase Impedances

## Contents

# 5.1 Introduction

## 5.1.1 The Holy Grail

Li-metal anodes are widely considered the holy grail of electrochemical energy storage owing to their high energy density enabled by storing lithium in its purest form without the need for a dead-weight host structure. [15, 29] When combined with energy-dense cathodes, a step increase in energy density can be achieved, which is necessary to electrify aerospace applications. [2, 6, 66] As a result of the low reduction potential of Li-metal ($-3.04\,\mathrm{V}$ vs SHE), which ultimately yields the desired energy density gains, most electrolytes rapidly react with lithium to form a SEI. [196] In fact, studies have shown that even before lithium has been brought in contact with an electrolyte, its surface is covered by a native passivation layer (NPL). The NPL is reported to be predominantly made of LiOH, $Li_2O$, and $Li_2CO_3$ [38, 52, 197] while the SEI composition is determined by the salt and solvent chemistry of the electrolyte. [15, 30]

The passivation layers' (SEI and NPL) microstructure and composition determine its physico-chemical properties. An ideal passivation layer is ionically conducting, electronically insulating, and insoluble to the electrolyte, resulting in a stable electrode-electrolyte interphase, which prevents continuous electrolyte and lithium consumption. [41, 196] Besides, the SEI dictates lithium plating and stripping morphology and thus affects the cycle life of lithium anodes. As a result, the characterization and design of the SEI are pivotal in Li-metal research, aiming to identify an SEI that passivates and facilitates uniform lithium cycling. [30]

Unfortunately, both NPL and SEI are difficult to study since they span over the nanometer length scale, are heterogeneous in composition and structure, and are sensitive to electron beam irradiation. [31] Furthermore, the SEI evolves during battery operation; thus, an operando characterization tool is required to investigate its properties accurately. One technique that has the potential to provide a plethora of information on materials and electrode reactions, is non-destructive, and can

be applied during battery operation is EIS. A detailed description of EIS can be found in section 2.1.1 of this thesis.

### 5.1.2 Historical Overview of Li-metal SEI Fitting

To account for the formation of heterogeneous interphases, Voigt-type ECM of parallel resistors and capacitors ($R||C$), connected in series, can be used. Each $R||C$ component reflects either $Li^+$ migration processes within an interlayer coupled with its interlayer capacitance or a charge transfer resistance coupled to double-layer charging. [42, 44]

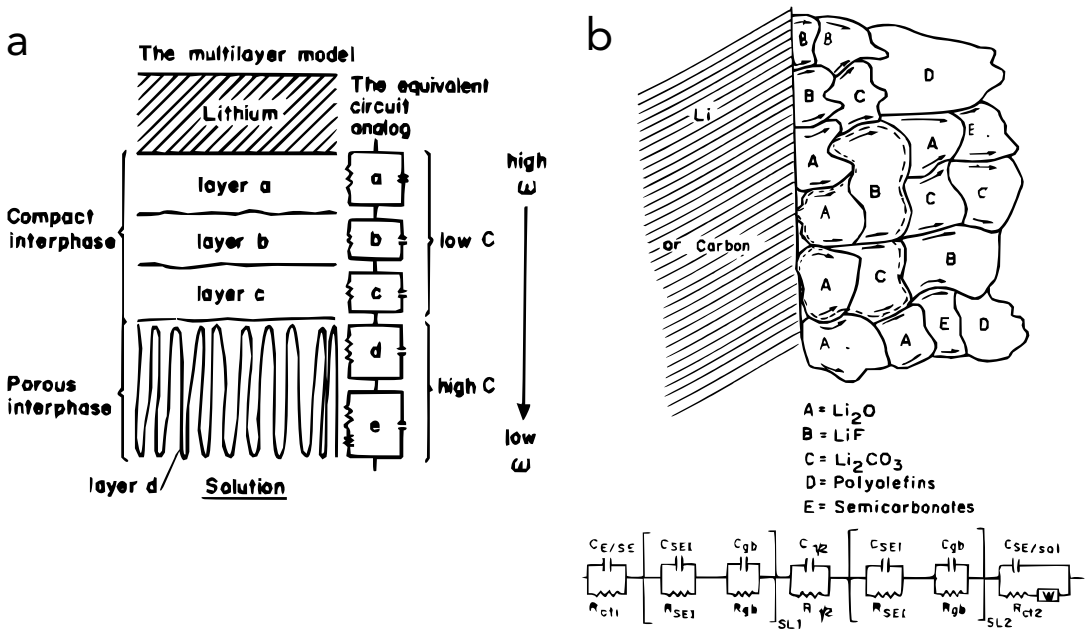


**Figure 5.1: Voigt-type based equivalent circuits for SEI fitting: a,** Multiple interphase films are represented by $R||C$ elements, reproduced from Aurbach and co-workers. [42] **b,** Mosaic-SEI model and corresponding equivalent circuit fit by Peled. [41]

Aurbach and co-workers published a series of studies on Li-metal electrodes in liquid electrolytes discussing a Voigt-type based equivalent circuit analog fitting model. [42, 198–200] The electrolytes they investigated included propylene carbonate (PC), ethylene carbonate (EC), diethyl carbonate (DEC), tetrahydrofuran (THF), and 1,3-dioxolane (DN) as the solvents, and $LiAsF_6$, $LiClO_4$, $LiBF_4$, and $LiPF_6$ as the salts. [42] In there, the authors assume that interlayer films spontaneously form on the lithium surface once lithium is brought in contact with the solution. Further,

those films vary in composition and thus comprise a multilayer structure due to their gradual formation. Upon initial contact, the lithium-electrolyte reaction occurs rapidly as the potential difference between lithium and electrolyte is at its maximum, forming an unordered film of decomposition products of species most present close to the lithium surface. Due to moderate salt concentrations, the decomposition products mostly originate from solvents and thus have a high organic content. Upon the growth of the SEI film, it acts as a passivation layer building up an additional resistance at the interphase, which slows down further reactions and results in more selective decomposition products. An illustration of this process is shown in Figure 5.2.

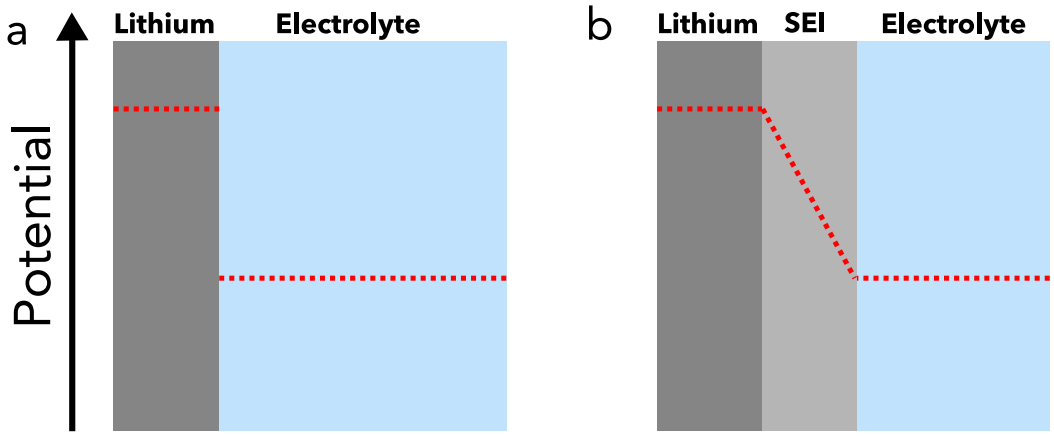


**Figure 5.2: Passivation of the Lithium Electrode: a,** Potential difference of metallic lithium and electrolyte **b,** Potential difference including a passivation layer.

Consequently, additional SEI layers of different chemical compositions are formed on top of the initial one. Aurbach *et al.* decided to use five $R||C$ elements (in series with a $R_0$ element for the ohmic drop and a Warburg finite space diffusion element) as they found the fitting quality significantly improved from 2 to 5 $R||C$ elements while no significant improvement was achieved by adding a sixth one. The authors then assigned each of the $R||C$ elements to a separate film layer by investigating the effect of different salt concentrations and compositions, water impurities, and temperature. They find that the first three $R||C$ showed a small capacitance (around $1\,\mu F\,cm^{-2}$) which was attributed to a dense, inner SEI, and the two latter $R||C$ had a

significantly larger capacitance, indicative of a more porous, large surface area layer as illustrated in Figure 5.1. Assuming a dielectric constant of $\epsilon = 5$ for the SEI layers and a tortuosity of one, the authors calculate layer thicknesses of the order of 1 nm to 4 nm. In addition, Aurbach *et al.* concluded that time constants of the equivalent circuit analogs ($\tau = R \cdot C$) increase according to their order of sedimentation on the lithium surface, *i.e.* films formed immediately after lithium is brought in contact with the electrolyte have the lowest time constant, and films formed last the highest. Their suggested model is still being used up to date [201] and has served to inspire other studies elucidating the physical origin of equivalent circuit elements for fitting AC measurements of lithium electrolyte interphases. However, our understanding of the nanostructure of the SEI has evolved, in particular, due to recent advancements made in the field of cryogenic transmission electron microscopy, deviating from some of the findings made by Aurbach *et al.* [30–32] For example, some reports claim significantly thicker SEI layers of the order of tens to hundreds of nanometers [33, 34], some an amorphous unlayered SEI nanostructure [35, 36], and others a high inorganic content close to the Li-metal surface. [41, 49]

Peled *et al.* published influential work on the composition of SEIs on metal and graphite electrodes, introducing the Mosaic model and suggesting an alternative physical interpretation for Voigt elements used in an ECM to fit EIS data. [41] By investigating the impedance response of a polyparticle solid electrolyte in a blocking electrode configuration, the authors find that grain boundary charge transfer resistance $R_{gb}$ is larger than the bulk ionic resistance $R_b$. The authors thus postulate one cannot neglect $R_{gb}$ resistances when fitting SEI EIS data and suggest a mosaic-type equivalent circuit that takes grain-boundary $R_{gb}||C_{gb}$ into account, as illustrated in Figure 5.1. [41] In addition, the authors point out that Aurbach *et al.* failed to include $R||C$ elements that represent the actual interfaces, that is, electrode-interlayer, interlayer-electrolyte, and potentially any additional interlayer-interlayer impedances. Simultaneously, the authors acknowledge that in many cases, Nyquist plots of SEIs obtained in various electrolytes show one single semicircle, which makes them believe that resistance due to ionic conduction $R_b$ through an SEI

layer is significantly larger than $R_{gb}$ or $R_{ct}$ and thus should be neglected in the fitting process. This emphasizes the complexity and sensitivity of the SEI nanostructure and electrical conduction mechanism towards electrolyte composition.

Recently, Srout *et al.* used a Voigt-element-based equivalent circuit to study Li-metal anodes in liquid electrolytes. [43] In their study, the authors aim to correlate an impedance contribution from the NPL to the shape of the Nyquist plots. Therefore, they compare three types of lithium electrodes (750 µm commercial, 50 µm commercial, 50 µm electrodeposited) in symmetric two and three-electrode EIS measurements. They used an ECM inspired by Auerbach *et al.*; however, they substituted all capacitors with CPEs without additional comment. They then ascribe a visually separate semi-circle in the mid-to low-frequency range (around 1 Hz) of the Nyquist plot to a charge transfer resistance $R_{ct}$ related to the NPL and the high-frequency semi-circle (around 500 Hz) to lithium migration resistances through the SEI. Summarizing all impedance contributions of the NPL into a single $R_{ct}$ value is somewhat ambiguous since the presence of an NPL is an additional interphase layer between lithium and SEI and therefore requires an equivalent circuit representation of two $R||C$ elements, one for NPL lithium migration and NPL capacitance $R_{NPL}||C_{NPL}$ and one for charge transfer and double layer capacitance $R_{ct}||C_{dl}$. $R_{ct}$ is connected to the exchange current density, which is dependent on the local salt concentration and electrolyte composition, whereas $R_{NPL}$ should be constant and independent of the electrolyte composition since it formed before electrolyte exposure. In their study, Srout *et al.* observed a substantial resistance dependence on the electrolyte composition and a steady increase with measurement time, which indicates $R_{ct} >> R_{NPL}$ and contradicts the scientific consensus on the magnitude of charge transfer resistances. [201–203] Besides, the reported NPL capacitances are of the order of magnitude of $10 \times 10^{-3}\,\mathrm{F\,cm^{-2}}$. Such capacitance values suggest a surface area nearly a thousand times greater than the geometrical surface area, which is highly improbable for a pristine, uncycled lithium electrode and would require further experimental evidence. Lastly, it can be seen that the ohmic drop scales inversely with lithium thickness in all of the

reported impedance fits which indicates the electrode spacing is changing for the lithium samples under investigation. This is expected to affect diffusion impedances and thus renders a comparison of NPLs in the mid-to low-frequency region, where diffusion is expected to dominate, ambiguous.

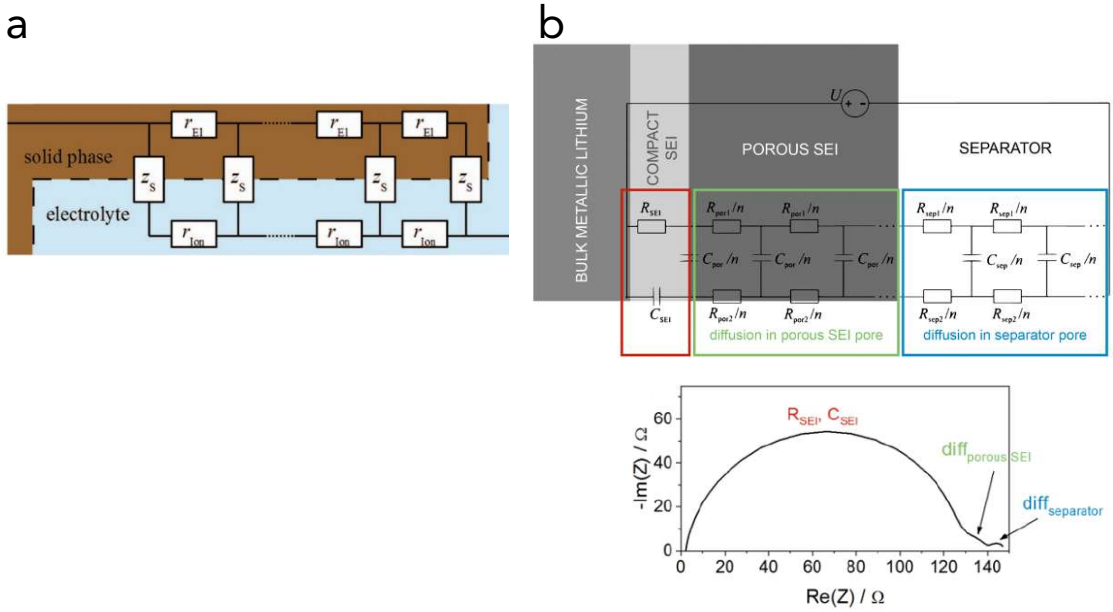


**Figure 5.3: Transmission Line Model: a,** Illustration of transmission line model (TLM) reproduced from Landesfeind *et al.* [204] **b,** Modified transmission line model (TLM) to fit Li-metal anodes in liquid electrolytes reproduced from Talian *et al.* [205]

Another approach to fitting EIS data focusing on the SEI's porous nanostructure is the transmission line model (TLM) developed by De Levie. [206, 207] In there, the system is modeled as an electronically conductive (ion-blocking) electrode intersected by cylindrical pores filled with ionically conductive electrolyte as illustrated in Figure 5.3a. This can be represented by two parallel circuit pathways (or rails), one electronic and one ionic, connected by a capacitor representing the double-layer capacitance inside the pores. If these circuit pathways were to extend infinitely, meaning there is an endless sequence of two parallel pathways connected through capacitors, the overall impedance of the system would mathematically converge to that of a Warburg diffusion element.

Bisquert further advanced the TLM by considering an electrode of finite thickness with macroscopic boundaries. The boundaries distinguish between ion-blocking

conditions, *i.e.* a reflective boundary, and redox-active conditions, *i.e.* a transmissive boundary. The electrical rails of the TLM then terminate with a capacitor (double layer charging) or resistor (charge transfer resistance), respectively. [208] The impedances only differ in the low-frequency region, where the imaginary part of the impedance approaches infinity for a reflective boundary, while it drops to zero for a transmissive boundary. To date, the TLM and variations (with simplifications, *e.g.* electronic resistance is often neglected) are widely applied to investigate and model porous electrodes. [204, 209, 210]

One study employing the TLM focusing explicitly on Li-metal anodes in liquid electrolytes was conducted by Talian *et al.* [205] The authors distinguish between a several nanometers thick compact SEI and an up to micrometer range thick porous SEI. Transport in the compact SEI is predominantly governed by lithium migration, whereas the porous SEI enables diffusion through the pores filled with liquid electrolyte. As illustrated in Figure 5.3b, their ECM comprises two electrical rails, the upper one for positive charges, *i.e.* lithium ions and the lower one for negative charges, *i.e.* the counter ion. This is different from conventional TLM, which, as illustrated in Figure 5.3a, distinguishes electronic and ionic transport on each rail, respectively. At high frequencies, Talian's porous transport representation collapses into resistors (the perpendicular capacitor short-circuits at high frequencies), aligning with the well-known electrolyte resistance observed due to ion migration. At lower frequencies, however, both ion migration resistors are coupled to the charging of the perpendicular capacitor. This effectively describes a chemical diffusion process, generally represented by Warbug diffusion. The upper rail terminates at the compact SEI with a resistor, representing the migration barrier for lithium transport through the SEI. The charge transfer resistance is neglected. The lower rail terminates with a capacitor since the compact SEI is anion-blocking. Towards the electrolyte side, the two rails are extended to account for diffusion inside the separator. Upon cycling of lithium, Talian *et al.* modified their ECM to account for the formation of live and dead lithium filaments. While their described model stems from an underlying physical understanding of the system, the accuracy to apply this model

to cells under non-OCV conditions is dubious. Once lithium has been stripped from one electrode to another the two electrodes are morphologically different. Srout *et al.* clearly showed in three-electrode measurements that the stripping and plating electrode impedances cannot be equated. [43] Extending Talian's model to account for electrode asymmetry is possible, as demonstrated in an earlier publication by the same group in a case study of lithium-sulfur cells. [211] It is noteworthy that the circuit illustrated in Figure 5.3b is a simplified version for cells under OCV conditions, and the complete modified circuit for dead and live lithium filaments designed for cycled cells can be found in the original publication. [205] To fit the model to experimental data, advanced fitting scripts are required due to the complex nature of this ECM, rendering the suggested model inaccessible to most researchers. In contrast, migration through the compact SEI, which according to current scientific understanding comprises multiple stacked layers (heterogeneous compact layered structure and possibly NPL [30, 41–43]), is simplified by a single $R_{SEI}$, $C_{SEI}$ pair and therefore more information could be deconvoluted by optimizing the ECM.

### 5.1.3 Project Goals

A systematic impedance investigation of Li-metal anodes is conducted in order to deconvolute interphase impedance contributions and assign a physical interpretation to the circuit components. For that, it is necessary to establish an understanding of the role of cell design and lithium preparation technique on the measured cell impedance. The approach is to simplify the experimental setup as much as possible to isolate interphase impedances from other contributions. Further, a LiFSI in G4 electrolyte is used due to the wealth of information available on its transport and thermodynamic properties established earlier (see chapter 4) [147], and the high reductive stability of G4. This study proposes and uses a suitable ECM based on previous research and our current understanding of the lithium-electrolyte interphase. Subsequently, three parameters, salt concentration, temperature, and lithium activity, are individually changed, and the cell impedance is monitored during OCV conditions.

## 5.2 Experimental

### 5.2.1 XPS

XPS was performed with an ULVAC PHI Versaprobe III XPS system generating monochromatic AlK X-rays (1486.6 eV, 15 kV anode voltage, 25 W beam power) under ultrahigh vacuum (UHV) conditions ($1 \times 10^{-7}$ Pa to $1 \times 10^{-7}$ Pa). Samples were prepared in an argon-filled glovebox using the same procedure as described for the impedance measurements as described in section 5.3.2. Samples were immediately transferred into the XPS chamber using a vacuum transfer vessel (ULVAC PHI GmbH) to avoid contamination and ambient exposure. A 500 µm times 500 µm area from each sample was analysed. Survey scans were acquired at pass energies of 224 eV, and a lower pass energy of 55 eV was used for core-level spectra. In-built electron and low-energy $Ar^+$ sources were utilized for charge neutralization. Depth-profiling was achieved with consecutive XPS analysis and $Ar^+$ sputtering (4 keV, 3 mm times 3 mm) for a total of 60 min. Acquired spectra were fitted with Voigt lineshapes after the application of a Shirley background, using CasaXPS software. [212] Data processing was conducted using CasaXPS software.

### 5.2.2 AFM

Lithium samples were prepared in an argon-filled glovebox using the same procedure as described for the impedance measurements. Lithium electrodes were fixed, with a small square of carbon tape, onto an AFM mounting disc which is held magnetically to the sample holder. The Bruker AFM was operated in ScanAsyst mode with a ScanAsyst-Air probe and an area of 90 µm times 90 µm was characterized. Data was processed using Gwyddion software and a Python script.

### 5.2.3 Electrochemical Impedance Spectroscopy

EIS measurements were performed using a *Biologic* potentiostat (VMP3) with cells placed inside an environmental chamber. Impedance data was collected from 200 kHz to 100 mHz collecting six points per decade, averaging two measures per frequency, at a voltage amplitude of 10 mV. All measurements conducted satisfied

the Kramers-Kronig relationship, and thus causality, linearity, and stability can be assumed for the collected impedance data as exemplary shown in Figure 5.4. [213]

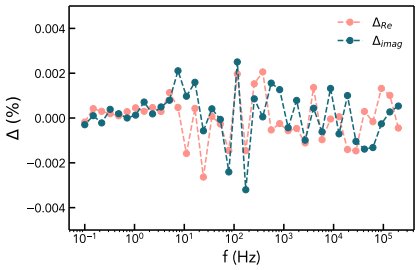


**Figure 5.4: Kramer Kronig Relationship:** Real and imaginary residues plotted as a function of frequency.

### 5.2.4 Coin Cell Assembly

Electrolytes were prepared by solving the right amount of salt (LiFSI from Fluorochem - battery grade) per gram of G4. All cells were assembled in an argon-filled glovebox using glass fiber separators (Whatman, GF/D), metallic lithium foil (Sigma, 99.9%, prepared as described in section 5.3.2) as the counter/reference electrodes, and 150 µL of electrolyte. Regular 2032 coin cell components with a polypropylene gasket were used (MTI Corporation).

### 5.2.5 Custom Made EIS Cells

A custom-designed cell was created to ensure an airtight environment, critical for accurate impedance measurements, and to avoid geometric inconsistencies that could influence the results. This cell features a chamber made of polyether ether ketone (PEEK), known for its chemical stability and geometric uniformity. Stainless steel is used for the current collectors, providing durability and efficient electrical conductivity. The seal is achieved with chemically resistant perfluoroelastomer (FFKM) O-rings, ensuring a tight closure that prevents any leakage. The development of this cell involved multiple design iterations and was initially inspired by work on diffusion measurements by Dhir *et al.* [180]. This iterative process was crucial to finalizing a design where the PEEK chamber maintains geometric homogeneity internally.

When assembling the cells, lithium (which had been prepared as described in section 5.3.2) was pressed onto the piston of the current collector. To ensure the lithium has a good contact with the current collector, a drop of hexane was added to the lithium surface before placing a stainless steel current collector on top. The assembly was then compressed using a hydraulic press at a force of 50 M Pa. The use of hexane ensures that the current collector disc does not stick to the lithium, promoting a smooth and even surface. Subsequent to pressing, the edges of the lithium electrode were trimmed with a razor blade to guarantee an exact fit within the PEEK chamber. The electrolyte was then added from the top. To finalize the assembly, the current collectors were tightened, and the O-rings were compressed, ensuring an airtight seal. Throughout this process, particular attention was given to maintaining the cell in a perfectly vertical orientation. This precaution prevents the entrapment of air bubbles within the cell, which is crucial for the integrity and performance of the cell.

### 5.2.6 Data Analysis

In this study, symmetric lithium-lithium cells were assembled in a custom-made cell in a LiFSI G4 electrolyte at a fixed temperature. The impedance was measured every two minutes for over 10 hours. Four different temperatures (20 °C, 30 °C, 40 °C, 50 °C) and three different concentrations (0.25 M, 1 M, 2 M) were investigated, and at least three cells per experimental condition were used for the analysis. Each cell had to fulfill "reproducibility requirements" to be included in the subsequent analysis. That is the $R_0$ value and the total cell interphase needed to be within $\pm$ 10% of the average value impedances determined for a given set of conditions. Further, the $R_0$ had to be stable over the entire measurement duration. All impedance spectra that are compared in the same cell design are not normalized since the true surface area of the lithium electrode is unknown. Since all electrodes were prepared in the same way it can be assumed the electrode surface area is constant throughout the measurements.

All impedance data was fit using an ECM specified in section 5.3.3. The fitting was done automatically using an in-house developed Python script, *auto_echem*, available on Github and the open source impedance.py package by Murbach *et al.* [55, 172]

### 5.2.7 Random Forest Model

A random forest classifier algorithm was used to analyze the EIS data. The model was imported from the scikit-learn machine learning library in Python. All analyzed impedance data was stored in a matrix format structure. The data set was then divided into a training (80%) and test (20%) data subset. The model was then trained using 100 trees. Some model variations introducing a minimum sample leaf restriction and a maximum tree depth were explored. However, the model was either not able to accurately predict the targets or the results yielded very similar permutation feature importances as described in 5.5.2. To reproduce the model, a random state was assigned to both the data set subdivision and the model training.

## 5.3 Results

### 5.3.1 Cell Design for EIS Measurements

Before setting up a systematic study to investigate the interphase formed on Li-metal anodes, it is necessary to decide on the right cell design for EIS measurements. As described before, the cell configuration, geometry, and cell wiring are crucial parameters that can lead to measurement artifacts that can obscure the interphase processes we are trying to monitor. [44, 45, 56] Therefore, appropriately shielded measurement cables supplied by Biologic were used to mitigate wire capacitance. In addition all electronic connections were kept as short as possible to minimize cable inductance and electronic resistances. A reference electrode is required to deconvolute impedances on the working and counter electrode. Unfortunately, implementing a reference electrode into the cell design is a challenging task. In general, reference electrodes are grouped into external and internal references. External references are placed outside the direct current lines of the electrodes. They

are generally easier to implement and commercially available in some cell designs (*e.g.* EL-cell). However, the position of the reference electrode can significantly affect the magnitude of cell impedance and thus lead to systematic errors. [57, 214] Dees *et al.* provide a good overview of how edge effects originating from electrode alignment during cell assembly and their interaction with the external reference electrode severely affect the impedance data. [57] This makes comparisons between measurements taken in different cell designs meaningless, and even within the same setup, it can lead to measurement errors due to imperfect alignment during cell assembly. In contrast, internal reference electrodes are placed in between the working and counter electrodes. As a result, the reference electrode unavoidably affects the cell's current distribution near the reference electrode and thus may also affect the voltage measurement. To minimize this effect, micro reference electrodes are commonly employed, which impose further constraints on cell design and complicate the assembly process, ultimately impeding measurement throughput. [57, 214]

Since the focus of this study is the deconvolution of interphase impedances, hoped to be achieved by simplifying the electrochemical system as much as possible while simultaneously providing a high reproducibility and cell throughout, it was decided to use a 2-electrode cell design with two identical Li-metal electrodes. Thus, the working and counter electrode interphases are connected in series, and the interphase impedance can be obtained by dividing the measured impedance by two. This assumption holds true as long as the cell is kept under OCV conditions, *i.e.* no electrode asymmetry is expected.

A commercial cell design ideally suited for high reproducibility and convenient assembly is coin cells. Initial experiments were therefore conducted in a symmetric coin cell configuration using a 1 M LiFSI G4 electrolyte. An exemplarily Nyquist plot for such a coin cell normalized by the geometrical lithium surface area is shown in Figure 5.5a. Two separate semi-circles can be clearly identified. This indicates that at least two separate processes can be deconvoluted in the mid to low-frequency region. However, coin cells are constructed in a stacked format, pressurized by a small spring, and filled with excess electrolyte. A separator is required to prevent

the cell from short-circuiting. As seen from other studies, the separator can give rise to impedance contributions in the high-frequency region (migration resistance due to separator tortuosity) and low-frequency region (effective diffusion coefficients through the separator). Since the impedance contributions are dependent on the separator's wettability, which in turn is affected by electrolyte composition, comparing different electrolytes introduces another variable to the analysis. [44, 204, 205] Ideally, a system without any separator can be constructed to reduce the number of cell components, simplifying the assembly and subsequent data analysis.

For that purpose, a custom-made cell design was developed. The setup is described in more detail in the experimental section 5.2.5. Since the electrodes are stuck to the current collector piston, no separator is necessary to keep the electrodes spatially separated in the custom-made cell design. Furthermore, removing the coin cell spacer and spring reduced the amount of inactive cell components in contact with the electrolyte. The new cell format can hold only as much electrolyte as can fit in between the electrodes since excess electrolyte is squeezed out of the cell when screwing in the pistons. This implies that, in contrast to coin cells, the custom-made cell is not pressurized.

An exemplary Nyquist plot using identical lithium and electrolyte to before, normalized to the new electrode size, is plotted in Figure 5.5b. The lithium electrodes were punched to a radius of 0.25 cm. The pistons were manufactured with a radius of 0.4 cm, which means some current collector is exposed to the electrolyte in this experiment. Visually, both spectra show a similar impedance size. The custom-made cell Nyquist plot, again, shows two separate semi-circles. However, the lower-frequency one appears to be slightly more compressed. The first semi-circle shows a very similar characteristic frequency, while the second one is shifted towards lower frequencies in the custom-made cell design.

A third cell was assembled using the custom-made cell design. This time the electrodes covered the entire piston. The normalized Nyquist plot is shown in Figure 5.5c. A substantial change in the shape can be observed. The two semi-circles visually collapsed into a single arc with a flat, almost horizontal, low-frequency

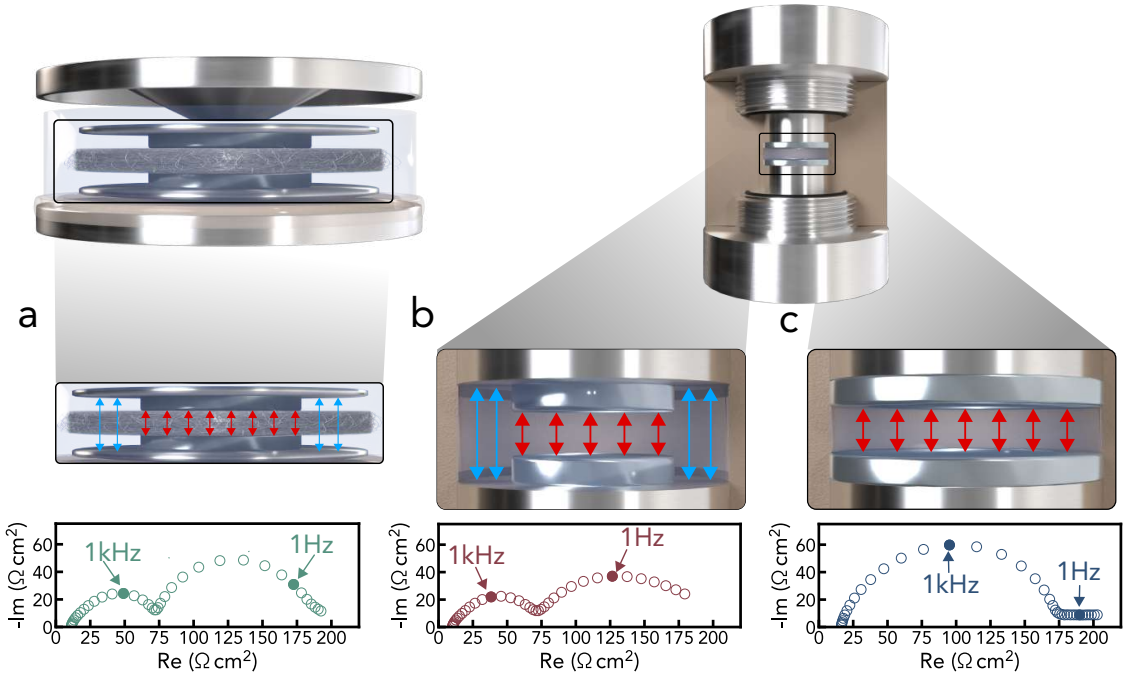


**Figure 5.5: Overview of different EIS Cell Designs: a,** A commercial coin cell configuration using a glass fiber separator **b,** a custom-made cell design which does not require a separator and reduced the number of cell components in contact with the electrolyte **c,** the same custom-made cell design with electrode covering the entire piston. All cells were measured in a 1 M LiFSI G4 after five hours of resting under OCV.

tail. The characteristic frequency of the first semi-circle was similar to the other two cells (around 1 kHz). Since the only difference between the cell described in Figure 5.5b and the one in Figure 5.5c is the lithium coverage of the piston, the change in impedance response must stem from the lateral electrode interface or the current collector interface with the electrolyte.

A systematic study by Talian *et al.* investigated the impact of cell design on impedance features. [215] The authors find a distortion or even split of the Nyquist impedance semi-circle into two separate arcs if the current collector is in contact with the electrolyte. The artifact was most prominent in coin cell configurations. The authors argue that a passivation layer is formed between the current collector (in the study, they tested steel, nickel, and copper) and electrolyte, enabling a second, parallel electrical pathway. Since this passivation enables lithium migration, it gives rise to an additional $R_{cc}||C_{cc}$ element in the equivalent circuit. Once the lithium ions

are migrated through the passivation layer, they are blocked at the current collector, which can be represented by connecting an additional capacitor ($C_{cc,dl}$) in series. The authors did XPS analysis on the current collector and indeed found traces of lithium, indicating the presence of some kind of passivation layer that allows lithium migration. [215] It is difficult to verify this hypothesis by modeling the corresponding Nyquist plots since $R_{cc}$, $C_{cc}$, and $C_{cc,dl}$ are all unknown. However, one can make reasonable assumptions to calculate the expected cell impedance. Multiple lithium salts including $ROCO_2Li$, ROLi, LiF, $Li_2CO_3$, LiCl have a dielectric constant of around 5. [42, 199] If one assumes that the passivation layer on the current collector comprises any of those compounds, it can be estimated that the dielectric constant is of similar magnitude. If one further assume its 1 nm thick, a capacitance of around $1 \times 10^{-10}\,\mathrm{F\,cm^{-1}}$ can be calculated. Assuming the migration resistance in such a layer is similar to a SEI, a Nyquist plot can be modeled as shown in Figure5.6a. Indeed, the semi-circle splits into two arcs aligning with observations made for the partially covered electrodes in Figure 5.5a and b.

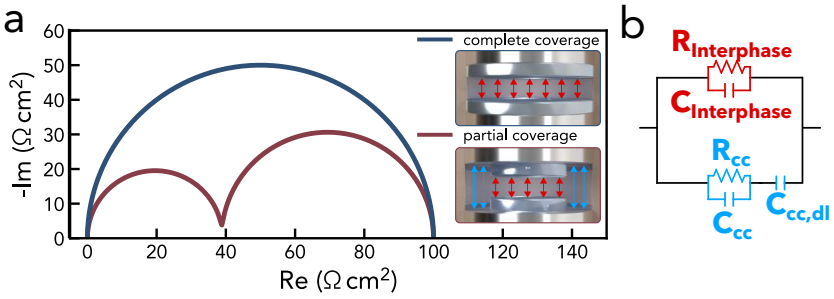


**Figure 5.6: Simulated Nyquist plots: a,** Simulated Nyquist plots for a cell covered partially ($r_{Li^+} = 0.25\,\mathrm{cm}$) and fully ($r_{Li^+} = 0.4\,\mathrm{cm}$) onto the cell piston ($r_{piston} = 0.4\,\mathrm{cm}$). For the simulation, the equivalent circuit in **b,** was used, originally proposed by Talian *et al.* [215]. The modeling parameters were estimated by assuming a dielectric constant of 5 and a current collector passivation layer thickness of 1 nm. $R_{SEI} = 100\,\Omega\,\mathrm{cm^2}$, $C_{SEI} = 1 \times 10^{-6}\,\mathrm{F\,cm^{-2}}$, $R_{cc} = 100\,\Omega\,\mathrm{cm^2}$, $C_{cc} = 1.1 \times 10^{-10}\,\mathrm{F\,cm^{-2}}$, $C_{cc,dl} = 1.1 \times 10^{-10}$

An alternative explanation could be that there is an additional migration and diffusion pathway laterally to the electrode surface if the electrode does not cover the entire current collector. To test this, a solution for Fickian diffusion in the

given electrode geometry could be derived and implemented into the ECM, however this is beyond the scope of this project.

In summary, it is concluded that the custom-made cell setup enables us to remove impedance contributions from the separator and other inactive cell components (current collector, spring). This is an integral requirement for the subsequent impedance analysis as it facilitates the isolation of impedance contributions from the electrode-electrolyte interphase. Nevertheless, coin cells can still be a useful design if one is only interested in the total interphase impedance ($R_{Interphase}$) due to their ease of assembly and high reproducibility.

### 5.3.2 Lithium Preparation and Surface Area

Before conducting an in-depth impedance analysis, attention is directed to the preparation of lithium electrodes throughout this study. As discussed before, lithium is covered by an NPL. Depending on the supplier and the lifetime of the lithium, its surface can be partially or entirely covered by a dark surface layer. As a result, different practices have been developed to remove the NPL and provide a clean and shiny lithium surface. These practices comprise surface brushing, lithium calendering or rolling, microtoming, and combinations thereof. [51, 200, 216] While these preparation techniques help mitigate surface contamination, they can also substantially alter the lithium surface morphology and, thus, the active surface area. Since the measured impedance of a system scales with its surface area, this can severely affect the interpretation of results. Therefore, it is of utmost importance to understand the effect different lithium preparation techniques have on the NPL, active surface area, and, ultimately, the resulting cell impedance. Lithium was prepared in three different ways and compared in the following:

- **Pristine:** Lithium electrodes were punched directly from the lithium foil purchased from Alfa Aesar at a thickness of 750 µm.
- **Brushed:** Lithium was calendered to a thickness of 300 µm and subsequently brushed using a conventional soft-bristled toothbrush. The lithium was brushed firmly for 30 s in various directions to keep the surface homogeneous.

- **Brushed Calendered:** Lithium was brushed and incrementally calendered to a thickness of 300 µm using a tabletop roll press (*MSK-2150* Rolling Machine).

Figure 5.7a-c shows optical and light microscopy images of the different lithium electrodes. The brushed and brushed calendered electrodes are visually shiny, indicating the NPL was altered. Bristle strokes can be identified under the light microscope on the brushed electrode, while the calendered and pristine electrodes show a smoother and patina-like surface, respectively.

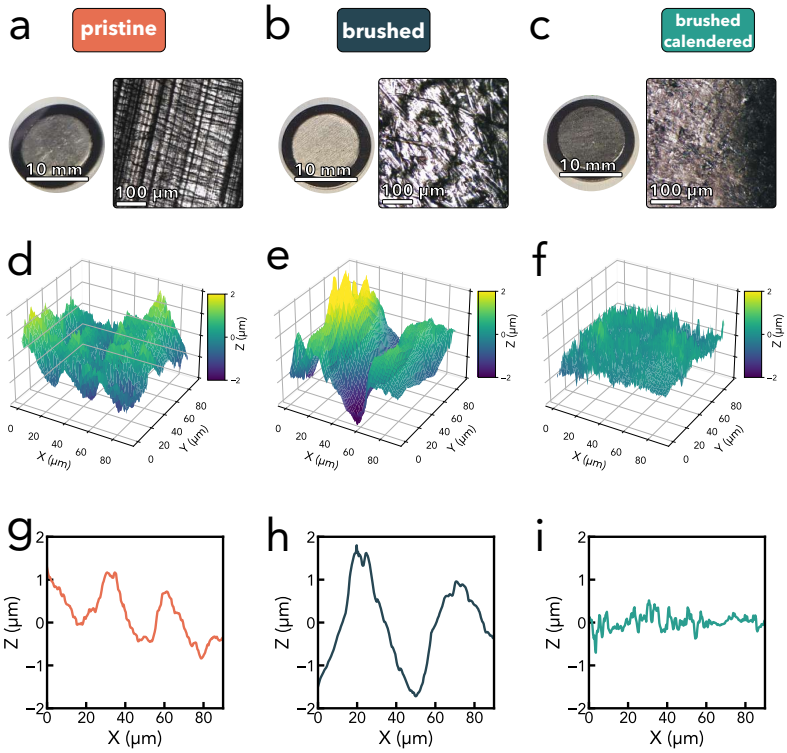


**Figure 5.7: Lithium Preparation Techniques a,** Optical and light microscopy images of a pristine lithium electrode **b,** optical and light microscopy images of a brushed lithium electrode **c,** optical and light microscopy images of a brushed calendered lithium electrode **d,** AFM height map of a pristine lithium electrode **e,** AFM height map of a brushed lithium electrode **f,** AFM height map of a brushed calendered lithium electrode **g,** 2D AFM height map of a pristine lithium electrode **h,** 2D AFM height map of a brushed lithium electrode **i,** 2D AFM height map of a brushed calendered lithium electrode. AFM data was collected by Saskia Krefting as part of her master's thesis. [64]

The electrodes were investigated using AFM to understand the lithium surface topography better. [64] More details on the experimental conditions can be found in

section 5.2.2. A 3D height map and a 2D cross-section of the surface are plotted in Figure 5.7d-i for the three electrodes, respectively. The electrodes display significant differences in feature density, waviness, and surface roughness. The feature density increases from brushed to pristine to brushed calendered while the amplitude of bespoke features is reduced in the same order. The same trend is observed for the waviness of the electrodes. This demonstrates that calendering the lithium surfaces enables flattening out surface features.

The key metrics relevant to this study are the surface roughness and the surface area. As discussed in more detail in the master thesis of Saskia Krefting [64], the surface roughness of all three electrodes displayed a scan-size dependency, rendering a meaningful interpretation challenging. Likewise, the surface area, which can be calculated by the sum of the length of each height profile curve multiplied by the width of the line-to-line separation, showed a measurement resolution dependency. This imposes practical challenges in determining surface areas. A higher resolution (more measurements for a given length scale) increases the measurement time, thus limiting the area that can be practically measured and simultaneously reducing the statistical significance of features. It further initiates a discussion on the scale length relevant to electrochemical measurements. It can be argued that surface wetting capabilities, which are dependent, amongst others, on surface tension and molecular interactions of the liquid, are key properties in determining a relevant length scale. [217, 218] An in-depth discussion on that topic is beyond the scope of this project. It must, therefore, be concluded that no active surface area can be reliably calculated from the collected AFM data. However, surface area differences are expected amongst the three electrode preparation techniques due to the significant differences observed in Figure 5.7.

Symmetric coin cells were prepared using three types of lithium described above in a 1 M LiFSI G4 electrolyte at 30 °C. Since the goal of this investigation is to quantify differences in the total interphase impedance as a result of lithium preparation techniques, the coin cell format was chosen over the custom-made cell design due to the ease of measuring a larger cell throughput. The total

interphase impedance can be calculated if the right equivalent circuit is used as described in section 5.3.1. Exemplary Nyquist plots of three symmetric cells are shown in Figure 5.8a.

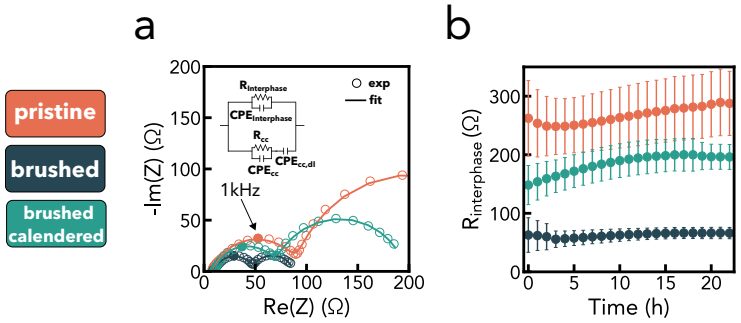


**Figure 5.8: EIS of symmetric coin cells using different lithium preparation techniques: a,** Three exemplary Nyquist plots measured in a 1 M LiFSI G4 electrolyte after ten hours of resting under OCV at 30 °C. The experimental data was fit using the circuit indicated in the inset and discussed in section 5.3.1. **b,** $R_SEI$ as a function of OCV resting time of at least six coin cells using different lithium preparation techniques in a 1 M LiFSI G4 electrolyte.

As expected, two separate semi-circles can be observed in all three coin cells. The magnitude of the cell impedance differs substantially depending on the way lithium was prepared. For quantification, the Nyquist plots were fit using an ECM appropriately for coin cells as discussed in section 5.3.1. The capacitors were substituted by a CPE, and the resistance is annotated with $R_{interphase}$ since multiple interphase contributions are expected to overlap in the given frequency range. For a quantitative comparison, the total interphase impedance is plotted as a function of resting time in Figure 5.8b.

The differences in impedance magnitudes are ascribed to differences in the NPL and the lithium's active surface area. The pristine lithium exhibits the highest interphase impedance of around 280 Ω as well as the largest cell-to-cell deviation indicated by the large error bar. This supports the heterogeneity of untreated, pristine lithium surfaces. The brushed lithium shows the lowest interphase impedance of around 80 Ω. The decrease can be ascribed to a significant increase in surface area, as indicated by the AFM surface maps (Figure 5.7) and a reduced impedance contribution from the NPL. The interphase impedance of brushed

calendered lithium falls in between at around 200 Ω. The surface area of the brushed calendered electrodes is expected to be smaller than the brushed ones due to the flattening of intensity features by calendering, thus resulting in an apparent larger interphase impedance.

Since an accurate active surface area could not be determined, impedances could not be surface area corrected, and contributions from the NPL could not be isolated. However, the impedance data shown in Figure 5.8 convincingly demonstrates that the way lithium is prepared severely changes the measured cell impedance. This highlights the importance of preparing lithium rigorously in the same way if impedances are compared amongst different batches of cells. In all of the following experiments, lithium is prepared using the brushed calendered method due to its high reproducibility. It is noteworthy that the electrodes in the custom-made cell design are smaller ($A_{Li} = 0.503\,\mathrm{cm}^2$) than in coin cells ($A_{Li} = 1.13\,\mathrm{cm}^2$ thus surface heterogeneity induced by bristle strokes (as clearly visible in Figure 5.3.2) is expected to yield less reproducible results in the customer made cell design.

### 5.3.3 Equivalent Circuit Model

In section 5.1.2, a historical overview of lithium SEI fitting was provided. In light of the described work, the following considerations for a suitable ECM are made.

- Capacitors should be used over CPEs as the goal of this study is to identify the physical origin of impedance contributions and CPEs do not have a physical origin. [53]

- To include the ohmic drop due to electronic resistance in the wires and the ionic conductivity of the electrolyte, a resistor $R_0$ is included in series to all other circuit elements

- $R||C$ elements are suitable to describe lithium migration through an interphase layer, both via the bulk and grain boundaries, and a charge transfer resistance coupled with an electrical double layer.

- The lithium surface is expected to be covered by at least two layers: a NPL, which is present on all lithium, and a SEI, which forms once the lithium has been brought in contact with the electrolyte. Following the argumentation by Peled [41] discussed in section 5.1.2, this should give rise to at least five Voigt elements, $R_{ct}||C_{dl}$, $R_{NPL}||C_{NPL}$, $R_{NPL,SEI}||C_{NPL,SEI}$, $R_{SEI}||C_{SEI}$, and $R_{SEI,electrolyte}||C_{SEI,electrolyte}$

- In reality, the SEI most likely has a heterogeneous microstructure and composition which should be, according to Aurbach *et al.* [42], modeled by multiple, stacked layers which would result in additional $R||C$ elements

- If any of those resistances are significantly smaller than other resistances in the circuit, or any of those capacitances are significantly larger than other capacitances in the circuit, their impedance contribution will be negligible, which leads effectively to a reduction of $R||C$ elements

- Due to the risk of overfitting, the amount of $R||C$ elements should be kept as low as possible

- A finite space Warburg diffusion element, *i.e.* a transmissive boundary, is most suitable to describe transport through the electrolyte and porous parts of the SEI

Taking this into account, an equivalent circuit similar to Aurbach *et al.* is proposed for the subsequent study (see Figure 5.10a). The key question is how many $R||C$ elements are required to adequately model the measured impedance without overfitting the data.

Due to the heterogeneous nature of the SEI, it is not possible to argue from a strictly physical point of view. Therefore, a mathematical approach to detect overfitting is considered. Schoenleber *et al.* developed a tool to detect the optimum amount of $R||C$ elements to fit electrochemical data to prevent under and overfitting in linear Kramers-Kronig validity tests (more details on Kramer-Kronig in section 2.1.1). [219] Their proposed algorithm is based on the observation that parameters

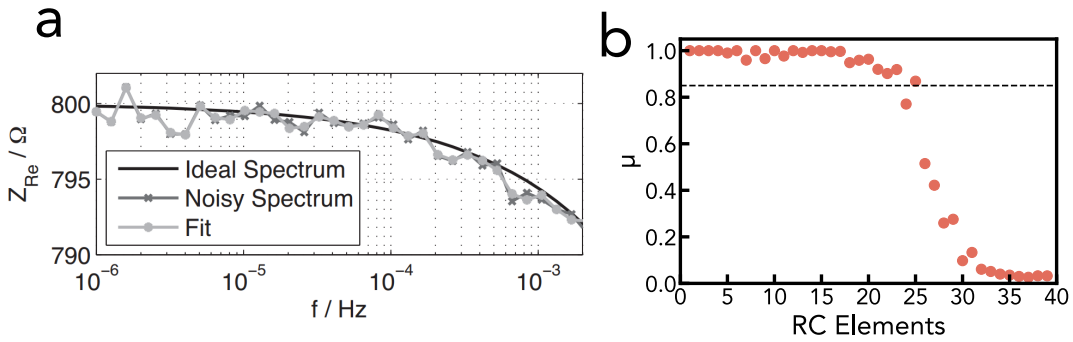


**Figure 5.9: Overfitting Detection: a,** shows the real part of an artificially constructed, ideal impedance spectrum over its frequencies (Ideal Spectrum). The ideal spectrum was modified by introducing measurement noise (Noisy Spectrum). The noisy spectrum was overfit using too many $R||C$ elements. The fit follows the trend of the noisy spectrum, i.e., it oscillates and, therefore, indicates degeneration. Reprinted from Schoenleber *et al.*[219] **b,** Calculation of the degeneration value $\mu$ as a function of $R||C$ elements used to fit the data of a custom-made lithium-lithium cell with a 1 M LiFSI G4 at 30 °C.

of the equivalent circuit start to degenerate if too many $R||C$ are used in the fitting. While Kramers-Kronig is conventionally used to detect invalidity in EIS measurements, the method proposed by Schoenleben *et al.* generally detects fitting degeneration. This is achieved by identifying that the noise part and the information part of an impedance spectrum can be distinguished by the fact that neither the real part nor the imaginary part of an ideal spectrum shows oscillatory behavior when plotted as a function of frequency. [219] Consequently, all oscillations contained in a measured impedance spectrum are caused by noise or measurement errors. If the fit of an impedance spectrum oscillates, it can be concluded that measurement noise or other errors have been fit, which is a sign of overfitting. This is exemplarily shown for an overfit spectrum in Figure 5.9a. Oscillations can be mathematically captured by a degeneration parameter $\mu$, which decreases from unity if negative resistance values are obtained from a fit, which occurs if the fit shows oscillating behavior. Setting an empirical threshold of $\mu = 0.85$ allows to determine the optimum amount of $R||C$ components for a given set of impedance data.

$$\mu = 1 - \frac{\sum_{R_k<0} |R_k|}{\sum_{R_k\geq 0} |R_k|} \tag{5.1}$$

The algorithm was applied to one of the impedance spectra collected in the custom-made cells using a 1 M LiFSI G4 at 30 °C. The degeneration parameter $\mu$ is calculated and plotted as a function of $R||C$ elements in Figure 5.9b. An optimum amount of 24 $R||C$ elements is determined. This by no means indicates that there are 24 independent physical processes but instead gives an upper threshold of how many $R||C$ could be fit to the experimental data collected in this study without fitting measurement noise. However, it was refrained from using 24 $R||C$ elements for the fitting since the identification of 24 separate physical processes is unfeasible within the scope of this project. Besides, as mentioned above, a Warburg diffusion element must be included in the ECM to describe the diffusive behavior of the symmetric lithium cells. The low-frequency impedance part is expected to be dominated by diffusion processes, and thus, the last $R||C$ pair should incorporate a finite-length Warburg diffusion component. When cutting off the low-frequency tail of the experimental data (all impedances below 1 Hz which is approximately the region where diffusion processes are expected to dominate), the Schoenleber algorithm yields an optimum amount of 20 Voigt elements which is still too intricate to analyze. However, 20 $R||C$ elements can serve as an upper limit for a suitable equivalent circuit.

Another approach was taken to reduce the amount of $R||C$ elements. All impedance spectra collected in this study (over 12000 spectra) were fit to circuits with a varying amount $R||C$ elements as depicted in Figure 5.10a. Noteworthy, all $R||C$ elements are ordered in sinking time constants *e.g.* $R_1||C_1$ corresponds to the fastest processes and $R_5||C_5$ to the slowest. An example '5 RC' fit and the corresponding ECM is shown in Figure 5.10b The root square mean error (rmse) of the fit and the experimental data were calculated and plotted for all measurements in Figure 5.10c ordered according to the measurement temperature. The mean rmse and the corresponding standard deviation of all spectra are plotted in Figure 5.10d. It can be seen that the fitting quality improves, *i.e.* the rmse reduces, with an increasing amount of $R||C$ components. This is particularly evident at lower temperatures. This indicates that the time constants of individual

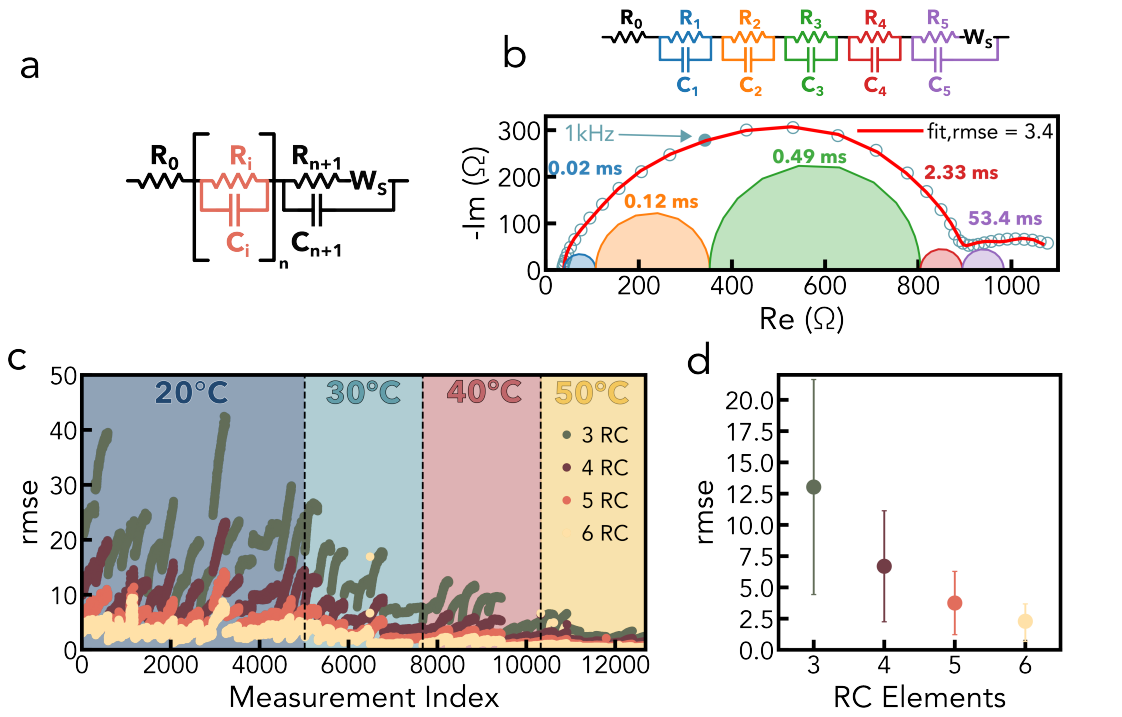


**Figure 5.10: Equvialent Circuit Determination: a,** General equivalent circuit with varying amount of $R||C$ components. **b,** Exemplary Nyquist plot of a cell cycled at measured at 30 °C and fit using five $R||C$ components. The impedance contributions from individual semi-circles are plotted below the experimental data. **c,** Root-square-mean-error of fit and experimental data for equivalent circuits with varying amount of $R||C$ components for all cells measured in this study. The rmse are ordered according to the measurement temperature. **d,** Mean rmse with standard deviation as an error bar.

lithium migration processes ($\tau = R \cdot C$) converge at elevated temperatures, making deconvolution more difficult yet enabling accurate fitting with fewer circuit elements. The most substantial fitting accuracy improvement is achieved up to five $R||C$ components, while adding a sixth one yields only a marginal rmse decrease. Upon visual inspection of the fit using five $R||C$ elements (see Figure5.10b), it is evident that all important features of the Nyquist plot can be captured. It was therefore concluded that the equivalent circuit with five $R||C$ elements is most suitable to model the impedance data collected in this study. The circuit provides enough degrees of freedom to adequately fit the data at different experimental conditions while keeping complexity as low as possible and preventing overfitting.

### 5.3.4 Temperature and Concentration Effects

In order to deconvolute the different contributions of the impedance spectra, identical cells were assembled and tested at different temperatures and concentrations. An overview of all those cells is given in Figure 5.11, where the individual resistances are plotted as a function of resting time.

The data contains a plethora of information, and the key observations will be described and further discussed. The focus is on the high—to mid-frequency region since interphase impedances are expected to dominate there.

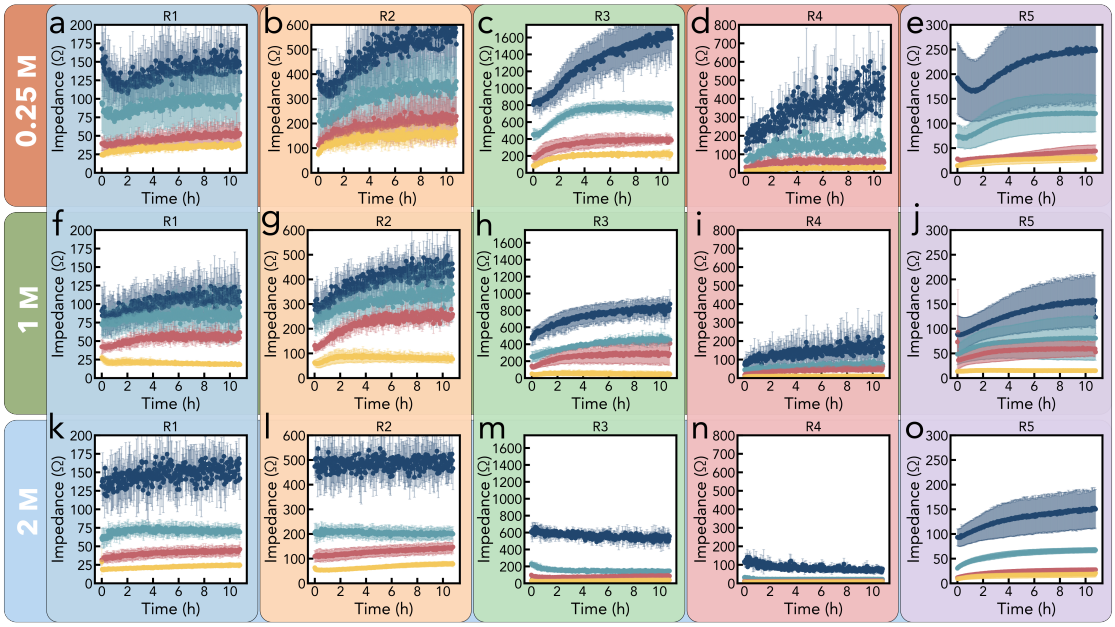


**Figure 5.11: Overview of temperature and concentration effects on the cell interphase impedance: a-e,** $R_1$ to $R_5$ for a 0.25 M LiFSI G4 electrolyte. **f-j,** for a 1 M LiFSI G4 electrolyte and **k-o,** for a 2 M LiFSI G4 electrolyte. The colors correspond to different operating temperatures where dark blue is 20 °C, turquoise is 30 °C, red 40 °C and, orange 50 °C.

- In all cells $R_1 < R_2 < R_3 > R_4 > R_5$
- With increasing temperature, all resistances decrease, indicating the lithium migration processes are accelerated.
- Resistances grow over time or remain constant. The growth rate is strongly dependent on the LiFSI concentration and varies for different resistances.

To facilitate a comparison, $R_1$ to $R_4$ of cells measured at 20 °C are plotted as a function of resting time in Figure 5.12

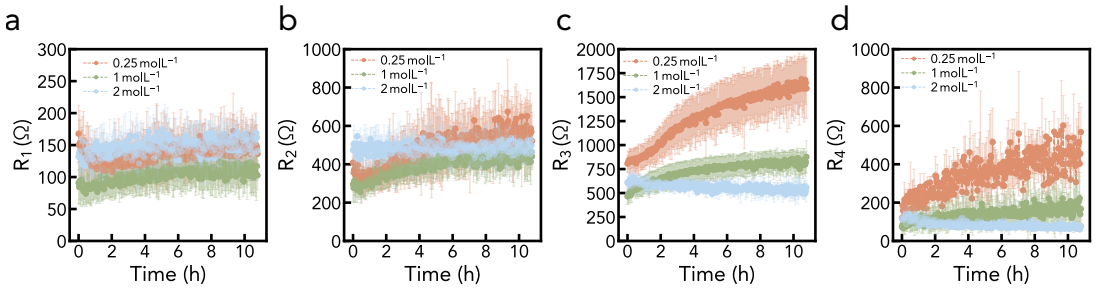


**Figure 5.12: Comparison of resistances for different concentrations at** 20 °C**: a,** $R_1$**, b,** $R_2$**, c,** $R_3$**, d,** $R_4$

The initial $R_i$ values (at time = 0 h) are all of a similar order of magnitude, and differences amongst the three concentrations are most visible the longer the cell has been exposed to the electrolyte, *i.e.* different $R_i$ growth rates can be observed for different concentrations. Figure 5.12a shows that $R_1$ is stable for the entire measurement duration for all three concentrations. In addition, within the uncertainty of the measurement, the magnitude of $R_1$ is independent of salt concentration (around 130 Ω). This is similar for $R_2$; however, a slow impedance increase can be observed for the 0.25 M and 1 M LiFSI electrolytes. A very different growth behavior is observed for $R_3$ and $R_4$. While at a 2 M LiFSI concentration, the resistances are stable, they rapidly grow at lower concentrations, particularly at 0.25 M. The concentration dependency of individual impedance growth can be used to guide the deconvolution of impedance contributions. Since $R_1$ is independent of salt concentration and stable in the electrolyte, it can be speculated that the $R_1||C_1$ component is related to the NPL. For more insights into the NPL, XPS depth profiling of pristine lithium electrodes (no exposure to the electrolyte) was conducted and plotted in Figure 5.13. XPS analysis reveals that the NPL at the surface comprises mostly lithium-carbonate and hydroxide. After around 10 min of argon sputter, lithium oxide is detected, and the overall composition remains roughly constant up to 60 min of sputtering time. Thus, it can be argued that after 10 min of sputtering, all the NPL is removed. A sputter rate of 3 nm $\text{min}^{-1}$ was

determined using a deposited $Li_2O$ sample with a known thickness. Consequently, the thickness of the NPL is estimated to be in the tens of nanometer range. Since the NPL comprises other elements than $Li_2O$, too, a more precise thickness cannot be determined at this point. The composition and thickness estimate align with literature values. [38, 52, 197]

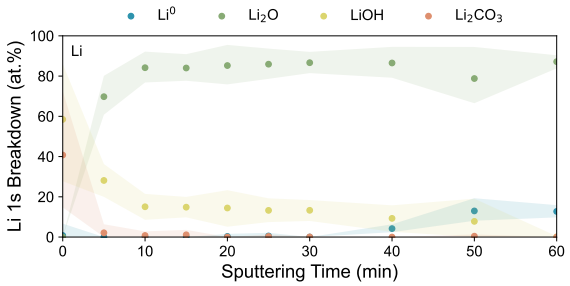


**Figure 5.13: XPS depth profiling of pristine lithium electrodes:** Lithium electrodes were prepared in the same way as for the impedance measurements as described in section 5.3.2. XPS depth profiling was conducted by argon sputtering. A sputter rate of 3 nm $min^{-1}$ had been determined by a sputtered $Li_2O$ calibration standard of known thickness. The XPS data was collected and analyzed by Ben Jagger.

If $R_1||C_1$ originates from a transport barrier through the NPL, the capacitances of $C_1$ should be stable and independent of electrolyte concentrations. Furthermore, it is reported that the dielectric constant of $Li_2O$ (11±1) does not change with temperature in between 20 °C to 400 °C. [220] As a result, the capacitance, which is dependent on layer thickness, surface area, and dielectric constant, should also be independent of the temperature. Figure 5.14 shows the $C_1$ capacitances for different temperatures and concentrations.

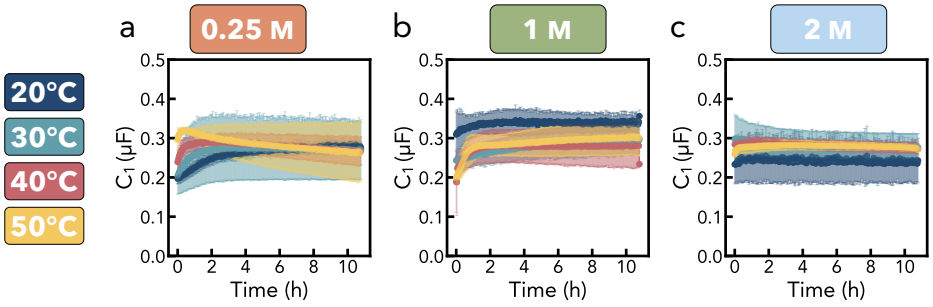


**Figure 5.14: $C_1$ capacitance for different concentrations and temperatures: a,** $C_1$ of a cell using a 0.25 M LiFSI G4 electrolyte, **b,** $C_1$ of a cell using a 1 M LiFSI G4 electrolyte, **c,** $C_1$ of a cell using a 2 M LiFSI G4 electrolyte

All twelve capacitances are constant, independent of concentration and temperature, and roughly at the order of 0.25 µF. Using the dielectric constant of $Li_2O$ and the geometrical surface area of the lithium electrode, a NPL thickness of 21 nm is calculated, closely aligning with the thickness estimate from XPS depth profiling. This further corroborates the hypothesis that $R_1||C_1$ originates from a transport process through the NPL. To the best of our knowledge, there is no scientific consensus if lithium migrates through the SEI to be reduced at the electrode-NPL interphase or if electrons transport through the NPL and lithium is reduced at the NPL-electrolyte interphase. Nevertheless, both mechanisms would give rise to a film capacitance.

In contrast to $R_1$, $R_3$ and $R_4$ show a concentration dependency on resistance growth. Consider a generalized, single-electron reaction:

$$Electrolyte + Lithium \longrightarrow SEI \tag{5.2}$$

The corresponding rate law is then defined as

$$v_{SEI} = k_{SEI}[Electrolyte]^a[Lithium]^b \tag{5.3}$$

The reaction rate $v_{SEI}$ is therefore dependent on the reaction constant $k_{SEI}$ and the electrolyte and lithium concentrations. Although equation 5.2 is oversimplified and the true SEI formation reaction is significantly more complex [196], it is clear that the SEI formation rate is dependent on the local electrolyte concentration. As an ether, G4 exhibits a high cathodic stability [154], and thus it can be assumed that electrolyte decomposition is predominantly driven by the reduction of the $[FSI]^-$. The concentration dependence of $R_3$ and $R_4$ is strong evidence that $R_3||C_3$ and $R_4||C_4$ are related to the SEI.

The collected EIS data can be used to discuss possible interpretations of the reaction kinetics in the SEI formation process. If one assumes that the observed resistance is directly proportional to the layer thickness, as has been done elsewhere [221], it can be speculated that at low concentration, the local LiFSI concentration at the lithium interphase depletes and the impedance growth

is limited by diffusion of the salt to the interphase. Diffusion might be either through the bulk electrolyte or a porous SEI structure. A diffusion limitation for SEI growth has been reported before. [221] At higher concentrations, enough LiFSI is present close to the interphase, and thus, the formed SEI can immediately passivate the metal surface, and consequently, a stable resistance is observed for the 2 M LiFSI G4 cells. There is evidence that the passivation of bare lithium in organic electrolytes occurs in less than one second. [222, 223] The time duration between cell assembly, *i.e.* when lithium was brought in contact with the electrolyte, and the first impedance measurement was around 5 min to 15 min. Therefore, it must be assumed that the lithium surface has already been passivated when the first impedance measurement is conducted, which could explain why no impedance growth is observed in 2 M LiFSI G4 electrolytes.

The resistance growth rates need to be scrutinized to test the hypothesis of diffusion-limited SEI formation at low concentrations. Equations derived from Fick's law of diffusion postulate a square root time dependence for the layer thickness and, thus, the resistance growth. To see if such square root growth can be detected in the data, $R_{3,normalized}$ for the 0.25 M and 1 M LiFSI G4 cells are plotted as a function of the square root of cell resting time in Figure 5.15a and Figure 5.15b respectively.

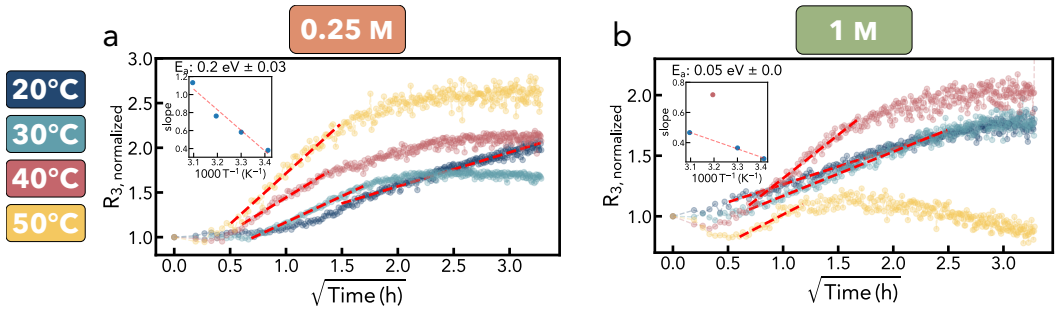


**Figure 5.15: Square Root Time Dependency of $R_{3,norm}$: a,** shows the normalized $R_3$ values for cells in a 0.25 M LiFSI G4 electrolyte and **b,** in a 1 M LiFSI G4 electrolyte. The resistances were normalized to the first resistance measured at $t = 0h$ to improve comparability. Just like in the other plots, the mean of at least three cells is reported however the standard deviation is not plotted to improve the readability of the plot. The 50 °C measurements were disregarded for the linear fit as they seem not to follow Arrhenius's behavior.

Both concentrations displayed in Figure 5.15 show a growth behavior that can be linearly fit when divided into sections. In the first 15 min ($\sqrt{Time} = 0.5h^{0.5}$) the resistances do not grow. This is attributed to the system reaching thermal equilibrium so temperature changes and resistance growths are expected to overlap. Subsequently, in both concentrations and for all temperatures, a square root resistance growth can be detected via the linear growth behavior observed in Figure 5.15. However, with the exception of the cells measured at 20 °C and 0.25 M LiFSI G4, all interphases passivate as the growth behavior starts to plateau after around 2.5 h to 4 h. If the data is sliced into sections after thermal equilibrium has been reached and before the interphase passivation, a good linear fit can be obtained, as indicated by a red-dotted line in Figure 5.15. Plotting the slope of the linear region as a function of inverse temperature (see Figure 5.15 insets) shows a good Arrhenius behavior at a concentration of 0.25 M with an activation energy of 0.2 eV. For comparison, the activation energy of the (bulk) apparent diffusion coefficient of LiFSI in a 1 M LiFSI G4 electrolyte is 0.23 eV (see section 4.3.2). In contrast, at a 1 M LiFSI concentration, the slopes deviate from an Arhenius behavior, and a reasonable fit can only be obtained if the cells at 30 °C are neglected which would yield an activation energy of 0.05 eV. No fits were conducted at a 2 M LiFSI concentration since the resistance is stable over measurement duration as shown in Figure 5.11 Hence, it could be argued that SEI growth, represented by $R_3$, is indeed diffusion-limited at a low salt concentration.

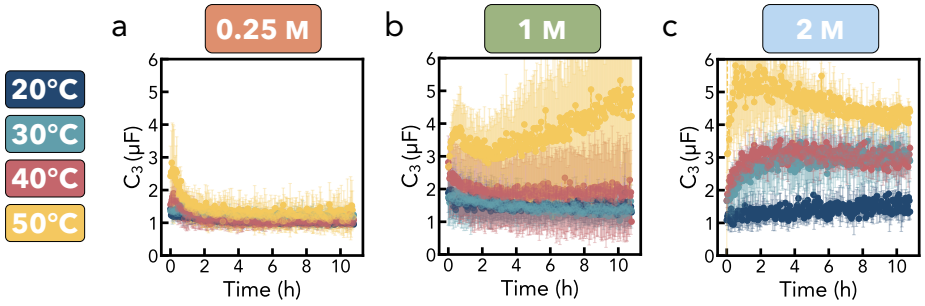


**Figure 5.16: Temperature Dependency of $C_3$: a,** shows the temperature dependency of $C_3$ for cells in a 0.25 M LiFSI G4 electrolyte, **b,** in a 1 M LiFSI G4 electrolyte, and **c,** in a 2 M LiFSI G4 electrolyte

Figure 5.16 shows the time-resolved $C_3$ capacitances for different concentrations and temperatures. Without knowledge of the SEI thickness, a porosity estimate of the SEI layer described by the $R_3||C_3$ circuit component from the corresponding capacitances is not possible. However, the $C_3$ values are at the order of magnitude of 2 µF, which could be used to claim a dense SEI structure when using general SEI thickness estimates from the literature of around 10 nm. [33, 34] As seen in Figure 5.16a, a slight capacity decrease over time can be observed for the 0.25 M LiFSI G4 cells. This corroborates the observation that $R_3$ values grow over time as described in Figure 5.15a.

One interesting observation is the temperature dependency of the capacitances shown in Figure 5.16 While at a 0.25 M LiFSI concentration, the capacitance is independent of the measurement temperature, the 1 M and 2 M LiFSI cells show a substantial capacity increase with temperature. The dielectric constant of the SEI layer is expected to be constant in the investigated temperature range. [220] Thus, a capacity increase with temperature indicates either a larger surface area or a thinner SEI layer. A larger surface area would generally indicate a more porous SEI structure which contradicts the previous observation of an immediate passivation of the interphase at 2 M LiFSI concentrations. Therefore, it could be speculated that the SEI layer thickness decreases with temperature. Since, as elaborated before, the SEI formation at 1 M and 2 M LiFSI is not limited by salt diffusion to the interphase, it is the reaction rate constant $k_{SEI}$ (see equation 5.3) that determines the formation rate. $k_{SEI}$ is expected to increase with temperature, and thus, it could be argued that faster passivation results in thinner SEI layers. However, additional experiments, visualization, and characterization of the SEI are required to confirm such speculation.

Analysis of the $R_4||C_4$ components is mostly analogous to $R_3||C_3$. However, the capacitances are of the order of magnitude of 1 mF, indicating a significantly higher porosity for the interphase layer.

Another way to quantify and compare the temperature dependency of different $R_i$ is to calculate the Arrhenius activation energies of their respective temperature

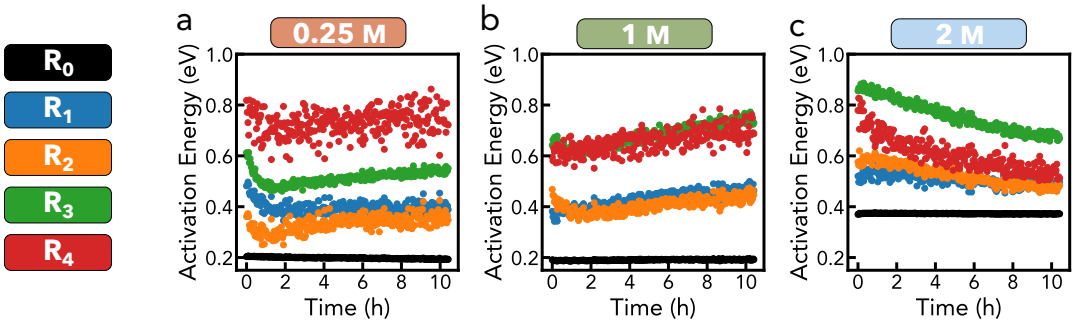


**Figure 5.17: Activation Energies of $R_0$ to $R_4$ at different concentrations: a** in cells using a 0.25 M LiFSi G4 electrolyte **b,** in cells using a 1 M LiFSi G4 electrolyte and **c,** cells using a 2 M LiFSi G4 electrolyte

dependencies. Figure 5.17 shows the activation energies for $R_0$ to $R_4$ for all three concentrations. It is noteworthy that error bars for the calculated activation energies are not plotted to facilitate a visual comparison.

Interestingly, the time dependency of the activation energies is changing with concentration. At 0.25 M LiFSI G4, all activation energies are approximately stable for 10 h, at 1 M LiFSI G4, a slight increase over time is observed, and at 2 M LiFSI G4 a slight decrease can be observed. The differences in growth behavior cannot be explained at this point. Lim *et al.* discussed activation energies measured in an interphase impedance study on alkali metal electrodes. The authors proposed that activation energies can be used to fingerprint the nature of ion transport. If the activation energy is above 0.8 eV, transport is predominantly through a solid, while activation energies below 0.2 eV indicate transport through a liquid phase. Activation energies in between present mixed transport through a porous SEI with electrolyte-filled channels. [224] An increase in activation energies was attributed to SEI densification, where more transport is conducted through the solid phase than the liquid phase over time. This analysis of activation energies is not directly applicable to the presented data set. In their study, Lim *et al.* fit all their impedance data (collected in a coin cell configuration, see section 5.5 for a discussion on the required circuit to analyze such impedance data) with a single $R||CPE$ component. Consequently, the authors analyze the total interphase resistance and are rightfully expecting mixed transport (liquid and solid) phenomena

in their impedance. However, the approach in this study is to deconvolute and isolate transport processes by the advanced fitting circuit discussed in section 5.3.3, rendering an interpretation like Lim *et al.* incompatible. [224]

Both 0.25 M and 1 M LiFSI G4 electrolyte show an activation energy of around 0.2 eV for $R_0$. This is in good agreement with measurements conducted in the ORGA setup (see section 4.3.2) Interestingly, the 2 M LiFSI G4 electrolyte shows an activation energy for $R_0$ almost double as high, indicating a change in the bulk ionic conduction mechanism. This aligns with an ORGA study reporting the transport properties of LiFSI G4 at different concentrations. [147] The activation energies of $R_1$ and $R_2$ appear to correlate strongly at all three concentrations. Once thermal equilibrium has been reached, the activation energies are around 0.45 eV for both processes in all three concentrations. Since similar activation energies are observed in all three concentrations, the hypothesis that $R_1||C_1$ is related to lithium migration through the NPL is corroborated. The strong correlation of the activation energy of $R_2$ to the activation energy of $R_1$ indicates that the $R_2||C_2$ interphase layer migration process is related to the NPL as well. The activation energies related to $R_3$ and $R_4$ are larger (around 0.7 eV) in all three concentrations than the one for $R_1$ and $R_2$. In particular, at 1 M LiFSI G4 electrolytes, a strong correlation can be observed for the $R_3$ and $R_4$ activation energies indicating both processes are related. For $R_3$ in 2 M LiFSI G4 cells, the highest activation energies are measured. This aligns with a previous observation where interlayer thinning was proposed for increasing temperatures in cells measured at a 2 M concentration (Figure 5.16c). Thinner interlayers at elevated temperatures would facilitate lithium migration, resulting in a more significant impedance reduction reflected in a larger activation energy.

### 5.3.5 Lithium Activity

To validate some of the observations made in section 5.3.4, a set of experiments was conducted using a lithium-magnesium alloy. A lithium-magnesium alloy with 5 at.% ($Li_{0.95}Mg_{0.05}$) has essentially the same reduction potential as a bare Li-metal electrode. However, it has a slightly different surface chemistry and reduced lithium

activity. [225] The low reduction potential of anodes is the main driving force for SEI formation and the magnitude of the potential difference between metal and electrolyte is believed to be the main determining factor for SEI composition. [42, 225] Accordingly, the SEI formed on a $Li_{0.95}Mg_{0.05}$ anode in an argyrodite electrolyte is reported to be identical to the one on bare lithium. [225] In contrast, the chemistry of the NPL is different in that a layer of MgO is covering the surface of ($Li_{0.95}Mg_{0.05}$). [225] Aspinall *et al.* systematically studied the NPL composition using XPS depth profiling. The authors found that with an increasing Mg content, the MgO content of the NPL increases while the lithium composition of the NPL remains unchanged. [225] Therefore, LiMg alloys exhibit unique properties that can be used to deconvolute interphase impedance contributions. Adding magnesium to the electrode is expected to affect the NPL migration resistance, while the SEI migration resistance should remain similar to that of bare lithium.

To investigate the effect of alloying lithium, $Li_{0.95}Mg_{0.05}$ electrodes were used in a 1 M LiFSI G4 at 20 °C. The same experimental procedure as described in section 5.3.2 was used, and the data was processed and fit as described in 5.3.3. An exemplary Nyquist plot after 5 h of electrolyte exposure is plotted in Figure 5.18a. The deconvoluted $R_1$ to $R_4$ and corresponding $C_1$ to $C_4$ values are plotted as a function of cell resting time in Figure 5.18b to i.

The overall interphase impedance is slightly smaller in $Li_{0.95}Mg_{0.05}$ cells compared to bare lithium. Magnification shown in Figure 5.18a inset indicates that the most significant differences in the shape of the Nyquist plot can be found in the high-frequency region. Indeed, when comparing the $R_1$ and $R_2$ resistances of the alloy (Figure 5.17b and c) with the one measured in lithium, they show a very similar time dependence but a smaller resistance. In contrast, $R_3$ (Figure 5.17d) is identical for both electrodes and $R_4$ (Figure 5.17e) is even slightly larger in the alloy. This corroborates our previous hypothesis that $R_1$, and possibly $R_2$, are related to transport through the NPL, whereas $R_3$ is related to transport through the SEI. It is a non-intuitive observation that the NPL resistance is smaller in the $Li_{0.95}Mg_{0.05}$ compared to lithium since the lithium activity is reduced. It can be speculated

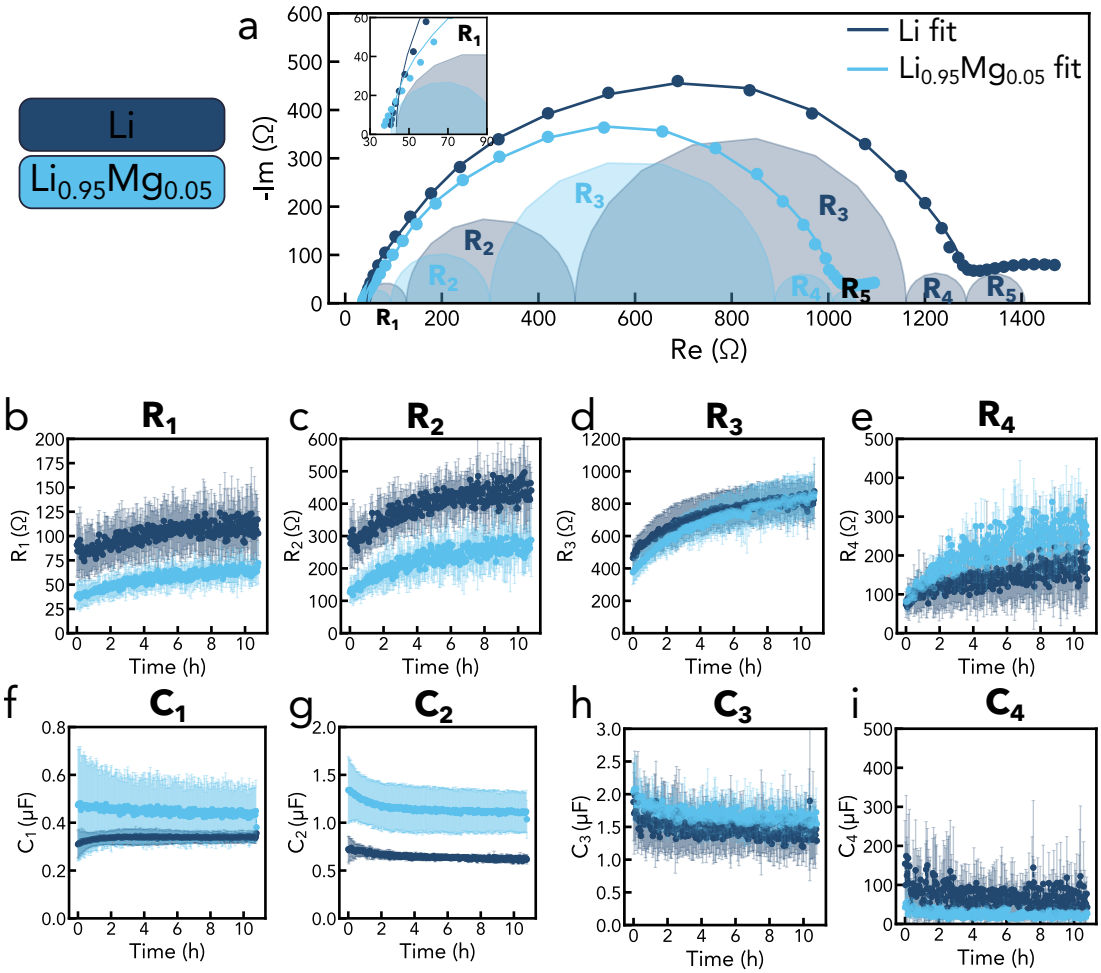


**Figure 5.18: $Li_{0.95}Mg_{0.05}$ vs Lithium Comparison: a,** show a Nyquist plots of two cells using a 1 M LiFSI G4 electrolyte at 20 °C. One cell comprises two lithium electrodes (dark blue), and the other one two $Li_{0.95}Mg_{0.05}$ electrodes (light blue). **b,** mean time-resolved $R_1$ values, **c,** mean time-resolved $R_2$ values, **d,** mean time-resolved $R_3$ values and **e,** mean time-resolved $R_4$ values, **f,** mean time-resolved $C_1$ values, **g,** mean time-resolved $C_2$ values, **h,** mean time-resolved $C_3$ values and **i,** mean time-resolved $C_4$ values. The average of at least three identical cells is plotted and the error corresponds to the standard deviation.

that lithium transport along $Li_2O$ and MgO interfaces is faster than through the bulk. Unfortunately, no direct comparison of the electrical conductivity of the main components found in the respective NPL, $Li_2O$ and MgO, could be found in the literature. There are studies covering the high-temperature conductivity behavior of MgO, and it appears to be strongly dependent on defect structures and lithium doping. [226] Further, the main conduction mechanism of MgO at room temperature appears to be primarily electronic. [227] This supports the argument that the

conduction mechanism through the NPL is predominantly electronic instead of ionic.

A comparison of the corresponding capacitances shows that $C_1$ (Figure 5.17f) and $C_2$ (Figure 5.17g) are larger in the alloy. This further corroborates that the NPLs are different on the alloy and the lithium. In contrast, $C_3$ and $C_4$ are very similar within the measurement uncertainty.

In summary, we conclude that adding small amounts of magnesium into the lithium electrode results in a slight decrease of the low frequency resistance, which is at least in parts ascribed to migration resistance through the NPL ($R_1$). In contrast the SEI resistance, described by $R_3$ and $R_4$ remains unchanged.

## 5.4 Summary

A systematic impedance study on Li-metal anodes in a LiFSI G4 electrolyte revealed several key findings relevant to the design of future EIS experiments. Further, evidence is provided that suggests interphase impedance contribution from the NPL can be found in the high-frequency region, whereas SEI contribution can be found in the mid-frequency region.

Initially, it is demonstrated how the cell design significantly affects the shape of Nyquist plots. In particular, a second semicircle can be observed when the current collector is in contact with the electrolyte. It was demonstrated that the two semi-circles merge if lithium covers the entire current collector. This is an important finding for future experiment design since the two-semi circles are often wrongly ascribed to a split between $R_{SEI}$ and $R_{CT}$ in literature. In accordance with a recent publication, it is argued that the origin of the second semi-circle is a parallel interphase impedance on the surface of the current collector. [215] The total lithium interphase impedance can still be calculated when using an adequate ECM to fit the data.

Subsequently, a comparative study on different lithium preparation techniques reveals how differences in surface topology severely affect the magnitude of measured impedance due to differences in surface area and resistances due to the NPL.

Therefore, lithium must be prepared identically to ensure reproducibility and meaningful interpretation of impedances across multiple batches of cells.

Based on a literature search of previous ECMs, our latest understanding of the SEI nanostructure, and by ensuring experimental data can be sufficiently modeled while ensuring the absence of overfitting, an ECM using five $R||C$ is suggested and used throughout a systematic impedance investigation. During the investigation, the salt concentration, temperature, and lithium activity are systematically changed, and the effect on cell impedance under open circuit conditions is monitored. The results indicate that $R_1||C_1$ (around $\tau = 0.01\,\mathrm{m\,sec}$ to $0.1\,\mathrm{m\,sec}$) and $R_2||C_2$ (around $\tau = 5\,\mathrm{m\,sec}$ to $10\,\mathrm{m\,sec}$) are related to a transport process through the NPL while $R_3||C_3$ (around $\tau = 10\,\mathrm{m\,sec}$ to $100\,\mathrm{m\,sec}$) and $R_4||C_4$ (around $\tau = 1\,\mathrm{m\,sec}$ to $5\,\mathrm{m\,sec}$) are contributions from the SEI. A more detailed physical description is not possible without additional experimental evidence.

## 5.5 Outlook

### 5.5.1 Advanced Data Analysis

One key achievement of the project is the collection of high-quality impedance data, isolating the interphase impedance by removing geometrical effects and separator contributions and providing a statistically relevant number of data points for different measurement conditions. There are significantly more ways to process and interpret the generated impedance data, which could provide additional evidence of the physical origins of impedance contributions. For example, the distribution of relaxation time (DRT) transforms the impedance data from the frequency domain into the time domain without the need for a physical model to fit the data. [228] Artifact-free impedance data is of utmost importance when analyzing with DRT as it would otherwise indicate the presence of an additional interphase process.

Another analysis technique for impedance data, that does not require knowledge of a physical model, is based on Padé approximants. [229, 230] Therein, impedance data can be modeled by rational functions to find Padé coefficients that describe the experimental data over the whole frequency range. Similar to electrical components

in an ECM, the Padé coefficients, or linear combinations thereof, might be ascribed to physical processes related to the interphase impedance. [231] Similar to DRT, artifact-free and reproducible data sets are integral for a meaningful Padé analysis. A comprehensive Padé analysis contains a mathematical determination of the optimum amount of Padé coefficients to adequately model a system without overfitting it. Such an analysis could be used to validate or update the ECM used in this analysis.

In total more than 12,000 EIS spectra were collected throughout this study. The amount of available spectra suggests the use of statistical analysis tools. Restructuring fitted impedance data into features (components of the ECM) and targets (temperature and concentration; not activity since not enough data was collected for a meaningful analysis) allows the usage of a machine-learning algorithm based on decision tree learning. The goal is to create a model that can predict the concentration or temperature of a given impedance spectrum solely based on the input of the respective ECM components. By identifying the importance of a feature, *i.e.* an ECM component, to accurately predict the target under varying conditions, one might learn something about the physical origin of the features.

A preliminary analysis was conducted using a random forest classifier and $R_1$ to $R_4$ as prediction features. The decision to use classification over regression was based on findings by prior research indicating that the local lithium solvation environment - crucial for influencing interphase formation processes and, consequently, the impedance response - undergoes significant changes at concentrations close to 2 M LiFSI. [147] Such abrupt changes align better with the discrete nature of classification rather than the gradual transitions implied by regression.

The data was divided into subsets of concentrations (0.25 M, 1 M, 2 M) when predicting the temperature and subsets of temperature (20 °C, 30 °C, 40 °C, 50 °C) when predicting the concentration. The model showed excellent accuracy in predicting the targets as seen by the low rmse listed in the Figure 5.19 caption. More details on the model can be found in section 5.2.7. The permutation feature importance quantifies the importance or contribution of a feature to the model's statistical performance in predicting targets. It provides a more realistic view of

feature importance compared to, for example, the mean decrease in impurity (MDI) when features are correlated. [232] The permutation feature importance involves shuffling the values of a single feature and monitoring the resulting degradation of the model's score. [232] The permutation feature importance is plotted as a function of concentration and temperature when predicting the temperature and concentration in Figure 5.19a and b, respectively.

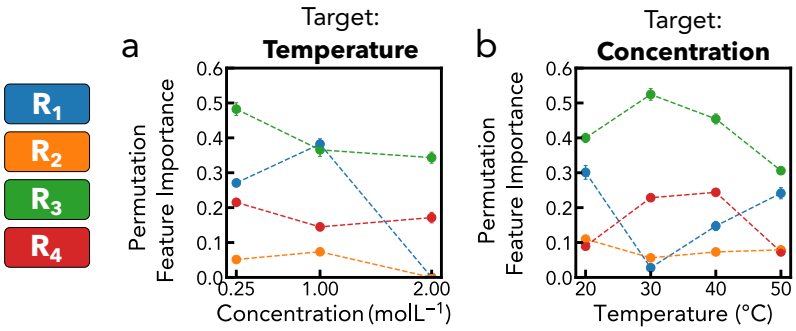


**Figure 5.19: Permutation Feature Importance: a,** Permutation Feature Importance when predicting the temperature at different salt concentrations. The mean squared error of the model was 1.86 °C$^2$, 1.33 °C$^2$, and 0 °C$^2$ for the subset of 0.25 M, 1 M, and 2 M salt concentrations respectively. **b,** Permutation Feature Importance when predicting the concentration at different temperatures. The mean squared error of the model was 0.031 M$^2$, 0.006 M$^2$, 0.003 M$^2$, and 0.028 M$^2$ for the subset of 20 °C, 30 °C, 40 °C, and 50 °C respectively.

The results show that $R_3$ has the highest permutation feature importance in almost all models, particularly for predicting concentrations. This is most evident for the models predicting the concentration at 30 °C and 40 °C where $R_3$ contributes significantly to the models' high accuracy (mse = 0.006 M$^2$ and mse = 0.003 M$^2$). This generally aligns with our previous conclusions that $R_3||C_3$ is related to the SEI since the SEI growth rate, and thus $R_3$ is severely affected by the salt concentration. However, a more in-depth analysis needs to be conducted, which could include training the models with more features (capacitances and Warburg) and binning the data sets according to the OCV resting time, i.e., the duration of lithium-electrolyte exposure time.

### 5.5.2 Dynamic Impedance Spectroscopy

To validate our conclusions in assigning NPL and SEI contributions to ECM components and expand the investigation of interphase impedance beyond OCV conditions, experiments where lithium is cycled through the cells should be conducted. There are key challenges when designing such experiments.

Firstly, as soon as lithium is stripped from one electrode and platted onto the other, the symmetry assumption used throughout this study, equating both electrodes and thus their respective impedance contributions (which justified the absence of a reference electrode), breaks down. Indeed, Srout *et al.* showed the arising asymmetry of working and counter electrodes in symmetric lithium-lithium cells upon lithium stripping and plating. [43]

Secondly, classic EIS must be conducted under stationary conditions when the system remains in a steady state. This requirement is already limiting the OCV investigation conducted herein to a fairly high frequency cut off of 100 mHz since a growing interphase layer contradicts stationary conditions (as shown in section Figure 5.4 Kramer Kronig relation are satisfied in this study).

Thirdly, classic EIS must be conducted under linearity requirements, which restricts it to small voltage perturbations (linearity assumption) since the relation between current and voltage is generally nonlinear. Dynamic impedance spectroscopy (DEIS) can be used to address the challenges of stationary and linearity and thus make EIS more broadly applicable to studying interphase corrosion and galvanostatic conditions. An extensive review elaborating on DEIS was published by Hallemans *et al.* recently. [233] Multi-sine excitation coupled with time-varying transfer functions could be combined to test symmetric lithium cells in a LiFSI G4 electrolyte. An in-situ cutting setup could be constructed similar to Odziemkowski *et al.* to probe the initial interphase formation reactions using DEIS. [222, 223] In addition, galvanostatic cycling can be conducted to monitor EIS during cell operation.

To initiate the investigation of the latter, preliminary experiments using galvanostatic electrochemical impedance spectroscopy (GEIS) were conducted. As illustrated in the measurement protocol shown in Figure 5.20a, symmetric lithium cells were

rested for 24 h under OCV to enable the interphase passivation. Subsequently, an areal current of 5 µA cm$^{-2}$ was applied for 10 min and simultaneously, a voltage perturbation was applied to determine the cell impedance. This procedure was repeated with an increasing amount of areal current with a stepsize of 5 µA cm$^{-2}$. Keeping the areal current low aims to mitigate the above-mentioned challenges on the stationary and linearity of the cells. To address the issue of electrode asymmetry, the impedance data was fit to a simple $R_0$ in series with $R_{interphase}||CPE_{interphase}$ circuit and the total interphase impedance $R_{interphase}$ of both electrodes was monitored as a function of areal current and stripping time (Figure 5.20b-d).

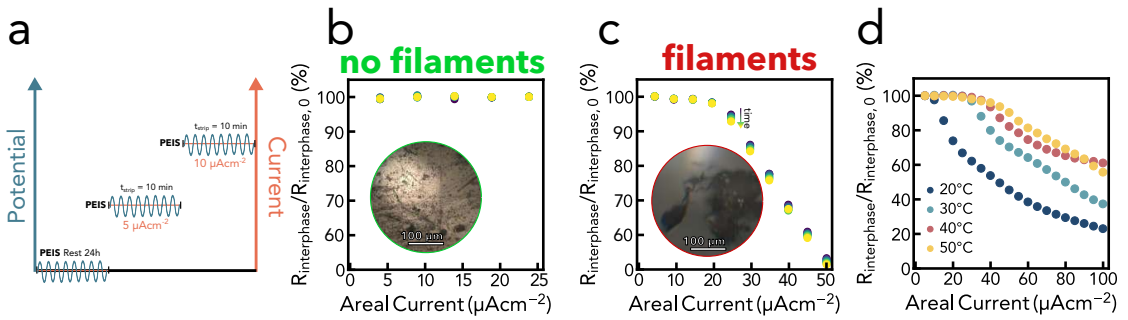


**Figure 5.20: Galvanostatic Electrochemical Impedance Spectroscopy: a,** Illustration of the measurement protocol of all cells. First the cells are rested for 24 h under OCV conditions, then an incrementally increasing amount of areal current is drawn which is overlaid by a voltage perturbation. **b,** Shows the $R_{interphase}$ as a function of areal current, stopped at 25 µA cm$^{-2}$. The dark to bright color indicates how time progresses for multiple EIS at a constant areal current. A light microscopy picture of the plating electrode is shown on the inset. **c,** shows the $R_{interphase}$ as a function of areal current, stopped at 50 µA cm$^{-2}$. The dark to bright color indicates how time progresses for multiple EIS at a constant areal current. A light microscopy picture of the plating electrode is shown on the inset. **d,** shows the $R_{interphase}$ as a function of areal current for cells at different temperatures. The dark to bright color indicates how time progresses for multiple EIS at a constant areal current.

As shown in Figure 5.20b, $R_{interphase}$ does not change below 25 µA cm$^{-2}$. If larger currents are drawn, a decrease $R_{interphase}$ can be observed as shown in Figure 5.20c. Post-mortem light microscopy images of the plating electrodes indicate the presence of filament structures on the electrode where an impedance drop was observed, while no such surface morphology could be detected on pristine electrodes or before the impedance drop. Consequently, the drop in $R_{interphase}$ might be ascribed to

a surface area increase due to filament nucleation. An impedance drop due to surface roughening caused by inhomogeneous lithium plating has been reported before. [234] When comparing cells at different temperatures (Figure 5.20d), a delay of the impedance drop can be detected. This could indicate that lithium plates more uniformly at higher currents if the operation temperature is increased. It generally aligns with a delayed filament nucleation onset at elevated temperatures detected in ORGA described in section 4.3.2 of this thesis. However, a more elaborate setup with advanced DEIS analysis is required to validate these preliminary results.

# 6 Conclusion

## Contents



## 6.1 Conclusion

To electrify the aviation space, a new generation of cell chemistry is required that provides higher energy densities, improved cell safety, and good performance at high cycling rates. TMF cathodes combined with Li-metal anodes could unlock the requirements for electric flight; however, its development is still at an early stage. In this thesis, $FeF_2$-Li-metal batteries in liquid electrolytes were investigated. The thesis is structured into three parts governing the cathode, electrolyte, and anode of the system, respectively.

In the first part, a new wet-milling strategy is developed, which enables the production of a homogeneous TMF particle size distribution. $FeF_2$ nanoparticles are then used to demonstrate that the particle median, which can be tuned with milling speed, correlates with the accessible discharge capacity of the active material at a slow cycling speed. In light of the poor electronic conductivity of TMF cathodes,

different carbon mixing strategies are compared, and a novel co-dispersion mixing technique is presented, which enables excellent capacity retention for over 500 cycles and a high cycling reversibility for composites with up to 85% active material. The cycled $FeF_2$ is studied, and the aging mechanism in $[FSI]^-$ electrolyte is elucidated. $[FSI]^-$ plays a critical role in forming a CEI, which prevents particle fusing and active material dissolution, the main degradation mechanism in TMF cathodes. However, a redox-active oxide phase is gradually formed and correlated with consumption of $[FSI]^-$ through cycling. Figure 3.33a and b illustrate the aging mechanism and the role of $[FSI]^-$ during cycling. Subsequent experiments were conducted at elevated temperatures, and cycling up to 120 °C is demonstrated. Higher thermal energy allows access to higher capacities and enables a better rate capability, yet the aging mechanism is accelerated as parasitic reactions exacerbate. A custom-made STA-cell setup is developed to investigate and compare the thermal stability of the $FeF_2$-Li-metal-IL chemistry to an oxide analog. The results indicate that a $FeF_2$-Li-metal-IL could be stable up to the melting point of lithium. Pouch cells were prepared to demonstrate the cycling reversibility in larger cell formats and energy density calculations indicate the competitiveness of the demonstrated cell chemistry under some assumptions. The development of an appropriate electrolyte formulation would enable a battery chemistry capable of advancing the electrification of the aviation industry.

The second part focused on electrolyte development, in particular, the characterization of lithium transport in solution. ORGA, a unified setup to measure transport and thermodynamic properties, is introduced, and its development into a holistic electrolyte characterization tool is described. In particular, a single-crystal sapphire cell body was incorporated into ORGA as an external reference standard. The reliability of this novel approach is validated using a model LiFSI G4 electrolyte. With the external reference visualization of concentration gradients of every Raman active species in the electrolyte is possible. Besides, lithium filament nucleation and propagation can be monitored and compared for different electrolytes and measurement conditions. Further, a temperature chamber was designed, which

enables the study of the temperature-dependency of lithium transport. Transport and thermodynamic properties of 1 M LiFSI G4 are reported and discussed between 20 °C to 50 °C.

The last part of this thesis addressed Li-metal anodes in liquid electrolytes, in particular, their interphase layers, and how they can be studied and deconvoluted using EIS. A suitable cell design and lithium preparation technique were developed to collect reproducible data that is not obscured by inactive cell components and thus enable the study of interphase impedances. The study revealed that the Nyquist plot of symmetric lithium cells yields two visually separate semicircles if lithium does not cover the entire current collector, a phenomenon that is often misunderstood as a deconvolution of interphase impedance contributions in the scientific community. Further, a comparison of different lithium preparation techniques reveals how differences in surface topology severely affect the magnitude of measured impedance due to differences in surface area and resistances in the NPL. Suitable models to fit this system are discussed in and an ECM is proposed and used throughout a systematic EIS study where the effect of temperature, salt concentration, and lithium activity on interphase impedance is investigated. The results indicate that impedance contributions from the NPL and SEI can be found and deconvoluted in the high-frequency and mid-frequency regions, respectively.

## 6.2 Further Work

Specific suggestions for future work in each of the three projects are provided in section 3.5, 4.5, and 5.5, respectively. From a holistic perspective, three key research fronts are identified that must be addressed to bring TMF-Li-metal batteries closer to application in the aviation space. First, the energy density of $FeF_2$ is on par with next-generation oxide cathodes. Since conversion chemistries are expected to exhibit inferior cycle life compared to intercalation compounds, the energy density must be further increased. This can be achieved by increasing the reduction potential of the metal center or decreasing its weight. The holy grail of the field, $CuF_2$, exhibits

limited cycling reversibility, and the origin, believed to be rooted in the solubility and mobility of $Cu^{1+}$ intermediates, must be further studied.

Second, the bottleneck of current TMF systems is the electrolyte. The role of $[FSI]^-$ has been elucidated in this work and should be transferred to alternative electrolyte formulations. ORGA can serve as a development tool to facilitate the selection of promising electrolyte formulations. Incorporating findings from advanced EIS fitting into ORGA can further help to extract meaningful information from the SEI and ultimately help to understand the origins of inhomogeneous lithium plating.

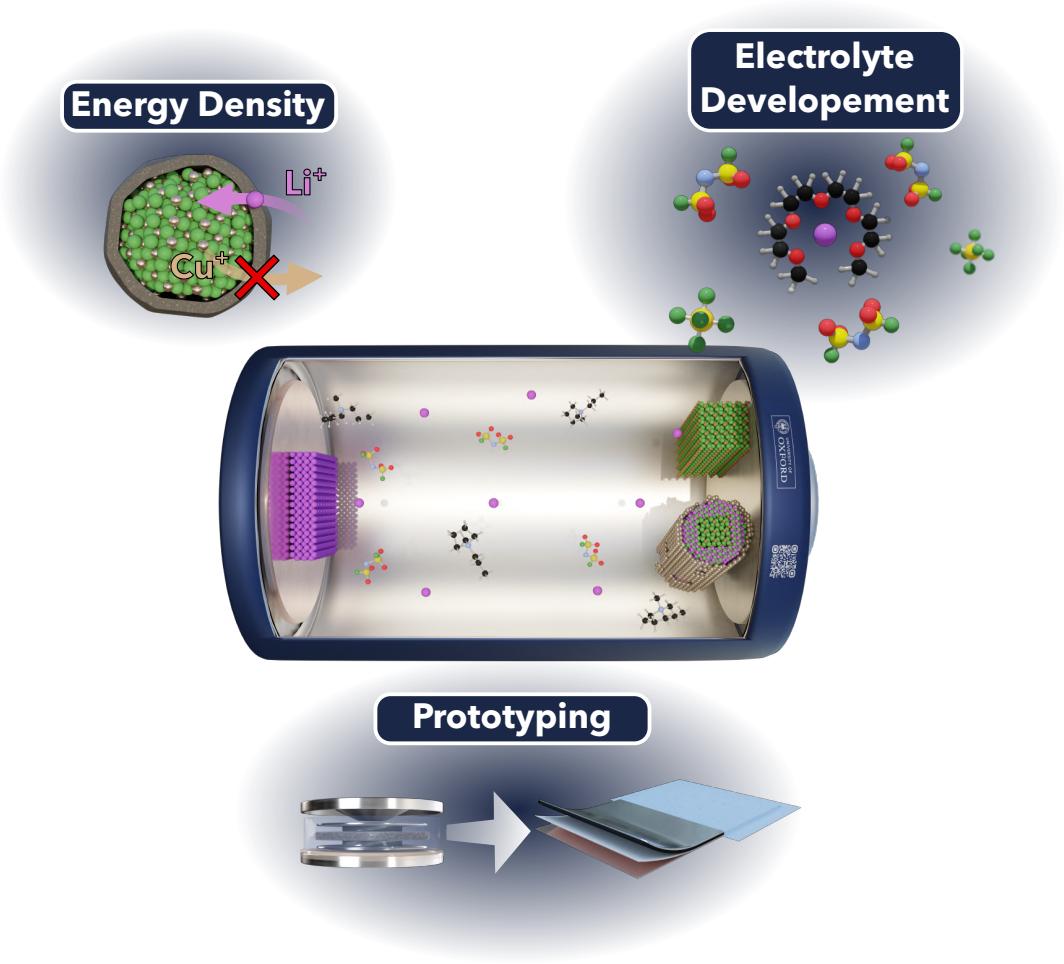


**Figure 6.1: Overview of research fronts for TMF-Li metal batteries**

Lastly, cell testing must be up-scaled to larger cell formats and ramped up with higher cell throughput. Cathode composites must be fine-tuned in mass loading and porosity towards physico-chemical properties of promising electrolyte formulations

and energy density goals. Prototypes must undergo rigorous safety testing to facilitate certification for their application in electric flight applications.

If progress is made on all three highlighted research fronts, TMF-Li-metal batteries could one day be used in electric aircrafts, thus providing significant value in decarbonizing the aviation industry.

# 7 Appendix

## 7.1 Techno Economic Analysis of TMF Cathodes

### 7.1.1 Energy Densities

The model is based on a conventional multilayer component stack with double-sided coating of electrode layers on current collector foils interleaved with separators/electrolyte layers. Complete filling of the void space in all layers with electrolyte is assumed. The density, cost, and thickness of the aluminum ($2.7\,\mathrm{g\,cm^{-3}}$, $0.3\,\$\,\mathrm{m^{-2}}$, $15\,\mu\mathrm{m}$) and copper ($8.96\,\mathrm{g\,cm^{-3}}$, $1.2\,\$\,\mathrm{m^{-2}}$, $10\,\mu\mathrm{m}$) current collector foils as well as the density and cost of the polyvinylidene fluoride binder ($1.77\,\mathrm{g\,cm^{-3}}$, $9.5\,\$\,\mathrm{kg^{-1}}$) and conductive carbon ($1.95\,\mathrm{g\,cm^{-3}}$, $6.6\,\$\,\mathrm{kg^{-1}}$) were taken from the BatPAC modeling software.[235] The separator used in all cells was modeled as polypropylene/polyethylene film with a porosity of 35% and a thickness of $16\,\mu\mathrm{m}$ the absolute density ($0.92\,\mathrm{g\,cm^{-3}}$) and cost ($1.1\,\$\,\mathrm{kg^{-1}}$) were assumed to be the same as the separator used in the BatPAC software. The NMC622 and NMC811 stacks were modeled with the same 1.2 M $LiPF_6$ in ethylene carbonate (EC)/ethylmethyl carbonate (EMC) electrolyte used in the BatPaC software.[235] The electrolyte chosen for the TMF cathodes was 1 M LiFSI in DME. The density of this electrolyte was determined to be $1.01\,\mathrm{g\,mL^{-1}}$ by direct experimental measurement.

The parameters used for all electrode active materials are shown in Supplementary table 7.1 below. In the case of the both NMC622-graphite and NMC811-lithium stacks, the parameters used were taken directly from the BatPAC model.[235] For both intercalation cathodes, the active material mass fraction was set to 96 wt% with 2 wt% each of conductive carbon and binder. The NMC622-graphite stack was modeled for the highest possible energy density with anode thickness of 100 µm, excess anode capacity of 15%, both electrodes calendared to 25% porosity, and a slim (15%) excess of electrolyte amounting to 250 µL $g^{-1}$ of cathode active material. The NMC811-lithium stack was modeled for high energy with a cathode thickness of 90 µm calendared to 30% porosity, 25% excess lithium capacity (∼34 µm thick Li foil), and 150% excess electrolyte amounting to ∼300 µL $g^{-1}$ of cathode material. For all the transition metal fluoride chemistries, the cathode thickness (90 µm) and porosity (30%) and excess electrolyte (150%) were maintained, while the excess lithium capacity was increased to 30% and the active material mass fraction decreased to 85 wt% with 10 wt% carbon and 5 wt% binder. The equilibrium cell potential for the transition metal fluoride cathodes was calculated from available thermodynamic data, and capacity was calculated based on full lithiation of from the discharged state.[236, 237] Based on what has been observed experimentally, a 300 mV overpotential was imposed on the conversion reaction, and the usable capacity was limited to 90% of the theoretical capacity.[88] A summary of the penalties imposed on conversion chemistries are summarized in table 7.1. The average cell potential and discharge capacity for the NMC622, NMC811, and graphite cathodes was taken from the BatPac software.

**Table 7.1: List of parameters used in the energy density calculations.** AM = active material, C = carbon

| **Chemistry** | **Cell Potential** (V) | **Usable Capacity** ($mA\,h\,g^{-1}$) | **Cathode Composition AM:C:Binder** (**wt%**) | **Cathode Thickness/Porosity** (µm/%) | **Anode Thickness/Porosity** (µm/%) | **Electrolyte Amount** ($mL\,g^{-1}_{cathode AM}$) |
|---|---|---|---|---|---|---|
| $FeF_2$-Li | 2.28 | 514.1 | 85:10:5 | 90/30 | 60.4/0 | 0.437 |
| $CoF_2$-Li | 2.38 | 497.7 | 85:10:5 | 90/30 | 62.2/0 | 0.411 |
| $NiF_2$-Li | 2.61 | 499.0 | 85:10:5 | 90/30 | 64.9/0 | 0.395 |
| $CuF_2$-Li | 3.19 | 475.1 | 85:10:5 | 90/30 | 57.2/0 | 0.427 |
| $FeF_3$-Li | 2.39 | 641.3 | 85:10:5 | 90/30 | 72.4/0 | 0.455 |
| NMC622-graphite | 3.72 | 180.0 | 96:2:2 | 69.5/25 | 100/25 | 0.251 |
| NMC811-Li | 3.92 | 212.0 | 96:2:2 | 90/30 | 34.1/0 | 0.307 |

The cell potentials used for the TMF represent a 300 mV overpotential on discharge. This value was based on what is commonly observed in the best $FeF_2$ cells and reflects a more realistic best-case scenario. At this stage, it would be unrealistic to assume a higher average discharge potential. The usable capacity is set to 90% of the theoretical capacity for TMF cathodes as the potential is known to drop significantly toward the end of discharge.[88] The electrolyte amount was set to 150% excess by volume and varies for the TMF cathodes primarily due to differences in active material density.

### 7.1.2 Economic Analysis

The cost of the transition metal active materials was estimated from the most recent bulk prices (late 2020) for the relevant commodity feedstock chemicals. In all cases calculations began with the price ($\$\,kg^{-1}$) of the metal (purity > 99%). From there the cost of the final product was estimated based on the series of chemical and physical processes required to synthesize the metal fluoride from the metal. While it is trivial to factor in changes in stoichiometry and the cost of additional chemical reagents, it is difficult to accurately predict the cost of production for each synthetic step. Ultimately, a full estimation of direct and indirect production costs based on a hypothetical plant design for each metal fluoride compound is beyond the scope of this perspective. All the processes involved in the synthesis of the metal fluorides considered herein are simple, single step, high-yield, reactions. So we instead estimate the production cost associated with each synthetic step as a lump sum ($\$\,kg^{-1}$) based on the relative price differences for representative commodity chemicals (e.g. Purified $Sb_2O_3$ is prepared via oxidation of Sb metal, so the difference in bulk price between the two compounds is used to approximate the cost of a calcining treatment). A 6% profit margin is further added at each step where a value-added chemical is produced. The prices of transition metal fluorides derived in this way represent a best-case scenario in which the scale of production is large and robust supply chains are already in place. While this is decidedly an oversimplification, the metal fluoride prices derived from these calculations reflect

the differences in abundance and value of the starting transition metal and appear to be quite reasonable when compared to the spot price of other battery materials. For example, the price predicted for $FeF_2$ is $7.02\,\$\,kg^{-1}$, while the spot price of slightly lithium deficient Lithium Iron Phosphate (LFP) is $5.35\,\$\,kg^{-1}$.[238]

In the case of Co and Ni, the metal is first converted to the oxide via a calcining treatment; a further production cost of $0.40\,\$\,kg^{-1}$ is added where the conversion of metal ingots to powder is required. With the exception of Cu, the metal or metal oxides are then converted to the corresponding metal chlorides using anhydrous HCl ($FeCl_2$, $CoCl_2$, $NiCl_2$) or $Cl_2$ ($FeCl_3$); the production cost associated with this process was estimated from the production of $LaCl_3$ from $La_2O_3$. Finally, the chlorides and metallic Cu are converted to the respective fluorides using anhydrous HF ($FeF_2$, $FeF_3$, $CoF_2$) or $F_2$ ($NiF_2$, $CuF_2$). A summary of all the assumed processes and production costs assumed in estimating the price of the transition metal fluorides is given in supplementary table 7.2 below.

**Table 7.2: Values used in the cost estimation for transition metal fluoride active materials.** ISE = Institut für seltene Erden und strategische Metalle (Institute for Rare Earths and Strategic Metals), LME = London Metal Exchange

| **Material** | **$FeF_2$** | **$CoF_2$** | **$NiF_2$** | **$CuF_2$** | **$FeF_3$** |
|---|---|---|---|---|---|
| Feedstock | Fe 99.9% | Co 99.5% | Ni 99.95% | Cu 99.9% | Fe 99.9% |
| Source | Li *et al.*[105] | ISE[238] | ISE | LME[239] | Li *et al.* |
| Price ($\$\,kg^{-1}$) | 1.00 | 45.43 | 20.39 | 7.67 | 1.00 |
| Process 1 | — | $Co + \frac{1}{2}O_2 \rightarrow CoO$ | $Ni + \frac{1}{2}O_2 \rightarrow NiO$ | — | — |
| Reagent/Cost ($\$\,kg^{-1}$) | — | $O_2$/0.00 | $O_2$/0.00 | — | — |
| Prod. Cost ($\$\,kg^{-1}$)/ % Profit Margin | — | $0.60^{a,b}$/6% | $0.65^{a,b}$/6% | — | — |
| Process 2 | $Fe + 2HCl \rightarrow FeCl_2 + H_2$ | $CoO + 2HCl \rightarrow CoCl_2 + H_2O$ | $NiO + 2HCl \rightarrow NiCl_2 + H_2O$ | — | $Fe + \frac{3}{2}Cl_2 \rightarrow FeCl_3$ |
| Reagent/Cost ($\$\,kg^{-1}$) | $HCl_{(g)}$/0.19 | $HCl_{(aq)}$/0.15 | $HCl_{(aq)}$/0.15 $HCl_{(g)}$/0.19 | — | $Cl_{2(g)}$/0.19 |
| Prod. Cost ($\$\,kg^{-1}$)/ % Profit Margin | $1.30^{a,b,d}$/6% | $1.30^{a,b,d}$/6% | $1.30^{a,b,d}$/6% | — | $1.30^{a,b,d}$/6% |
| Process 3 | $FeCl_2 + 2HF \rightarrow FeF_2 + 2HCl$ | $CoCl_2 + 2HF \rightarrow CoF_2 + 2HCl$ | $NiCl_2 + F_2 \rightarrow NiF_2 + Cl_2$ | $Cu + F_2 \rightarrow CuF_2$ | $FeCl_3 + 3HF \rightarrow FeF_3 + 3HCl$ |
| Reagent/Cost ($\$\,kg^{-1}$) | $HF_{(g)}$/2.12 | $HF_{(g)}$/2.12 | $F_{2(g)}$/2.23 | $F_{2(g)}$/2.23 | $HF_{(g)}$/2.12 |

Continued on next page

**Table 7.2 continued from previous page**

| **Material** | **$FeF_2$** | **$CoF_2$** | **$NiF_2$** | **$CuF_2$** | **$FeF_3$** |
|---|---|---|---|---|---|
| Prod. Cost ($\$\,kg^{-1}$)/ % Profit Margin | $3.00^{e,f}$/6% | $3.00^{e,f}$/6% | $3.00^{e,f}$/6% | $3.00^{e,f}$/6% | $3.00^{e,f}$/6% |
| Final Cost ($\$\,kg^{-1}{}_{fluoride}$) | 7.02 | 39.29 | 21.22 | 9.11 | 6.58 |

Production Costs:

a = \$0.25 for calcining or heat treatment

b = \$0.35 for chemical purification <1%

c = \$0.40 for grinding of metal to powder

d = \$0.70 for chlorination reactions

e = \$0.80 for fluorination reactions

f = \$2.20 for preparation of battery-grade active material

**Table 7.3:** Cost inputs for other battery components.

| Material | Price | Source |
|---|---|---|
| NMC622 | $20.6\,\$\,kg^{-1}$ | BatPaC |
| NMC811 | $22.0\,\$\,kg^{-1}$ | BatPaC |
| 1.2 M $LiPF_6$ in EC/EMC | $18\,\$\,kg^{-1}$ | BatPaC |
| Conductive carbon | $6.6\,\$\,kg^{-1}$ | BatPaC |
| PVDF | $6.6\,\$\,kg^{-1}$ | BatPaC |
| Separator | $1.1\,\$\,m^{-2}$ | BatPaC |
| Aluminum Foil | $0.3\,\$\,m^{-2}$ | BatPaC |
| Copper Foil | $1.2\,\$\,m^{-2}$ | BatPaC |
| Graphite | $12.5\,\$\,kg^{-1}$ | BatPaC |
| Lithium | $78.2\,\$\,kg^{-1}$ | ISE |

The price for metallic cobalt is already for a metal powder. Hydrated nickel chloride is converted to anhydrous $NiCl_2$ by heating with anhydrous HCl gas. A production cost of $2.20\,\$\,kg^{-1}$ was estimated for the preparation of battery active material by comparing the bulk price of NMC and $LiCoO_2$ with that of their respective precursor oxides.[238]

## 7.2 Energy Density Calculation from US Cathodes

**Table 7.4: Parameters used to calculate the cell level energy density:** The cell level energy densities were calculated using the cycling data in the chapter 3. In addition, some parameters were approximated based on industry standards and marked in yellow in the table below.

| Parameter | Component | Specification | Value |
|---|---|---|---|
| **Cathode** | | | |
| Composition | Active material | $FeF_2$ | 70wt% |
| | Carbon additive | Super-P | 20wt% |
| | Binder | PVDF | 10wt% |
| Density | Active material | $FeF_2$ | 4.09 g/cm$^3$ |
| | Carbon additive | Super-P | 2.1 g/cm$^3$ |
| | Binder | PVDF | 1.78 g/cm$^3$ |
| | Current Collector | Al | 2.7 g/cm$^3$ |
| Cathode layer | Porosity | | 30% |
| | Cathode density | | 2.7 g/cm$^3$ |
| | Double sided coating | | 359.4$\mu$m |
| | Current collector thickness | Al | 20 $\mu$m |
| A/C ratio | | | 1.05 |
| Cathode Electrode | Loading (one side) | | 39 mg/cm$^2$ |
| | Discharge capacity | | 461 mAh/g |
| | | Charge capacity | 461 mAh/g |
| | | Areal discharge capacity | 12 mAh/cm$^2$ |
| **Anode** | | | |
| Composition | Active material | Li metal | 100 wt% |
| Material density | Active material | Li metal | 0.534 g/cm$^3$ |
| | Current collector | Cu | 8.96 g/cm$^3$ |
| Anode layer | Porosity | Cu | 0% |
| | Electrode density | | 0.534 g/cm$^3$ |
| | Double sided coating | | 64.1$\mu$m |
| | Current collector thickness | Cu | 10$\mu$m |
| Anode electrode | Loading (one side) | | 3.42 mg/cm$^2$ |
| **Separator** | | | |
| Separator | | Celgard | 100 wt% |

Continued on next page

**Table 7.4 continued from previous page**

| Parameter | Component | Specification | Value |
|---|---|---|---|
| Material density | | Celgard | 1 g/cm$^3$ |
| Separator layer | Porosity | | 30% |
| | Layer density | | 0.7 g/cm$^3$ |
| | Thickness | | 30$\mu$m |
| **Electrolyte** | | | |
| Electrolyte | Material | 1 M LiFSI $Pyr_{1,3}FSI$ | 100 wt% |
| | Density | | 1.4 g/cm$^3$ |
| **Cell Design** | | | |
| Cathode | Double layer | Number | 34 |
| | Current Collector | Length | 161.5 mm |
| | | Width | 121.5 mm |
| | Margin (current collector) | Length | 4 mm |
| | | Width | 4 mm |
| | Coated area | Length | 157.5 mm |
| | | Width | 117.5 mm |
| | Margin (outer current collector) | Length | 38.5 mm |
| | | Width | 8.5 mm |
| Anode | Double layer | Number | 33 |
| | One side | Number | 2 |
| | Current Collector | Length | 161.5 mm |
| | | Width | 121.5 mm |
| | Margin (current collector) | Length | 2 mm |
| | | Width | 2 mm |
| | Coated area | Length | 159.5 mm |
| | | Width | 119.5 mm |
| | Margin (outer current collector) | Length | 38.5 mm |
| | | Width | 8.5 mm |
| Separator | | Number | 68 |
| | | Length | 161.5 |
| | | Width | 121.5 |
| Outer laminate (excluding tab) | | Number | 2 |
| | | Length | 200 mm |

Continued on next page

**Table 7.4 continued from previous page**

| Parameter | Component | Specification | Value |
|---|---|---|---|
| Outer laminate (including tab) | PET | Width | 130 mm |
| | | Thickness | 0.15 mm |
| | | Number | 2 |
| | Laminate | Length | 250 mm |
| | | Width | 170 mm |
| | | Thickness | 0.148 mm |
| | | Density | 205 g/m$^2$ |
| Tab | Cathode side | Length | 50 mm |
| | | Width | 40 mm |
| | | Thickness | 0.2 mm |
| | | Density | 2.7 g/cm$^3$ |
| | Anode side | Thickness | 0.2 mm |
| | | Density | 9.0 g/cm$^3$ |
| **Cell Level** | | | |
| Total Cell Weight | | 790.3 g | |
| Cell Capacity | | 158.4 Ah | |
| Average Cell Potential | | 2.0 V | |
| Cell Energy Density (vol) | | 684.7 Wh/L | |
| Cell Energy Density (grav) | | 400.3 Wh/kg | |

# References


[1] "Paris Agreement". In: *United Nations Treaty Collection* (2015).

[2] Jürgen Janek and Wolfgang G. Zeier. "A solid future for battery development". In: *Nature Energy* 1.9 (2016), pp. 1–4. URL: http://dx.doi.org/10.1038/nenergy.2016.141.

[3] Hannah Ritchie. *The price of batteries has declined by 97% in the last three decades - Our World in Data*. URL: https://ourworldindata.org/battery-price-decline.

[4] IEA. *The Role of Critical Minerals in Clean Energy Transitions*. Tech. rep. 2021. URL: https://www.iea.org/reports/the-role-of-critical-minerals-in-clean-energy-transitions.

[5] IEA. *Global EV Outlook 2020 – Analysis - IEA*. Paris, 2020. URL: https://www.iea.org/reports/global-ev-outlook-2020.

[6] Venkatasubramanian Viswanathan et al. "The challenges and opportunities of battery-powered flight". In: *Nature* 601.7894 (Jan. 2022), pp. 519–525.

[7] Shashank Sripad and Venkatasubramanian Viswanathan. "The promise of energy-efficient battery-powered urban aircraft". In: *Proceedings of the National Academy of Sciences of the United States of America* 118.45 (2021). URL: https://doi.org/10.1073/pnas.2111164118.

[8] Mark Moore. *Whisper Aero Reveal Part 8: The Whisper Jet*. Tech. rep. Whisper Aero, 2023.

[9] John Newman and Thomas W. Chapman. "Restricted diffusion in binary solutions". In: *AIChE Journal* 19.2 (Mar. 1973), pp. 343–348. URL: https://onlinelibrary.wiley.com/doi/full/10.1002/aic.690190220%20https://onlinelibrary.wiley.com/doi/abs/10.1002/aic.690190220%20https://aiche.onlinelibrary.wiley.com/doi/10.1002/aic.690190220.

[10] Feixiang Wu and Gleb Yushin. "Conversion cathodes for rechargeable lithium and lithium-ion batteries". In: *Energy and Environmental Science* 10.2 (2017), pp. 435–459.

[11] Arumugam Manthiram. "A reflection on lithium-ion battery cathode chemistry". In: *Nature Communications 2020 11:1* 11.1 (Mar. 2020), pp. 1–9. URL: https://www.nature.com/articles/s41467-020-15355-0.

[12] Lorenz F. Olbrich, Albert W. Xiao, and Mauro Pasta. "Conversion-type fluoride cathodes: Current state of the art". In: *Current Opinion in Electrochemistry* 30 (2021), p. 100779. URL: https://doi.org/10.1016/j.coelec.2021.100779.

[13] Chaofeng Liu, Zachary G. Neale, and Guozhong Cao. "Understanding electrochemical potentials of cathode materials in rechargeable batteries". In: *Materials Today* 19.2 (Mar. 2016), pp. 109–123.

[14] John S. Newman and Nitash P. Balsara. *Electrochemical Systems - The Electrochemical Society Series*. 4th Editio. Wiley, 2021.

[15] Gustavo M. Hobold et al. *Moving beyond 99.9% Coulombic efficiency for lithium anodes in liquid electrolytes*. Oct. 2021.

[16] Ilya A. Shkrob et al. "Why bis(fluorosulfonyl)imide is a "magic anion" for electrochemistry". In: *Journal of Physical Chemistry C* 118.34 (2014), pp. 19661–19671.

[17] Xia Cao et al. "Review—Localized High-Concentration Electrolytes for Lithium Batteries". In: *Journal of The Electrochemical Society* 168.1 (Jan. 2021), p. 010522. URL: https://iopscience.iop.org/article/10.1149/1945-7111/abd60e%20https://iopscience.iop.org/article/10.1149/1945-7111/abd60e/meta.

[18] Tianhong Hou and Charles W. Monroe. "Composition-dependent thermodynamic and mass-transport characterization of lithium hexafluorophosphate in propylene carbonate". In: *Electrochimica Acta* 332 (Feb. 2020), p. 135085.

[19] Lars Ole Valoen and Jan N. Reimers. "Transport Properties of LiPF[sub 6]-Based Li-Ion Battery Electrolytes". In: *Journal of The Electrochemical Society* 152.5 (Mar. 2005), A882. URL: https://iopscience.iop.org/article/10.1149/1.1872737%20https://iopscience.iop.org/article/10.1149/1.1872737/meta.

[20] Andrew A. Wang et al. "Shifting-reference concentration cells to refine composition-dependent transport characterization of binary lithium-ion electrolytes". In: *Electrochimica Acta* 358 (Oct. 2020), p. 136688.

[21] Johannes Landesfeind et al. "Determination of Transport Parameters in Liquid Binary Lithium Ion Battery Electrolytes". In: *Journal of The Electrochemical Society* 164.4 (Feb. 2017), A826. URL: https://iopscience.iop.org/article/10.1149/2.1131704jes%20https://iopscience.iop.org/article/10.1149/2.1131704jes/meta.

[22] Jack Fawdon et al. "Insights into the Transport and Thermodynamic Properties of a Bis(fluorosulfonyl)imide-Based Ionic Liquid Electrolyte for Battery Applications". In: *Journal of Physical Chemistry Letters* 13.7 (Feb. 2022), pp. 1734–1741.

[23] Andreas Nyman, Mårten Behm, and Göran Lindbergh. "Electrochemical characterisation and modelling of the mass transport phenomena in LiPF6–EC–EMC electrolyte". In: *Electrochimica Acta* 53.22 (Sept. 2008), pp. 6356–6365.

[24] Andrew R. Crothers, Clayton J. Radke, and John M. Prausnitz. "110th Anniversary: Theory of Activity Coefficients for Lithium Salts in Aqueous and Nonaqueous Solvents and in Solvent Mixtures". In: *Industrial and Engineering Chemistry Research* 58.39 (Oct. 2019), pp. 18367–18377. URL: https://www.researchgate.net/publication/334623581_110th_Anniversary_Theory_of_Activity_Coefficients_for_Lithium_Salts_in_Aqueous_and_Nonaqueous_Solvents_and_in_Solvent_Mixtures.

[25] R.A. Robinson R.H. Stokes. *Electrolyte Solutions: Second Revised Edition*. Courier Corporation, 2002.

[26] M. S. Ding et al. "Change of Conductivity with Salt Content, Solvent Composition, and Temperature for Electrolytes of LiPF[sub 6] in Ethylene Carbonate-Ethyl Methyl Carbonate". In: *Journal of The Electrochemical Society* 148.10 (Sept. 2001), A1196. URL: https://iopscience.iop.org/article/10.1149/1.1403730%20https://iopscience.iop.org/article/10.1149/1.1403730/meta.

[27] E. R. Logan et al. "A Study of the Physical Properties of Li-Ion Battery Electrolytes Containing Esters". In: *Journal of The Electrochemical Society* 165.2 (Jan. 2018), A21–A30. URL: https://iopscience.iop.org/article/10.1149/2.0271802jes%20https://iopscience.iop.org/article/10.1149/2.0271802jes/meta.

[28] Tesla. *2020 Annual Meeting of Stockholders and Battery Day | Tesla United Kingdom*. Tech. rep. Sept. 2020. URL: https://www.tesla.com/en_gb/2020shareholdermeeting.

[29] Jun Liu et al. "Pathways for practical high-energy long-cycling lithium metal batteries". In: *Nature Energy 2019 4:3* 4.3 (Feb. 2019), pp. 180–186. URL: https://www.nature.com/articles/s41560-019-0338-x.

[30] Ben Jagger and Mauro Pasta. "Solid electrolyte interphases in lithium metal batteries". In: *Joule* 7.10 (Oct. 2023), pp. 2228–2244.

[31] Yuzhang Li et al. "Atomic structure of sensitive battery materials and interfaces revealed by cryo–electron microscopy". In: *Science* 358.6362 (Oct. 2017), pp. 506–510. URL: https://www.science.org/doi/10.1126/science.aam6014.

[32] Chengcheng Fang et al. "Pressure-tailored lithium deposition and dissolution in lithium metal batteries". In: *Nature Energy 2021 6:10* 6.10 (Oct. 2021), pp. 987–994. URL: https://www.nature.com/articles/s41560-021-00917-3.

[33] Michael J. Zachman et al. "Cryo-STEM mapping of solid–liquid interfaces and dendrites in lithium-metal batteries". In: *Nature 2018 560:7718* 560.7718 (Aug. 2018), pp. 345–349. URL: https://www.nature.com/articles/s41586-018-0397-3.

[34] Chen Gong et al. "Revealing the Role of Fluoride-Rich Battery Electrode Interphases by Operando Transmission Electron Microscopy". In: *Advanced Energy Materials* 11.10 (Mar. 2021), p. 2003118. URL: https://onlinelibrary.wiley.com/doi/full/10.1002/aenm.202003118%20https://onlinelibrary.wiley.com/doi/abs/10.1002/aenm.202003118%20https://onlinelibrary.wiley.com/doi/10.1002/aenm.202003118.

[35] Xia Cao et al. "Monolithic solid–electrolyte interphases formed in fluorinated orthoformate-based electrolytes minimize Li depletion and pulverization". In: *Nature Energy 2019 4:9* 4.9 (Sept. 2019), pp. 796–805. URL: https://www.nature.com/articles/s41560-019-0464-5.

[36] Zhiao Yu et al. "Molecular design for electrolyte solvents enabling energy-dense and long-cycling lithium metal batteries". In: *Nature Energy 2020 5:7* 5.7 (June 2020), pp. 526–533. URL: https://www.nature.com/articles/s41560-020-0634-5.

[37] Katherine J. Harry et al. "Detection of subsurface structures underneath dendrites formed on cycled lithium metal electrodes". In: *Nature Materials 2013 13:1* 13.1 (Nov. 2013), pp. 69–73. URL: https://www.nature.com/articles/nmat3793.

[38] Svenja K. Otto et al. "In-Depth Characterization of Lithium-Metal Surfaces with XPS and ToF-SIMS: Toward Better Understanding of the Passivation Layer". In: *Chemistry of Materials* 33.3 (Feb. 2021), pp. 859–867. URL: https://pubs.acs.org/doi/full/10.1021/acs.chemmater.0c03518.

[39] Doron Aurbach. "Review of selected electrode–solution interactions which determine the performance of Li and Li ion batteries". In: *Journal of Power Sources* 89.2 (Aug. 2000), pp. 206–218.

[40] Wei Wei Wang et al. "Evaluating Solid-Electrolyte Interphases for Lithium and Lithium-free Anodes from Nanoindentation Features". In: *Chem* 6.10 (Oct. 2020), pp. 2728–2745.

[41] E. Peled, D. Golodnitsky, and G. Ardel. "Advanced Model for Solid Electrolyte Interphase Electrodes in Liquid and Polymer Electrolytes". In: *Journal of The Electrochemical Society* 144.8 (Aug. 1997), pp. L208–L210. URL: https://iopscience.iop.org/article/10.1149/1.1837858%20https://iopscience.iop.org/article/10.1149/1.1837858/meta.

[42] Arie Zaban, Ella Zinigrad, and Doron Aurbach. "Impedance spectroscopy of Li electrodes. 4. A general simple model of the Li-solution interphase in polar aprotic systems". In: *Journal of Physical Chemistry* 100.8 (Feb. 1996), pp. 3089–3101. URL: https://pubs.acs.org/sharingguidelines.

[43] Mohammed Srout et al. “Insights into the Importance of Native Passivation Layer and Interface Reactivity of Metallic Lithium by Electrochemical Impedance Spectroscopy”. In: *Small* 19.7 (Feb. 2023), p. 2206252. URL: https://onlinelibrary.wiley.com/doi/full/10.1002/smll.202206252%20https://onlinelibrary.wiley.com/doi/abs/10.1002/smll.202206252%20https://onlinelibrary.wiley.com/doi/10.1002/smll.202206252.

[44] Alexandros Ch Lazanas and Mamas I. Prodromidis. “Electrochemical Impedance SpectroscopyA Tutorial”. In: *ACS Measurement Science Au* 3.3 (June 2023), pp. 162–193. URL: https://pubs.acs.org/doi/full/10.1021/acsmeasuresciau.2c00070.

[45] Mark E Orazem, Pankaj Aganval ’, and Luis H Garcia-Rubio ’. “Critical issues associated with interpretation of impedance spectra l”. In: *Journal of Electroanalytical Chemistry* 378 (1994), pp. 51–62.

[46] J. E.B. Randles. “Kinetics of rapid electrode reactions”. In: *Faraday Discussions* 1 (1947), pp. 11–19.

[47] H. Schranzhofer et al. “Electrochemical impedance spectroscopy study of the SEI formation on graphite and metal electrodes”. In: *Journal of Power Sources* 153.2 (Feb. 2006), pp. 391–395.

[48] Georg Bieker, Martin Winter, and Peter Bieker. “Electrochemical in situ investigations of SEI and dendrite formation on the lithium metal anode”. In: *Physical Chemistry Chemical Physics* 17.14 (Mar. 2015), pp. 8670–8679. URL: https://pubs.rsc.org/en/content/articlehtml/2015/cp/c4cp05865h%20https://pubs.rsc.org/en/content/articlelanding/2015/cp/c4cp05865h.

[49] Kyungmi Lim et al. “Porosity of Solid Electrolyte Interphases on Alkali Metal Electrodes with Liquid Electrolytes”. In: *ACS Applied Materials and Interfaces* 13.43 (2021), pp. 51767–51774.

[50] Liping Wang et al. “Long lifespan lithium metal anodes enabled by Al2O3 sputter coating”. In: *Energy Storage Materials* 10 (Jan. 2018), pp. 16–23.

[51] Jens Becking et al. “Lithium-Metal Foil Surface Modification: An Effective Method to Improve the Cycling Performance of Lithium-Metal Batteries”. In: *Advanced Materials Interfaces* 4.16 (Aug. 2017).

[52] Bo Zhao et al. “In vacuo XPS investigation of surface engineering for lithium metal anodes with plasma treatment”. In: *Journal of Energy Chemistry* 66 (Mar. 2022), pp. 295–305.

[53] Nina Meddings et al. “Application of electrochemical impedance spectroscopy to commercial Li-ion cells: A review”. In: *Journal of Power Sources* 480 (Dec. 2020), p. 228742.

[54] C. H. Hsu and F. Mansfeld. “Concernng the conversion of the constant phase element parameter Y0 into a capacitance”. In: *Corrosion* 57.9 (2001), pp. 747–748.

[55] Matthew D. Murbach et al. "impedance.py: A Python package for electrochemical impedance analysis". In: *Journal of Open Source Software* 5.52 (Aug. 2020), p. 2349. URL: https://joss.theoj.org/papers/10.21105/joss.02349.

[56] Shangshang Wang et al. "Electrochemical impedance spectroscopy". In: *Nature Reviews Methods Primers* 1.1 (2021).

[57] Dennis W. Dees, Andrew N. Jansen, and Daniel P. Abraham. "Theoretical examination of reference electrodes for lithium-ion cells". In: *Journal of Power Sources* 174.2 (Dec. 2007), pp. 1001–1006.

[58] *EL-CELL - electrochemical test equipment*. URL: https://www.el-cell.com/.

[59] Mohamed Henini. "Scanning electron microscopy: an introduction". In: *III-Vs Review* 13.4 (July 2000), pp. 40–44.

[60] *Interaction Volume — St Paul's School Intranet*. URL: https://intranet.stpaulsschool.org.uk/halley-research-community/scanning-electron-microscope-sem/interaction-volume.

[61] Fred A. Stevie and Carrie L. Donley. "Introduction to x-ray photoelectron spectroscopy". In: *Journal of Vacuum Science & Technology A: Vacuum, Surfaces, and Films* 38.6 (Dec. 2020), p. 63204. URL: /avs/jva/article/38/6/063204/1024200/Introduction-to-x-ray-photoelectron-spectroscopy.

[62] Bruker. *Atomic Force Microscopy for Materials*. 2017. URL: https://www.bruker.com/en/products-and-solutions/microscopes/materials-afm/resource-library/e-book-atomic-force-microscopy-for-materials.html.

[63] *Atomic force microscopy - Wikipedia*. URL: https://en.wikipedia.org/wiki/Atomic_force_microscopy.

[64] Krefting Saskia. "Linking Lithium's Surface Topography to the Electrochemistry of Lithium Metal Batteries". PhD thesis. University of Oxford, 2022.

[65] D. J. (Derek J.) Gardiner, P. R. (Pierre R.) Graves, and H. J. (Heather J.) Bowley. *Practical Raman spectroscopy*. Springer-Verlag, 1989, p. 157. URL: https://search.worldcat.org/title/18740652.

[66] Andreas W. Schäfer et al. "Technological, economic and environmental prospects of all-electric aircraft". In: *Nature Energy* 4.2 (2019), pp. 160–166. URL: http://dx.doi.org/10.1038/s41560-018-0294-x.

[67] Li Wang et al. "Anion effects on the solvation structure and properties of imide lithium salt-based electrolytes". In: *RSC Advances* 9.71 (2019), pp. 41837–41846.

[68] Feixiang Wu, Joachim Maier, and Yan Yu. "Guidelines and trends for next-generation rechargeable lithium and lithium-ion batteries". In: *Chemical Society Reviews* 49.5 (2020), pp. 1569–1614.

[69] F. Badway et al. “Carbon Metal Fluoride Nanocomposites”. In: *Journal of The Electrochemical Society* 150.10 (2003), A1318.

[70] F. Badway et al. “Carbon-Metal Fluoride Nanocomposites”. In: *Journal of The Electrochemical Society* 150.9 (2003), A1209.

[71] Hong Li, Gunther Richter, and Joachim Maier. “Reversible formation and decomposition of LiF clusters using transition metal fluorides as precursors and their application in rechargeable Li batteries”. In: *Advanced Materials* 15.9 (2003), pp. 736–739.

[72] F. Badway et al. “Structure and electrochemistry of copper fluoride nanocomposites utilizing mixed conducting matrices”. In: *Chemistry of Materials* 19.17 (2007), pp. 4129–4141.

[73] Li Liu et al. “Excellent cycle performance of Co-doped FeF 3/C nanocomposite cathode material for lithium-ion batteries”. In: *Journal of Materials Chemistry* 22.34 (2012), pp. 17539–17550.

[74] M. Anji Reddy et al. “CFx derived carbon-FeF2nanocomposites for reversible lithium storage”. In: *Advanced Energy Materials* 3.3 (2013), pp. 308–313.

[75] Jisheng Zhou et al. “Carbon-nanotube-encapsulated FeF2 nanorods for high-performance lithium-ion cathode materials”. In: *ACS Applied Materials and Interfaces* 6.23 (2014), pp. 21223–21229.

[76] Xiulin Fan et al. “In situ lithiated FeF3/C nanocomposite as high energy conversion-reaction cathode for lithium-ion batteries”. In: *Journal of Power Sources* 307 (2016), pp. 435–442. URL: `http://dx.doi.org/10.1016/j.jpowsour.2016.01.004`.

[77] Sanghyeon Kim et al. “Improved Performance in FeF2 Conversion Cathodes through Use of a Conductive 3D Scaffold and Al2O3 ALD Coating”. In: *Advanced Functional Materials* 27.35 (2017), pp. 1–8.

[78] Robert E. Doe et al. “First-principles investigation of the Li-Fe-F phase diagram and equilibrium and nonequilibrium conversion reactions of iron fluorides with lithium”. In: *Chemistry of Materials* 20.16 (2008), pp. 5274–5283.

[79] Feng Wang et al. “Conversion reaction mechanisms in lithium ion batteries: Study of the binary metal fluoride electrodes”. In: *Journal of the American Chemical Society* 133.46 (2011), pp. 18828–18836.

[80] Feng Wang et al. “2 , 3 , 2 )”. In: 50.1 (2012), pp. 19–25.

[81] Chilin Li, Lin Gu, and Joachim Maier. “Enhancement of the Li conductivity in LiF by introducing glass/crystal interfaces”. In: *Advanced Functional Materials* 22.6 (2012), pp. 1145–1149.

[82] Ying Ma and Stephen H. Garofalini. “Atomistic insights into the conversion reaction in iron fluoride: A dynamically adaptive force field approach”. In: *Journal of the American Chemical Society* 134.19 (2012), pp. 8205–8211.

[83] Ying Ma and Stephen H. Garofalini. "Interplay between the ionic and electronic transport and its effects on the reaction pattern during the electrochemical conversion in an FeF2 nanoparticle". In: *Physical Chemistry Chemical Physics* 16.23 (2014), pp. 11690–11697.

[84] Linsen Li et al. "Visualization of electrochemically driven solid-state phase transformations using operando hard X-ray spectro-imaging". In: *Nature Communications* 6 (2015), pp. 1–8.

[85] Linsen Li et al. "Origins of Large Voltage Hysteresis in High-Energy-Density Metal Fluoride Lithium-Ion Battery Conversion Electrodes". In: *Journal of the American Chemical Society* 138.8 (2016), pp. 2838–2848.

[86] Chilin Li et al. "Electrochemically driven conversion reaction in fluoride electrodes for energy storage devices". In: *npj Computational Materials* 4.1 (2018). URL: http://dx.doi.org/10.1038/s41524-018-0079-6.

[87] Khim Karki et al. "Revisiting Conversion Reaction Mechanisms in Lithium Batteries: Lithiation-Driven Topotactic Transformation in FeF 2". In: *Journal of the American Chemical Society* 140.51 (2018), pp. 17915–17922.

[88] Albert W. Xiao et al. "Understanding the conversion mechanism and performance of monodisperse FeF2 nanocrystal cathodes". In: *Nature Materials* 19.6 (2020), pp. 644–654. URL: http://dx.doi.org/10.1038/s41563-020-0621-z.

[89] Xiao Hua et al. "Revisiting metal fluorides as lithium-ion battery cathodes". In: *Nature Materials* (Jan. 2021). URL: http://www.nature.com/articles/s41563-020-00893-1.

[90] Qianwen Huang, Yun Yang Lee, and Burcu Gurkan. "Pyrrolidinium Ionic Liquid Electrolyte with Bis(trifluoromethylsulfonyl)imide and Bis(fluorosulfonyl)imide Anions: Lithium Solvation and Mobility, and Performance in Lithium Metal-Lithium Iron Phosphate Batteries". In: *Industrial and Engineering Chemistry Research* 58.50 (2019), pp. 22587–22597.

[91] Jonathan K. Ko et al. "Transport, phase reactions, and hysteresis of iron fluoride and oxyfluoride conversion electrode materials for lithium batteries". In: *ACS Applied Materials and Interfaces* 6.14 (2014), pp. 10858–10869.

[92] Wentian Gu et al. "Lithium-Iron Fluoride Battery with in Situ Surface Protection". In: *Advanced Functional Materials* 26.10 (2016), pp. 1507–1516.

[93] Wenbin Fu et al. "Iron Fluoride–Carbon Nanocomposite Nanofibers as Free-Standing Cathodes for High-Energy Lithium Batteries". In: *Advanced Functional Materials* 28.32 (2018), pp. 1–8.

[94] Enbo Zhao et al. "Lithium–Iron (III) Fluoride Battery with Double Surface Protection". In: *Advanced Energy Materials* 8.26 (2018), pp. 1–11.

[95] Xiaopeng Li et al. "Three-dimensional iron oxyfluoride/N-doped carbon hybrid nanocomposites as high-performance cathodes for rechargeable Li-ion batteries". In: *Inorganic Chemistry Frontiers* 6.2 (2019), pp. 465–472.

[96] Xiaodi Ren et al. “Role of inner solvation sheath within salt–solvent complexes in tailoring electrode/electrolyte interphases for lithium metal batteries”. In: *Proceedings of the National Academy of Sciences of the United States of America* 117.46 (2020), pp. 28603–28613.

[97] Jianhui Wang et al. “Superconcentrated electrolytes for a high-voltage lithium-ion battery”. In: *Nature Communications* 7.May (2016), pp. 1–9.

[98] Yuki Yamada et al. “Advances and issues in developing salt-concentrated battery electrolytes”. In: *Nature Energy* 4.4 (2019), pp. 269–280. URL: http://dx.doi.org/10.1038/s41560-019-0336-z.

[99] Deyang Yu et al. “Room Temperature to 150 °C Lithium Metal Batteries Enabled By a “Molecular Ionic Composite” Solid Electrolyte”. In: *ECS Meeting Abstracts* MA2020-02.5 (2020), pp. 964–964.

[100] Weixiong Wu et al. “A critical review of battery thermal performance and liquid based battery thermal management”. In: *Energy Conversion and Management* 182.January (2019), pp. 262–281. URL: https://doi.org/10.1016/j.enconman.2018.12.051.

[101] Huawei Song, Hao Cui, and Chengxin Wang. “Extremely high-rate capacity and stable cycling of a highly ordered nanostructured carbon-FeF2 battery cathode”. In: *Journal of Materials Chemistry A* 3.44 (2015), pp. 22377–22384. URL: http://dx.doi.org/10.1039/C5TA06297G.

[102] Feixiang Wu et al. “Metal-Organic Framework-Derived Nanoconfinements of CoF2and Mixed-Conducting Wiring for High-Performance Metal Fluoride-Lithium Battery”. In: *ACS Nano* (2021).

[103] Jingru Zhai, Zhengyu Lei, and Kening Sun. “3D Starfish-Like FeOF on Graphene Sheets: Engineered Synthesis and Lithium Storage Performance”. In: *Chemistry - A European Journal* 25.32 (2019), pp. 7733–7739.

[104] Christoph P. Guntlin et al. “Nanocrystalline FeF3 and MF2 (M = Fe, Co, and Mn) from metal trifluoroacetates and their Li(Na)-ion storage properties”. In: *Journal of Materials Chemistry A* 5.16 (2017), pp. 7383–7393.

[105] Matthew Li et al. “New Concepts in Electrolytes”. In: *Chemical Reviews* 120.14 (2020), pp. 6783–6819.

[106] Wentian Gu et al. “Metal fluorides nanoconfined in carbon nanopores as reversible high capacity cathodes for Li and Li-Ion rechargeable batteries: FeF2 as an example”. In: *Advanced Energy Materials* 5.4 (2015), pp. 1–7.

[107] Yangmei Han et al. “Hierarchical Mesoporous Iron Fluoride with Superior Rate Performance for Lithium-Ion Batteries”. In: *ACS Applied Materials and Interfaces* 8.48 (2016), pp. 32869–32874.

[108] Qi Zhang et al. “Packing FeF3 · 0.33H2O into porous graphene/carbon nanotube network as high volumetric performance cathode for lithium ion battery”. In: *Journal of Power Sources* 447.August 2019 (2020), p. 227303. URL: https://doi.org/10.1016/j.jpowsour.2019.227303.

[109] Min Liu et al. “Band-Gap Engineering of FeF3 · 0.33H2O Nanosphere via Ni Doping as a High-Performance Lithium-Ion Battery Cathode”. In: *ACS Sustainable Chemistry and Engineering* 8.41 (2020), pp. 15651–15660.

[110] Xiulin Fan et al. “High energy-density and reversibility of iron fluoride cathode enabled via an intercalation-extrusion reaction”. In: *Nature Communications* 9.1 (2018), pp. 1–12. URL: http://dx.doi.org/10.1038/s41467-018-04476-2.

[111] Licheng Ju et al. “Significantly Improved Cyclability of Conversion-Type Transition Metal Oxyfluoride Cathodes by Homologous Passivation Layer Reconstruction”. In: *Advanced Energy Materials* 10.9 (2020), pp. 1–8.

[112] Xiulin Fan et al. “PEDOT Encapsulated FeOF Nanorod Cathodes for High Energy Lithium-Ion Batteries”. In: *Nano Letters* 15.11 (2015), pp. 7650–7656.

[113] Luwen Wang et al. “A “4-cell” modular passive DMFC (direct methanol fuel cell) stack for portable applications”. In: *Energy* 82 (Mar. 2015), pp. 229–235.

[114] Jinli Tan et al. “Iron fluoride with excellent cycle performance synthesized by solvothermal method as cathodes for lithium ion batteries”. In: *Journal of Power Sources* 251 (2014), pp. 75–84. URL: http://dx.doi.org/10.1016/j.jpowsour.2013.11.004.

[115] Jie Li et al. “Lithium oxalyldifluoroborate/carbonate electrolytes for LiFePO4/artificial graphite lithium-ion cells”. In: *Journal of Power Sources* 195.16 (2010), pp. 5344–5350.

[116] Qingxin Chu et al. “Facile preparation of porous FeF3 nanospheres as cathode materials for rechargeable lithium-ion batteries”. In: *Journal of Power Sources* 236 (2013), pp. 188–191. URL: http://dx.doi.org/10.1016/j.jpowsour.2013.02.026.

[117] H. C. Yu et al. “Designing the next generation high capacity battery electrodes”. In: *Energy and Environmental Science* 7.5 (2014), pp. 1760–1768.

[118] Joon Kyo Seo et al. “Revisiting the conversion reaction voltage and the reversibility of the CuF2 electrode in Li-ion batteries”. In: *Nano Research* 10.12 (2017), pp. 4232–4244.

[119] Fadwa Badway, New Brunswick, and Related U S Application Data. “( 12 ) United States Patent”. In: 2.12 (2015).

[120] Fredrick Omenya et al. “Intrinsic Challenges to the Electrochemical Reversibility of the High Energy Density Copper(II) Fluoride Cathode Material”. In: *ACS Applied Energy Materials* 2.7 (2019), pp. 5243–5253.

[121] Xiao Hua et al. “Comprehensive study of the CuF2 conversion reaction mechanism in a lithium ion battery”. In: *Journal of Physical Chemistry C* 118.28 (2014), pp. 15169–15184.

[122] Daniel Gordon et al. “Mixed Metal Difluorides as High Capacity Conversion-Type Cathodes: Impact of Composition on Stability and Performance”. In: *Advanced Energy Materials* 8.19 (2018), pp. 1–10.

[123] Cesar Villa et al. "Cu-Substituted NiF 2 as a Cathode Material for Li-Ion Batteries". In: *ACS Applied Materials and Interfaces* 11.1 (2019), pp. 647–654.

[124] Jiale Xia et al. "Super-Reversible CuF2 Cathodes Enabled by Cu2+-Coordinated Alginate". In: *Advanced Materials* 34.43 (Oct. 2022), p. 2205229. URL: https://onlinelibrary.wiley.com/doi/full/10.1002/adma.202205229%20https://onlinelibrary.wiley.com/doi/abs/10.1002/adma.202205229%20https://onlinelibrary.wiley.com/doi/10.1002/adma.202205229.

[125] Yinzhu Jiang et al. "Breaking the voltage hysteresis of conversion electrodes for high energy batteries". In: (Apr. 2024). URL: https://www.researchsquare.com%20https://www.researchsquare.com/article/rs-2395682/v1.

[126] N. Pereira et al. "Iron Oxyfluorides as High Capacity Cathode Materials for Lithium Batteries". In: *Journal of The Electrochemical Society* 156.6 (2009), A407.

[127] Hyea Kim et al. "In situ formation of protective coatings on sulfur cathodes in lithium batteries with lifsi-based organic electrolytes". In: *Advanced Energy Materials* 5.6 (2015), pp. 1–8.

[128] Shinya Tawa, Kazuhiko Matsumoto, and Rika Hagiwara. "Reaction Pathways of Iron Trifluoride Investigated by Operation at 363 K Using an Ionic Liquid Electrolyte". In: *Journal of The Electrochemical Society* 166.10 (2019), A2105–A2110.

[129] Yayun Zheng et al. "Charge-discharge properties and reaction mechanism of". In: *Electrochimica Acta* (2021), p. 139627. URL: https://doi.org/10.1016/j.electacta.2021.139627.

[130] Lorenz F. Olbrich et al. "Iron fluoride-lithium metal batteries in bis(fluorosulfonyl)imide-based ionic liquid electrolytes". In: *Cell Reports Physical Science* 5.2 (Feb. 2024), p. 101787.

[131] Isaac Capone et al. "Effect of the Particle-Size Distribution on the Electrochemical Performance of a Red Phosphorus-Carbon Composite Anode for Sodium-Ion Batteries". In: *Energy and Fuels* 33.5 (2019), pp. 4651–4658.

[132] Yicong Zhou et al. "Viscous Solvent-Assisted Planetary Ball Milling for the Scalable Production of Large Ultrathin Two-Dimensional Materials". In: *ACS nano* 16.7 (2022), pp. 10179–10187.

[133] Mauro Pasta and Albert W. XIAO. *Ionic liquids in lithium ion batteries*. Oct. 2019.

[134] Qiao Huang et al. "Insights into the Effects of Electrolyte Composition on the Performance and Stability of FeF 2 Conversion-Type Cathodes". In: *Advanced Energy Materials* 9.17 (2019), pp. 1–11.

[135] Feng Wang et al. "Tracking lithium transport and electrochemical reactions in nanoparticles". In: *Nature Communications* 3 (2012), pp. 1201–1208. URL: http://dx.doi.org/10.1038/ncomms2185.

[136] Chilin Li et al. “Carbon nanotube wiring of electrodes for high-rate lithium batteries using an imidazolium-based ionic liquid precursor as dispersant and binder: A case study on iron fluoride nanoparticles”. In: *ACS Nano* 5.4 (2011), pp. 2930–2938.

[137] Seung Taek Myung et al. “Iron trifluoride synthesized via evaporation method and its application to rechargeable lithium batteries”. In: *Journal of Power Sources* 223 (Feb. 2013), pp. 1–8.

[138] Li Liu et al. “A comparison among FeF3 · 3H2O, FeF 3 · 0.33H2O and FeF3 cathode materials for lithium ion batteries: Structural, electrochemical, and mechanism studies”. In: *Journal of Power Sources* 238 (2013), pp. 501–515.

[139] Bowen Shao et al. “Enabling Conversion-Type Iron Fluoride Cathode by Halide-Based Solid Electrolyte”. In: *Advanced Functional Materials* 32.49 (Dec. 2022).

[140] Lei Zhang et al. “Formation of Fe 2O 3 microboxes with hierarchical shell structures from metal-organic frameworks and their lithium storage properties”. In: *Journal of the American Chemical Society* 134.42 (Oct. 2012), pp. 17388–17391.

[141] Lei Zhang, Hao Bin Wu, and Xiong Wen Lou. “Metal-organic-frameworks-derived general formation of hollow structures with high complexity”. In: *Journal of the American Chemical Society* 135.29 (July 2013), pp. 10664–10672.

[142] S. Ito et al. “Lithium battery having a large capacity using Fe3O4 as a cathode material”. In: *Journal of Power Sources* 146.1-2 (2005), pp. 319–322.

[143] Yong Su et al. “Enabling Long Cycle Life and High Rate Iron Difluoride Based Lithium Batteries by In Situ Cathode Surface Modification”. In: *Advanced Science* 9.21 (2022), pp. 1–11.

[144] A. P. Grosvenor et al. “Investigation of multiplet splitting of Fe 2p XPS spectra and bonding in iron compounds”. In: *Surface and Interface Analysis* 36.12 (Dec. 2004), pp. 1564–1574.

[145] Tami E Westre et al. “A Multiplet Analysis of Fe K-Edge 1s f 3d Pre-Edge Features of Iron Complexes”. In: *Journal of the American Chemical Society* 7863.20 (1997), pp. 6297–6314.

[146] Hayley Simon et al. “Fe K-edge x-ray absorption spectroscopy of corrosion phases of archaeological iron: Results, limitations, and the need for complementary techniques”. In: *Journal of Physics Condensed Matter* 33.34 (2021).

[147] Jack Fawdon et al. “Characterising lithium-ion electrolytes via operando Raman microspectroscopy”. In: *Nature Communications* 12 (1) 4053 (Dec. 2021).

[148] Junyi Zhao et al. “Transport and Thermodynamic Properties of KFSI in TEP by Operando Raman Gradient Analysis”. In: *submitted to XX* (2024).

[149] Ziyu Song et al. "Bis(fluorosulfonyl)imide-based electrolyte for rechargeable lithium batteries: A perspective". In: *Journal of Power Sources Advances* 14 (2022), p. 100088. URL: https://doi.org/10.1016/j.powera.2022.100088.

[150] Office of Energy Efficiency & Renewable Energy. *Battery500: Progress Update*. 2020. URL: https://www.energy.gov/eere/articles/battery500-progress-update.

[151] QuantumScape. *Q4 Fiscal 2022 Letter To Shareholders*. Tech. rep. QuantumScape, 2023, pp. 1–14.

[152] Nils DeVos, Cédric Maton, and Christian V. Stevens. "Electrochemical Stability of Ionic Liquids: General Influences and Degradation Mechanisms". In: *ChemElectroChem* 1.8 (2014), pp. 1258–1270.

[153] Hajime Matsumoto et al. "Fast cycling of Li/LiCoO2 cell with low-viscosity ionic liquids based on bis(fluorosulfonyl)imide [FSI]-". In: *Journal of Power Sources* 160.2 SPEC. ISS. (2006), pp. 1308–1313.

[154] Shoshi Terada et al. "Liquid Structures and Transport Properties of Lithium Bis(fluorosulfonyl)amide/Glyme Solvate Ionic Liquids for Lithium Batteries". In: *Australian Journal of Chemistry* 72.2 (Sept. 2018), pp. 70–80. URL: https://www.publish.csiro.au/ch/CH18270.

[155] Luis Aguilera et al. "A structural study of LiTFSI–tetraglyme mixtures: From diluted solutions to solvated ionic liquids". In: *Journal of Molecular Liquids* 210 (Oct. 2015), pp. 238–242.

[156] Lorenz F. Olbrich et al. "Operando Raman Gradient Analysis for Temperature-Dependent Electrolyte Characterization". In: *ACS Energy Letters* (2024), pp. 3636–3642. URL: https://pubs.acs.org/doi/abs/10.1021/acsenergylett.4c00954.

[157] Xin Bing Cheng et al. "Toward Safe Lithium Metal Anode in Rechargeable Batteries: A Review". In: *Chemical Reviews* 117.15 (2017), pp. 10403–10473.

[158] Aniruddha Jana et al. "Electrochemomechanics of lithium dendrite growth". In: *Energy & Environmental Science* 12.12 (Dec. 2019), pp. 3595–3607. URL: https://pubs.rsc.org/en/content/articlehtml/2019/ee/c9ee01864f%20https://pubs.rsc.org/en/content/articlelanding/2019/ee/c9ee01864f.

[159] Lu Wang et al. "Grid Impact of Electric Vehicle Fast Charging Stations: Trends, Standards, Issues and Mitigation Measures - An Overview". In: *IEEE Open Journal of Power Electronics* 2 (2021), pp. 56–74.

[160] E. R. Logan and J. R. Dahn. "Electrolyte Design for Fast-Charging Li-Ion Batteries". In: *Trends in Chemistry* 2.4 (Apr. 2020), pp. 354–366. URL: http://www.cell.com/article/S2589597420300368/fulltext%20http://www.cell.com/article/S2589597420300368/abstract%20https://www.cell.com/trends/chemistry/abstract/S2589-5974(20)30036-8.

[161] Kazuo Onda et al. "Thermal behavior of small lithium-ion battery during rapid charge and discharge cycles". In: *Journal of Power Sources* 158 (2006), pp. 535–542.

[162] X. Fleury et al. "Fast-charging of Lithium Iron Phosphate battery with ohmic-drop compensation method: Ageing study". In: *Journal of Energy Storage* 16 (Apr. 2018), pp. 21–36.

[163] J. David Bazak et al. "Mapping of Lithium-Ion Battery Electrolyte Transport Properties and Limiting Currents with In Situ MRI". In: *Journal of The Electrochemical Society* 167.14 (Oct. 2020), p. 140518.

[164] Andrew A. Wang et al. "Potentiometric MRI of a Superconcentrated Lithium Electrolyte: Testing the Irreversible Thermodynamics Approach". In: *ACS Energy Letters* 6.9 (Sept. 2021), pp. 3086–3095.

[165] Matilda Klett et al. "Quantifying mass transport during polarization in a Li Ion battery electrolyte by in situ 7Li NMR imaging". In: *Journal of the American Chemical Society* 134.36 (Sept. 2012), pp. 14654–14657.

[166] Athinthra Krishnaswamy Sethurajan et al. "Accurate Characterization of Ion Transport Properties in Binary Symmetric Electrolytes Using In Situ NMR Imaging and Inverse Modeling". In: *Journal of Physical Chemistry B* 119.37 (Aug. 2015), pp. 12238–12248.

[167] Go Kamesui et al. "In situ observation of the formation and relaxation processes of concentration gradients in a lithium bis(fluorosulfonyl) amide–tetraglyme solvate ionic liquid using digital holographic interference microscopy". In: *Electrochemistry Communications* 151 107506 (June 2023).

[168] Marc Doyle, Thomas F. Fuller, and John Newman. "Modeling of Galvanostatic Charge and Discharge of the Lithium/Polymer/Insertion Cell". In: *Journal of The Electrochemical Society* 140.6 (1993), pp. 1526–1533.

[169] J.O. Hirschfelder, Curtiss C.F., and Bird R.B. *The Molecular Theory of Gases and Liquids*. New York: John Wiley & Sons, 1954.

[170] George D. Verros and Fotios Giovannopoulos. "On the Maxwell-Stefan Equations for Multi-component Diffusion". In: *AIP Conference Proceedings* 1148.1 (Aug. 2009), pp. 262–266. URL: `/aip/acp/article/1148/1/262/832964/On-the-Maxwell-Stefan-Equations-for-Multi`.

[171] Jack Fawdon. "Characterising Liquid Electrolytes for Lithium-Ion and Lithium Metal Batteries". PhD thesis. University of Oxford, 2021.

[172] Lorenz Olbrich F. *https://github.com/lfo96/auto_echem*. 2024.

[173] Jing Liu and Charles W. Monroe. "Solute-volume effects in electrolyte transport". In: *Electrochimica Acta* 135 (2014), pp. 447–460. URL: `http://dx.doi.org/10.1016/j.electacta.2014.05.009`.

[174] Andreas Nyman, Mårten Behm, and Göran Lindbergh. "A Theoretical and Experimental Study of the Mass Transport in Gel Electrolytes I. Mathematical Analysis of Characterization Method". In: *Journal of The Electrochemical Society* 158.6 (Mar. 2011), A628. URL: https://iopscience.iop.org/article/10.1149/1.3560025%20https://iopscience.iop.org/article/10.1149/1.3560025/meta.

[175] Benjamin T. Chorpening et al. "Raman scattering in single-crystal sapphire at elevated temperatures". In: *Applied Optics, Vol. 56, Issue 31, pp. 8598-8606* 56.31 (Nov. 2017), pp. 8598–8606. URL: https://opg.optica.org/viewmedia.cfm?uri=ao-56-31-8598&seq=0&html=true%20https://opg.optica.org/abstract.cfm?uri=ao-56-31-8598%20https://opg.optica.org/ao/abstract.cfm?uri=ao-56-31-8598.

[176] Kang Xu. "Nonaqueous liquid electrolytes for lithium-based rechargeable batteries". In: *Chemical Reviews* 104.10 (Oct. 2004), pp. 4303–4417. URL: https://pubs.acs.org/doi/full/10.1021/cr030203g.

[177] Kang Xu. "Electrolytes and interphases in Li-ion batteries and beyond". In: *Chemical Reviews* 114.23 (Dec. 2014), pp. 11503–11618. URL: https://pubs.acs.org/doi/full/10.1021/cr500003w.

[178] Andrew A. Wang et al. "Current-driven solvent segregation in lithium-ion electrolytes". In: *Cell Reports Physical Science* 3.9 (Sept. 2022), p. 101047.

[179] Juddha Thapa et al. "Raman scattering in single-crystal sapphire at elevated temperatures". In: *Applied Optics* 56.31 (Oct. 2017), p. 8598.

[180] Shobhan Dhir et al. "Fundamental investigations on the ionic transport and thermodynamic properties of non-aqueous potassium-ion electrolytes". In: *Nature Communications 2023 14:1* 14.1 (June 2023), pp. 1–12. URL: https://www.nature.com/articles/s41467-023-39523-0.

[181] Johannes Landesfeind and Hubert A. Gasteiger. "Temperature and Concentration Dependence of the Ionic Transport Properties of Lithium-Ion Battery Electrolytes". In: *Journal of The Electrochemical Society* 166.14 (Sept. 2019), A3079–A3097. URL: https://iopscience.iop.org/article/10.1149/2.0571912jes%20https://iopscience.iop.org/article/10.1149/2.0571912jes/meta.

[182] Henrik Lundgren, Mårten Behm, and Göran Lindbergh. " Electrochemical Characterization and Temperature Dependency of Mass-Transport Properties of LiPF 6 in EC:DEC ". In: *Journal of The Electrochemical Society* 162.3 (Dec. 2015), A413–A420. URL: https://iopscience.iop.org/article/10.1149/2.0641503jes%20https://iopscience.iop.org/article/10.1149/2.0641503jes/meta.

[183] Alexandra J. Ringsby et al. "Transport Phenomena in Low Temperature Lithium-Ion Battery Electrolytes". In: *Journal of The Electrochemical Society* 168.8 (Aug. 2021), p. 080501. URL: https://iopscience.iop.org/article/10.1149/1945-7111/ac1735%20https://iopscience.iop.org/article/10.1149/1945-7111/ac1735/meta.

[184] Sergey A. Krachkovskiy et al. " Determination of Mass Transfer Parameters and Ionic Association of LiPF 6 : Organic Carbonates Solutions ". In: *Journal of The Electrochemical Society* 164.4 (Mar. 2017), A912–A916. URL: https://iopscience.iop.org/article/10.1149/2.1531704jes%20https://iopscience.iop.org/article/10.1149/2.1531704jes/meta.

[185] Kenta Fujii et al. "Unusual Li+ ion solvation structure in bis(fluorosulfonyl)amide based ionic liquid". In: *Journal of Physical Chemistry C* 117.38 (Sept. 2013), pp. 19314–19324. URL: https://pubs.acs.org/doi/full/10.1021/jp4053264.

[186] Yosuke Ugata et al. "Temperature Dependency of Ion Transport in Highly Concentrated Li Salt/Sulfolane Electrolyte Solutions". In: *Journal of Physical Chemistry C* 126.45 (Nov. 2022), pp. 19084–19090. URL: https://pubs.acs.org/doi/full/10.1021/acs.jpcc.2c06699.

[187] Lisa Neumaier et al. "Dielectric constant of mixed solvents based on perturbation theory". In: *Fluid Phase Equilibria* 555 (Apr. 2022), p. 113346.

[188] Long Hoang Bao Nguyen et al. "Investigating the abnormal conductivity behaviour of divalent cations in low dielectric constant tetraglyme-based electrolytes". In: *Physical Chemistry Chemical Physics* 24.36 (Sept. 2022), pp. 21601–21611. URL: https://pubs.rsc.org/en/content/articlehtml/2022/cp/d2cp03200g%20https://pubs.rsc.org/en/content/articlelanding/2022/cp/d2cp03200g.

[189] Adam Maraschky and Rohan Akolkar. "Temperature Dependence of Dendritic Lithium Electrodeposition: A Mechanistic Study of the Role of Transport Limitations within the SEI". In: *Journal of The Electrochemical Society* 167.6 (Mar. 2020), p. 062503. URL: https://iopscience.iop.org/article/10.1149/1945-7111/ab7ce2%20https://iopscience.iop.org/article/10.1149/1945-7111/ab7ce2/meta.

[190] Henry S. Sand. "On the Concentration at the Electrodes in a Solution, with special reference to the Liberation of Hydrogen by Electrolysis of a Mixture of Copper Sulphate and Sulphuric Acid". In: *Proceedings of the Physical Society of London* 17.1 (Oct. 1899), p. 496. URL: https://iopscience.iop.org/article/10.1088/1478-7814/17/1/332%20https://iopscience.iop.org/article/10.1088/1478-7814/17/1/332/meta.

[191] Louise Frenck et al. "Effect of salt concentration profiles on protrusion growth in lithium-polymer-lithium cells". In: *Solid State Ionics* 358 (Dec. 2020), p. 115517.

[192] Guanchen Li and Charles W. Monroe. "Modeling Lithium Transport and Electrodeposition in Ionic-Liquid Based Electrolytes". In: *Frontiers in Energy Research* 9 (May 2021), p. 660081.

[193] Patrick Judeinstein et al. "Interplay of structure and dynamics in Lithium/Ionic liquid electrolytes: Experiment and molecular simulation". In: *Journal of Physical Chemistry B* 125.6 (Feb. 2021), pp. 1618–1631. URL: https://pubs.acs.org/doi/full/10.1021/acs.jpcb.0c09597.

[194] Xiaojing Wang, Yanling Chi, and Tiancheng Mu. "A review on the transport properties of ionic liquids". In: *Journal of Molecular Liquids* 193 (May 2014), pp. 262–266.

[195] K. Oldiges et al. "Understanding transport mechanisms in ionic liquid/carbonate solvent electrolyte blends". In: *Physical Chemistry Chemical Physics* 20.24 (June 2018), pp. 16579–16591. URL: https://pubs.rsc.org/en/content/articlehtml/2018/cp/c8cp01485j%20https://pubs.rsc.org/en/content/articlelanding/2018/cp/c8cp01485j.

[196] Aiping Wang et al. "Review on modeling of the anode solid electrolyte interphase (SEI) for lithium-ion batteries". In: *npj Computational Materials 2018 4:1* 4.1 (Mar. 2018), pp. 1–26. URL: https://www.nature.com/articles/s41524-018-0064-0.

[197] Yuzhang Li et al. "Revealing nanoscale passivation and corrosion mechanisms of reactive battery materials in gas environments". In: *Nano Letters* 17.8 (Aug. 2017), pp. 5171–5178. URL: https://pubs.acs.org/doi/full/10.1021/acs.nanolett.7b02630.

[198] Doron Aurbach and Arie Zaban. "Impedance spectroscopy of lithium electrodes: Part 1. General behavior in propylene carbonate solutions and the correlation to surface chemistry and cycling efficiency". In: *Journal of Electroanalytical Chemistry* 348.1-2 (Apr. 1993), pp. 155–179.

[199] Doron Aurbach and Arie Zaban. "Impedance spectroscope of lithium electrodes: Part 2. The behaviour in propylene carbonate solutions — the significance of the data obtained". In: *Journal of Electroanalytical Chemistry* 367.1-2 (Mar. 1994), pp. 15–25.

[200] Doron Aurbach and Arie Zaban. "Impedance spectroscopy of lithium electrodes: Part 3. The importance of Li electrode surface preparation". In: *Journal of Electroanalytical Chemistry* 365.1-2 (Feb. 1994), pp. 41–45.

[201] David T. Boyle et al. "Transient Voltammetry with Ultramicroelectrodes Reveals the Electron Transfer Kinetics of Lithium Metal Anodes". In: *ACS Energy Letters* 5.3 (Mar. 2020), pp. 701–709. URL: http://pubs.acs.org/journal/aelccp.

[202] Mark W. Verbrugge and Brian J. Koch. "Microelectrode Study of the Lithium/Propylene Carbonate Interface: Temperature and Concentration Dependence of Physicochemical Parameters". In: *Journal of The Electrochemical Society* 141.3053 (1994).

[203] Soshi Shiraishi, Kiyoshi Kanamura, and Zen Ichiro Takehara. "Study of the surface composition of highly smooth lithium deposited in various carbonate electrolytes containing HF". In: *Langmuir* 13.13 (June 1997), pp. 3542–3549. URL: https://pubs.acs.org/sharingguidelines.

[204] Johannes Landesfeind et al. "Tortuosity Determination of Battery Electrodes and Separators by Impedance Spectroscopy". In: *Journal of The Electrochemical Society* 163.7 (2016), A1373–A1387.

[205] Sara Drvarič Talian et al. "Transmission Line Model for Description of the Impedance Response of Li Electrodes with Dendritic Growth". In: *Journal of Physical Chemistry C* 123.46 (Nov. 2019), pp. 27997–28007. URL: https://pubs.acs.org/doi/full/10.1021/acs.jpcc.9b05887.

[206] R. de Levie. "On porous electrodes in electrolyte solutions—IV". In: *Electrochimica Acta* 9.9 (Sept. 1964), pp. 1231–1245.

[207] H. Gerischer. "Wechselstrompolarisation von Elektroden mit einem potentialbestimmenden Schritt beim Gleichgewichtspotential II". In: *Zeitschrift für Physikalische Chemie* 201.1 (Nov. 1952), pp. 55–67. URL: https://www.degruyter.com/document/doi/10.1515/zpch-1952-20105/html.

[208] J. Bisquert. "Influence of the boundaries in the impedance of porous film electrodes". In: *Physical Chemistry Chemical Physics* 2.18 (Jan. 2000), pp. 4185–4192. URL: https://pubs.rsc.org/en/content/articlehtml/2000/cp/b001708f%20https://pubs.rsc.org/en/content/articlelanding/2000/cp/b001708f.

[209] He Li et al. "Operando characterization of active surface area and passivation effects on sulfur-carbon composites for lithium-sulfur batteries". In: *Electrochimica Acta* 403 (Jan. 2022), p. 139572.

[210] Sara Drvarič Talian et al. "Transmission Line Model Impedance Analysis of Lithium Sulfur Batteries: Influence of Lithium Sulfide Deposit Formed During Discharge and Self-Discharge". In: *Journal of The Electrochemical Society* 169.1 (Jan. 2022), p. 010529. URL: https://iopscience.iop.org/article/10.1149/1945-7111/ac4a4e%20https://iopscience.iop.org/article/10.1149/1945-7111/ac4a4e/meta.

[211] Michel Adamič et al. "A Transmission Line Model of Electrochemical Cell's Impedance: Case Study on a Li-S System". In: *Journal of The Electrochemical Society* 166.3 (Nov. 2019), A5045–A5053. URL: https://iopscience.iop.org/article/10.1149/2.0061903jes%20https://iopscience.iop.org/article/10.1149/2.0061903jes/meta.

[212] Neal Fairley et al. "Systematic and collaborative approach to problem solving using X-ray photoelectron spectroscopy". In: *Applied Surface Science Advances* 5.May (2021), p. 100112. URL: https://doi.org/10.1016/j.apsadv.2021.100112.

[213] Mirna Urquidi-Macdonald, Silvia Real, and Digby D. Macdonald. "Applications of Kramers—Kronig transforms in the analysis of electrochemical impedance data—III. Stability and linearity". In: *Electrochimica Acta* 35.10 (Oct. 1990), pp. 1559–1566.

[214] J. Costard et al. "Three-Electrode Setups for Lithium-Ion Batteries". In: *Journal of The Electrochemical Society* 164.2 (Dec. 2016), A80. URL: https://iopscience.iop.org/article/10.1149/2.0241702jes%20https://iopscience.iop.org/article/10.1149/2.0241702jes/meta.

[215] Sara Drvarič Talian et al. "Influence of the Cell Casing on the Impedance of the Lithium Metal Electrode". In: *Journal of The Electrochemical Society* 170.11 (Nov. 2023), p. 110529. URL: https://iopscience.iop.org/article/10.1149/1945-7111/ad0b45%20https://iopscience.iop.org/article/10.1149/1945-7111/ad0b45/meta.

[216] Melissa L. Meyerson et al. "The effect of local lithium surface chemistry and topography on solid electrolyte interphase composition and dendrite nucleation". In: *Journal of Materials Chemistry A* 7.24 (June 2019), pp. 14882–14894. URL: https://pubs.rsc.org/en/content/articlehtml/2019/ta/c9ta03371h%20https://pubs.rsc.org/en/content/articlelanding/2019/ta/c9ta03371h.

[217] J. F. Oliver and S. G. Mason. "Liquid spreading on rough metal surfaces". In: *Journal of Materials Science 1980 15:2* 15.2 (Feb. 1980), pp. 431–437. URL: https://link.springer.com/article/10.1007/BF02396792.

[218] Mengyi Zhang et al. "Wetting Phenomena and their Effect on the Electrochemical Performance of Surface-Tailored Lithium Metal Electrodes in Contact with Cross-linked Polymeric Electrolytes". In: *Angewandte Chemie International Edition* 59.39 (Sept. 2020), pp. 17145–17153. URL: https://onlinelibrary.wiley.com/doi/full/10.1002/anie.202001816%20https://onlinelibrary.wiley.com/doi/abs/10.1002/anie.202001816%20https://onlinelibrary.wiley.com/doi/10.1002/anie.202001816.

[219] M. Schönleber, D. Klotz, and E. Ivers-Tiffée. "A Method for Improving the Robustness of linear Kramers-Kronig Validity Tests". In: *Electrochimica Acta* 131 (June 2014), pp. 20–27.

[220] Simon Lorger, Robert Usiskin, and Joachim Maier. "Transport and Charge Carrier Chemistry in Lithium Oxide". In: *Journal of The Electrochemical Society* 166.10 (June 2019), A2215–A2220. URL: https://iopscience.iop.org/article/10.1149/2.1121910jes%20https://iopscience.iop.org/article/10.1149/2.1121910jes/meta.

[221] Maryam Nojabaee et al. *Solid Electrolyte Interphase Evolution on Lithium Metal in Contact with Glyme-Based Electrolytes*. 2020.

[222] M. Odziemkowski and D. E. Irish. "An Electrochemical Study of the Reactivity at the Lithium Electrolyte/Bare Lithium Metal Interface: I . Purified Electrolytes". In: *Journal of The Electrochemical Society* 139.11 (Nov. 1992), pp. 3063–3074. URL: https://iopscience.iop.org/article/10.1149/1.2069033%20https://iopscience.iop.org/article/10.1149/1.2069033/meta.

[223] M. Odziemkowski and D. E. Irish. "An Electrochemical Study of the Reactivity at the Lithium Electrolyte/Bare Lithium Metal Interface: II . Unpurified Solvents". In: *Journal of The Electrochemical Society* 140.6 (June 1993), pp. 1546–1555. URL: https://iopscience.iop.org/article/10.1149/1.2221600%20https://iopscience.iop.org/article/10.1149/1.2221600/meta.

[224] Kyungmi Lim et al. “Porosity of Solid Electrolyte Interphases on Alkali Metal Electrodes with Liquid Electrolytes”. In: *ACS Applied Materials and Interfaces* 13.43 (Nov. 2021), pp. 51767–51774. URL: https://pubs.acs.org/doi/full/10.1021/acsami.1c15607.

[225] Jack Aspinall et al. “Preprint: Lithium magnesium alloys: a framework for investigating lithium alloy anodes for solid state batteries”. In: *Research Square* (2023).

[226] Truls Norby and Arnfinn G. Andersen. “Electrical conductivity and defect structure of lithiumdoped magnesium oxide”. In: *Applied Catalysis* 71.1 (Apr. 1991), pp. 89–102.

[227] Jeffrey G. Smith et al. “Intrinsic Conductivity in Magnesium-Oxygen Battery Discharge Products: MgO and MgO2”. In: *Chemistry of Materials* 29.7 (Apr. 2017), pp. 3152–3163. URL: https://pubs.acs.org/doi/full/10.1021/acs.chemmater.7b00217.

[228] T. Paul et al. “Computation of distribution of relaxation times by Tikhonov regularization for Li ion batteries: usage of L-curve method”. In: *Scientific Reports 2021 11:1* 11.1 (June 2021), pp. 1–9. URL: https://www.nature.com/articles/s41598-021-91871-3.

[229] George A. Baker and Peter Graves-Morris. “Padé Approximants”. In: *Padé Approximants Second Edition* (1996). URL: https://www.cambridge.org/core/books/pade-approximants/A98B8DD2AFC0AF094EB6BF96C5C77A06.

[230] L. Pauwels et al. “Key issues for reproducible impedance measurements and their well-founded error analysis in a silver electrodeposition system”. In: *Electrochimica Acta* 47.13-14 (May 2002), pp. 2135–2141.

[231] Richard Chukwu et al. “Statistical Analysis of the Measurement Noise in Dynamic Impedance Spectra”. In: *ChemElectroChem* 9.14 (July 2022), e202200109. URL: https://onlinelibrary.wiley.com/doi/full/10.1002/celc.202200109%20https://onlinelibrary.wiley.com/doi/abs/10.1002/celc.202200109%20https://chemistry-europe.onlinelibrary.wiley.com/doi/full/10.1002/celc.202200109.

[232] Leo Breiman. “Random forests”. In: *Machine Learning* 45.1 (Oct. 2001), pp. 5–32. URL: https://link.springer.com/article/10.1023/A:1010933404324.

[233] Noël Hallemans et al. “Electrochemical impedance spectroscopy beyond linearity and stationarity—A critical review”. In: *Electrochimica Acta* 466 (Oct. 2023), p. 142939.

[234] Svetlana Menkin et al. “Insights into soft short circuit-based degradation of lithium metal batteries”. In: *Faraday Discussions* 248.0 (Jan. 2024), pp. 277–297. URL: https://pubs.rsc.org/en/content/articlehtml/2024/fd/d3fd00101f%20https://pubs.rsc.org/en/content/articlelanding/2024/fd/d3fd00101f.

[235] Paul A Nelson et al. "Modeling the Performance and Cost of Lithium-Ion Batteries for Electric-Drive Vehicles, Third Edition". In: ANL/CSE-19/2 (2019). URL: http://www.osti.gov/servlets/purl/1209682/%0Ahttp://www.osti.gov/servlets/purl/1503280/.

[236] W M Haynes, David R Lide, and Thomas J Bruno, eds. *CRC Handbook of Chemistry and Physics*. 97th ed. Boca Raton, FL: CRC Press, 2017, pp. 1–2643.

[237] L B Pankratz. *Thermodynamic Properties of Halides*. Tech. rep. Washington D.C., USA: United States Bureau of Mines, 1984.

[238] Institute for rare earths and metals AG. *Metal Prices*. 2021. URL: https://en.institut-seltene-erden.de/our-service-2/Metal-prices/strategic-metals-prices/.

[239] London Metal Exchange. *LME Copper*. 2021. URL: https://www.lme.com/en-GB/Metals/Non-ferrous/Copper#tabIndex=0.